Scope of Computational Organometallic Chemistry

Structure, Reactivity and Properties

Manuel Ángel Ortuño Maqueda

PhD Thesis

Theoretical and Computational Chemistry

Supervisors:

Gregori Ujaque Pérez

Agustí Lledós Falcó

Departament de Química

Facultat de Ciències

2014

Universitat Autònoma de Barcelona
Departament de Química
Unitat de Química Física

Memoria presentada para aspirar al Grado de Doctor por
Manuel Ángel Ortuño Maqueda

Manuel Ángel Ortuño Maqueda

Visto bueno

Gregori Ujaque Pérez

Agustí Lledós Falcó

Bellaterra, 9 de Septiembre de 2014

Acknowledgments

I am delighted to dedicate this section to all people who have been involved, either actively or passively, in the dissertation. *Unofficial Acknowledgments* is mostly written in Spanish, my native language, whilst *Official Acknowledgments* is composed in English.

Unofficial Acknowledgments

"Al César lo que es del César". Todo este trabajo ha sido posible gracias a mis directores de tesis, Gregori Ujaque y Agustí Lledós. Les estoy enormemente agradecido por la ciencia y los valores que me han enseñado, así como por la confianza que han depositado en mí todos estos años. *I would also like to express my gratitude to Prof. Michael Bühl (University of St. Andrews) for his pleasant treatment and great support.*

Pero no habría sido capaz de llegar hasta aquí sin la excelente disciplina que aprendí de mis profesores en la Universidad de Almería, Ignacio Fernández de las Nieves y Fernando López Ortiz. Me acogieron en su laboratorio cuando aún estaba en la carrera y me transmitieron su gran motivación por la investigación.

A toda la unidad de química física de la UAB por su cálida acogida. Mención especial para Carles Acosta, el *sysadmin* que más me ha aguantado, Xavi Solans, con quien he compartido —y sufrido— horas y horas de docencia biotecnóloga, ¡y la máquina *Nespresso*!

To my colleagues abroad, particularly to Ludovic, Ava, Neetika and Lazaros, who made easier my stay in Scotland. I enjoyed the way we changed British tea time into Magic time.

Al grupo *transmet* y a toda la gente que ha pasado por él: Aleix, Gabor y Óscar, entre otros muchos. A Salva por guiar mis primeros pasos sobre terreno computacional. A Pietro que, por lo mucho que me ha enseñado, podría haber sido mi tercer director de tesis. A Max, quien ha sido mi ejemplo a seguir durante todos estos años. A Laia Sparrow y Almudena por su agradable compañía. A Luca por sacarme siempre una carcajada con sus extrañas anéctodas. Y finalmente a Sergi, que pese a sus *bacallades*, ha sido un compañero genial y un amigo excepcional.

A la célula *biomet*, con Jean-Didier a la cabeza. A Lur por sus deliciosos *brownies* y a Jaime por el humor absurdo con el que tanto nos reímos. A Bea por su eterna y contagiosa risa. A Victor por todas las *pissarres* y situaciones divertidas que sólo él es capaz de crear. A Elisabeth por la complicidad que nos caracteriza y los incontables *Dunkins*, cafés y *frikadas* varias que hemos disfrutado juntos. *Last but not least*, a Rosa por su gran ayuda y sinceridad; su amistad es una de las mejoras cosas que me llevo de esta etapa de mi vida.

Volviendo al sur, a todos mis amigos de Almería, en particular a Alba, Alberto, Cristóbal, Jesús, Miguel, Nacho y Samanta. A pesar de todas las técnicas computacionales que he aprendido durante el doctorado, su apoyo moral sigue siendo incalculable.

Por último, a mi padre Manuel, a mi madre Llani y a mi hermana Marta. Sé que la familia no se elige, pero si existiera tal posibilidad, no habría mejor elección que vosotros. Tenéis mi eterno agradecimiento por estar ahí siempre.

Official Acknowledgments

I would like to thank the *Ministerio de Educación, Cultura y Deporte* (Government of Spain) for (i) the predoctoral FPU fellowship that made possible the present PhD thesis and (ii) the travel scholarship that allowed me to stay for three months in the research group of Prof. Michael Bühl (University of St. Andrews). CESCA and BSC are also acknowledged for providing computational resources.

Prof. Salvador Conejero (CSIC–Universidad de Sevilla, Instituto de Investigaciones Científicas) and Prof. Ernesto de Jesús (Universidad de Alcalá) are acknowledged for their collaboration in some of the studies presented herein.

Make it simple,
but significant.

Don Draper in Mad Men

List of Abbreviations

The most common abbreviations used along the dissertation are collected as follows.

Abbreviation	Meaning
AIMD	Ab initio molecular dynamics
B3LYP	Becke's three parameters, Lee–Yang–Parr density functional
BZ	Benzene
CN	Coordination number
COD	1,5-Cyclooctadiene
D3	Grimme's dispersion function
DCM	Dichloromethane
DFT	Density functional theory
Dipp	2,6-Diisopropylphenyl
DMF	Dimethylformamide
DZ	Double-ζ (zeta)
en	Ethylenediamine
GIAO	Gauge-including atomic orbitals
HE	Heck mechanism
HI	Hiyama mechanism
HR	Heck-reinsertion mechanism
HT	Heck-transmetalation mechanism
IMe	1,3-Dimethylimidazol-2-ylidene
IMes	1,3-Bis(2,4,6-trimethylphenyl)imidazol-2-ylidene
IMes*	1,3-Bis(2,4,6-trimethylphenyl)-4,5-dimethylimidazol-2-ylidene
IPr	1,3-Bis(2,6-diisopropylphenyl)imidazol-2-ylidene
I^{t}Bu	1,3-Di-*tert*-butylimidazol-2-ylidene
JTE	Jahn–Teller effect
M06	Zhao and Truhlar's Minnesota 06 density functional
MAD	Mean absolute deviation
MD	Molecular dynamics
MM	Molecular mechanics
NHC	N-Heterocyclic carbene
NHC'	Cyclometalated N-heterocyclic carbene

NMR	Nuclear magnetic resonance
OA	Oxidative addition
P–P	Bis(phosphine)
PBE0	Perdew–Burke–Ernzerhof hybrid density functional
QM	Quantum mechanics
RDF	Radial distribution function
RE	Reductive elimination
σ-CAM	σ-Complex assisted metathesis
SMD	Solvent model density
SOMO	Single occupied molecular orbital
THF	Tetrahydrofuran
TOL	Toluene
TS	Transition state
TZ	Triple-ζ (zeta)
XC	Exchange–correlation

Atom Caption

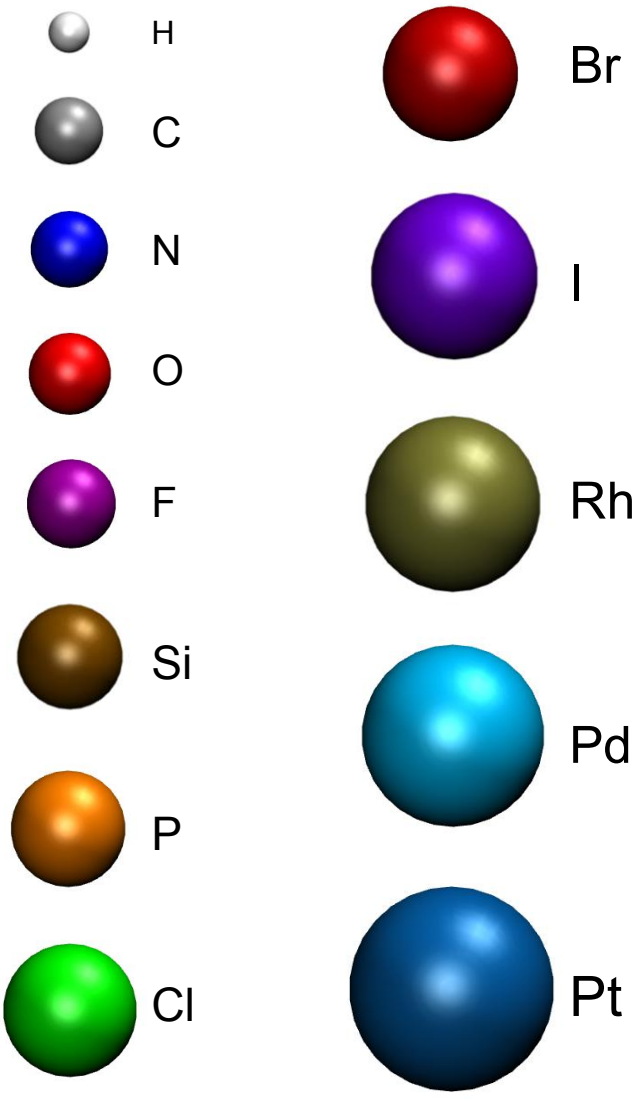

Preface

Long time ago, a younger version of myself decided to join the computational chemistry community *in blind way*. No regrets nowadays, it was totally worthy. Nobody could expect the outstanding and extensive knowledge I have received during these years of research training. I have learnt the potential of computation in resolving chemical problems as well as in understanding the essential engine of phenomena. After all, the final outcome has been captured in the text you already have in your hands.

The dissertation I proudly present here pursues to reflect both the competence and the impact of computational chemistry in the organometallic chemistry scene. Forthcoming chapters are lightly overviewed as follows. *Introduction* gathers the general concepts of the topics under further discussion and provides a simplistic sketch of the theoretical methodology employed. *Objectives* points towards the general targets this work pretends to achieve. The body of the results is divided into three different parts. *Structure* analyses the geometry of paramagnetic Pt(III) complexes and evaluate the presence of agostic interactions in low-coordinate Pt(II) species. *Reactivity* unravels the reaction mechanisms of selected transition metal-mediated processes, i.e., C–H bond activation and cross-coupling reactions. *Properties* applies several computational methods to reproduce and predict some properties of transition metal compounds, in particular, NMR chemical shifts and acid dissociation constants. *Conclusions* collects the most important remarks obtained along the study. Ultimately, in *Annex A* and *Annex B* one can find the first page of the published material I am co-author of.

I hope you enjoy the dissertation as much as I did. Thanks for reading and have fun!

Manu

Contents

1

Introduction

You don't need to be a genius to do chemistry;
you just need to be smarter than molecules.

John E. Anthony in The Organometallic Reader

1. Organometallic Chemistry

Coordination chemistry concerns a certain sort of compounds —named coordination complexes— in which a metal binds molecules or ions, so-called ligands. As a part of this area of expertise, organometallic chemistry manages to join organic and inorganic worlds, taking advantage from both of them (Figure 1.1). Common organic chemistry is plenty of covalent bonds and relatively restricted valences, whereas inorganic species exhibit ionic and dative bonds in a wide range of oxidation states. As a bridge between them, organometallic chemistry is constituted by inorganic metal centres, M, bounded to organic ligands, L. It mostly entails compounds that contain M–C or M–H bonds. However, closely related species frequently become relevant in organometallic processes, and the previous definition could seem too strict. In these cases, the previous statement is kindly broadened to include additional moieties, such as M–O or M–N bonding interactions.[1,2]

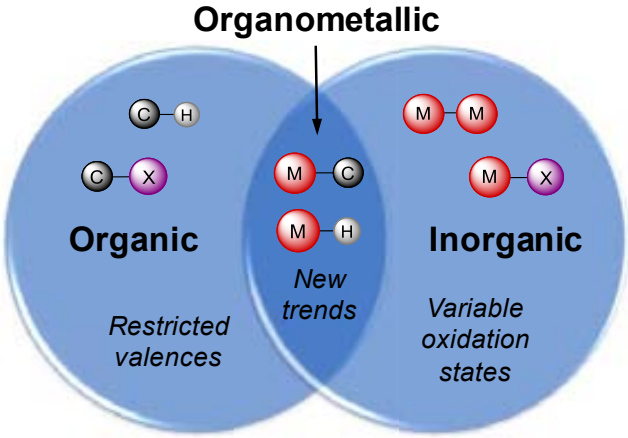

Figure 1.1 Venn diagram defining organometallic chemistry.

Organometallic chemistry comprises both metalloid and metal atoms. Transition metals including groups 3–12 stand out among other elements because of the presence of electrons in their valence *d*-subshells, which provides a quite interesting chemistry. As a result, a massive amount of organometallic studies are focused on them.[3,4]

But, how did everything begin? To answer this, a brief timeline of organometallic chemistry is shown in Figure 1.2. Detailed historical records can be consulted in proper literature.[1,2] The first organometallic species were synthesised in 1757, when Cadet unconsciously obtained a mixture of organoarsenic compounds. However, it was not until late 1830s when Bunsen characterised the so-called Cadet's fuming liquid as a mixture of $[As_2Me_4]$ —cacodyl— and $[(AsMe_2)_2O]$ —cacodyl oxide—, the first organometallic compounds.[5] The next landmark leads us to 1827, when the first olefin complex was synthesised by Zeise.[6] Afterwards, several compounds were described, such as $[Ni(CO)_4]$ or

[$PtMe_3I$], among others.[1,2] In the 1950s, the synthesis[7,8] and characterisation[9] of ferrocene species [$Fe(C_5H_5)_2$], generally known as *sandwich* complexes, became a milestone in the field.[a] From that moment on, organometallic chemistry was explosively boosted. As selected examples, two relevant cases are intentionally highlighted. In 1983, Brookhart and Green coined the term *agostic* interaction to those situations in which C–H bonds may act as ligands in metal complexes through a two-electron, three-centre, intramolecular contact.[10,11] In 1984, Kubas et al. achieved success in the characterisation of transition metal complexes with a coordinated dihydrogen molecule.[12]

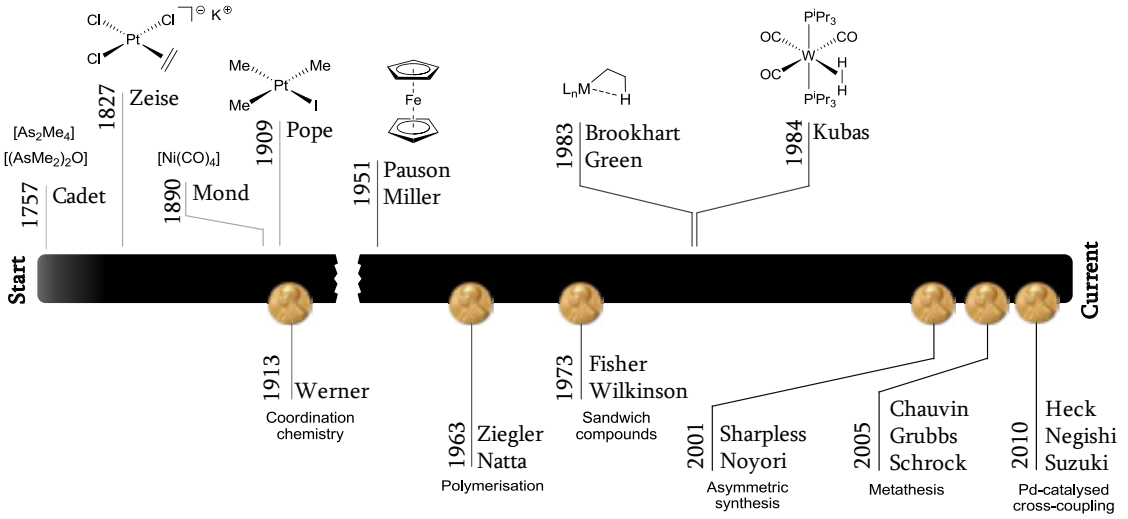

Figure 1.2 Timeline of organometallic chemistry.

Organometallic chemistry has brought up outstanding insights all along its history. In this regard, the Nobel foundation notably recognised the astonishing advances and contributions that organometallics did provide, and still does, to science (Figure 1.2).[13] One key point is that organometallic compounds either promote or undergo reactions that cannot simply be performed using straightforward organic chemistry. The main reason lies in the rich chemistry afforded by the versatile transition metals, together with the fine tuning of the ligands attached to them. From an academic point of view, this field offers unexpected behaviours uncovering new concepts, structures, and reactions. These outcomes directly bring about revolutionary applications in fine chemical synthesis[14] and materials science.[15,16] What is more, this field takes part actively in biochemistry[17] and, consequently, in medicinal chemistry.[18] Last but not least, it can also invest in sustainable features[19,20] and contribute to the energy challenge.[21]

[a] For the story about the discovery of the structure of ferrocene, see P. Laszlo, R. Hoffmann, *Angew. Chem. Int. Ed.* **2000**, *39*, 123–124.

Under this scene, computational chemistry can perfectly play its role to analyse, understand, and even predict the behaviour of organometallic compounds.[22–27] The pioneering frontier orbital theory developed by Fukui and Hoffmann paved the way to rationalise chemical reactions.[28] Another cornerstone in the field was the first ab initio study of a full catalytic cycle —olefin hydrogenation by the Wilkinson catalyst— reported by Morokuma and co-workers.[29] Since then, computational chemistry has spread massively. Computation has now a full toolbox of techniques at its disposal to inspect chemical processes at molecular level. To name a few, one can analyse bonding situations, predict structures, characterise transition states, propose reaction mechanisms, and estimate spectroscopic properties. In the organometallic ambit, computation has to handle two main issues, i.e., the description of the metal centre and the size of the ligands. Improvement of current approaches and development of new methodologies can overcome these situations. Consequently, the field has matured remarkably rapid. The emergence of user-friendly program packages makes easier the application of extremely elaborate methods, spreading the number of users. Computational chemistry also profits from advances in computer technology by improving the computing power. Indeed, the size of the systems that supercomputing machines can model becomes larger and larger every day. The whole scenario depicts a nice picture in which the breadth and depth scope of computational organometallic chemistry can be truly appreciated.

What is next? The future of organometallic chemistry looks quite promising and, definitely, it will be an ongoing research area.[30–32] Critical challenges should be addressed by science —e.g., renewable energies, water safety and supply, pharmaceutical development, and new age materials— and organometallic chemistry has a huge arsenal available to deal with them. Despite metal-free processes may occasionally become more convenient, the chemistry associated to the *d* and *f* orbitals of transition metals is unique, precious, and irreplaceable, thus chemists should take care of it and prevent it to fall into oblivion.

The current dissertation regards diverse sides of organometallic chemistry addressed from a computational point of view. For this reason, the aim of this introduction is to make a first contact with the main topics, rather than provide a detailed description, since they will be covered in future sections. In a nutshell, the structure of chemical compounds (Chapter III) serves as core foundation from which reactivity (Chapter IV) and properties (Chapter V) can be rationalised. Following this path, the geometries of four- and three-coordinate transition metal complexes are first commented and the general engines of C–H bond activation and cross-coupling reactions are subsequently discussed. To close up, the acidic properties of dihydrogen complexes are presented and transition metal nuclear magnetic resonance is introduced.

1.1. Structure of Transition Metal Complexes

As stated before, transition metal complexes are formed by metal atoms surrounded by ligands. Given the close relationship between chemical properties and molecular structure, a further understanding requires insight about the disposition of the ligands around the metal centre. Even though in main-group chemistry the geometry can be relatively easy to predict, in transition metal organometallic chemistry it is not. For instance, the nature of the metal, its spin state, and both steric and electronic effects of the ligands are some aspects that one should ponder on.

The most extended guide to rationalise coordination compounds is the 18-electron rule.[33] Analogous to the octet rule, the metal atom can fulfil 1 *s*, 3 *p*, and 5 *d* orbitals which overall count to 18 e^-. It means that the number and the nature of the M–L bonds will be devoted to accomplish this requirement. This rule is largely empirical and should not be taken *ad pedem litterae*. Indeed, literature is plenty of exceptions, especially 16-electron transition metal complexes and their 16-electron rule.[33] Considering these premises, the simplest approach to predict and explain geometries is based on the coordination number (CN) which is defined as the number of occupied coordination sites on a metal centre. Figure 1.3 relates the most common coordination numbers to their usual geometries.[1,4] Complexes with high CNs —with a maximum value of 9, one ligand per metal orbital— contain small ligands, whereas complexes with low CNs usually encompass bulky moieties. Importantly, the denticity of a ligand (κ) denotes the number of atoms in the ligand bonded to the metal. When those atoms are contiguous, the term is renamed as hapticity (η).[34] Hence, the coordination number may be different from the number of ligands.

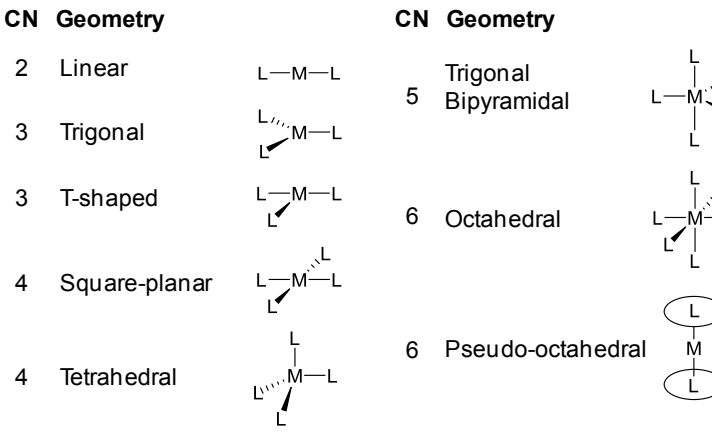

Figure 1.3 Common coordination numbers (CNs) and geometries.

The transition metal evidently plays an undeniable role in setting the structure, particularly the number of electrons in *d* orbitals. In this regard, the crystal field model is able to account for some properties by analysing electrostatic interactions between the

metal and ligands. Initially, the *d* orbitals of an isolated metal have the same energy. However, the approach of ligands along the space disturbs the metal centre and the formerly-degenerated *d* orbitals now split. The energy difference between orbitals is called crystal field splitting and is depicted by Δ. Figure 1.4 shows the effect of contacting four and six ligands with a metal centre in tetrahedral and octahedral fashions, respectively.[4] The magnitude of the splitting depends on the oxidation state of the metal as well as the nature of the ligands. Species that provide small Δ values are known as weak field ligands. Whenever the splitting is small enough, Hund's rule of maximum multiplicity applies and electrons tend to be unpaired giving rise to paramagnetic high-spin complexes. Analogously, those species that generate large Δ gaps are called strong field ligands. Here the pairing up of electrons is favoured and diamagnetic low-spin complexes are found instead.

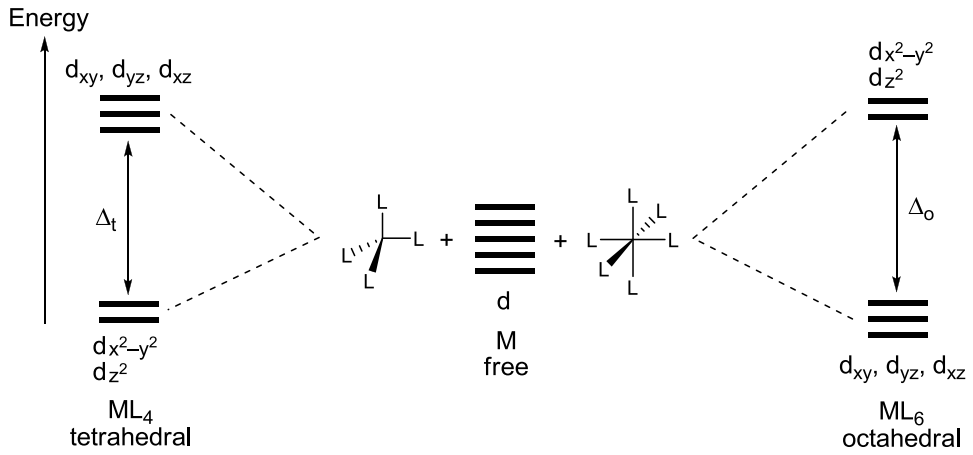

Figure 1.4 Crystal field splitting in ML_4 tetrahedral (left) and ML_6 octahedral (right) complexes.

The former approach is mostly qualitative. To move forward for a better understanding, one should appeal to the more advanced ligand field model. This theory allows to derive molecular orbital diagrams resulting from the interaction between metal and ligand orbitals of proper symmetry.[35,36]

Among the vast diversity of structures, attention is drawn herein to four- and three-coordinate platinum species.

1.1.1. Four-coordinate Pt(III) species

Four-coordinate complexes are extensively widespread throughout transition metal chemistry. Generally, a coordination number of 4 entails tetrahedral or square-planar structures (Figure 1.3) but, sometimes, unusual geometries as see-saw —also known as sawhorse or butterfly— can be found. This latter structure arranges *trans* ligands at 180° and *cis* ligands at 90–120°. A qualitative orbital diagram with those four-coordinate geometries is displayed in Figure 1.5.[36,37]

At this point, it is necessary to introduce the Jahn–Teller effect (JTE). This phenomenon can be divided into two categories.[38] The first group concerns the mixing of degenerate or nearly degenerate orbitals in incomplete shells, namely first-order JTE and pseudo JTE, respectively. The second group involves the interaction between the highest occupied molecular orbital (HOMO) and the lowest unoccupied molecular orbital (LUMO) within the same molecule, namely second order JTE. It is worth noting that distortions produced by the first group are rather small, but the effects coming from second order contributions may cause large modifications. Applying this knowledge to the symmetric tetrahedral geometry, the three upper orbitals (Figure 1.5 centre) are indeed degenerate and JTEs can take place. Therefore, see-saw (Figure 1.5 left) and square-planar (Figure 1.5 right) structures can be considered as Jahn–Teller distortions from the tetrahedral one.[39]

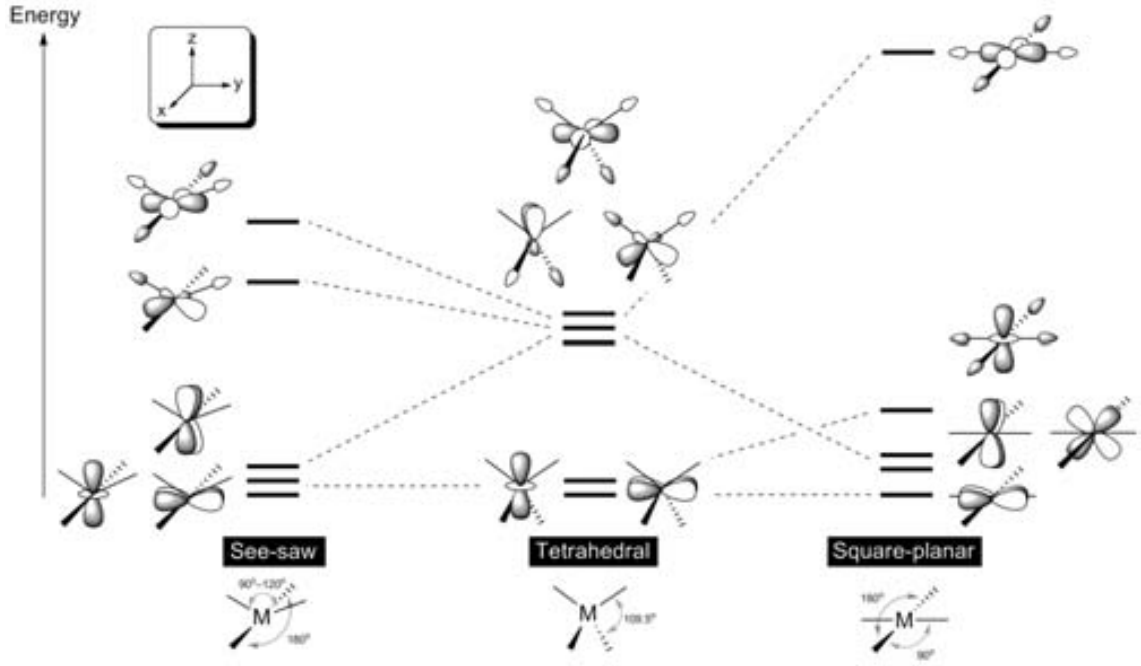

Figure 1.5 Qualitative orbital diagram of see-saw, tetrahedral, and square-planar four-coordinate complexes (σ-donor scheme). Angles in degrees.

In d^0 and d^{10} complexes, the orbitals of each *d* shell are equally occupied and, therefore, steric effects dominate establishing a tetrahedral geometry.[4] Four-coordinate d^8 complexes are mostly square-planar rather than tetrahedral since the electrons are better accommodated in the low energy orbitals of the former arrangement (Figure 1.5 right). However, less systematic trends are accepted for other d^n configurations.

Particularly, d^7 complexes can appear as tetrahedral or square-planar structures,[40] albeit the final geometry relies on additional aspects. For instance, the spin state of a complex can determine its geometry yielding different stereospinomers.[37] In d^7 complexes, high-spin states (S = 3/2) favour tetrahedral structures, whereas low-spin states (S = 1/2) enhance

square-planar ones. When second and third period transition metals are involved, the square-planar geometry is preferred in low-spin configurations.[37] Denticity of ligands is also relevant because their coordination modes may impose or distort specific shapes.[40]

The d^7 Pt(III) centre is not a common oxidation state and their complexes are characterised by one electron unpaired. Likely, they tend to either disproportionate or dimerise, hence mononuclear species are rarely characterised. Hitherto, a few square-planar and only one see-saw Pt(III) structures have been reported. The structural analysis of this novel see-saw Pt(III) complex, stabilised by bulky N-heterocyclic carbenes ligands (NHC), will be presented in Section 3.

1.1.2. Three-coordinate Pt(II) species

The coordination number 3 is less common among transition metal complexes.[41] They usually perform T-shaped and trigonal structures (Figure 1.3), although Y-shaped dispositions may also be found. A qualitative orbital diagram with these three-coordinate geometries is displayed in Figure 1.6.[35,36]

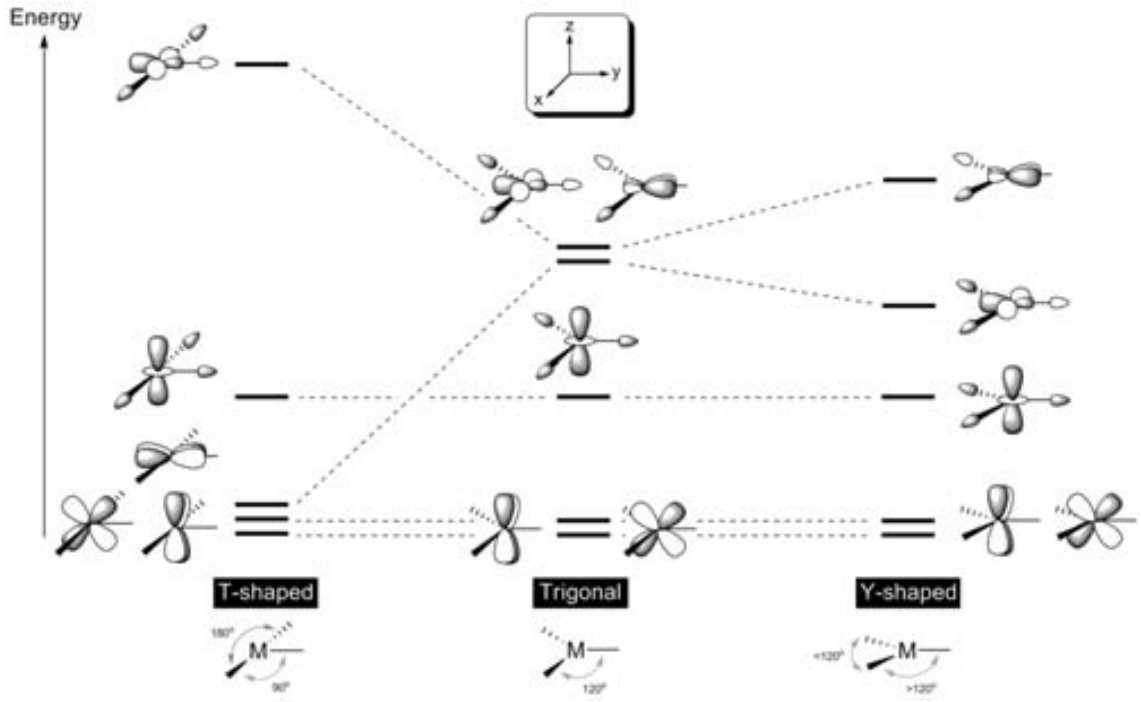

Figure 1.6 Qualitative orbital diagram of T-shaped, trigonal, and Y-shaped three-coordinate complexes (σ-donor scheme). Angles in degrees.

In line with four-coordinate species, three-coordinate T and Y shapes can be envisaged as Jahn–Teller distortions from the symmetric trigonal geometry (Figure 1.6).[42] The two upper degenerate orbitals in trigonal structures are sensitive to undergo JTEs and their mixing produces T and Y shapes. In three-coordinate d^8 systems, such as Au(III)[42] and Pd(II),[43,44]

theory predicts a T-shaped geometry as the most feasible scenario with 8 e^- occupying the four low-energy molecular orbitals.

Indeed, T-shaped structures can be derived from four-coordinate, square-planar complexes by removing one ligand.[35,36] This process generates an open site in the coordination sphere of the metal, i.e., a coordinative unsaturation. Such vacant site decreases the stability of the complex and, at the same time, increases its reactivity. As consequence, they are often invoked as transient intermediates in homogeneous catalysis and bond activation reactions.

Drawing the attention to three-coordinate Pt(II) species, T shapes also dominate[45] since they are isoelectronic with respect to the aforementioned Au(III) and Pd(II) systems. As a result of their unsaturated nature, these complexes are not particularly stable. Whenever each ligand contributes with 2 electrons, the resulting species formally contain 14-electron species —the 16-electron rule is not accomplished— and the electrophilic metal centre tends to fulfil the vacancy. According to this, one can distinguish between *true* and *masked* T-shaped complexes.[45,46] True T-shaped species do not form contacts to stabilise the open coordination site. However, this is not easy to achieve; indeed, the vacant site is usually masked by intra- or intermolecular interactions. The most common situations are compiled in Figure 1.7. On one hand, the C–H bonds of the ligands can approach the empty site forming agostic interactions.[10,47] On the other hand, the chemical environment becomes crucial because both counteranions or solvent molecules can coordinate to the metal centre, even in a competitive way.[48] In any case, whether these interactions are labile, the complexes can be considered as *operationally three-coordinate* in a kinetic sense.[49] Occasionally, T-shaped species are simply no stable and, when non-bulky bridging ligands are involved, dimerisation processes may occur.

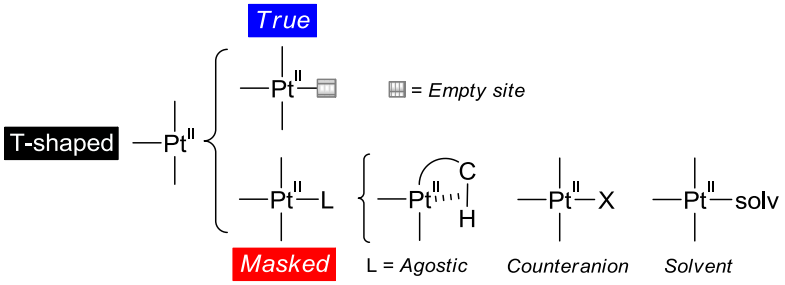

Figure 1.7 General classification of T-shaped complexes.

Agostic T-shaped structures characterised so far will be reviewed in Section 4. A dynamical perspective on agostic interactions in masked T-shaped Pt(II)–NHC species will be presented in such section. The author refers to literature for a detailed collection of true T-shaped Pt(II) species as well as counteranion and solvent adducts.[45]

Interestingly, an unique Y-shaped Pt(II) species has been reported by Markó et al.,[50] the complex [(IPr)Pt($SiMe_2Ph)_2$] (IPr = 1,3-bis(2,6-diisopropylphenyl)imidazol-2-ylidene). X-ray diffraction studies on this species show a Si–Pt–Si angle of ca. 80° and Si–Pt-C_{IPr} angles of ca. 140°. Authors appeal to the steric hindrance and the *trans* influence exerted by both carbene and silyl ligands in order to account for the unusual geometry. However, theoretical calculations performed by Takagi and Sakaki sustain that, despite the large Si···Si distance of 2.980 Å,[50] the complex is better described as a Pt(0) σ-disilane than as a Pt(II) disilyl.[51] In addition, the ^{195}Pt NMR chemical shifts fit better with Pt(0) species. Lastly, Vidossich and Lledós claim back the Pt(II) disilyl scenario based on localised orbital calculations.[52]

1.2. Reaction Mechanisms

A reaction mechanism is a detailed description of the elementary steps that take place during a chemical transformation.[53,54] The main issue is hardly *what* happened, but *how*. In the course from reactants to products, species undergo bond forming and bond breaking steps through transition states (TS), visiting different intermediate structures in the way (Figure 1.8). Both the order and the manner these processes occur depict the whole mechanistic scene. Recognition of decisive stages can lead to a rationalised design of processes, evading the trial-and-error approach. In other words, knowing the most relevant features of the mechanism sheds light on which guidelines should be followed to efficiently improve the reaction in terms of rate, yield, or selectivity. However, a number of reactions proceed rapidly and smoothly and the experimental detection of transient species is limited. In this ambit, theory appears as an excellent tool since it allows to analyse the whole mechanistic landscape by computing the energy of all intermediates and transition states. All this knowledge is compiled in the potential energy surface (PES) which will be discussed in Section 2.5.1.

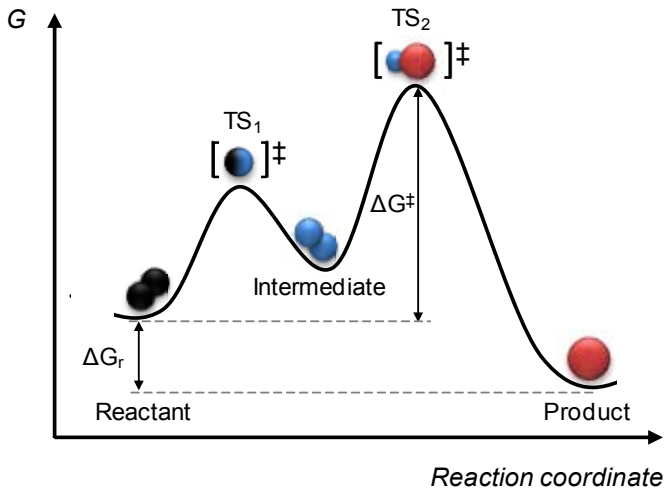

Figure 1.8 Qualitative two-step Gibbs energy reaction profile.

In order to disclose whether a mechanism is feasible or not, several aspects must be considered. To cover them, a qualitative two-step reaction profile is shown in Figure 1.8. It encompasses the evolution of the Gibbs energy (Y axis) along a certain reaction coordinate (X axis). In first term, thermodynamics concerns the Gibbs energy difference between reactants and products, ΔG_r, and rules the *spontaneity* of the process. However, the reaction does occur effectively only when kinetics permits, it means, when the chemical system gains enough energy to overcome the most significant Gibbs energy barrier, $\Delta G^{\ddagger}$.

It is noteworthy that experimentalists usually deal with reaction rates (k-representation), but theoreticians operate better with energies (E-representation). Eyring transition state theory connects the two worlds by means of

$$k = \frac{k_B T}{h} e^{-\Delta G^{\ddagger}/RT} \qquad [1.1]$$

being k_B the Boltzmann constant, h the Planck constant, R the universal gas constant, and T the absolute temperature.

Regarding exoergic reactions ($\Delta G_r < 0$), one aspect of interest is the understanding of reaction kinetics. A widespread concept in chemical kinetics to evaluate reaction mechanisms is the rate-determining step (RDS). Unfortunately, definitions of RDS found in literature may be unambiguous and misleading. For instance, it has been stated as the slowest step of the reaction, the step with the smallest rate constant, or the one with the highest-energy transition state. Nevertheless, all these definitions present drawbacks.[55] Instead, the so-called *degree of rate control* becomes a suitable concept for evaluating the relevance of states —i.e., intermediates and transition states— in intricate reaction mechanisms.[55–57] It quantifies the extent to which a differential change in the Gibbs energy of any state influences the net reaction rate.[57] The transition state and intermediate with the highest degree of rate control are called rate-determining transition state (RDTS) and rate-determining intermediate (RDI), respectively. It is more physically appropriate to define rate-determining states than steps because the latter entail two consecutive points and this requirement is not always fulfiled.[55] In catalysis, this theory has been applied to derive the *energetic span model*,[58–60] which allows for the estimation of turnover frequencies (TOF)[60] and turnover numbers (TON).[61] Herein, the RDS will be associated to the process in which the RDTS is involved.

As featured before, by analysing both thermodynamic and kinetic aspects of the chemical reaction one can give the green light to mechanistic proposals. Notably, this procedure is applicable to almost any field of chemistry including organometallics. Plenty of transition

metal-mediated reactions can be studied, e.g., oxidative addition, reductive elimination, insertion, substitution, transmetalation, and so on and so forth. In regard to the current dissertation, C–H bond activation, Heck, and cross-coupling reactions —corresponding to Sections 5–7— will be addressed.

1.2.1. Pt(II) C–H bond activation

C–H bonds are no longer inert in chemistry. Their activation —and subsequent functionalisation— is an ongoing research topic of great importance.[62–66] The intramolecular version, including cyclometalation[67,68] and rollover[69] processes, is also widely documented. Particularly, platinum species play a remarkable role,[70,71] as in the bond activation of methane, see for instance Periana-Catalytica[72] and Shilov[66] systems. In this regard, Pérez and co-workers have recently reported the methane functionalisation in supercritical CO_2 solvent catalysed by silver complexes.[73]

Given the relevance of functionalising C–H bonds, the reaction mechanism has drawn a lot of attention.[74–76] A general hydrogen transfer scenario in Pt(II) chemistry via C–H bond activation is illustrated in Scheme 1.1. The first step concerns the coordination of the C–H moiety. The majority of substitution reactions involving Pt(II) centres proceed associatively via five-coordinate, 18-electron intermediates.[70] Nevertheless, three-coordinate, 14-electron, Pt(II) species are indeed feasible —as previously discussed— thus the dissociative pathway must be taken into account.[45,77] Afterwards, the C–H bond activation *per se* takes place (Scheme 1.1). There are two extreme well-established mechanisms for hydrogen transfers. On one hand, the oxidative addition/reductive elimination (OA/RE) process displays an intermediate in which the platinum has increased its oxidation state by two units and one Pt–H bond has been formed. On the other hand, the σ-bond metathesis is characterised by a single four-centred transition state with no Pt···H interactions. In between, the transition metal can interact in more or less extent with the migrating hydrogen, which provides a range of flavours. As a consequence, a puzzling set of acronyms arises in literature. The mechanism can be coined as oxidatively added transition state (OATS),[75] metal-assisted σ-bond metathesis (MAσBD),[76] oxidative hydrogen migration (OHM),[78] and σ-complex assisted metathesis (σ-CAM).[79] Actually, a wide spectrum of situations for metal-mediated hydrogen transfers can be found.[76,80]

Finally, according to the electronic properties of the metal centre, the C–H bond activation can be classified as electrophilic, ambiphilic, or nucleophilic,[81] regardless of the operating mechanism.[82] In line with the electron-poor nature of its metal centre, Pt(II) species related to Periana-Catalytica and Shilov systems have been catalogued as electrophilic.[82]

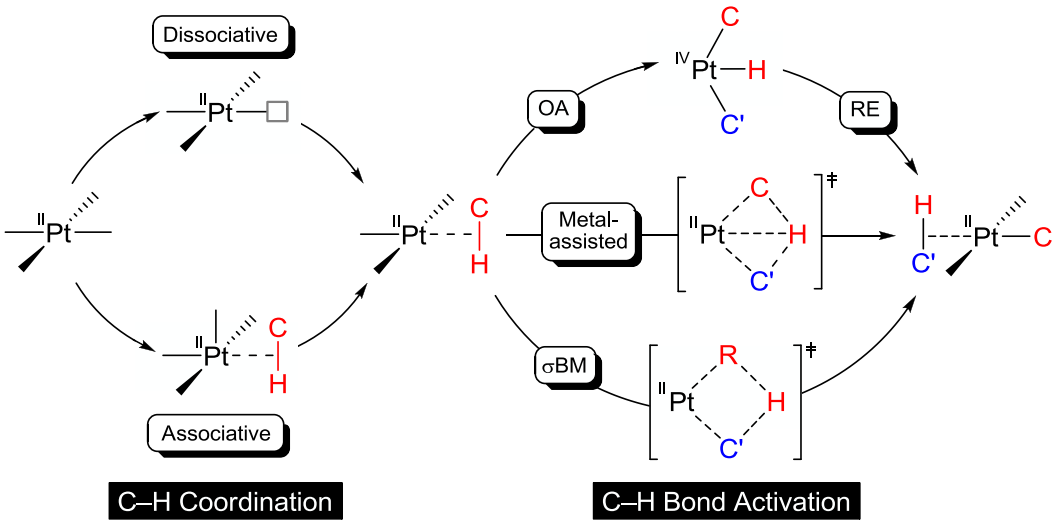

Scheme 1.1 C–H coordination and C–H bond activation mechanisms: oxidative addition/reductive elimination (OA/RE), metal-assisted process, and σ-bond metathesis (σBM).

Section 5 will be devoted to discuss intermolecular C–H bond activation reactions of arenes promoted by three-coordinate Pt(II)–NHC species.

1.2.2. Cross-coupling reactions

The development of straightforward protocols to construct C–C bonds is certainly a valuable tool in synthesis. A powerful example is the so-called *cross-coupling* reaction.[83] The process means the Pd-catalysed coupling between organic electrophiles and organometallic reagents (Scheme 1.2). Several kinds of cross-coupling reactions appear depending on the nature of the organometallic reagent R'–*m*. For instance, the Suzuki–Miyaura conditions involves organoboranes,[84,85] the Negishi reaction profits from organozinc reagents,[86] and the Hiyama process encompasses organosilicon compounds.[87,88] These procedures have been successfully applied to industrial processes and nowadays a plethora of high-value chemicals are prepared using this technology.[89–91] Accordingly, this great advance has been recognised and Suzuki and Negishi were awarded with the Nobel Prize in Chemistry in 2010.[13,92]

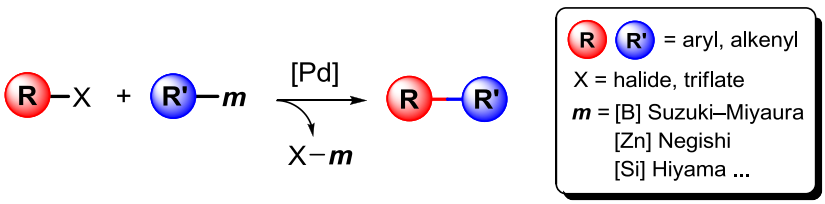

Scheme 1.2 Pd-catalysed cross-coupling reactions.

The general catalytic cycle proceeds by a sequence of three main steps as shown in Scheme 1.3: (i) oxidative addition, (ii) transmetalation, and (iii) reductive elimination. Firstly, the R–X is oxidatively added to the Pd(0) catalyst which results in the formation of [Pd(R)(X)]. According to C–X bond dissociation energies, the reactivity usually follows the

trend I > Br > Cl. For unreactive bonds, such as C–Cl, the oxidative addition can even constitute the rate-determining step. The next step is known as *transmetalation* because the R' group is transferred from one metal, *m*, to another one, Pd, yielding [Pd(R)(R')]. This stage makes the difference among cross-coupling reactions and it cannot be generalised. Finally, reductive elimination takes place between the R and R' groups, the product R–R' is released and the Pd(0) catalyst is recovered. A number of computational reports have nicely covered the mechanistic features of cross-coupling reactions.[93–95]

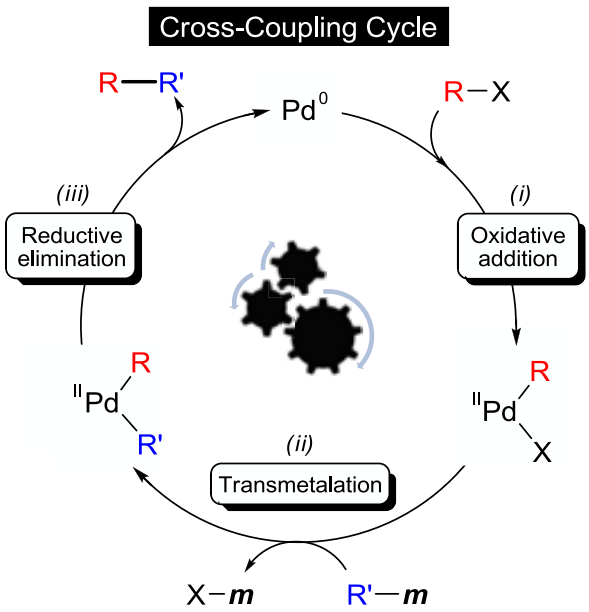

Scheme 1.3 General cross-coupling catalytic cycle.

As an alternative to the previous textbook or *neutral* mechanism, some authors support the so-called *anionic* mechanism.[96,97] This proposal considers the mediation of three- and five-coordinate anionic palladium species along the catalytic cycle. However, calculations do not provide unequivocal and clear answers. For instance, for a catalytic coupling between PhCl and $[SH]^-$, gas-phase calculations provide a better turnover efficacy for the anionic pathway,[60,98] but solvent-corrected Gibbs energies favours the neutral one.[60] Conversely, according to calculations on a Suzuki coupling involving acetate ligands, both neutral and anionic pathways —i.e., considering $[Pd(PMe_3)_2]$ and $[Pd(PMe_3)_2(OAc)]^-$ as active species— are plausible.[99]

Calculations on the transmetalation process of Pd-catalysed Suzuki–Miyaura cross-coupling reactions will be presented in Section 6, whereas a Hiyama reaction mechanism in water will be discussed in Section 7.

1.2.3. Heck reaction

Together with cross-coupling processes, the Heck reaction has been a major breakthrough in C–C bond forming chemistry. It was first reported independently by Mizoroki[100] and Heck.[101] The traditional process represents the Pd-catalysed arylation and alkenylation of olefins in the presence of a base (Scheme 1.4).[102–104] Although there is no organometallic reagent —hence, no transmetalation step—, sometimes it is catalogued as a cross-coupling reaction in which *m* in Scheme 1.2 stands for H. The reaction is also useful in fine chemical processes[89,91,105] and Heck was awarded with the Nobel Prize in Chemistry in 2010.[13,92]

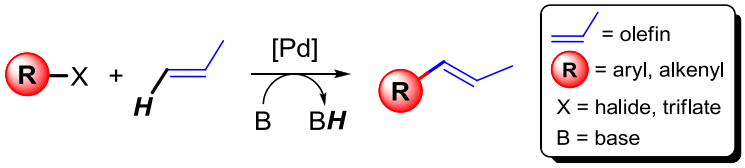

Scheme 1.4 Pd-catalysed Heck reaction.

The main steps of the Heck reaction mechanism are displayed in Scheme 1.5: (i) oxidative addition, (ii) alkene coordination, (iii) insertion, (iv) β-hydride elimination, and (v) catalyst regeneration. Firstly, in presence of R–X the Pd(0) catalyst undergoes oxidative addition to give rise to [Pd(R)(X)]. Then, the olefin reaches the metal centre and inserts into the Pd–R bond. The recently formed alkyl moiety is susceptible to suffer a β-hydride elimination yielding a transient hydride species. Finally, an auxiliary base regenerates the Pd(0) catalyst. The regiochemistry (branch vs. linear alkene) is dictated at the insertion step, whereas the stereochemistry (*Z*- vs. *E*-alkene) is imposed at the β-hydride elimination. Several computational studies have been carried out on the title reaction.[94]

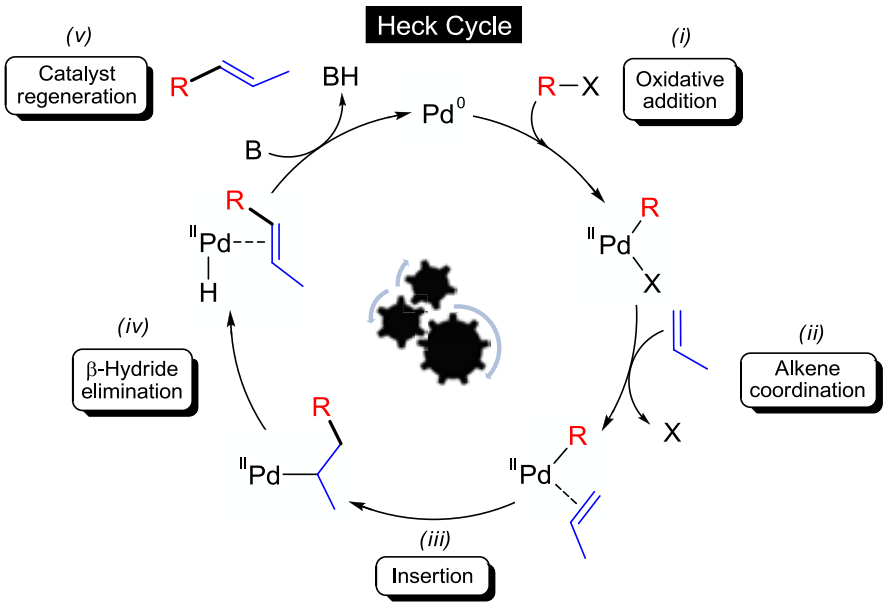

Scheme 1.5 General Heck catalytic cycle.

The previously discussed anionic mechanism is proposed to operate in this reaction.[96] In certain systems, a Pd(II)/Pd(IV) mechanism has also been claimed.[106–108] According to computation, the insertion energy barriers for Pd(0)/Pd(II) and Pd(II)/Pd(IV) systems are similar, but the oxidative addition —even with aryl iodides— is the rate-determining step for the latter.[109] For pincer-type catalysts, theory indicates that Pd(IV) intermediates are thermally accessible.[110]

Calculations on the Pd-catalysed Heck reaction mechanism —together with the above-mentioned Hiyama reaction— will be presented in Section 7.

1.3. Acidity of Dihydrogen Complexes

Given the imminent consumption of fossil fuels, alternative energy sources should receive the baton. As pointed out in earlier sections, organometallic chemistry can indeed contribute to this goal. In this concern, the dihydrogen molecule is not only a feedstock in several hydrogenation processes but also a potential fuel.[111] Accordingly, the production and storage of molecular H_2 are critical issues which can be addressed through detailed studies on transition metal dihydrogen species.[112–116] In the 80s Kubas et al. reported that transition metals can bind dihydrogen molecules in a η^2 fashion (Figure 1.2).[12] Since then, a wide variety of dihydrogen complexes have been characterised.[117]

The M–H_2 bonding in σ-complexes is usually described by a three-centre, two-electron interaction stabilised by back donation of electrons from a *d* orbital of M to a σ^* orbital of H_2, similar to the Dewar–Chatt–Duncanson model for olefin coordination.[118] The extent of back donation can tune the M–H_2 interaction in such a manner that the H–H bond distance can range from 0.8–0.9 Å in *true* dihydrogen complexes to 1.0–1.3 Å in *elongated* dihydrogen complexes, becoming a dihydride species at the oxidative addition limit (Scheme 1.6).[119,120]

The extent of the M–H_2 interaction leads to the H–H bond activation *per se*. The H–H bond splitting can be achieved by homolytic or heterolytic cleavages (Scheme 1.6). In the homolytic pathway, the dihydrogen ligand is oxidatively added to form the dihydride complex, increasing the oxidation state of the metal centre by two units. In the heterolytic counterpart, a metal hydride is formed by removing one hydrogen atom as a proton. The involvement of hydrogen bonded species in the latter mechanism has been proposed.[121,122] Interestingly, metal-free systems based on the frustrated Lewis pair machinery have also demonstrated potential to split H–H bonds.[123,124]

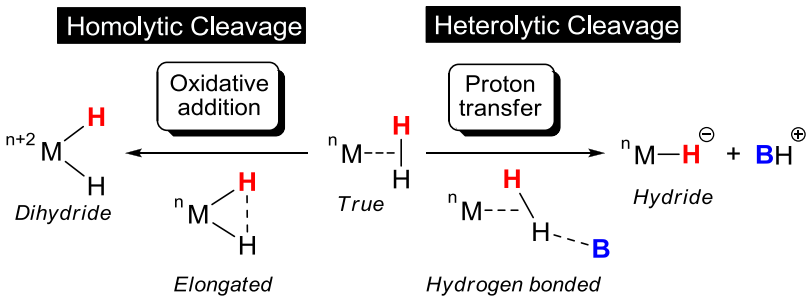

Scheme 1.6 Mechanisms for H–H bond cleavage in transition metal chemistry.

The previous heterolytic H–H bond cleavage (Scheme 1.6 right) can be actually recognised as a textbook acid–base reaction; as a result, an acid dissociation constant K_a —normally expressed as pK_a— pertains. For that matter, acid constants are good probes to obtain useful information about the deprotonation state of molecules in solution.

Despite the acidity of free H_2 is almost negligible (pK_a of ca. 35 in THF[125]), it can be dramatically increased when transition metals come into play. The first pK_a measurement of a ruthenium dihydrogen complex was performed in acetonitrile by Heinekey et al. who quantified a value of 17.6.[126] Afterwards, a vast collection of experimental pK_a values have been reported in organic solvents.[127–129] As one can expect, the acidity is strongly influenced by the ligands as well as the metal centre. For series of isostructural compounds, the presence of more electron donating ligands and heavier transition metals tends to decrease the acidity.[129] Remarkably, some dihydrogen complexes exhibit superacidic properties, e.g., monocationic rhenium[130], dicationic ruthenium,[131] and osmium species[131,132] with pseudo-aqueous pK_a values ranging from –2 to –6.

As concerns the dissertation, pK_a values of aqueous iron, ruthenium, and osmium dihydrogen complexes have been estimated. Background and results can be consulted in Section 8.

1.4. Nuclear Magnetic Resonance of Transition Metals

It is well known that nuclear magnetic resonance (NMR) is an essential tool for chemists. This extraordinarily multipurpose technique is employed to characterise compounds, elucidate structures, or study dynamic processes, among other applications. Whereas ^{1}H, ^{13}C, ^{19}F, and ^{31}P nuclei are routinely acquired, the inspection of transition metals is less extended —it may be hampered by low receptivity or significant quadrupole moments— but still suitable to handle bio-[133] and organometallic scenarios.[134,135] Indeed, some advantages should be pointed out. For instance, hydrogen atoms are usually located at the periphery of organometallic compounds whereas the metal is located at the centre. Since the reactivity is associated with the coordination centre, the metal surroundings arise as a promising feature

to probe. Another interesting matter concerns the broader chemical shift span of transition metals —ca. 12000 ppm for ^{103}Rh— compared to that of common nuclei —ca. 12 ppm for ^{1}H. As a result, subtle steric or electronic changes on the chemical environment of the metal can entail appreciable variations on its chemical shift, turning this technique into a very sensitive tool.

From a computational standpoint,[136,137] the prediction of nuclear magnetic parameters is an ongoing research field that closely connects theory with experience. The computation of transition metal chemical shifts is helpful to confirm assignments, validate structures, rationalise trends, build chemical shift–structure correlations, etc. Unfortunately, the sensitivity depends on the computational set up, thus validation of the protocol is strongly recommended.[138,139] Moreover, environmental effects such as solvent and temperature may come into play.[140,141]

Along the d-block, rhodium stands out in homogeneous catalysis —e.g., hydrogenation and hydroformylation of alkenes. In the way to develop new catalysts or improve older ones, ^{103}Rh NMR spectroscopy becomes highly convenient.[142,143] Although a priori there is no global, unequivocal relationship between chemical shifts and reactivity, empirical correlations can be established within families of compounds. For instance, such kinds of relationships have been found for rate constants of ligand exchanges[144] and migration reactions,[145] enantioselectivities,[146] and stability constants.[147] More recently, rates of water substitutions in rhodium clusters were also related to chemical shifts.[148] In this scene, theory may be useful to predict ^{103}Rh chemical shifts and reveal latent correlations. Thorough analysis on a set of Rh–bis(phosphine) derivatives will be presented in Section 9.

2. Computational Methods

The term *theoretical chemistry* stands for the combination of mathematical methods with quantum —or classical— mechanics to approach chemical systems. The subfield *computational chemistry* arises from the implementation of these chemical concepts into working computer programs.[149] Likewise, people can also be classified. According to Cramer,[150] (i) *theorists* develop new theories and models to improve the older ones, (ii) *molecular modelling researchers* focus on chemical systems of relevance, sometimes at the expense of theoretical rigor, and (iii) *computational chemists* attend to computer-related tasks, such as development of algorithms, encoding, or visualisation of data.

Computational chemistry can be roughly divided into quantum —ab initio— mechanics and classical mechanics calculations. Quantum mechanics presents several levels of theory, but only density functional theory is applied herein. Discussion about the representation of molecular orbitals by mathematical functions —i.e., basis sets, effective core potentials, and plane waves— can be extensively consulted in literature.[149] On the other hand, classical mechanics relies on parameterisation of *simple* equations and therefore it can handle large systems with less computational effort.

Quantum mechanics was born from the failure of classical mechanics in describing phenomena at the microscopic level. Astounding concepts as wave-particle duality or discretisation of energy built the foundations during the beginning of the 20th century. Pioneer scientists behind such great advances were awarded with five Nobel Prizes in Physics from 1918 to 1933 (Figure 2.1). At that time, the enormous mathematical requirements of theory prevented the computation of *real* systems. Further development of theory together with progress in computer science has paved the road towards a broad scope of application.

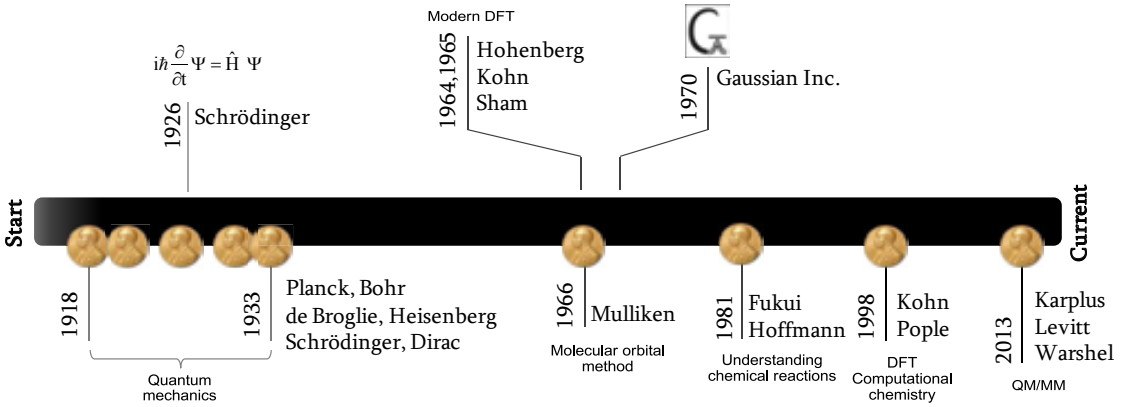

Figure 2.1 Timeline from quantum mechanics to computational chemistry.

In the modern times, the major relevance of theoretical and computational chemistry has been recognised by the Nobel Foundation, awarding Nobel Prizes in Chemistry to Kohn and Pople in 1998 and, more recently, to Karplus, Levitt and Warshel in 2013 (Figure 2.1).[13] Indeed, this is not the end but the beginning. Computational chemistry is relatively young and there is plenty of room for improvement.

As concerns the present section, density functional theory and pertinent aspects about some of their density functionals are primarily discussed. A brief overview on molecular mechanics and molecular dynamics is introduced afterwards. Finally, treatment of solvent and application of previous methodologies on the current dissertation are presented. The author feels free to reject a strictly pure *theoretical* point of view in favour of a *computational* —perhaps pragmatic— perspective. The following overview attempts to meet theory in a general taste.

2.1. Density Functional Theory

The very centre of quantum mechanics (QM) is the Schrödinger equation.[151] It is mostly applied in the time-independent non-relativistic formalism,

$$E\ \Psi = \hat{H}\ \Psi \qquad [2.1]$$

meaning E total energy, Ψ wave function, and $\hat{H}$ Hamilton operator of total energy. Ψ contains all knowable information about the quantum system and depends on the 3N spatial coordinates of electrons $\{\mathbf{r}_i\}$, N spin coordinates of the electrons $\{s_i\}$, and 3M spatial coordinates of the nuclei $\{\mathbf{R}_I\}$, being N the number of electrons and M the number of nuclei,

$$\Psi\left(\vec{r}_1, \vec{r}_2, \ldots, \vec{r}_N, s_1, s_2, \ldots, s_N, \vec{R}_1, \vec{R}_2, \ldots, \vec{R}_M\right) \qquad [2.2]$$

At this point, the Schrödinger equation [2.1] for molecular systems can be simplified by introducing the Born–Oppenheimer approximation. It is built on the fact that nuclei are much heavier than electrons and, as a consequence, they move much slowly. The problem is then reduced to solve the electronic Schrödinger equation [2.3], i.e., to compute the electronic energy for a fixed frame of nuclei,

$$E_{el}\Psi_{el} = \hat{H}_{el}\Psi_{el} \qquad [2.3]$$

in which Ψ_{el} now depends on electron (spatial and spin) coordinates $\{\mathbf{x}_i\}$,

$$\Psi_{el}\left(\vec{r}_1, \vec{r}_2, \ldots, \vec{r}_N, \vec{s}_1, \vec{s}_2, \ldots, \vec{s}_N\right) \equiv \Psi_{el}\left(\vec{x}_1, \vec{x}_2, \ldots, \vec{x}_N\right) \qquad [2.4]$$

Ψ_{el} is not an observable, but $|\Psi_{el}|^2$ in [2.5] is interpreted as the probability that electrons 1, 2, ..., N are found simultaneously in volume elements $d\mathbf{x}_1$, $d\mathbf{x}_2$, ..., $d\mathbf{x}_N$.

$$\left|\Psi_{el}\left(\vec{x}_1,\vec{x}_2,...,\vec{x}_N\right)\right|^2 d\vec{x}_1,d\vec{x}_2,...,d\vec{x}_N \qquad [2.5]$$

The most common method to solve the electronic Schrödinger equation [2.3] is the Hartree–Fock (HF) approximation, which can be consulted elsewhere.[151] Still, Ψ_{el} relies on 4N variables, $\{\mathbf{x}_i\}$, and the usual chemical systems of interest contain many atoms and many electron, thus wave function based methods are not affordable. To overcome that, the *electron density* ρ is here introduced through [2.5].[152] $\rho(\mathbf{r})$ determines the probability of finding any of the N electrons within the volume element $d\mathbf{r}_1$. Since electrons are indistinguishable, the probability of finding any electron at this position ($d\mathbf{r}_1$) is just N times the probability for one particular electron,

$$\rho\left(\vec{r}\right) = N\int\cdots\int\left|\Psi_{el}\left(\vec{x}_1,\vec{x}_2,...,\vec{x}_N\right)\right|^2 ds_1,d\vec{x}_2,...,d\vec{x}_N \qquad [2.6]$$

Importantly, $\rho(\mathbf{r})$ is a function of only three spatial coordinates $\{\mathbf{r}_1\}$ and, indeed, is an observable that can be measured.

Density functional theory (DFT) profits from the above-mentioned properties of the electron density $\rho(\mathbf{r})$.[152] DFT as is known nowadays[153,154] was born in 1964, when Hohenberg and Kohn published their homonym theorem.[155] They demonstrated by *reduction ad absurdum* that the electron density determines the Hamiltonian and, therefore, all properties of the system. To put it differently, any observable of a non-degenerated ground state can be calculated as a functional of the electronic density.[a] From a chemical point of view, the most interesting observable is the energy of the system, which acquires the following formulation,

$$E[\rho] = T[\rho] + E_{ee}[\rho] + E_{Ne}[\rho] \qquad [2.7]$$

meaning T kinetic energy, E_{ee} electron–electron repulsion, and E_{Ne} nuclei–electron attraction. The two first terms are collected into the universal Hohenberg–Kohn functional $F_{HK}[\rho]$ which form is the same for all N-electron systems. Furthermore, the E_{ee} term can be split into the classical Coulomb part J, which is exactly known, and the non-classical contributions E_{ncl}, which is completely unknown,

[a] A functional is defined as a function that takes as argument another function —instead of a number— and gives a scalar.

$$F_{HK}[\rho] = T[\rho] + E_{ee}[\rho] = T[\rho] + J[\rho] + E_{ncl}[\rho] \quad [2.8]$$

The major task of DFT is therefore the quest of explicit expressions for T and E_{ncl}. With this target in mind, current DFT is applied as implemented by Kohn and Sham in 1965.[156] This formalism established a way to approach the functional F_{HK} by finding a reliable approach for the kinetic energy. Although the true kinetic energy T is unknown, one can compute exactly the kinetic energy of a non-interacting reference system, T_S, being $T_S < T$. F_{HK} is then rewritten as

$$F_{HK}[\rho] = T_S[\rho] + J[\rho] + E_{XC}[\rho] \quad [2.9]$$

where the so-called exchange–correlation energy E_{XC} collects everything that is unknown,

$$E_{XC}[\rho] = (T[\rho] - T_S[\rho]) + E_{ncl}[\rho] = T_C[\rho] + E_{ncl}[\rho] \quad [2.10]$$

being T_C the residual part of the true kinetic energy that is not evaluated.

Hitherto, this strategy contains no approximation. Whether the exact form of E_{XC} is known, the Kohn–Sham formalism would lead to the exact energy. Thus, the challenge of modern DFT[157] revolves around the development of exchange–correlation expressions.

2.1.1. Classification of density functionals

As stated before, the exchange–correlation functional E_{XC} represents the core of DFT. Both exchange and correlation contributions are usually beheld separately,

$$E_{XC}[\rho] = E_X[\rho] + E_C[\rho] \quad [2.11]$$

Exchange term E_X encompasses the fact that electrons of same spin do not move independently from each other, but this effect vanishes for two electrons with different spin. Correlation term E_C covers the electrostatic repulsion between electrons. Exchange contributions are notably larger than correlation ones. In principle, each exchange functional can be coupled with any correlation functional, but some combinations just work better; likely, they profit from error cancelation. For further discussion, it is worth noting that the HF approximation computes exchange exactly but neglects correlation.[151]

The first approach is called *local density approximation* (LDA). It supposes a local behaviour, i.e., E_{XC} only depends on the density at **r** and not the values at other point **r**'. This approximation attains the *uniform electron gas* (UEG) model, which is formed by electrons moving on a positive background charge distribution, being the total ensemble neutral. Although it is very far from realistic situations, the model is useful because of the

corresponding exchange and correlation functionals are highly accurate or even exactly known. E_X has an explicit form, equal to the one derived by Slater in HF theory.[158] Conversely, E_C must be estimated, for instance, through the implementation by Vosko, Wilk and Nusair (VWN).[159] The local-spin density approximation (LSDA) is a generalization of the LDA extended to open-shell systems.

In order to account for the non-homogeneity of the true electron density, the information about $\rho(\mathbf{r})$ can be supplemented with its gradient, $\nabla\rho(\mathbf{r})$. Actually, it is not such simple, and some restrictions must be enforced.[152] This methodology is called *generalised gradient approximation* (GGA). These functionals still feature a fully local nature in a mathematical sense, but sometimes they are careless defined as semilocal. As interesting GGA examples, one emphasises B86 for exchange,[160] LYP for correlation,[161] and PBE.[162]

The next step guides to the *meta-generalised gradient approximation* (meta-GGA) which incorporates an explicit dependence on kinetic energy density in the exchange term. Second order density gradient $\nabla^2\rho(\mathbf{r})$ may be also considered. Examples include VSXC[163] and TPSS.[164]

One should remind that HF theory provides an explicit expression for the exact exchange, which has a non-local nature. In this sense, another proposal may rely on approximating functionals only for the part that HF does not cover. It can be proved that taking the whole exchange from HF is not a feasible option for molecules and chemical bonding, thus only a certain portion of pure exchange is considered. Because of that mixing, they are called *hybrid* functionals (also hyper-GGA). To further discuss, the *adiabatic connection* should be introduced. Shortly, it links a non-interacting system with the real one by means of the *coupling strength factor* λ. This parameter ranges from 0 to 1, being 0 for a non-interacting system and 1 for a fully interacting one. E_{XC} can then be written as

$$E_{XC} = \int_0^1 E_{ncl}^{\lambda} d\lambda \qquad [2.12]$$

For $\lambda = 0$, E_{ncl} only contains exchange which can be computed exactly. For $\lambda = 1$, E_{ncl} is composed of both exchange and correlation terms and can be estimated by any exchange–correlation functional. However, for intermediate values of λ, E_{ncl} is unknown, thus the relationship between E_{ncl} and λ should be estimated. The simplest approach is known as half-and-half combination, HH,[165] which assumes a linear behaviour of E_{ncl} with respect to λ, i.e., 50% exact exchange.

$$E_{XC}^{HH} = \frac{1}{2} E_{XC}^{\lambda=0} + \frac{1}{2} E_{XC}^{\lambda=1} \qquad [2.13]$$

The next stage introduces empirical fitted parameters to control the weight of the different contributions,[a] as in the popular B3LYP hybrid functional [2.14] where a = 0.2, meaning 20% exact exchange,[161,166,167]

$$E_{XC}^{B3LYP} = (1-a)E_X^{LSDA} + a\ E_{XC}^{\lambda=0} + b\ E_X^{B88} + c\ E_C^{LYP} + (1-c)E_C^{LSDA} \qquad [2.14]$$

Recent efforts include the hybrid functionals M06 with 27% exact exchange and M06-2X with 54% exact exchange, fitting ca. 30 parameters each one.[168] Additionally, Perdew et al. have proposed a fixed amount of exact exchange, 25% in [2.15], based on perturbation theory arguments.[169,170] For the special case where GGA in [2.15] means PBE, the functional is called PBE0.[162,170,171]

$$E_{XC}^{hybrid} = E_{XC}^{GGA} + 0.25\ (E_X^{\lambda=0} - E_X^{GGA}) \qquad [2.15]$$

Finally, fully non-local functionals —which also consider unoccupied orbitals— can be obtained using the exact exchange and evaluating a part of the correlation exactly. An example of that is the *random phase approximation* (RPA).[172] Unfortunately, the computational cost scales rapidly but some advances begin to appears.[173] The so-called double hybrid functionals, which combine the correlation of density functionals and MP2-like corrections, are making progesses.[174]

All these categories have been gathered into the biblical *Jacob's ladder* (Figure 2.2) proposed by Perdew et al.[175,176] It shows the different rungs from the *HF World* to the *Heaven of Chemical Accuracy*. Nevertheless, there is no genuine, systematic way to improve since DFT energy has not a variational behaviour with respect to the exchange–correlation potential. More likely, one should climb or descend according to the needs.

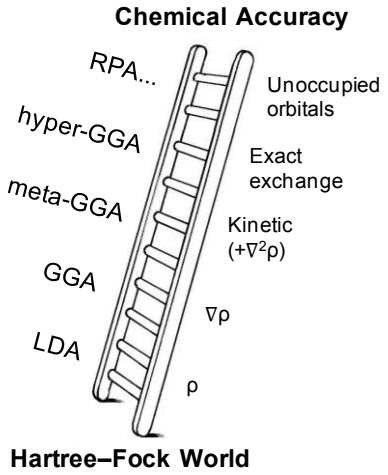

Figure 2.2 Jacob's ladder of density functional approximations towards E_{XC}.

[a] Because of such parameterisation, some authors argue that DFT should not be considered ab initio.

Complementing the taxonomy previously discussed, different flavours of functionals can be distinguished according to the degree of parameterisation, i.e., non-empirical, empirical, and over-empirical.[177] For instance, PBE is parameter-free —it is not fitted to any molecular properties— whereas B3LYP contains three of them. As take home messages, (i) good non-empirical functionals are widely applicable at the expense of losing accuracy and (ii) good empirical functionals are often more accurate. One should be able to find a proper balance for the chemical system under study.

2.1.2. Which functional should one choose?

Every computational chemist has pondered on this question quite often.[a] One must face the fact that there is no unequivocal, universal answer. Indeed, the choice of functional strongly depends on the chemical system[177] and, frequently, the performance of density functionals should be validated beforehand.[178,179]

According to literature, it seems that scientific community has already made its election. Figure 2.3 collects the occurrence of selected functionals across journal papers in 2000 (green bars), 2010 (orange bars), and 2013 (blue bars). The hybrid functional B3LYP overwhelmingly appears as the most popular choice in DFT, but it is not free of drawbacks. Indeed its occurrence has slightly decreased in 2013 at the expense of other functionals. Zhao and Truhlar have enthusiastically remarked the shortcomings of B3LYP, notably, the failure in describing non-covalent interactions.[180] Instead, they propose a suite of density functionals —e.g., M06 family— which provide a proper description of dispersion interactions.[180,181] Alternatively, one can also approach this issue using the methodology proposed by Grimme et al.[182] It consists in empirical corrections to standard DFT based on atom-pairwise coefficients and cut-off radii. It means, the correction can be easily added to any functional to consider dispersion interactions. In comparison to other methods, this procedure is fast and simple —only Cartesian coordinates and atom numbers are needed— and still offers reliable results.[183]

In regards to organometallic chemistry, several benchmark studies have been compiled in literature covering the performance of different density functionals and their application to structures, reactivity, spin states, etc.[184] As convenient cases for the current dissertation, selected papers are discussed straightaway.

[a] Every year since 2010, Swart, Bickelhaupt and Duran rank the popularity of density functionals within the scientific community by means of the so-called *density functionals poll*. In 2013, PBE was the most popular choice, closely followed by PBE0. See http://www.marcelswart.eu/

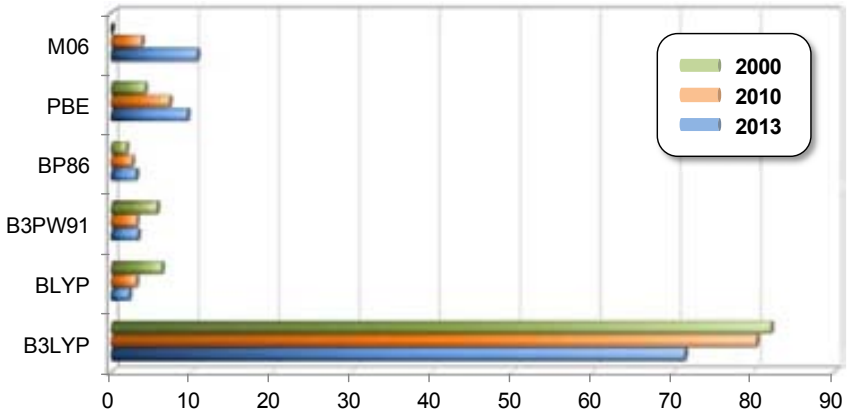

Figure 2.3 Percentage of occurrence of functional names in journal title and abstract in selected years (ISIS Web of Science, 2014).

Quintal et al. have considered some transition metal-mediated reactions, such as Pd(0) oxidative addition, Pd-catalysed Heck reaction, and Rh-catalysed hydrogenation of acetone.[185] They do not found an outstanding functional but a cluster of them that perform fairly well. Among them, PBE0, B1B95, and PW6B95 are highlighted.

Lai et al. have computed several C–H bond activation reactions promoted by transition metal —Rh, Pd, Ir, and Pt— pincer complexes.[186] Among the density functionals under consideration, B3LYP appears as the most accurate density functional. Other good options are the double hybrids B2GP-PLYP and B2-PLYP and the hybrid PBE0. Interestingly, the empirical dispersion correction D3 has a small influence on energy barriers.

Steinmetz and Grimme have tested 23 density functionals against several bond activation processes catalysed by Ni and Pd complexes.[187] The best performance was shown by the hybrid PBE0 supplemented with the dispersion correction D3, followed by PW6B95-D3, PWPBB95-D3, and B3LYP-D3. In line with Lai et al.,[186] energy barriers do not dramatically depend on medium-range contacts, although reaction energies do.

Weymuth et al. have recently tested 9 density functionals against experimentally reported dissociation energies involving relatively large transition metal complexes.[188] They conclude that, although there is no reliable density functional for all the reactions under consideration, PBE0 and TPSSh provide the most accurate results. Additionally, for some of the reactions under consideration, the inclusion of the D3 dispersion scheme increases the deviation from the experimental values.

Zhao and Truhlar have tested 14 density functionals against databases involving transition metal reaction energies and metal ligand bond energies.[168] According to the results, they recommend M06, M06-L, and M05 for transition metal chemistry.

Sieffert and Bühl have attempted to reproduce the experimental binding enthalpy of PPh_3 in a Ru(II) complex using both dispersion-corrected and empirical parameterised density functionals.[189] They disclosed that a proper description of non-covalent interactions is crucial, suggesting the dispersion-corrected B97-D and the empirical parameterised M06 family as prime options.

Pantazis et al. have reported that some functionals fail to locate the agostic structure of a Nb(III) complex.[190] Among the 24 density functionals considered, 11 of them reproduce both agostic and anagostic minima —e.g., PBE0, PBE, TPSS— whereas 2 of them only identify the former. Also, there are 11 functionals that cannot describe agostic interactions, and anagostic situations are found instead. As conclusion, functionals that do not obey the UEG limit —as LYP— are unable to locate the agostic situation. Extending this inquiry, Tognetti et al. pointed out the fundamental role of the exchange counterpart.[191]

Bühl et al. have tested the performance of several density functionals against geometries of second-[192] and third-row[193] transition metal complexes. Using precise experimental data as reference, they observed that PBE0, B3PW91, and B3P86 hybrid functionals perform best. Jiménez-Hoyos et al. have extended the test set of Bühl and co-workers by including other functionals.[194] Regarding second- and third-row complexes, M06 performed worse than PBE0. As general trend, all functionals predicted larger bond distances when moving down from 3d to 5d transition metals.

Finally, Sodupe and co-workers have studied open-shell Cu(II)–water complexes with density functionals containing different amounts of exact exchange.[195,196] Compared to high level calculations computed with large basis sets —couple cluster including single and double (and estimated triple) excitations, CCSD(T)—, functionals with higher exact exchange values are recommended, e.g., BHLYP with 50% exact exchange.

2.2. Molecular Mechanics

Contrary to the high-level description of atoms in DFT methods, in molecular mechanics (MM) molecules are simplified as networks of solid spheres (atoms) that are connected through springs (bonds).[197] They behave according to classical physics. The energy of such systems, U_{total}, is computed as follows

$$U_{total} = \sum_{molecule} \left(E_b + E_\theta + E_\phi + E_{nb} \right) \qquad [2.16]$$

in which E_b refers bond deformations, E_θ valence angle deformations, E_ϕ dihedral angle deformations, and E_{nb} non-bonded interactions (Figure 2.4). Each contribution is evaluated

using rather simple equations that include various parameters. As plain examples: harmonic potentials are used for bond and angle deformations, periodic functions are needed for dihedral torsions, and Lennard-Jones potentials are implemented for van der Waals interactions (Figure 2.4). Additionally, out-of-plane deformation E_{δ}, electrostatic E_{ε}, and hydrogen bonding E_{hb} are nowadays adjoined to [2.16]. All these functions together with their corresponding parameters form the so-called *force field*. Analogous to the previously discussed density functionals, a similar question may arise here. Which force field should one choose? There is neither an unambiguous answer. But, one would emphasise that force fields are specifically parameterised to describe a certain kind of molecules. Whereas the *ideal* density functional should perform well for all systems, force fields should not. For instance, AMBER mainly focuses on DNA and proteins[198] and GLYCAM takes special care of carbohydrates.[199]

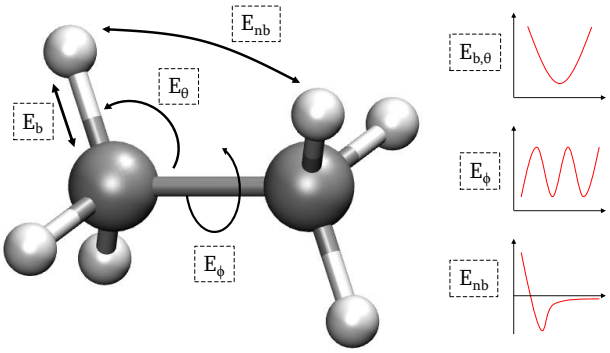

Figure 2.4 Parameters (left) and functions (right) considered in typical molecular mechanics schemes.

The *simple* math related to force field equations allows the treatment of an enormous number of atoms. Such cheap computational cost facilitates the performance of dynamics simulations (see Section 2.3). Ergo, this technique has become absolutely dominant in the biological field where is successfully applied on macromolecules ranging from small proteins (hundred atoms) to the capsid of HIV (64 millions atoms).[200]

Despite the above-mentioned perks, the methodology is still limited in organometallic chemistry. Transition metals are not described by common force fields because their parameterisation is a hard, challenging task. Even so, several approaches have been proposed to expressly gather transition metal features.[197,201] More strikingly, bond-breaking situations are not permitted in the molecular mechanics ensemble, thus reactivity cannot be investigated. Instead, the combination of MM with QM methods (see Section 2.5.2) can overcome these troubles, providing a powerful tool to deal with more intricate and larger chemical systems.

2.3. Molecular Dynamics

DFT and MM methods have been addressed from a static point of view, i.e., the explicit motion of atoms for a period of time has not been considered so far. In this regard, molecular dynamics simulations do concern the time evolution of atoms. Contrary to quantum dynamics (QD) which solves the time-dependent Schrödinger equation, molecular dynamics (MD) invokes classical Newton's equations of motion[202]

$$\vec{F} = m \cdot \vec{a} = -\frac{dE}{d\vec{r}} = m\frac{d^2r}{dt^2} \qquad [2.17]$$

$$\vec{a}_i = \frac{\vec{F}_i}{m_i} = \frac{d^2\vec{r}_i}{dt^2} \qquad [2.18]$$

Each molecular dynamics step represents a change in atom positions (**r**) over time (t). The magnitude and direction of motion are ruled by forces (**F**) that are computed from force fields —classical MD— or quantum mechanics methods —ab initio MD— (stage 2 in Figure 2.5). Then, the equations of motion are solved by means of numerical methods according to a certain time step Δt (stage 3 in Figure 2.5). One simple, robust, and widely-used approach to integrate such equations is the Verlet algorithm.[203] Regarding the time step, small Δt values provide accurate results but slow down the computation rate significantly. The reverse applies for large Δt values; the calculation process is accelerated but the conclusions may become pointless. The recommended time step should be an order of magnitude smaller that the larger vibrational frequency, usually X–H bond stretching. Therefore, typical Δt values are close to femtoseconds. When the atoms are propagated, the forces are computed again and the loop continues (stages 2–4 in Figure 2.5). Finally, the resulting atom configurations —snapshots— are collected into the so-called *trajectory* which represents the evolution of atom positions over time.

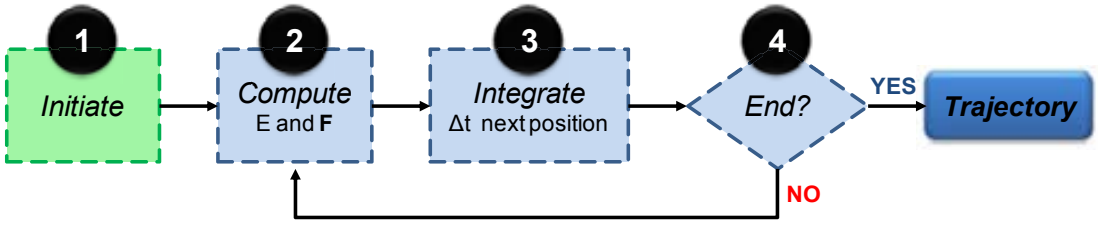

Figure 2.5 Simplified flow chart of a general MD procedure.

A typical simulation setup contains N atoms confined to a certain *box* of volume V. When dealing with simulation of liquids,[204] the interactions between the fluid and the walls of the box are not desired, thus they must be removed by using *periodic boundary conditions* (PBC). The initial volume V is considered a portion of the bulk and is called

primary cell. Then, this primary cell is periodically replicated in all directions to represent the bulk substance. These replicas, also known as *image cells*, move in exactly the same way the initial cell does. That is, when a molecule leaves the primary box, one of its images will enter through the opposite face (dashed blue circle, Figure 2.6). When computing the forces **F**, in principle, one must take into account all interactions between molecules lying in surrounding boxes and, consequently, infinite terms are generated. This is not practical and a truncation is needed, i.e., only a region of same size and shape as the initial box is considered around each molecule (dashed red square, Figure 2.6). This approximation is called *minimum image convention*.

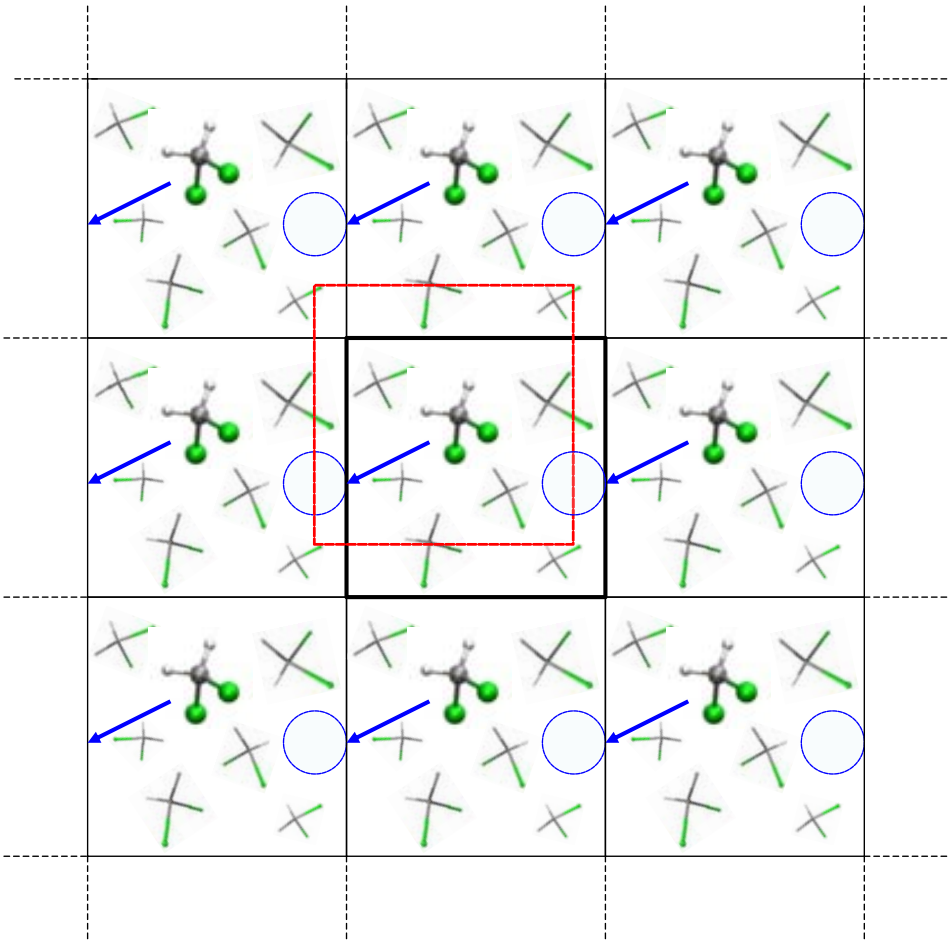

Figure 2.6 Two-dimensional periodic boundary scheme for bulk dichloromethane.

To conclude, the major advantage of MD is its ability to deal with environmental —solvent and temperature— effects from a dynamic point of view. Low-cost, classical MD appears as a powerful tool to tackle large macromolecules in realistic surroundings. However, the above-mentioned MM drawbacks arise again; the connectivity between atoms does not permit to break or make bonds and transition metal chemistry is not properly described with force fields. As discussed below, one can appeal to ab initio MD simulations to overcome these situations in either biological[205] or transition metal[206] areas.

2.3.1. Born–Oppenheimer molecular dynamics

Ab initio molecular dynamics (AIMD)[207] —also DFT-based MD— involves the motion of particles within a quantum mechanics framework, e.g., DFT. Particularly, Born–Oppenheimer molecular dynamics (BOMD) solves the time-independent Schrödinger equation for a fixed set of nuclear positions in each step. In other words, the interatomic forces are evaluated from electronic structure calculations (stage 2 in Figure 2.5) as MD simulation proceeds (stage 3 in Figure 2.5). These operations consequently entail expensive computational demands; whereas classical MD can easily cover hundred of nanoseconds —even a microsecond[208]—, AIMD runs on the picoscale. Nevertheless, the benefit that one can obtain by describing the environment quantum mechanically is undeniable worthwhile.

Because of such expensive computational cost, AIMD simulations cannot be extended careless. Then the question is, for how long should one run a molecular dynamics simulation? It depends on the size of the system as well as the kind of event one seeks to reproduce. Small structural changes that occur relatively fast —i.e., involving energy barriers comparable to k_BT— can be affordable. However, large conformation arrangements and chemical reactions are out of the time scale, thus techniques such as umbrella sampling[209] and metadynamics[210] are invoked to boost the occurrence of these events.

Before closing the section, one can alternatively use the popular Car–Parrinello approach (CPMD)[211] instead of BOMD. Despite it has not been employed herein, it became a cornerstone in the AIMD field. One refers to literature for inquiring readers.[207,212]

2.4. Solvent

In homogeneous systems, solvent is ubiquitous. One must face this aspect regardless of the computational method —QM or MM, with or without MD. In most cases, solvent acts innocently, but it can indeed come into play. There are three main approaches to describe solvent in computational chemistry (Figure 2.7), i.e., implicit, hybrid implicit–explicit, and fully explicit models. Again, the level of description is adapted to each particular system.

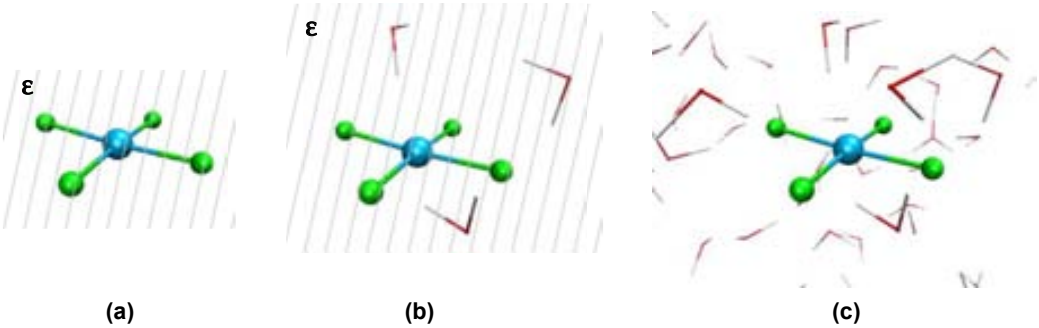

Figure 2.7 Solvent models for $[PdCl_4]^{2-}$ in water: (a) implicit, (b) hybrid implicit–explicit, and (c) fully explicit.

In implicit models (Figure 2.7a), solute is placed into a void molecular-shaped cavity and solvent is represented as a continuum with a dielectric constant ε.[213,214] This is the fastest and simplest way to implement qualitative solvent contributions and is recommended when solvent does not actively participate in the reaction. Among the available implementations, the SMD model has been elected for this dissertation.[215] It is composed by (i) the bulk electrostatic interaction and (ii) the cavity-dispersion-solvent-structure term which accounts for short-range interactions between solute and solvent in the first solvation shell. Authors claim for the universality of the model, meaning that it can be applied to any —charged or uncharged— solute in any liquid medium for which a few descriptors are known or can be reasonably estimated. That is, SMD relies on parametric functions —rather than constants— that take as input physical properties of the given solvent.

Whenever solute–solvent interactions really make the difference,[216] implicit models become inadequate. An initial approach consists in the inclusion of explicit solvent molecules in the QM calculation together with the continuum representation, which is named as either cluster–continuum or implicit–explicit model (Figure 2.7b). The number of solvent molecules as well as their configuration space are issues that one should deal with. Unfortunately, such considerations may increase the computational cost prohibitively.

Finally, the fully explicit model (Figure 2.7c) is the most accurate one but, at the same time, the most computationally demanding. In this treatment the solute is surrounded by a large number of solvent molecules. The description of such a bulk solvent requires the performance of MD simulations under periodic boundary conditions (Section 2.3).

2.5. Scope of Application

At this point, all the computational methodologies employed in the current dissertation have been briefly introduced. This section is then devoted to expound the applications. Unfortunately, the wide scope of the topics under consideration hampers a deeply discussion of each technique; proper literature is cited instead.

Routine electronic analyses are shown in Section 3 and no detailed introduction is required. The rest of techniques are gathered accordingly with future discussion. A concise initiation to QM/MM used in Section 4 is presented. Then, the potential energy surface concept is introduced since it represents the core of geometry optimisations in Section 3 and reactivity studies in Sections 5–7. Finally, protocols to estimate interesting chemical properties are commented; particularly, pK_a values in Section 8 and chemical shifts via magnetic shielding tensors in Section 9.

2.5.1. QM/MM

In previous sections, the pros and cons of the QM and MM methodologies have been mentioned. But, why not profit from both of them simultaneously? The fundamental concept is to save computational effort —as in MM— as well as to describe chemical properties accurately —as in QM. A major breakthrough was then introduced in the seminal work by Warshel and Levitt, who combined the two worlds forming a multiscale ensemble capable of handling complex systems.[217] They, along with Karplus, were honoured with the Nobel Prize in Chemistry in 2013.[13]

Nowadays, the term QM/MM has been adopted for such hybrid methods. A typical organometallic QM/MM scenario is illustrated in Figure 2.8. The QM partition concerns the atoms that either cannot be described by MM methods —e.g., transition metals— or undergo interesting events —e.g., bond-breaking and bond-forming reactions. Conversely, the MM region collects the rest of atoms and additional species that do not participate actively. By doing that, one can calculate the entire chemical system —no structural simplifications applied— in reasonable computation times. This technique is indeed very attractive in transition metal chemistry[218,219] and essential in biological systems.[220] Even more, DFT/MM approaches perform better than dispersion-lacked full DFT methods in describing dispersion interactions.[221] Regarding transition metal chemistry, the author would like to mention the IMMOM implementation which integrates a QM layer with an MM partition.[222] This protocol evolved towards the current ONIOM version,[223] in which n-layers are now available and each partition can be described with QM or MM, indistinctly.

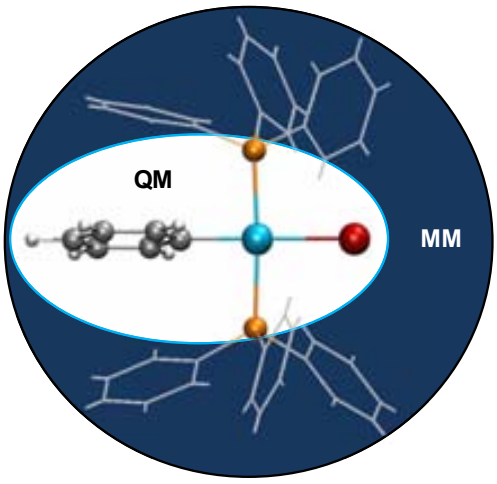

Figure 2.8 Typical QM/MM scheme for [Pd(Ph)(Br)(PPh_3)$_2$].

An interesting point is still missing. Where should one establish the border to separate the two worlds? The choice of QM/MM partitions may be non-trivial and can influence the outcome,[190] thus one should attempt to preserve the chemical integrity as much as possible.

Whether the boundaries pass through covalent bonds, several approaches are available to recover this artificial situation.[220]

In the same way that QM and MM (Section 2.3), QM/MM can be used to run MD simulations[207] as will be presented in Section 4. The system under study is shown in Figure 2.9, where no bonds were *cut*. The QM region is formed by a full cationic Pt(II) complex, while the MM partition collects the counteranion and the bulk dichloromethane solvent.

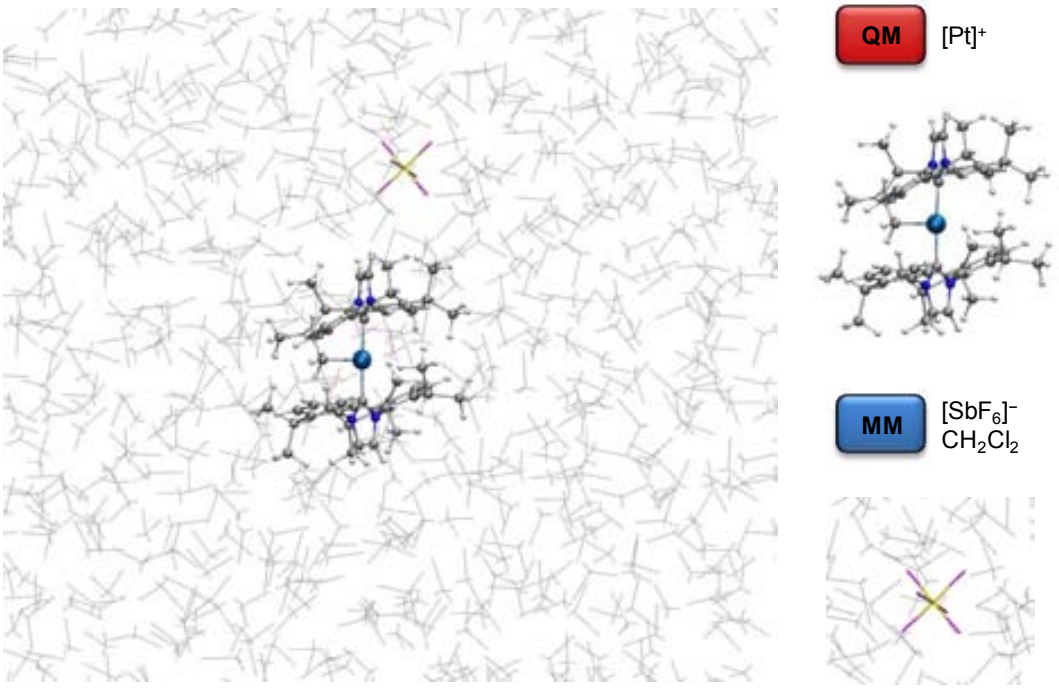

Figure 2.9 QM/MM scheme for $[Pt]^+$ and $[SbF_6]^-$ in explicit dichloromethane solvent. QM in balls-and-sticks and MM in lines.

2.5.2. Potential energy surface

The potential energy surface (PES)[224,225] represents the energy of a system according to the positions of the nuclei. It is built by computing the electronic energy —e.g., by means of DFT methods— within the Born–Oppenheimer framework for each nuclei configuration. Overall, the PES shows the energy landscape of a particular chemical system.

The computation of the entire surface is only feasible for small systems containing a few atoms. Actually, for reactivity studies of practical situations, only key stationary points —first derivative zero— on the energy surface are needed, i.e., minima and saddle points. All second derivatives of the energy —collected in the Hessian matrix— are positive in the former, but one negative value is found in the latter. From a chemical perspective, minima correspond to reactant, intermediates, and products, whereas saddle points of first order represent transition state structures (Figure 2.10). Certainly, energy profiles similar to Figure 1.8 are indeed cross-sections of the PES along a specific reaction coordinate.

As general manner to proceed, one should optimise the geometry of reactants and products —minima— and locate the corresponding transition state structures —maxima— that connect them. While optimisation towards minima is a routine job, location of transition state structures is not. There are methods to approach the topic,[224,225] but success is not always guaranteed. Somewhat a transition state structure may be considered a *piece of handicraft*. By computing the energy of these stationary points one can obtain insight about ΔE —difference between intermediates— and $\Delta E^{\ddagger}$ —difference between intermediates and transition states. The idea can be extended to ΔG and $\Delta G^{\ddagger}$ whether Gibbs energies are computed by means of using statistical thermodynamics formulas.

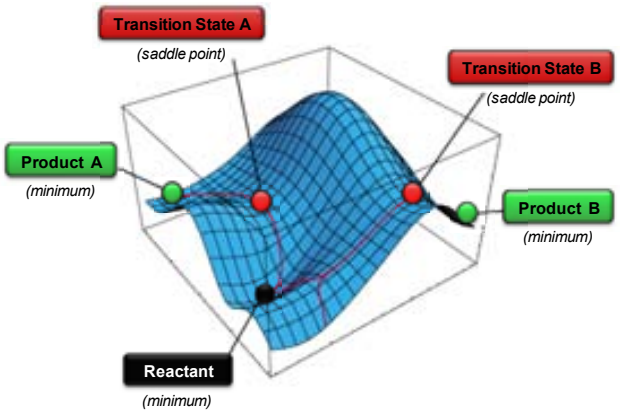

Figure 2.10 Conventional potential energy surface.

This widely-used procedure has been applied to analyse the PESs corresponding to C–H bond activation processes (Section 5) and cross-coupling reactions (Sections 6 and 7).

2.5.3. Computation of pK$_a$

Thermodynamics states that standard reaction Gibbs energies can be related to equilibrium constants as follows,

$$\Delta G^{\circ}_{r} = -RT \ \ln K_{eq} \qquad [2.19]$$

Applying this concept to acid–base chemistry, the estimation of an acid constant in a certain solvent, K_a^{sol} (Scheme 2.1), is apparently as simple as computing the standard Gibbs energy for the corresponding deprotonation process. However, important issues not considered at first glance complicate the path. For instance, the computation of accurate Gibbs energies of charged species in solution remains challenging; particularly, the proton contains no electrons thus the Gibbs energy must be computed indirectly.

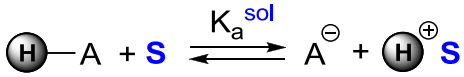

Scheme 2.1 Deprotonation equilibrium of an acid HA in solvent S.

To deal with solvation of species, the proper description of the solvent becomes crucial. As exposed in Section 2.4, one can simulate the solvent as a continuum (Figure 2.7a). Even though this method may provide accurate solvation Gibbs energies for neutral and ionic species, they intrinsically neglect explicit solute–solvent interactions. Hence, the next stage involves the inclusion of solvent molecules together with the implicit continuum description (Figure 2.7b). Many efforts have been focused in water, where solute–solvent interactions may become decisive. Variants of the same idea have been reported, namely cluster–continuum[226–228] or implicit–explicit[229] models.

Concerning the calculation of acid constants, several procedures can be found in literature.[230–232] As stated before, whenever explicit solvent molecules are considered in Scheme 2.1, pK_a values can be computed using analogous hybrid cluster–continuum models. Indeed, the importance of strong solute–solvent interactions in aqueous solution has been claimed.[233,234] The study has been extended to non-aqueous solvents.[235]

Computation of pK_a values is herein performed using an hybrid cluster–continuum approach[226,227] as shown in Scheme 2.2. In this thermodynamic cycle solvent molecules (S) are explicitly considered forming a cluster configuration (S_n). $\Delta G^{o}_{g,deprot}$ means the deprotonation Gibbs energy in gas phase and $\Delta G^{o\rightarrow *}$ stands for the conversion factor from an ideal gas standard state of 1 atm "o" to a standard state of 1 M "*".[a] $\Delta G^{*}_{sol}(X)$ terms account for standard solvation Gibbs energies of species X. Lastly, RT·ln([sol]/n) represents the correction term for the Gibbs energy change of 1 mol of [sol]/n M liquid state to 1 M.

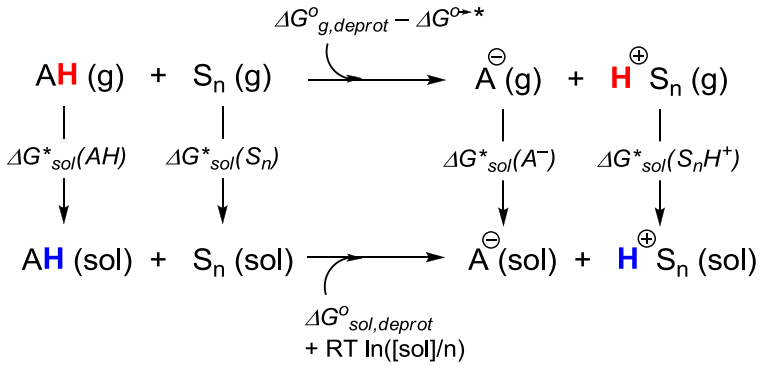

Scheme 2.2 Cluster-type thermodynamic cycle for pK_a computation.

Following the thermodynamic cycle previously discussed (Scheme 2.2), the deprotonation Gibbs energy in solution is calculated as

[a] $\Delta G^{o\rightarrow *} = RT\ \ln(R_gT) = 1.9$ kcal mol^{-1} where $R = 1.986\ 10^{-3}$ kcal K^{-1} mol^{-1}, $R_g = 0.082$ atm L K^{-1} mol^{-1}, and $T = 298.15$ K.

$$\Delta G^{o}_{sol,deprot} = \Delta G^{o}_{g,deprot} - \Delta G^{o\rightarrow *} + \Delta G^{*}_{sol}\left(A^{-}\right) + \Delta G^{*}_{sol}\left(H^{+}S_{n}\right) - \Delta G^{*}_{sol}\left(AH\right) - \Delta G^{*}_{sol}\left(S_{n}\right) - RT\ln\left([sol]/n\right) \quad [2.20]$$

Then, isolating pK_a from [2.19] (ln (10) = 2.303) one obtains

$$pK_a^{sol} = \Delta G^{o}_{sol,deprot} / 2.303\ RT \quad [2.21]$$

It can be deduced from [2.21] that Gibbs energy errors of 1.4 kcal mol^{-1} results in an error of 1 pK_a unit at room temperature. Therefore, an error of 2 pK_a units is usually accepted.[230]

One last parameter still unknown is n, the number of solvent molecules. This value is usually optimised to properly account for the solvation Gibbs energy of the proton, $\Delta G^{*}_{sol}(H^{+})$. In aqueous solution, the current accepted value is –265.9 kcal mol^{-1} obtained by Tissandier et al.[236,237], albeit another approximation claiming for more negative values in aqueous and non-aqueous solvents has been reported.[238] This value has been computationally confirmed by using hybrid cluster–continuum (–266.7 kcal mol^{-1})[226] and implicit–explicit (–266.1 kcal mol^{-1})[229] models. For the cluster-type thermodynamic cycle in Scheme 2.3, the actual $\Delta G^{*}_{sol}(H^{+})$ is obtained when $n\rightarrow\infty$.[226] Hence, the number of solvent molecules is that which provides a converged value of $\Delta G^{*}_{sol}(H^{+})$. Zhan and Dixon included 4 water molecules[227] and Bryantsev et al. increased this number up to 10.[226]

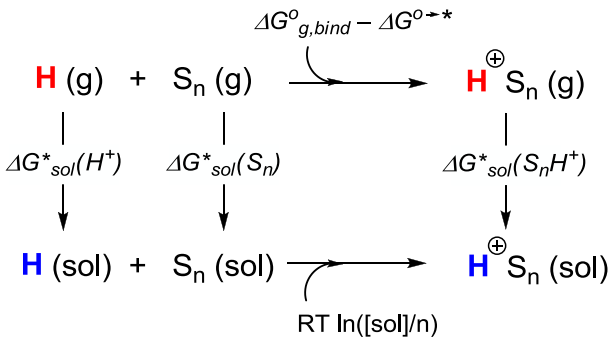

Scheme 2.3 Cluster-type thermodynamic cycle for $\Delta G^{*}_{sol}(H^{+})$ computation.

According to Scheme 2.3, $\Delta G^{*}_{sol}(H^{+})$ is finally expressed as

$$\Delta G^{*}_{sol}\left(H^{+}\right) = \Delta G^{o}_{g,bind} - \Delta G^{o\rightarrow *} + \Delta G^{*}_{sol}\left(H^{+}S_{n}\right) - \Delta G^{*}_{sol}\left(S_{n}\right) - RT\ln\left([sol]/n\right) \quad [2.22]$$

The above-mentioned procedure will be applied in Section 8 to compute pK_a values in THF and water. Firstly, the number of solvent molecules is estimated according to Scheme 2.3. Then, pK_a values of several dihydrogen transition metal complexes are evaluated in THF and water following Scheme 2.2.

2.5.4. Computation of chemical shift

From an ab initio standpoint,[239,240] the chemical shift of a nucleus (δ) is acquired by computing the magnetic shielding 3×3 tensor (σ) as the second derivative of the total energy with respect to the external magnetic field and the magnetic moment. A priori, this derivative can be evaluated by any QM method, e.g., DFT.[241,242]

A point to consider is the so-called gauge origin problem. It means that the results depend on the particular origin of coordinates selected for the calculation and, consequently, the comparison of results computed with different origins becomes meaningless. This issue is irrelevant for other types of calculations —PES analysis or geometry optimisations— but applies to molecular properties which appear in presence of external magnetic fields, such as NMR parameters. Among the several ways to overcome this obstacle, the gauge-including atomic orbital method (GIAO) is the most common.[243] It introduces a factor in the description of the atomic orbitals which depends on both the position of the atom and the magnetic field.

Following the path to obtain chemical shift values, symmetrisation and diagonalisation of the tensor σ are required. This procedure yields three eigenvalues, which average value is denoted as *isotropic shielding* σ_{iso}. Actually, only differences between σ_{iso} can be measured in solution due to averaging caused by molecular motion. By comparison with a standard value σ_{iso}(standard) the chemical shift can be approximate as

$$\delta = \delta_{iso} = \sigma_{iso}(\text{standard}) - \sigma_{iso} \qquad [2.23]$$

σ_{iso}(standard) is computed for the experimental reference compound in the same way as described above. Whenever the reference species is tricky to calculate or is not available for the target nucleus —such is the case of ^{103}Rh—, calculated σ_{iso} values for a large set of compounds are correlated with experimental δ in a linear regression. The value of σ at δ = 0 is taken as σ_{iso}(standard). This kind of approach is frequently applied to profit from error cancellations.

Quoting Schreckenbach et al., chemical shift is *sensitive to everything*.[244] In the DFT framework, it depends on the functional as well as the basis set. In first term, Bühl disclosed that the hybrid B3LYP functional performs quite better than the pure BPW91 one for ^{57}Fe and ^{103}Rh nuclei, thus the inclusion of exact exchange was recommended.[245] The choice of density functional (Section 2.1.2) indeed dictates the reliability of the molecular geometry, which is a deciding point in the computation of NMR parameters. Regarding basis sets, a proper description of the core electrons is mandatory in spectroscopy. Special functions for

such kind of calculations have been developed; see for instance, IGLO basis set.[246] When computing the chemical shift of transition metals, they should not profit from usual effective core potentials anymore and all electrons basis sets are required instead. Alternatively, the frozen-core approximation, which properly describes the asymptotic behaviour of orbitals near the nucleus, is also available.[242,247]

A quick mention concerning relativistic effects is deserved here,[248,249] particularly for the calculation of NMR parameters.[250,251] Relativity arises when particles approach the speed of light. As the nucleus becomes heavier, such contribution gains importance. As regards the chemical shift computation of *3d* and *4d* transition metal nuclei (e.g., ^{103}Rh), the relativistic heavy atom effects on their own shieldings (heavy atom–heavy atom effect, HAHA) are fairly systematic and cancel each other to a large extend,[138,139] at least whether no other heavier atoms are present in the neighbourhood (heavy atom–other heavy atom effect, HAOHA).[250] Otherwise, such as *5d* transition metal nuclei (e.g. ^{195}Pt), scalar and spin-orbit corrections should be taken into account.

Together with all previous issues, temperature and solvent effects may be relevant.[136] Regarding transition metal systems, Bühl and Parrinello carried out ab initio molecular dynamics simulations on vanadium complexes in water.[140] They computed ^{51}V chemical shifts using representative snapshots along the trajectory. This computational protocol allows the inclusion of thermal —via dynamic averaging— and solvent effects, though in their particular case both contributions were small. Likewise, Truflandier and Autschbach also performed ab initio molecular dynamics simulations on aqueous platinum complexes to further compute ^{195}Pt chemical shifts.[141] As previously hinted for *5d* metals, relativity matters. This improved procedure provided chemical shifts in very good agreement with experimental values.[141]

Computed ^{103}Rh chemical shifts on optimised Rh–bis(phosphine) structures will be presented in Section 9 according to equation [2.23]. σ_{iso}(standard) is obtained through an experiment–theory correlation as discussed above. No relativistic effects are considered in the calculations.

II

Objectives

To me, there's only one form of human depravity
—the man without a purpose.

Hank Rearden in “Atlas Shrugged” by Ayn Rand

The current dissertation seeks the clear purpose of applying selected computational protocols to analyse and interpret a broad scope of chemical scenarios, particularly those involving organometallic compounds. The central objectives are divided into three general chapters: *Structure*, *Reactivity*, and *Properties*.

Structure

Computation allows the calculation and rationalisation of transition metal geometries as well as bonding situations. In this line, the particular goals tackled herein are:

- Unravelling the unusual see-saw structure of a paramagnetic Pt(III) complex bearing alkyl and N-heterocyclic carbene ligands.
- Analysing agostic interactions in low-coordinate T-shaped Pt(II) species as well as revealing their behaviour in solution.

Reactivity

Computation provides useful tools to devise and evaluate reaction mechanisms at microscopic level. As concerns organometallic reactivity, the targets addressed in this dissertation are:

- Rationalising the reactivity trends of T-shaped Pt(II) species towards intermolecular C–H bond activation processes through the inspection of the stereoelectronic properties of N-heterocyclic carbene ligands.
- Disclosing the mechanistic role of the base —hydroxide anion— in Pd-catalysed Suzuki–Miyaura cross-coupling reactions.
- Providing a full mechanistic picture of Si-based Pd-catalysed vinylation reactions in water in order to account for the experimentally reported products.

PROPERTIES

Computation allows the prediction and subsequent understanding of several chemical properties. The particular purposes of this chapter are:

- Estimating acid constants as pK_a values in water solvent for a set of transition metal dihydrogen complexes.
- Calculating ^{103}Rh NMR chemical shifts and finding potential correlations to understand trends in NMR parameters.

III

Structure

—As simple as that? You didn't use magic?

—Only common sense. It's a lot more reliable in the long run.

"Mort" by Terry Pratchett

3. Unusual See-Saw Pt(III) Structure

This study is devoted to analyse the electronic and structural features of an unusual see-saw Pt(III) complex bearing N-heterocyclic carbene (NHC) ligands. Each section is presented as follows. Firstly, *Introduction* focuses on experimentally reported Pt(III) structures, neglecting reactivity issues deliberately, and *Computational Details* specifies the particular theoretical procedures that have been performed. Concerning the results, *Ligand- or Metal-Centred Radical?* discloses the location of the unpaired electron over the molecule whereas *Origin of the See-Saw Structure* analyses both steric and electronic factors to account for the unexpected see-saw structure. Finally, *Conclusions* collects the fundamental outcomes that computation has provided.

Most of these computational results have been published as shown in Annex A.[252]

3.1. Introduction

The activation of C–H bonds of hydrocarbons is a quite interesting process in which platinum compounds take part actively (Section 1.2.1). In this regard, the oxidation of Pt(II) species is closely involved in the Shilov process. Pt(IV) compounds are mostly formed as transient intermediates, but occasionally their paramagnetic Pt(III) counterparts can be stable enough to take them into account.[253,254] As concerns the formation of Pt(III) species, the use of bulky ligands can prevent dimerisation, but disproportion may remain.[254]

Due to the above-mentioned handicaps, characterised mononuclear Pt(III) compounds are indeed scarce.[255] Selected complexes are gathered in Figure 3.1. In 1984, Usón et al reported the first mononuclear Pt(III) species **1** containing perchlorophenyl ligands.[256–258] The solid state structure clearly displays a square-planar environment around the platinum centre. Later, Bois et al. obtained the dithilolate-based square-planar Pt(III) anion **2** in presence of a Pt(II) species as countercation, being the closest Pt···Pt distance 3.514 Å.[259] Alves et al. also employed related dithiolate ligands.[260] Stephen et al. isolated a six-coordinate Pt(III) species **3** which exhibits two thioether macrocycles in a distorted octahedral arrangement.[261] Recently, the cationic Pt(III) complex **4** bearing bulky IPr (1,3-bis(2,6-diisopropylphenyl)imidazol-2-ylidene) ligands has been successfully characterised by means of crystallographic, spectroscopic, electrochemical, and computational techniques.[262] The square-planar geometry of **4** was confirmed by X-ray diffraction studies showing C_{IPr}–Pt–C_{IPr} and I–Pt–I angles of 179.5° and 177.1°, respectively. Among the predominance of four-coordinate square-planar shapes (Section 1.1.1), the uncommon see-saw Pt(III) structure **5** emerges (Figure 3.1).[252] As in **4**, **5** also contains bulky IPr ligands but

now one of them, labelled as IPr', forms a metalocycle involving a former methylic carbon of one isopropyl group. The see-saw structure is easily disclosed by examining angles; the C_{IPr}–Pt–$C_{IPr'}$ moiety is almost linear (178.2°) but the C–Pt–Br angle is rather bent (149.5°).

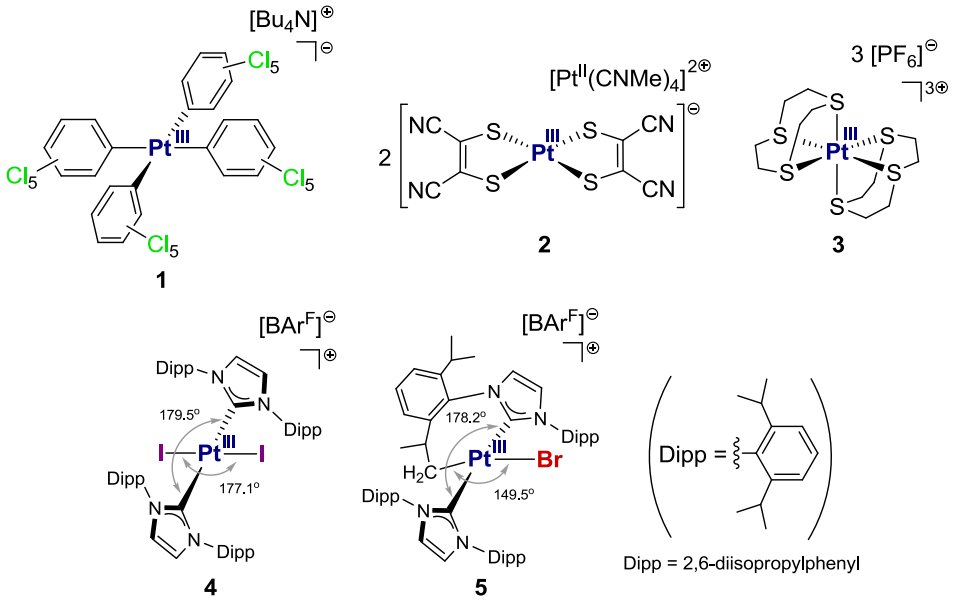

Figure 3.1 Characterised mononuclear Pt(III) species reported in literature. Angles from X-ray studies.

Paying attention to paramagnetic third-row NHC-based transition metal complexes, only a few studies appear in literature. Tumanskii et al. reported a strong participation of the IMes ligand (1,3-bis(2,4,6-trimethylphenyl)imidazol-2-ylidene) in [Re(CO)$_5$(IMes)].[263] Conversely, Roberts et al. described several [CpW(CO)$_2$(NHC)] species as metaloradicals.[264]

The current computational investigation attempts to accomplish two main purposes, i.e., (i) to disclose the ligand- or metal-centred nature of the radical and (ii) to find out the origin of the see-saw structure of **5**.

3.2. Computational Details

Forthcoming calculations were performed at the DFT level by means of the BHLYP functional[161,165] —suitable for open-shell complexes[195,196]— as implemented in Gaussian 09.[265] The Pt, Br, and I heavy atoms were described using scalar-relativistic Stuttgart-Dresden SDD effective core potentials and their associated double-ζ basis sets,[266] complemented with a set of f-polarisation functions.[267,268] The 6-31G** basis set was used for the H,[269] C, N, O, and Si atoms,[270] including diffuse functions for the O atoms.[271] All structures were fully optimised in gas phase without any symmetry restriction. Computation of the Hessian matrix confirmed that structures corresponded to minima. Population analyses were performed by computing Mulliken spin densities —fairly suitable for transition metal complexes[272]— and Natural Spin Orbitals.

3.3. Ligand- or Metal-Centred Radical?

The computational study is focused on the novel see-saw Pt(III) structure **5**. However, as test probes, the well-established complex **1** and the closely-related species **4** are also calculated. Gas-phase optimisations of **1** and **4** successfully predict square-planar geometries as experimentally reported (Figure 3.1). Subsequent population analyses are performed to get insight into their electronic features. In agreement with electron paramagnetic resonance (EPR) experiments,[a] the spin density of **1** is totally localised over Pt (98%),[258,262] whereas **4** splits the spin density among Pt (41%) and I (29% each).[262] These values are reflected on the shape of the single occupied molecular orbitals (SOMO) as shown in Figure 3.2. The SOMO of **1** is definitively described as a Pt d_{z^2} orbital, whereas the SOMO of **4** reveals contributions from Pt d_{xz} and I p_x orbitals. Similarly, the reported SOMO of the octahedral complex **3** (Figure 3.1) represents 30% Pt, 48% axial S, and 12% equatorial S.[261]

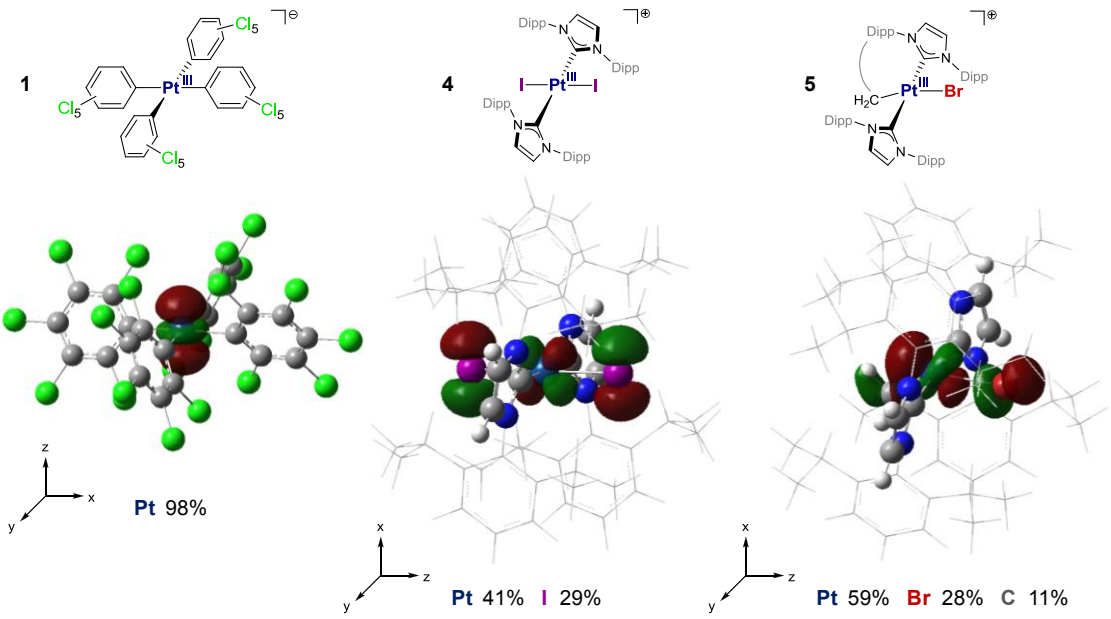

Figure 3.2 Mulliken spin densities and SOMO representation (isovalue 0.05) of complexes **1**, **4**, and **5** (Dipp = diisopropylphenyl).

As concerns **5**, the optimised geometry fits the experimental see-saw shape displaying a C_{IPr}–Pt–$C_{IPr'}$ angle of 178.0° (178.2° in solid state) and a C–Pt–Br angle of 143.2° (149.5° in solid state). The spin density is mainly localised over Pt (59%), albeit Br (28%) and cyclometalated C (11%) also contribute. No significant spin density is found over the IPr ligand. In comparison with the similar complex **4**, the SOMO of **5** is now more spread but mostly accounts for the spin density values (Figure 3.2).

[a] Briefly, large deviations of measured g-values with respect to the free electron g_e (2.0023) generally indicate participation of metal orbitals.

3.4. Analysis of the See-Saw Structure

As previously commented (Figure 1.5 and Figure 3.1), four-coordinate Pt(III) species are expected to be square-planar. Since **5** clearly shows a see-saw geometry, calculations will be devoted to this special case by inspecting both steric and electronic effects.

Firstly, steric effects are evaluated by optimising the simplified model complex **5M** (Figure 3.3), in which the Dipp (diisopropylphenyl) arms of the IPr ligand have been replaced by methyl groups forming the new IMe ligand (1,3-dimethylimidazol-2-ylidene). Additionally, possible structural constrains imposed by the cyclometalated arm are removed by introducing a methyl ligand bound to platinum. As a matter of fact, less hindered **5M** still adopts a see-saw structure, i.e., C_{IMe}–Pt–C_{IMe} angle of 178.6° and C–Pt–Br angle of 148.3°. The spin densities contributing to the SOMO of **5M** (56% Pt, 32% Br, and 11% C in Figure 3.3) are essentially the same as those of **5** (59% Pt, 28% Br, and 11% C in Figure 3.2). Since the see-saw structure persists, steric effects can be discarded.

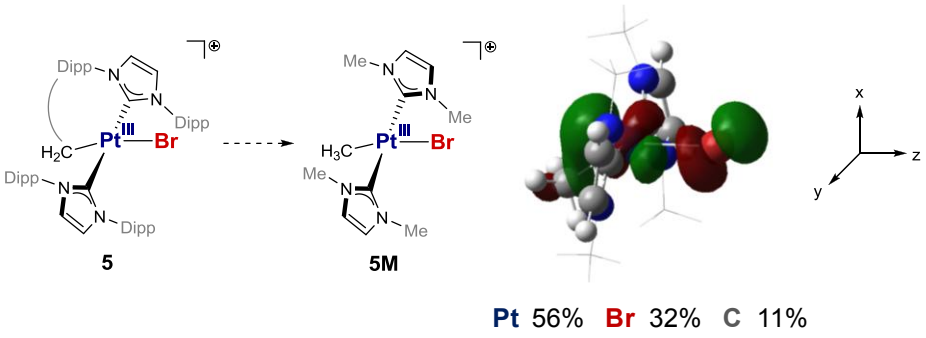

Figure 3.3 SOMO representation (isovalue 0.05) of model **5M**.

As stated above, the model **5M** is indeed a good representation of the actual complex **5**. Therefore, to gain further insight, the deformation from see-saw to square-planar geometry is applied to **5M** taking as a reaction coordinate the C–Pt–Br angle, θ, and optimising all the geometrical parameters at fixed values of θ. This angle is gradually varied ($\Delta\theta \approx 10°$) from 148.3°, the optimised value in **5M**, to 180.0°, the ideal value in square-planar structures. The resulting geometries and SOMOs are collected in Figure 3.4. The C_{IMe}–Pt–C_{IMe} angle, φ, remains constant at ca. 179°. As expected from the imposed structural restrains, the energy raises 5.6 kcal mol^{-1} above the see-saw minimum. In the square-planar limit, two main events are observed; (i) the Pt and Br orbital contributions evolve towards pure d_{xz} and p_x orbitals, respectively, in agreement with the SOMO of the square-planar complex **4** (Figure 3.2), and (ii) the overlapping of orbitals coming from Pt and C vanishes at this level of isovalue.

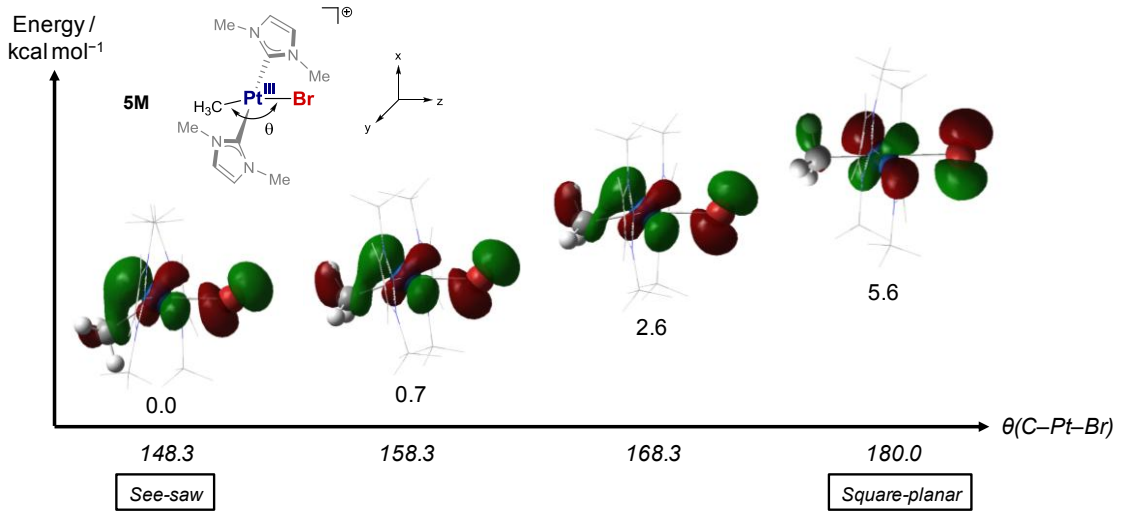

Figure 3.4 Evolution of the SOMO of **5M** (isovalue 0.05) along the C–Pt–Br reaction coordinate, θ.

The precedent mixing of methyl and platinum orbital contributions seems to drive the distortion from the square-planar geometry; in other words, the presence of the methyl ligand does influence the structure of **5M**. Generally speaking, ligands in *trans* position to bromide may exert a strong impact in deciding the geometry.

To stress this point, the closely-related square-planar complex **4** is simplified to **4M** in the same manner as **5M** —replacing Dipp arms of IPr by methyl groups— and an analogous procedure of bending along the I–Pt–I angle, θ', is then applied. This angle is gradually varied (Δθ' = 10°) from 180°, the optimised value in **4M**, to 150°, the value in the see-saw environment of **5M**. The resulting geometries and SOMOs are shown in Figure 3.5. The C_{IMe}–Pt–C_{IMe} angle, φ', stays invariable at 180°. Contrary to **5M** (Figure 3.4), the potential energy surface of **4M** seems smoother and, more interestingly, no relevant mixing between Pt and I is observed in the see-saw limit at this level of isovalue.

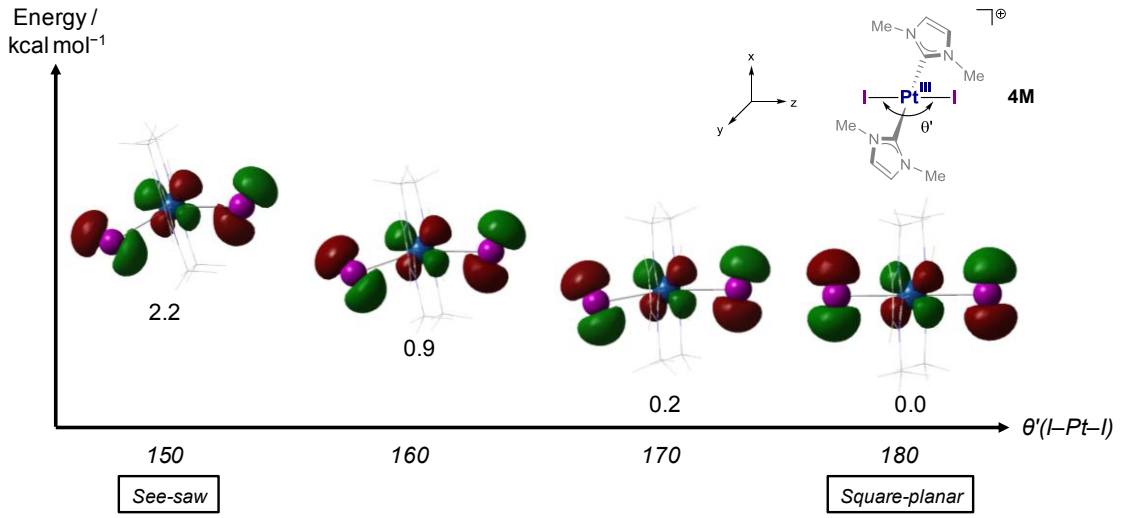

Figure 3.5 Evolution of the SOMO of **4M** (isovalue 0.05) along the I–Pt–I reaction coordinate, θ'.

Due to the putative role of alkyl groups in deciding the geometry, electronic effects are now considered by changing the methyl ligand in **5M** by other ligands L of distinct electronic nature. One should remind that only the electronic character of L with respect to the ligand in *trans* position —bromide in this case— is analysed here. Since the monitoring of the two largest angles in four-coordinate species has proved to be useful,[40,273] the resulting complexes are plotted in Figure 3.6 according to θ(L–Pt–Br) and φ(C_{IMe}–Pt–C_{IMe}) angles. Dashed grey squares give support delimitating regions where see-saw and square-planar structures prevail. Three different kinds of electron-donating anionic ligands are evaluated: strong σ-donors in red, moderate σ-donor in blue, and weak σ-donors and π-donors in green. To implicate the previously studied complexes, perchlorophenyl and iodide ligands —as found in **1** and **4**— are also considered. Strong σ-donor ligands such as silyl and hydride favour see-saw structures, displaying θ angles of 138.4° and 140.7°, respectively. This effect is however less marked for cyanide and alkenyl ligands, where θ angles are ca. 160°. Otherwise, the presence of less donating ligands such as hydroxide and bromide recovers the square-planar shape. In all these situations, φ angles remain almost constant, ranging from 175° (L = Ph) to 179° (L = Me). The trend shows that ligands with strong σ-donor character correlate to large structural deformations towards see-saw geometries. Extending the results of **5M** towards **5**, electronic effects of the alkyl ligand of IPr' mostly account for the see-saw structure.

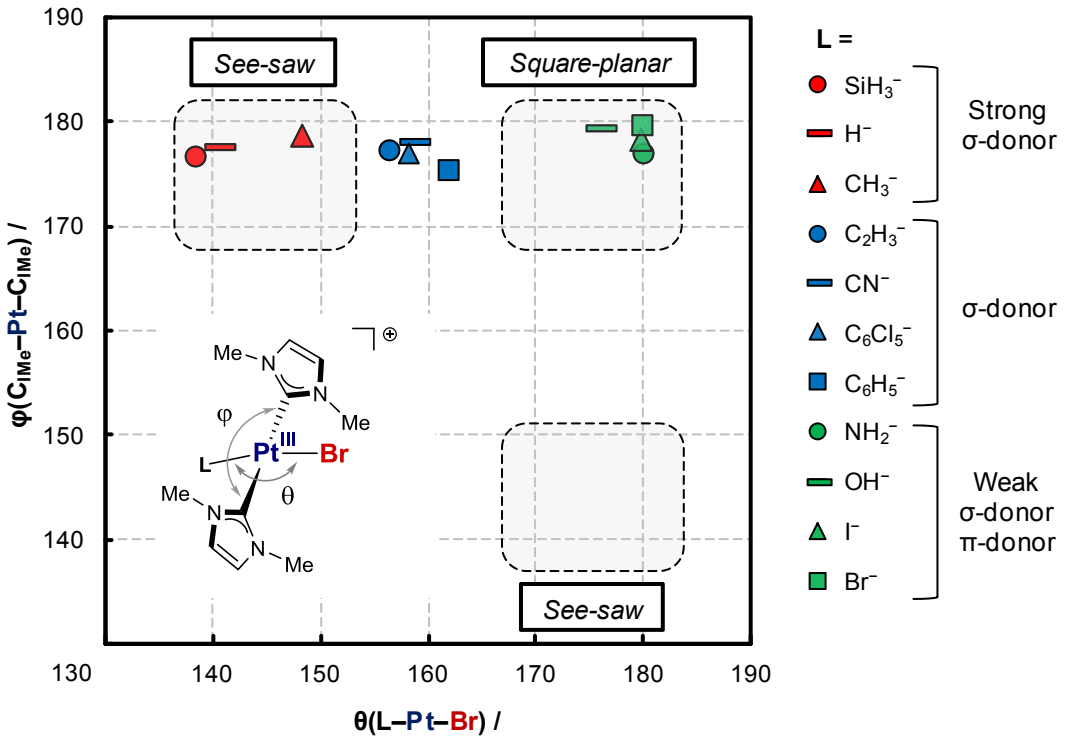

Figure 3.6 Distribution of $[Pt^{III}(IMe)_2(L)(Br)]^+$ complexes according to φ and θ angles.

3.5. Conclusions

Paramagnetic Pt(III) species $[Pt(IPr)(IPr')(Br)]^+$ **5** has been investigated by means of DFT-based geometry optimisations and electronic population analyses. Computational results are summarised as follows.

- Pt(III) complex **5** is mostly described as a metaloradical species where NHC ligands act innocently.
- The see-saw geometry in **5** is not explained by steric effects. Instead, this unusual structure is supposed to be dictated by the electronic influence of the alkyl moiety in the IPr' ligand.
- Based on calculations of the model complex **5M**, strong σ-donor ligands in *trans* position to bromide drive deformations from square-planar geometries.

4. Dynamics of T-Shaped Pt(II) Species in Solution

This study reveals dynamic features of agostic interactions in T-shaped Pt(II) complexes. Each section is presented as follows. *Introduction* provides a general overview of the agostic interaction as well as selected characterised Pt(II) species in which one can find this kind of bonding. *Computational Details* indicates the particular theoretical aspects used in the calculations. Concerning the results, *Gas Phase Structures* initially explores the agostic bonding by analysing gas-phase geometries whereas *Dynamic Perspective of Agostic Interactions* further addresses how such agostic contacts evolve over time in presence of explicit solvent. *Discussing Agostic Situations* sums up the results and emphasises key factors when dealing with agostic interactions. Finally, *Conclusions* gathers the main ideas that computation has provided.

These computational results have been published as shown in Annex A.[274]

4.1. Introduction

The *agostic* interaction is typically defined as an intramolecular contact between a metal centre M and a C–H bond.[10,11] Depending on the number of atoms that form the chelating ligand, n, the agostic bonding is labelled as α, β, γ, δ, and remote ζ for n = 1, 2, 3, 4, and more than 4 links, respectively (Figure 4.1). Some structural and spectroscopic guidelines (Figure 4.1) have been suggested to characterise agostic interactions[47] and to discern them from *anagostic* situations.[275] Whereas the former exhibits a 3-centre-2-electron bonding nature, the latter is largely electrostatic. On the other side one can find a 3-centre-4-electron intramolecular hydrogen bond in which the metal M acts as H-bond acceptor.[276,277] All these parameters are quite general and several factors such as large chain sizes can influence the agostic moiety.

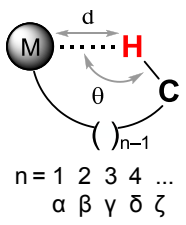

	Agostic	*Anagostic*	*H-bond*
d(M···H)	1.8–2.3 Å	2.3–2.9 Å	variable
θ(M···H–C)	90–140	110–170	~180
^{1}H δ(H)	Upfield	Downfield	Downfield

Figure 4.1 Main features of agostic and non-agostic situations.

The agostic coordination mode is now a recurring event in organometallic chemistry.[47] It is involved in important reactions such as polymerisation or C–H bond activation. An interesting example of that concerns low-coordinate Pt(II) species, in which the presence of open coordination sites prompts the formation of agostic interactions. These species indeed

participate in a number of reactions, for instance, β-H elimination, intra- and intermolecular C–H bond activation, H_2 bond activation, ligand substitution, and so on and so forth.[45]

Selected cationic phosphine-based Pt(II) complexes are compiled in Figure 4.2. Orpen, Spencer and co-workers firstly described a series of complexes $[Pt(alkyl)(P–P)]^+$ (P–P = bidentate phosphine) in which norbornyl[278,279] and ethyl-derivative groups[280–282] were able to form β-agostic interactions. X-ray studies of **1** —norbornyl[278]— and **2** —ethyl[280]— confirmed the agostic structures. In some cases, the β-agostic contact was strong enough to generate hydride–ethylene isomers. Later, some bisphosphine complexes were reported in which one alkyl substituent of a phosphine —instead of an alkyl ligand— can reach the metal centre. Baratta, Carmona and co-workers synthesised complexes $[Pt(P)(P')]^+$ **3**[283] and **4**[284] where the phosphine P' underwent a cyclometalation process. The vacant site *trans* to the cyclometalated alkyl ligand was fulfilled by a δ-agostic interaction according to X-ray studies. Further hydrogenation could recover the original phosphine arm, thus generating hydrides $[Pt(H)(P_2)]^+$.[283,284] In these hydride complexes the agostic interactions were deduced on the basis of NMR coupling constants.[45] Related species $[Pt(L)(P_2)]^+$ were also reported exhibiting γ-agostic contacts *trans* to L, being methyl in **5**[285] and catecholatoboryl in **6**.[286]

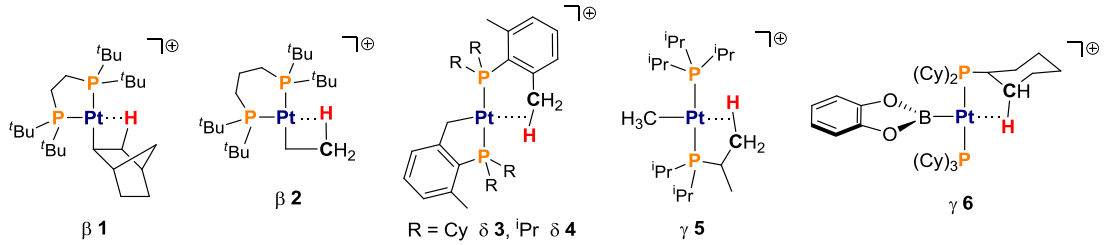

Figure 4.2 Phosphine-based agostic Pt(II) complexes.

Referring to other ligands, some examples are collected in Figure 4.3. The neutral phenylpyridyl complex **7** displayed an uncommon bifurcated agostic interaction.[287] In the same way as phosphines P' in **3** and **4**, NHC ligands can also undergo cyclometalation processes forming $[Pt(NHC)(NHC')]^+$, where NHC' stands for the cyclometalated ligand. Complexes **8** with I^{t}Bu (1,3-di-*tert*-butylimidazol-2-ylidene) and **9** with IPr (1,3-bis(2,6-diisopropylphenyl)imidazol-2-ylidene) were described, but only the latter has been characterised in solid state.[288]

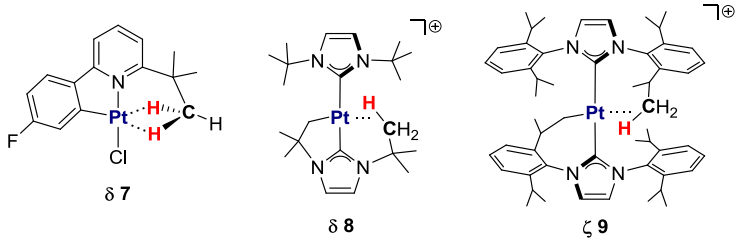

Figure 4.3 Phenylpyridine- and NHC-based agostic Pt(II) complexes.

As previously noted, obtaining structural data is an important point to evidence agostic contacts (Figure 4.1). From a theoretical point of view, geometry optimisation becomes the initial step to reveal them, but several computational procedures allow to inspect the agostic bonding in detail, for instance, Atoms in Molecules and Natural Bond Orbital analyses.[289–291] Particularly, Thakur and Desiraju performed Natural Bond Orbital calculations on a set of first-, second-, and third-row transition metal complexes to investigate M···H–C interactions.[292] Among the Pt(II) complexes that were analysed, M···H–C contacts in **1**–**3** were definitively classified as agostic, albeit in the case of **5** both agostic and H-bond characters could be assigned. Besides, the calculation of NMR parameters have been used as probes to meet agostic interactions in alkylidene species[293,294] and d^8 transition metal complexes.[295,296]

Literature proves that much effort has been put into analysing the *static* agostic bonding, but little attention has been drawn to its *dynamic* behaviour. Early investigations focused on the study of polymerisation reactions by means of ab initio molecular dynamics simulations in gas phase. Meier and co-workers dealt with olefin insertion processes in Zr-catalysed polymerisations, where α- and γ-agostic structures were located.[297] Ziegler and co-workers described several exchange processes between different agostic situations in Ti- and Zr-based catalysts.[298–300] Recently, Rowley and Woo performed molecular dynamics simulations on a Zr-catalysed polymerisation reaction by treating counteranion and pentane solvent explicitly in a QM/MM framework.[301] They were able to detail fast β- to α-agostic isomerisation processes in a zirconocene catalyst.

In this scene, AIMD simulations indeed appear as promising tools to gain further insight on agostic interactions taking into account both temperature and solvation factors.[206,207] Particularly, this study analyses agostic Pt(II) species in explicit dichloromethane solvent by means of QM/MM MD simulations. Complexes **8** and **9** were considered because the experimental characterisation is challenging to achieve.[288] The agostic bonding in **8** was determined in solution by NMR spectroscopy since no crystals suitable for X-ray studies were obtained. On the other hand, complex **9** showed agostic interactions in solid state but no information about its solution behaviour could be disclosed from NMR experiments; overlapping of signals and signal averaging hampered its elucidation. For the sake of comparison, the well-defined β-agostic complex **1** was also investigated.[280]

The current investigation is directed towards (i) characterisation of agostic interactions in solution, and (ii) discussion about how dynamics can impact such agostic bonding.

4.2. Computational Details

Forthcoming calculations —both gas-phase optimisations and MD simulations— were performed using the freely available CP2K program package.[302,303] Ab initio molecular dynamics (AIMD) simulations were run on complexes **2**, **8**, and **9** according to the Born-Oppenheimer approach (Section 2.3.1) at the DFT level by means of the PBE exchange-correlation functional[162] which correctly describes agostic interactions.[190] An additional simulation of **9** was run by adding the dispersion correction D3 of Grimme et al.[182] AIMD simulations were set up at constant volume and temperature (300 K) through a velocity rescaling thermostat which guarantees canonical sampling.[304] The Quickstep algorithm[305,306] was used to solve the electronic structure problem using a double-ζ plus polarization (DZVP) basis set[307] to represent the orbitals and plane waves (up to 300 Ry) for the electron density. Core electrons were described using pseudopotentials.[308,309] Wave function optimisation was achieved through the orbital transformation method using electronic gradients of $5{\cdot}10^{-7}$ as convergence criterion.[310]

Simulations of complexes **2**, **8**, and **9** were run in explicit dichloromethane, the solvent used in experiments.[280,288] Around 1000 dichloromethane (DCM) molecules were included in a cubic box of 47.482 Å edge to reproduce the experimental density.[311] The simulation cell was treated under periodic boundary conditions. The Poisson solver developed by Martyna and Tuckerman was used to remove the periodicity intrinsic in the plane wave representation.[312] A counteranion $[SbF_6]^-$ was included in the model to neutralize the simulation cell. The organometallic complexes were treated by quantum mechanics (QM) whereas the DCM molecules and counteranion were described using molecular mechanics (MM) as shown in Figure 2.9. The QM box was cubic of 25 Å edge for each complex. DCM solvent was described by the fully flexible all-atom potential developed by Fox and Kollman.[313] The force field was shown to reproduce the macroscopic properties of liquid DCM, including density, heat of vaporisation, and diffusion constant, in good agreement with experimental data. Suitable parameters were particularly designed for the counteranion $[SbF_6]^-$ using the method developed by Seminario.[314]

Initially, each model underwent 1 ns classical MD simulation keeping the organometallic complex fixed and the final structure was used to start the QM/MM MD simulations[315] during ca. 15 ps.

Interaction energies were computed in gas phase and corrected using the counterpoise method to deal with basis set superposition errors.[316]

4.3. Gas Phase Structures

Geometries of **2**, **8**, and **9** are firstly optimised in gas phase at PBE level, being the structural parameters in good agreement with available X-ray data (Figure 4.4).[280,288] For the larger complex **9**, an optimisation using the dispersion correction D3 is also performed, providing a similar outcome (Figure 4.4).

In **2** the CH moiety is located close to the metal centre. This proximity together with the significant lengthening of the C–H bond already confirm a strong β-agostic interaction. In **8** a δ-agostic contact is formed by one methyl group from the *tert*-butyl arm of the cyclometalated I^{t}Bu (I^{t}Bu'). Contrarily, in **9** the ζ-agostic interaction —with a chelating size of six members— involves one methyl group from the Dipp arm of the non-cyclometalated IPr. Since Pt···H and Pt···C distances in **8** are slightly larger than in **9**, the agostic interaction in the former seems to be weaker, although in both cases the C–H bond distance is scarcely elongated. The larger Pt···H and Pt···C distance values found in δ-agostic **8** could be due to the restricted mobility of the methyl group imposed by the cyclometalated ligand. Regarding the Pt–H–C angle, it becomes larger as the chelating ring size increases along **2** (β), **8** (δ), and **9** (ζ).

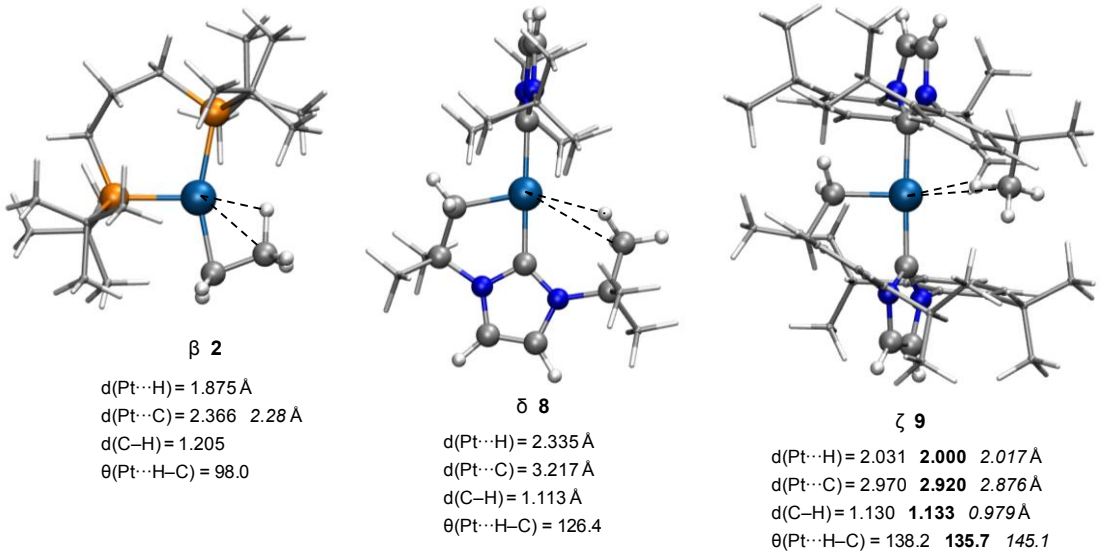

Figure 4.4 Optimised structures of **2**, **8**, and **9**. Structural parameters computed at PBE level. X-ray data in italics and PBE-D3 values in bold.

The geometry of **2** clearly denotes the strongest agostic bonding among the species under investigation. However, no definitive conclusions about the relative strength of the agostic interaction in **8** and **9** can be deduced from gas-phase optimised structures. Instead, their dynamic behaviour in solution will be inspected to establish differences between them.

4.4. Dynamic Perspective of Agostic Interactions

Complexes **2**, **8**, and **9** will be analysed separately. For each case, the experimental information is firstly commented; then, the QM/MM MD simulations are presented and the most relevant results are discussed.

Complex 2

The agostic interaction in complex **2** was ascertained in both solid state (X-ray studies) and solution (NMR spectroscopy). According to experimental reports,[280] an equilibrium between agostic–ethyl and hydride–ethylene isomers was detected in dichloromethane solution at room temperature. As a result, all five protons and two carbon atoms appear equivalents in NMR spectra above 240 K. Interestingly, the ethyl complex **2** was recovered at low temperature. ^{13}C NMR experiments at 145 K show a doublet triplet multiplicity with $^{1}J_{C,H}$ coupling constants of 60 and 153 Hz, respectively, for the agostic methylic carbon atom. In other words, the carbon nucleus perceives the agostic proton differently from the other ones, which means that the agostic exchange via methyl rotation is slow in the NMR time scale at that temperature. Additionally, the small coupling constant of 60 Hz is also a symptom to identify agostic interactions.[11,293]

QM/MM MD simulation of **2** is performed in explicit dichloromethane solvent for 14 ps. Evolution of selected structural parameters of **2** along the simulation is plotted in Figure 4.5. For the time spanned, the simulation shows almost constant values for Pt···H (blue line in Figure 4.5) and Pt···C distances (grey line in Figure 4.5) of ca. 1.9 and 2.4 Å, respectively. In line with low-temperature NMR experiments,[280] the agostic interaction in **2** neither disappears nor exchanges via methyl rotation. The isomerisation processes observed at room temperature[280] are beyond the time scale accessible by the simulation.

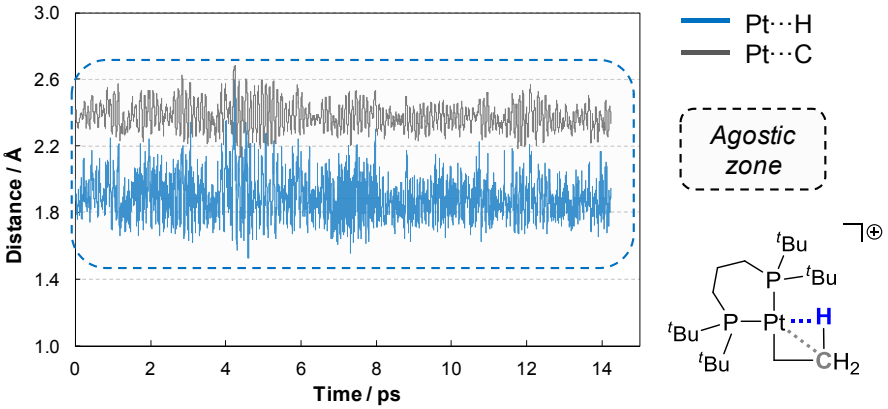

Figure 4.5 Pt···H (blue line) and Pt···C (grey line) distances during the PBE simulation of **2**.

Complex 8

No solid structure is available for complex **8**, hence the agostic bonding was inferred from NMR data.[288] The small $J_{Pt,C}$ of 25 Hz between the platinum and the methylic carbon atoms of the non-cyclometalated *tert*-butyl in NHC' was considered as an indicative of putative agostic interactions. Notably, the three methyl groups of this *tert*-butyl group appear equivalent in NMR spectroscopy at 298 K.

QM/MM MD simulation of **8** is performed in explicit dichloromethane solvent for 15 ps. Evolution of selected structural parameters of **8** along the simulation is plotted in Figure 4.6. During the first 7 ps, the agostic interaction is maintained, where Pt···H (blue line in Figure 4.6) and Pt···C distances (grey line in Figure 4.6) are 2.4 and 3.1 Å, respectively. After 7.5 ps an agostic exchange is observed via *tert*-butyl rotation, i.e., a new methyl group (black C atom) displaces the former (grey C atom) and establishes a new agostic interaction (red and black lines in Figure 4.6). This recent contact —with the same structural features as the previous one— is hold for the rest of the simulation. This facile agostic exchange agrees with the equivalence of NMR signals observed in the experiments.[288] On one hand, carbon atoms can become equivalent through *tert*-butyl rotations. On the other hand, hydrogen atoms can be exchanged via methyl or consecutive *tert*-butyl rotations, albeit the former process was not observed for this particular simulation run.

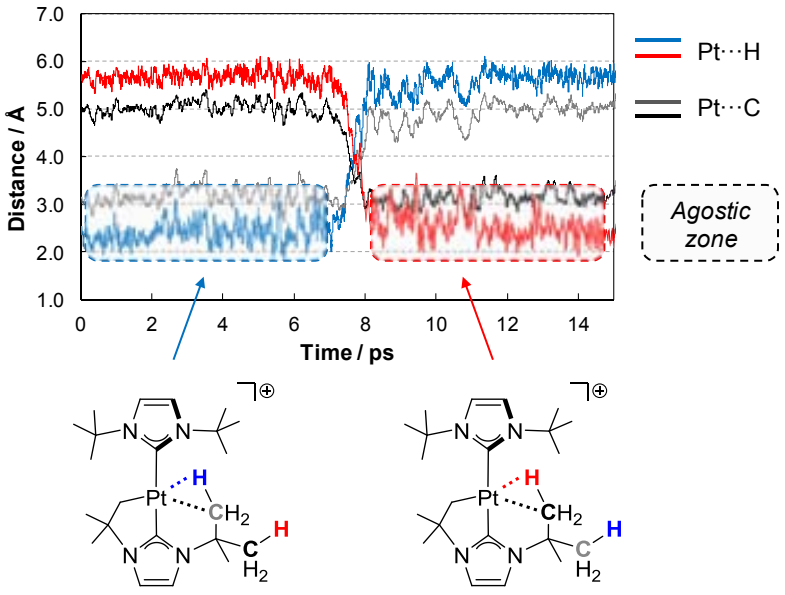

Figure 4.6 Pt···H (blue and red lines) and Pt···C (grey and black lines) distances during the PBE simulation of **8**.

Complex 9

The solid-state structure of complex **9** was determined by means of X-ray studies.[288] Unfortunately, NMR spectra recorded at room and low temperature provided no information about agostic interactions in solution mainly due to signal overlapping signal and averaging issues.

To get insight about the structure of **9** in solution, QM/MM MD simulations are performed in explicit dichloromethane using PBE and PBE-D3 functionals. The PBE simulation maintains an agostic interaction during the first 7 ps; afterwards, the methyl group moves away and the agostic bonding is lost.[274] In order to dismiss the lack of dispersion as the driving force for such event, the simulation is also run in the PB3-D3 framework. Evolution of selected structural parameters of **9** along the PBE-D3 simulation is plotted in Figure 4.7. Initially, the agostic interaction remains at Pt···H (red line in Figure 4.7) and Pt···C distances (grey line in Figure 4.7) of ca. 2.0 and 3.0 Å, respectively. After 1 ps, one new agostic interaction (blue line in Figure 4.7) is established via methyl rotation. Then, similarly to PBE results,[274] the agostic contact vanishes at 5 ps. After 3 ps, the agostic situation is recovered and hold for the rest of the simulation. At the end, a different agostic interaction is formed (green line in Figure 4.7) involving another methyl rotation. No exchanges between agostic methyl groups are observed via isopropyl rotation for this particular simulation run.

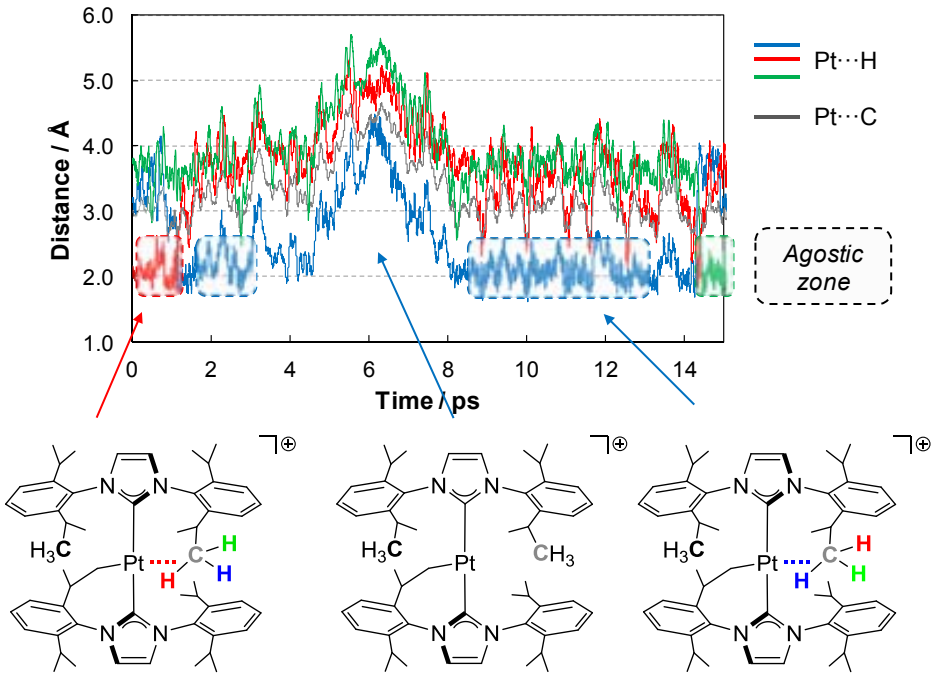

Figure 4.7 Pt···H (blue, red, and green lines) and Pt···C (grey line) distances during the PBE-D3 simulation of **9**.

In order to inspect the transient absence of agostic interactions in detail, Pt···C distances and C'–Pt–C_{IPr}–N dihedral angle (φ) have been monitored and plotted in Figure 4.8a and Figure 4.8b, respectively. Snapshots of both agostic and non-agostic situations are also displayed in Figure 4.8c. The agostic carbon atom is labelled as C_1 and the non-agostic carbon atom coming from a different isopropyl group of the same IPr ligand —the one which eventually approaches the metal— is named as C_2. At the beginning and the end of the simulation, the Pt···C_1 distance is ca. 3.0 Å, in agreement with the presence of agostic bonding (grey line in Figure 4.8a). In the interval when the agostic contact vanishes, from 5 to 8 ps, C_1 moves away at the same time as C_2 comes closer to Pt (black line in Figure 4.8a). C_2 attempts to stabilise the metal vacancy but no agostic interactions are detected. This conformational event implies a slight rotation of the IPr ligand across the Pt–C_{IPr} bond as shown in Figure 4.8b, which can be related to the IPr rotations observed for the non-cyclometalated analogous $[Pt(Me)(IPr)_2]^+$.[288]

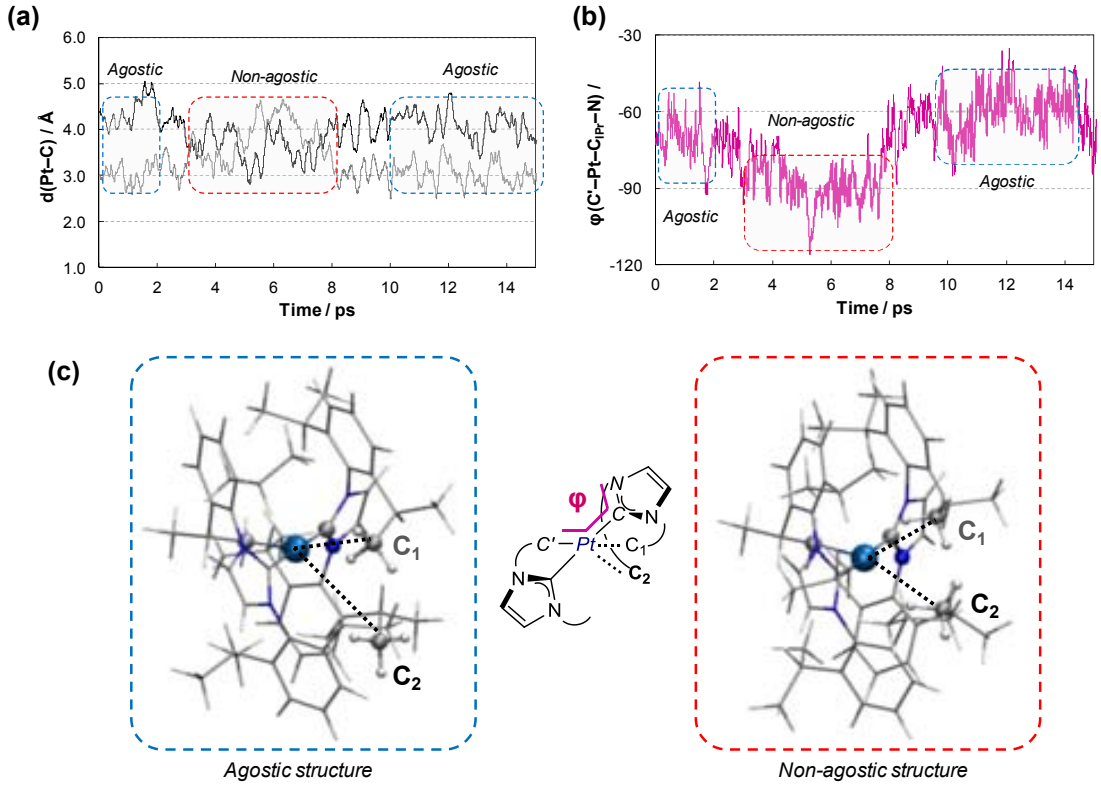

Figure 4.8 (a) Pt···C (grey and black lines) distances and (b) C'–Pt–C_{IPr}–N (magenta line) dihedral angle during the PBE-D3 simulation of **9**, (c) selected agostic and non-agostic snapshots.

Radial distribution functions (RDF) are computed to analyse the solvent organisation around carbon atoms C_1 and C_3 of the agostic isopropyl group (Figure 4.9). C···C_{DCM} RDFs plot the occurrence of DCM molecules —by monitoring the carbon atoms C_{DCM}— at certain distances from agostic C_1 and non-agostic C_3 atoms for the time span 8–15 ps, i.e., when the agostic interaction is more stable. RDFs of C_1···C_{DCM} and C_3···C_{DCM} show maximum peaks at

4.2 and 3.8 Å (Figure 4.9), integrating for ca. 1 and 5 DCM molecules (cut-off distance of 4.5 Å). As a result, non-agostic C_3 appears quite more exposed to solvent than agostic C_1.

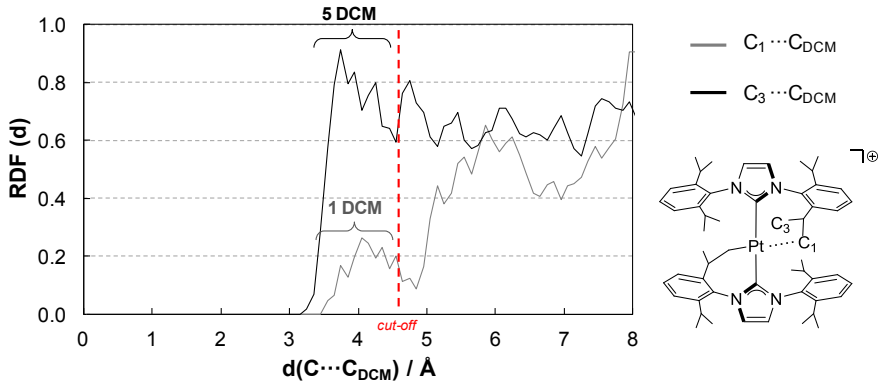

Figure 4.9 C···C_{DCM} radial distribution functions during 8–15 ps in the PB3-D3 simulation of **9**. Agostic C_1 in grey and non-agostic C_3 in black.

4.5. Discussing Agostic Situations

The present work approaches *the agostic question* from a dynamic perspective. The previous section stated the diverse agostic dynamics of the three complexes. In **2** the β-agostic interaction remains intact during the simulation time. In **8** the δ-agostic interaction is preserved for the entire simulation but a fast exchange is observed via *tert*-butyl rotation. In **9** the ζ-agostic interaction switches on and off. When the agostic contact stays, quick exchanges via methyl rotations are also detected. Consequently, in those cases in which the contact may be weak and fluxional, for instance in **9**, the essential point may be for how long the agostic bonding exists. Although the time span is limited, it has been enough to describe certain fast events, such as agostic exchanges in **8** and **9** as well as the transient absence of agostic interactions in **9**. However, the lack of statistics does not allow to estimate the time scale of these events. More intricate changes can indeed occur taking longer times, but they are beyond the scope of these AIMD simulations.

When dealing with weak contacts, solvent may impact the outcome. Previously, it has been shown that only one DCM molecule is close to the agostic methyl group in **9** (Figure 4.9). To investigate this point, the interaction energy between the agostic C_1 in **9** and one DCM molecule is shown in Figure 4.10. The maximum interaction energy is found at 5.5 Å with a value of –4.5 kcal mol^{-1}. Contrary to gas- and solid-phase structures, where the agostic interaction prevails (Figure 4.4), the picture of loose interactions can change in solution and the solvent influence should be evaluated. Indeed, the vacancy can be occupied by solvent molecules instead,[45] e.g., dichloromethane.[317–320]

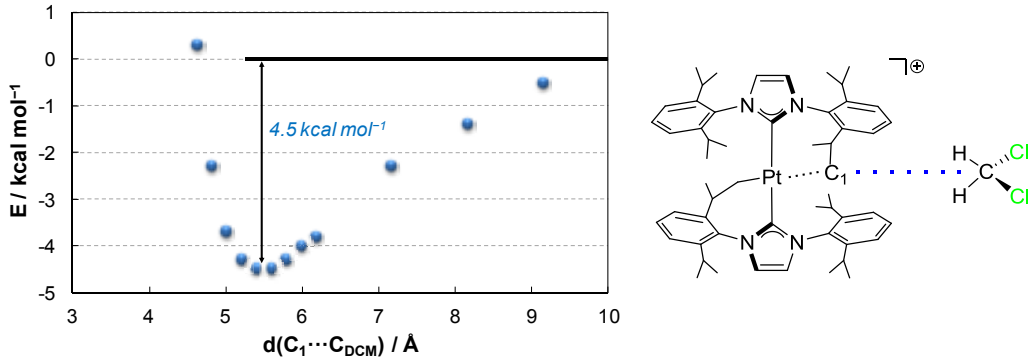

Figure 4.10 Interaction energy E as a function of the $C_1 \cdots C_{DCM}$ distance between **9** and one DCM molecule.

As stated above, for subtle interactions the *static picture* may be deficient to account for the *dynamic behaviour* of the system in solution. For instance, according to Pt···C and Pt···H distances (Figure 4.4), the agostic bonding in **9** should be stronger than in **8**, but this is in contrast to the fleeting existence of the former (Figure 4.7). Therefore, a proper configurational sampling is needed. In this line, some authors have already applied this concept in estimating dynamically averaged NMR parameters of transition metal complexes. NMR chemical shifts[140,141,321] and coupling constants[322] were calculated for sets of snapshots extracted from AIMD simulations in explicit solvent.

Further, agostic interactions can stabilise reaction intermediates as well as transition states, which in turn increase reaction rates.[323] Since the agostic species is usually considered as an initial stage in C–H bond activation processes, the extent to which the C–H bond is weakened is here evaluated. As initial evidence, the C–H elongation from gas-phase geometries should be inspected (Figure 4.4). In **2** the C–H bond distance of 1.205 Å is clearly lengthened, whereas in **8** and **9** the values of 1.113 and 1.133 Å suggest more subtle deformations.[a] To support this point, C–H bonds are analysed in terms of maximally localised Wannier orbitals[324,325] where the electronic charge is concentrated in dots denoted as Wannier function centroids (WFC). This procedure largely simplifies spread molecular orbitals and can be applied to analyse chemical bonding situations.[52,326,327] Figure 4.11 show several WFCs for representative bonds, especially, the agostic C–H bond in gas-phase geometries of **2**, **8**, and **9**. The displacement of such point from the C–H bond axis is taken as a measure of the agostic strength. The higher displacement is observed for **2** (0.202 Å), followed by **9** (0.073 and 0.084 Å for PBE and PBE-D3 optimisations, respectively) and **8** (0.043 Å). Whereas in **2** an initial stage of C–H bond activation is envisaged, in **8** and **9** the remote agostic bonding only suggests a stabilising role towards the open coordination site. That means, the agostic bond may not involve reactivity. As a matter of fact, Häller et al.

[a] For comparative purposes, a C–H bond distance of ca. 1.09 Å is considered as reference value.

reported the X-ray structure of a δ-agostic [Ru–NHC] complex in which the Ru···H and Ru···C distances are ca. 2.05 and 2.83 Å and the Ru–H–C angle is 135°, similar to those parameters observed for **9** in Figure 4.4. Interestingly, this species underwent a cyclometalation process through a base-assisted C–H bond activation reaction which does not involve the agostic moiety but other C–H bond that is geminal to the agostic one.[328]

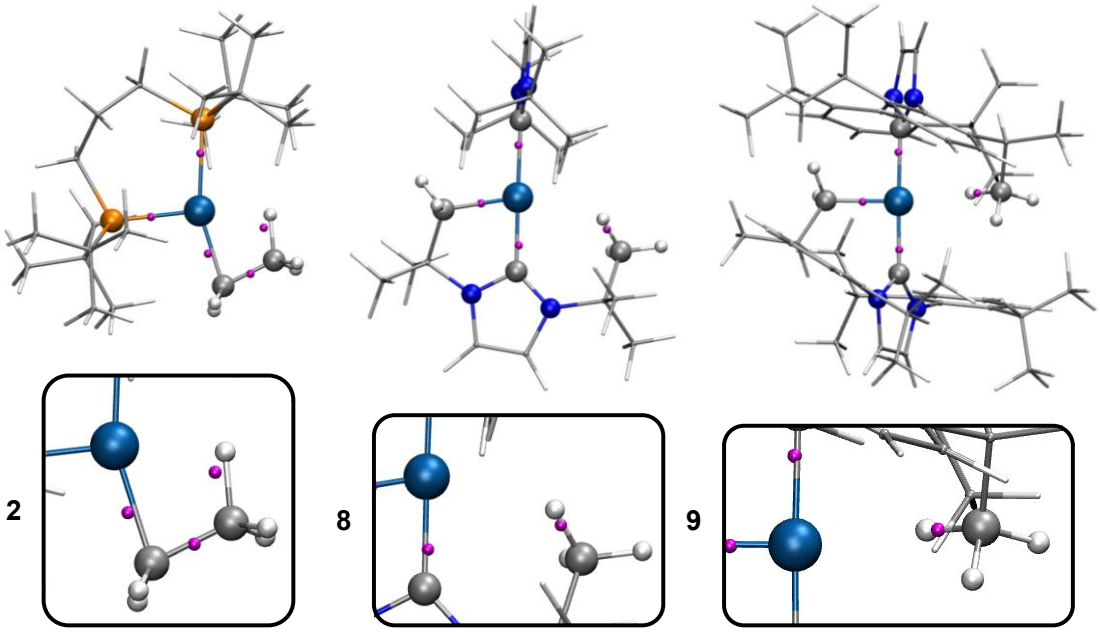

Figure 4.11 Selected Wannier function centroids (magenta dots) in **2**, **8**, and **9**.

Hence, a dual effect of the agostic interaction can be envisaged according to its strength. They can either promote C–H bond activation reactions, as in **2**, or provide stabilisation of low-coordinate situations, as in **8** and **9**. However, which are the factors that govern the different behaviour? The small set of complexes studied herein hampers a reliable generalisation of results, but some important points are highlighted as follows: (i) degree of flexibility of the dangling CH fragment, (ii) steric crowding of substituents around the agostic moiety,[329–331] and (iii) nature of the ligand in *trans* position to the agostic interaction. Delving into the latter point in more detail, strong σ-donor ligands *trans* to agostic bonds weaken the interaction.[332–334] Braunschweig et al. reported a series of true T-shaped Pt(II) complexes which contain σ-donor boryl and borylene ligands in *trans* position to the vacant site.[286,335,336] The fact that these species lack agostic interactions was attributed to the high *trans* influence exerted by these ligands. Interestingly, when the *weaker* σ-donor catecholatoboryl ligand is employed as in **6** (Figure 4.2), an agostic interaction indeed appears, displaying a Pt···C distance of 2.322 Å in solid state.[286] As regards complexes **2**, **8**, and **9**, the stronger σ-donor character of alkyl groups in **8** and **9** with respect to phosphine ligand in **2** likely contributes to weaken the agostic situation in the former species.

Finally, the different structural scenarios found in the three complexes do also influence. In one hand, the chain length differs from each other, increasing from n = 2 in β-agostic **2** to n = 6 in remote ζ-agostic **9**. In this regard, an interesting colour change which depends on β- and γ-agostic coordination modes has been reported for the complex $[CpMo(CO)_2(P^iPr_3)]^+$.[337] On the other hand, geometrical constrains can also play a role. Since the agostic CH group in **8** comes from the anchored I*t*Bu', the motion of ligands is restricted. Conversely, fluxional processes become more reliable when the non-cyclometalated IPr ligand is involved in **9**.

4.6. Conclusions

Three agostic T-shaped Pt(II) species have been inspected by means of QM/MM MD simulations in explicit dichloromethane solvent. Computational evidence is summarised as follows.

- Simulations have demonstrated particular dynamics behaviours for each agostic interaction, being strong and stable in **2**, weak and stable in **8**, and weak and fluctuating in **9**.
- When dealing with fragile interactions, the inclusion of explicit solvent molecules is recommended to account for its dynamics.
- Additional aspects such as geometrical constrains and *trans* influence of spectator ligands are emphasised.

IV

Reactivity

By the essence and nature of existence, contradictions cannot exist.
If you find it inconceivable that an invention of genius should be abandoned among ruins,
and that a philosopher should wish to work as a cook in a diner
—check your premises.

Hugh Akston in “Atlas Shrugged” by Ayn Rand

5. Pt-Mediated Intermolecular C–H Bond Activation

This study analyses the capability of NHC-based 14-electron Pt(II) species to promote intermolecular C–H bond activation reactions of arenes. Each section is presented as follows. *Introduction* surveys previous works about intermolecular C–H bond activations involving 14-electron Pt(II) intermediates. *Computational Details* collects the specifications of the theoretical procedures. As concerns the results, *C–H Bond Activation of Benzene and Toluene* describes the different reactivity of Pt-NHC complexes by means of optimising geometries and computing energies of reactants, products, and transition states. Structures and reaction energy profiles are discussed therein. *Exploring the Role of NHCs* investigates the chemical aspects that govern the observed reactivity trends. Lastly, *Conclusions* brings together the outcome that computation has provided.

These computational results have been published as shown in Annex A.[338]

5.1. Introduction

The importance of Pt-promoted C–H bond activation reactions has already been noticed in Section 1.2.1 and the general mechanistic scenario is shown in Scheme 1.1. The intermolecular C–H bond activation involving 16-electron Pt(II) species is a well established process.[70,71] The participation of 14-electron Pt(II) intermediates is however less common but still feasible.[45] Relevant examples in the field are reviewed below.

Goldberg and co-workers reported the C–H bond activation of both alkane and arene solvent molecules (*n*-pentane, cyclohexane, benzene, and toluene) by means of the low-coordinate intermediate [Pt(Tp')(Me)] **A**, where Tp' stands for tris(3,5-dimethylpyrazolyl)borate (Scheme 5.1).[339,340] **A** could be generated via methyl abstraction from Pt(II)[339] or via reductive elimination from Pt(IV).[340] The open coordination site in **A** allows coordination of solvent molecules and subsequent C–H bond activation, forming Pt(IV) species **B** and **C**. Indeed, **A** can be trapped as an acetonitrile adduct in perfluorobenzene solutions.[340]

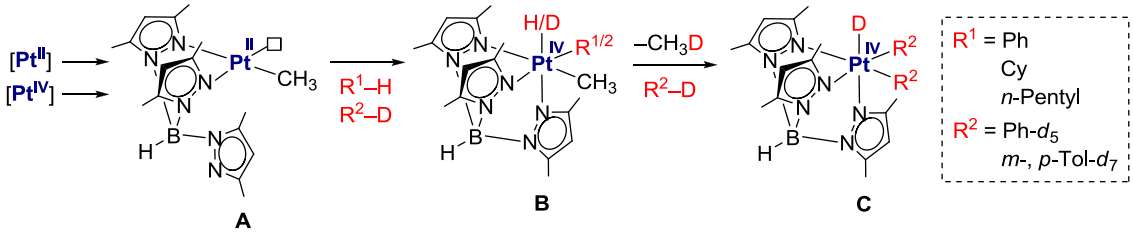

Scheme 5.1 Intermolecular C–H bond activation via [Pt(Tp')(Me)] **A**.

Schwarz and co-workers addressed the C–H bond activation of benzene in gas-phase ion-molecule reactions involving the T-shaped species [Pt(N–N)(Me)]$^+$ **D** (Scheme 5.2).[341] The complex **D** bearing the bipyridyl ligand also reacted with toluene and methane molecules.[342] Calculations using M05-2X[341] and BP86[342] functionals suggested that both OA/RE (via intermediate **E**) and σ-CAM (via transition state **F**) are competitive reaction mechanisms.

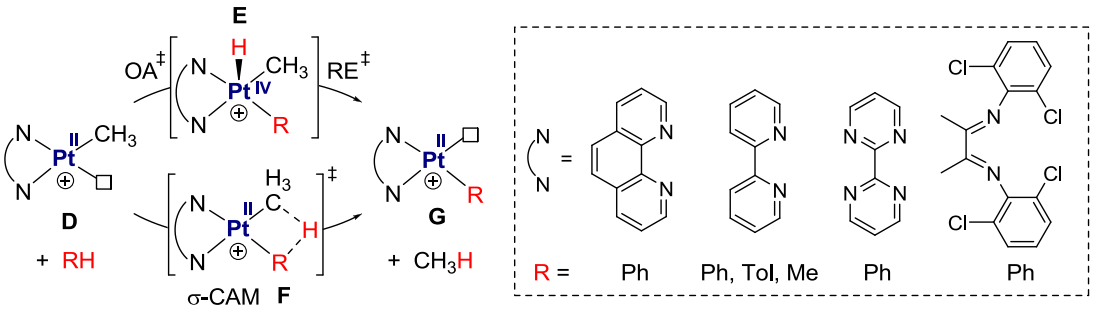

Scheme 5.2 Gas-phase intermolecular C–H bond activation via [Pt(N–N)(Me)]$^+$ **D**.

Soon after the forthcoming study, Ozerov and co-workers demonstrated the potential of the pincer complex [Pt(PNP)]$^+$ **H** in activating C–H bonds of arenes (Scheme 5.3).[343] Triflate removal from **H** generates the putative unsaturated species **I** which finally evolves towards the corresponding aryl complex **J**.

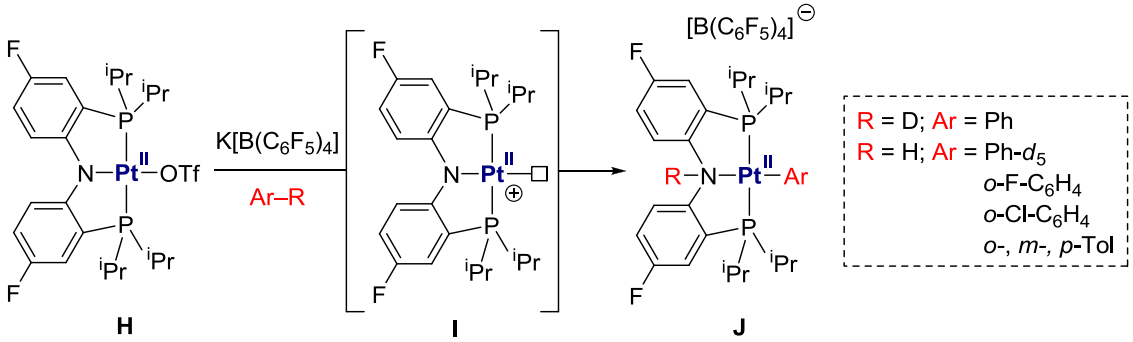

Scheme 5.3 Intermolecular C–H bond activation via [Pt(PNP)]$^+$ **I**.

The use of electron-rich N-heterocyclic carbenes (NHC) as ligands in organometallic chemistry[344] appears as a powerful tool since they allow fine tunning of both steric and electronic properties of complexes.[345–347] In this regard, Conejero and co-workers achieved success in promoting intermolecular C–H activation of arenes by means of stable 14-electron Pt–NHC species.[338] Firstly, benzene activation was tested against complexes [Pt(NHC)(NHC')]$^+$ **1** containing four different NHC ligands (Scheme 5.4), i.e., I^{t}Bu **a** (1,3-di-*tert*-butylimidazol-2-ylidene), IPr **b** (1,3-bis(2,6-diisopropylphenyl)imidazol-2-ylidene), IMes* **c** (1,3-bis(2,4,6-trimethylphenyl)imidazol-4,5-dimethyl-2-ylidene), and IMes **d** (1,3-bis(2,4,6-trimethylphenyl)imidazol-2-ylidene). Neither **1a** nor **1b** could activate benzene molecules even at high temperature, although **1b** underwent a β-H elimination side

reaction. Interestingly, upon heating at 120 °C, **1c** was found in equilibrium with the corresponding phenyl product **2c**. In the case of **1d**, only traces of **2d** were detected.

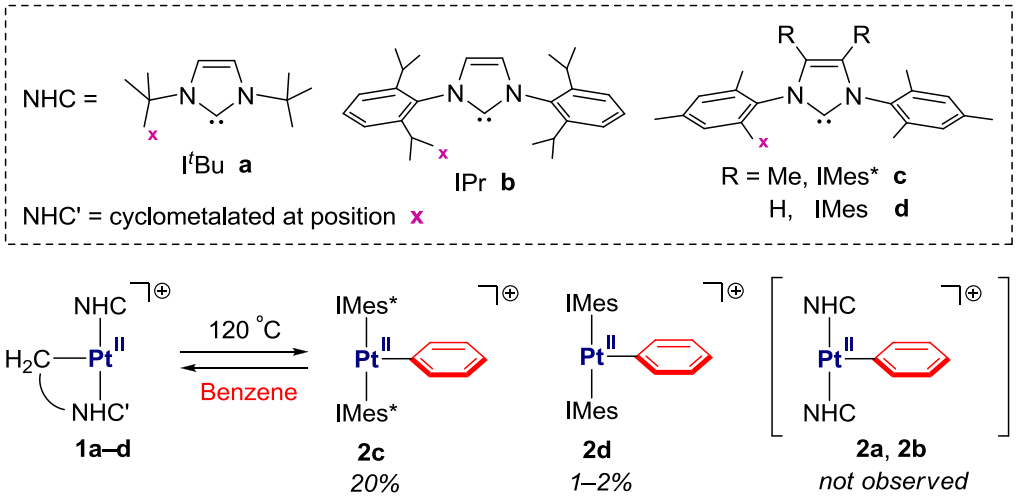

Scheme 5.4 Intermolecular C–H bond activation of benzene via [Pt(NHC)(NHC')]$^+$ **1**.

According to the promising results obtained for the IMes* ligand **c**, the activation of other arenes was investigated.[338] Heating of **1c** in toluene solution at 120 °C indeed allowed the detection of tolyl product **3c** in equilibrium with reactant (Scheme 5.5). Only C–H bond activations in *meta* (*m*-**3c**) and *para* (*p*-**3c**) positions were observed in a ratio of 5:1. Besides, C–H bonds were chemoselectively cleaved over C–F ones in fluorobenzene derivatives.

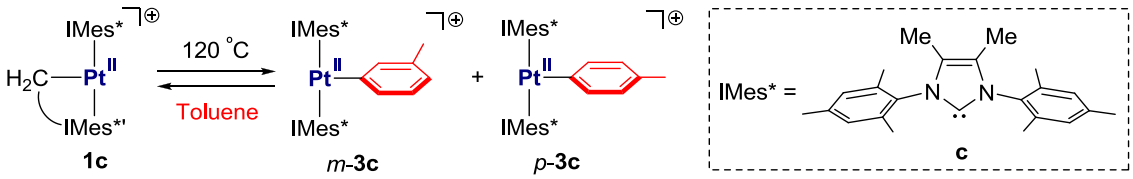

Scheme 5.5 Intermolecular C–H bond activation of toluene via **1c**.

In the framework of these experiments,[338] the computational study pursues (i) to reproduce the experimentally reported reactivity of Pt–NHC complexes for arene C–H bond activations and (ii) to get insight into the role of the NHC ligands in such processes.

5.2. Computational Details

Forthcoming calculations were performed at the DFT level by means of the PBE0 functional[162,170,171] —suitable for describing agostic interactions[190] and third-row transition metal geometries[193]— as implemented in Gaussian 09.[265] Test calculations were carried out with the M06 functional.[168] The Pt heavy atom was described using scalar-relativistic Stuttgart-Dresden SDD effective core potential and its associated double-ζ basis set,[266] complemented with a set of f-polarisation function.[267] The 6-31G** basis set was used for the

H,[269] C, and N atoms.[270]. Benzene (BZ, ε = 2.27) and toluene (TOL, ε = 2.37) solvent effects were included through SMD[215] single-point calculations on gas-phase optimised geometries. The structures of reactants, intermediates, transition states, and products were fully optimised without any symmetry restriction. Transition states were identified by having one imaginary frequency in the Hessian matrix. It was confirmed that transition states connect with the corresponding intermediates by means of application of an eigenvector corresponding to the imaginary frequency and subsequent optimisation of the resulting structures. Energies in solution (ΔE_{BZ} and ΔE_{TOL}) are here presented to discuss reactivity trends. Gibbs energies strongly overestimate the reaction profiles due to the intermolecular nature of the process. Since for the C–H bond activation the solvent itself is also the reactant, the complexes can easily access to such molecules and entropy is not decisive.

Buried volume values[348] (%V_{bur}, see Section 5.4) were computed by means of the freely available web application Samb*V*ca.[349] Default parameters were used to set up the calculation (R = 3.5 Å and d = 2.1 Å). Hydrogen atoms were included in the calculation.

5.3. C–H Bond Activation of Benzene and Toluene

First, benzene (Scheme 5.4) and toluene (Scheme 5.5) C–H bond activations promoted by 14-electron Pt(II) complexes are computed. The optimised geometries of reactants **1** are shown in Figure 5.1. **1a** exhibits a δ-agostic interaction through a *tert*-butyl group, in agreement with NMR data[288] and AIMD simulations.[274] **1b** forms a remote ζ-agostic interaction involving one methyl from an isopropyl group. This contact was confirmed in solid state,[288] although a labile behaviour is proposed in solution.[274] Conversely, neither **1c** nor **1d** display agostic interactions, becoming true T-shaped Pt(II) species.

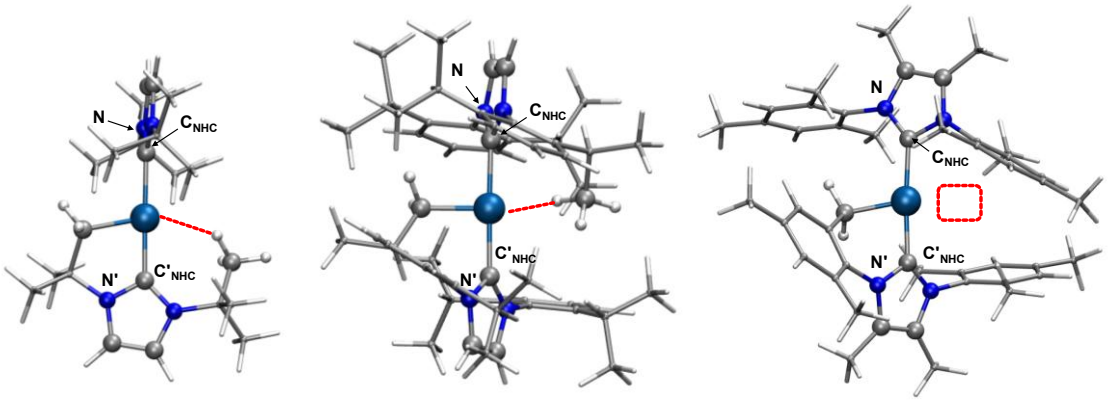

Figure 5.1 Optimised geometries of **1a–c** and structural parameters of **1a–d**.

An OA/RE mechanism is initially proposed for the benzene C–H bond activation reaction (Scheme 5.6).[a] Common to all reactants **1a–d**, benzene is oxidatively added to Pt(II) species **1** via **TS1-4** forming hydride Pt(IV) intermediates **4**. Then, reductive elimination between the hydride and the CH_2 fragment via **TS4-2** yields phenyl Pt(II) complexes **2**.

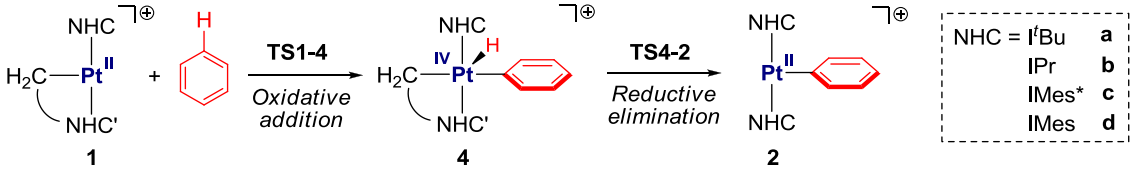

Scheme 5.6 Reaction mechanism for C–H bond activation of benzene via **1**.

Optimised geometries of products **2** are shown in Figure 5.2. No agostic contacts are observed for any species. The predicted true T-shaped species **2c** —and likely **2d**— is in line with the X-ray structure of the related compound $[Pt(C_6HF_4)(IMes^*)_2]\cdot[BAr^F{}_4]$.[338] Interestingly, both **2c** and **2d** exhibit CH-π stacking interactions between two *o*-methyl groups of the mesityl wing and the phenyl ligand. The distances between the hydrogen atoms and the centroid of the phenyl ring, CH···Ph, are 2.629 Å in **2c** and 2.725 Å in **2d**. A note of caution is worth here, since the PBE0 functional is not able to describe putative π-π stacking between mesityl and phenyl moieties. To evaluate this effect, structures of **2c** containing CH-π (**M06-2c**) and π-π (**M06-2c'**) interactions are optimised by means of the M06 functional. According to M06 energies in benzene, the CH-π contact in **M06-2c** is preferred over the π-π one in **M06-2c'** by 1.6 kcal mol^{-1}. This result suggests that PBE0 can reasonably describe the phenyl products.

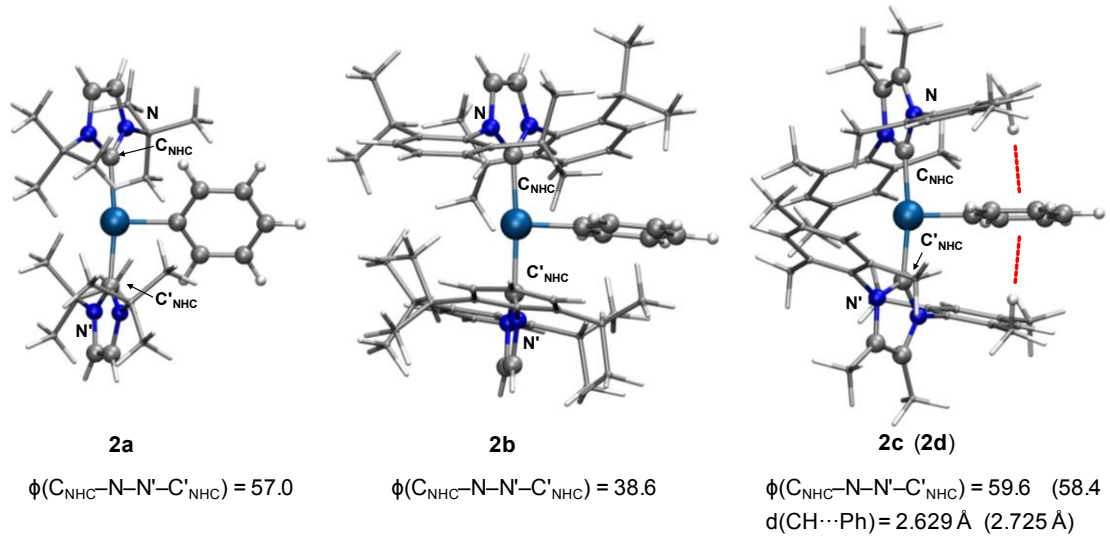

Figure 5.2 Optimised geometries of **2a–c** and structural parameters of **2a–d**.

[a] The feasibility of a σ-CAM process is discussed later.

The energy profiles (ΔE_{BZ}) for these reactions are shown in Figure 5.3. The cyclometalated complexes **1** plus one benzene molecule are taken as zero of energies. In all cases, the potential energy surface in the transition state region appears quite flat because the energies of intermediates **4** are rather similar to those of transition states **TS1-4** and **TS4-2**. **1a** demands 40.4 and 41.3 kcal mol^{-1} for OA (**TS1a-4a**) and RE (**TS4a-2a**) processes (black line in Figure 5.3), and the product **2a** is located at 13.8 kcal mol^{-1} above reactants. **1b** also entails high energy barriers, i.e., 48.7 kcal mol^{-1} for **TS1b-4b** and 44.9 kcal mol^{-1} for **TS4b-2b** (red line in Figure 5.3). Similarly to **2a**, the phenyl complex **2b** is not stable, lying 11.8 kcal mol^{-1} above **1b**. Thus, both kinetics and thermodynamics prevents the C–H bond activation of benzene when I^{t}Bu (**a**) and IPr (**b**) ligands are involved. These results agree with the experiments described in Scheme 5.4. On the contrary, **1c** and **1d** require lower energy barriers of ca. 30 kcal mol^{-1} to overcome OA and RE transition states (dashed blue and green lines in Figure 5.3, respectively). Although these barriers are still high, the reaction could become feasible at the high temperature used in the experiments (120 °C). The relative stabilities of **2c,d** appear quite different from those regarding **2a,b**. **2c** is almost isoenergetic with respect to **1c**, whereas **2d** is 2.2 kcal mol^{-1} less stable than **1d**. These results are in line with the equilibrium observed for **1c,d** and **2c,d**, being **2d** hardly detected (Scheme 5.4).

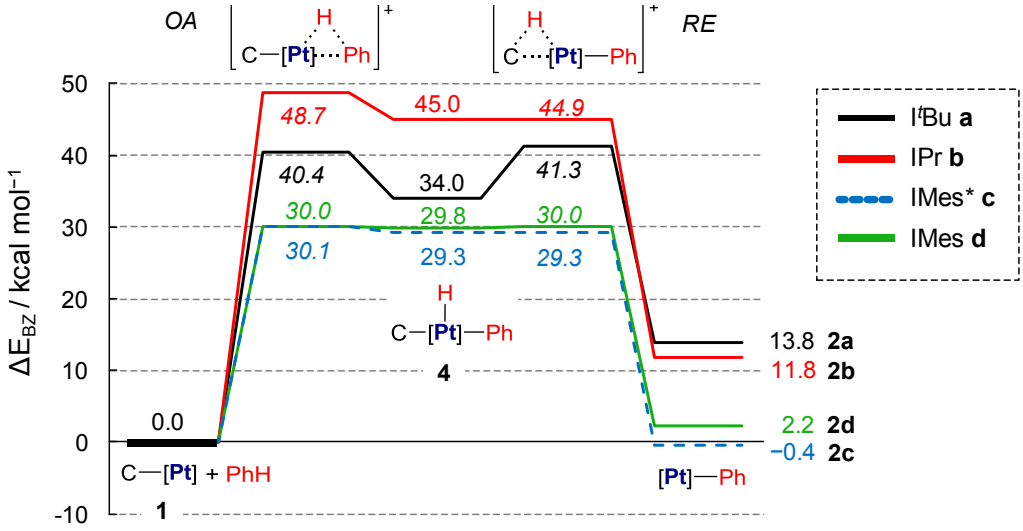

Figure 5.3 Energy profiles for benzene C–H bond activations via **1**.

Overall, for I^{t}Bu (**a**) and IPr (**b**) species both kinetics and thermodynamics do not favour the C–H bond activation process. Conversely, for IMes* (**c**) and IMes (**d**) species kinetics allows the reaction to proceed and thermodynamics rules the amount of product formed. In these situations where bulky ligands are involved, the σ-CAM mechanism[79] was not considered since it requires a *cis* disposition of ligands. Although this reaction mechanism can indeed operate for I^{t}Bu derivatives, the relative stability of **2a** will remain the same, i.e., precluding its formation.

According to the positive outcome of IMes* (**c**) ligands in activating the C–H bond of benzene, the reaction of **1c** towards toluene is also performed (Scheme 5.5). In the case of the toluene molecule, there are four kinds of C–H bonds, i.e., the reaction can take place at benzyl b-, *ortho o*-, *meta m*-, or *para p*- positions. Since previous results pointed out to a thermodynamic control, the energies (ΔE_{TOL}) of all possible products **3c** are initially computed (Scheme 5.7). In agreement with experimental equilibria, only the products *m*-**3c** and *p*-**3c** coming from *meta* and *para* activations are energetically comparable to **1c**. Detection of either b-**3** or *o*-**3** is unlikely expected since they lay 5.0 and 3.1 kcal mol^{-1} above **1c**. A similar chemoselectivity pattern has been observed previously.[340,343] However, Schwarz and co-workers predicted a stable benzyl product in the case of [Pt(bipyridine)(CH_2Ph)]$^+$ **G** (Scheme 5.2).[342] The reason is that the benzyl ligand coordinates to Pt in a η^3 fashion in **G**, whereas it only exhibits a η^1 coordination mode in b-**3c**.

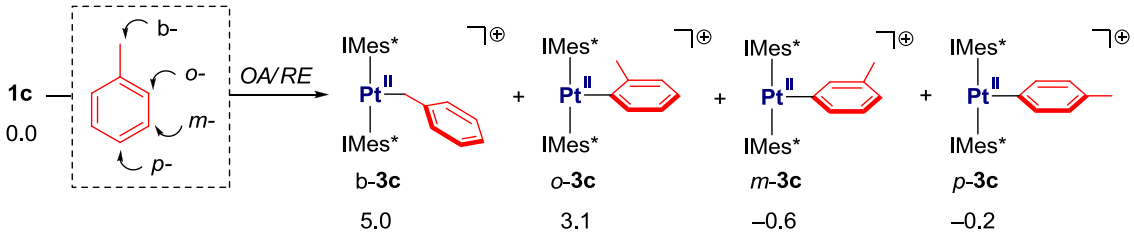

Scheme 5.7 Products **3c** coming from C–H bond activation of toluene via **1c**. ΔE_{TOL} in kcal mol^{-1}.

Optimised geometries of **3c** are shown in Figure 5.4. In line with the structure of phenyl derivative **2c** (Figure 5.2), two CH-π stacking interactions are observed in *m*-**3c** and *p*-**3c** (CH···Ph distances of 2.600 and 2.625 Å, respectively), whereas only one of those contacts is found in *o*-**3c** (CH···Ph distance of 2.587 Å). No agostic interactions are detected at the vacant coordination site.

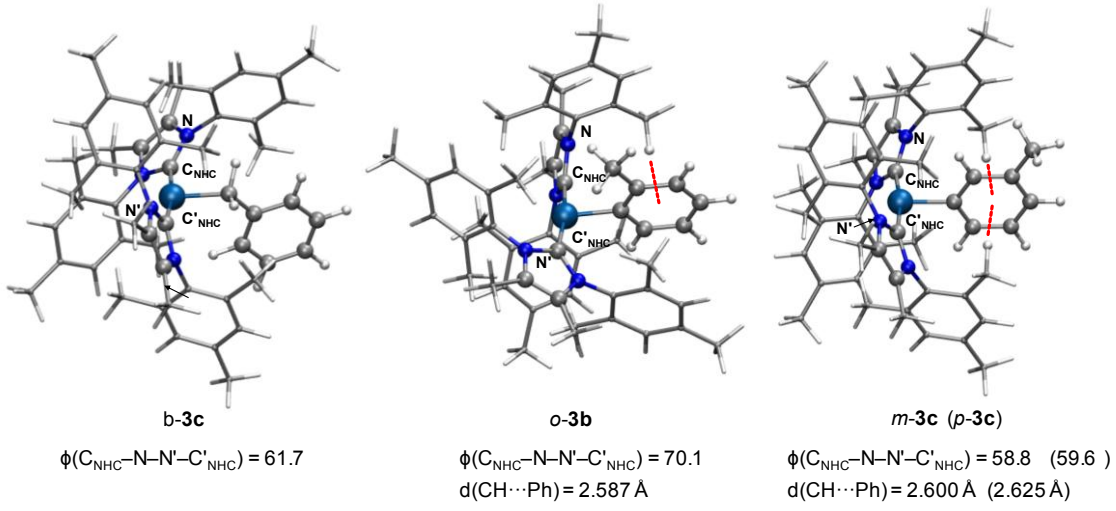

Figure 5.4 Optimised geometries of b-**3c**, *o*-**3c**, and *m*-**3c**, and structural parameters of all **3c**.

To fully confirm the feasible formation of *m*-**3c** and *p*-**3c**, the corresponding energy barriers are computed (Figure 5.5). Again, OA/RE reaction mechanism is assumed to operate. Complex **1c** plus one toluene molecule are taken as zero of energies. Both *meta* and *para* activation routes entail energy barriers of ca. 30 kcal mol^{-1} (dashed light blue and dark blue lines in Figure 5.5, respectively), same as those obtained for benzene C–H bond activation (dashed blue line in Figure 5.3).

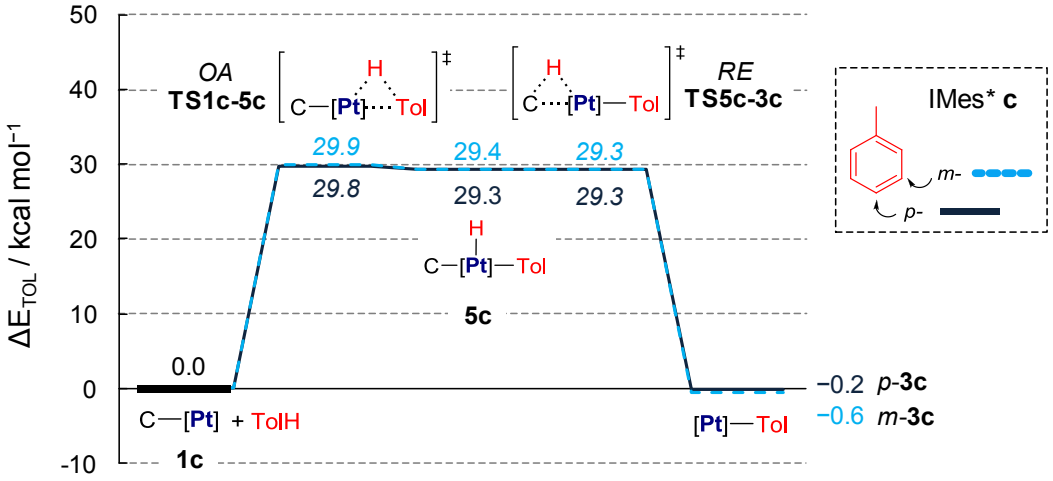

Figure 5.5 Energy profiles for *m*- and *p*-toluene C–H bond activations via **1c**.

5.4. Exploring the Role of NHCs

Previous section has proved the different behaviour of NHC-based Pt(II) complexes towards C–H bond activation process. Whilst no reaction is observed for I^{t}Bu and IPr derivatives, thermodynamic control operates for IMes* and IMes in both benzene and toluene C–H bond activations. Forthcoming discussion provides some insight in order to rationalise these observations.

To evaluate the steric hindrance of NHC ligands, the so-called *buried volume* %V_{bur} is invoked.[348,349] In a similar manner as the Tolman cone angle,[350] this parameter estimates the space which is occupied by the NHC ligand around the metal M. A graphical representation is depicted in Figure 5.6.[348] Firstly, a sphere of radius R and centre M is defined; then, a M–C_{NHC} distance d is set. Under this scheme, %V_{bur} represents the percentage of such sphere that is *buried* by overlap with atoms of the NHC ligand. In other words, larger the %V_{bur}, larger the steric hindrance. Regarding the reactants **1**, the %V_{bur} values computed for the non-cyclometalated NHC ligands (Table 5.1) are 38.9% for I^{t}Bu (**1a**), 40.1% for IPr (**1b**), 35.1% for IMes* (**1c**), and 34.9% for IMes (**1d**). I^{t}Bu and IPr ligands are bulkier than IMes* and IMes and, consequently, their presence hampers the approaching of benzene molecules.

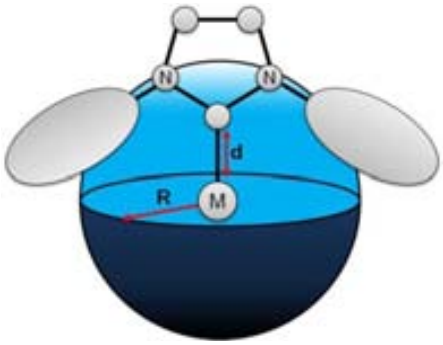

Figure 5.6 Representation of the sphere built to compute $\%V_{bur}$.

To examine in depth the role of steric effects on the energy barriers, one can call for distortion energy analyses of transition state structures.[351–353] As previously mentioned, $\%V_{bur}$ only accounts for the geometry of the NHC ligands of the complex. Therefore, in order to better compare the energy analyses with this later term, just the distortion of the complex —but not benzene— has been considered herein. Since both OA and RE transition states are rather similar in energy, only the former ones are considered. Initially, benzene is removed from **TS1-4**, generating the distorted structures **TS1-4'**. The distortion energies for platinum species, $\Delta E_{BZ}{}^{\ddagger}{}_{d}$, are computed as the difference between fully optimised **1** and distorted **TS1-4'**. The resulting values represent the energy required by the reactants to adopt the oxidative addition transition state structure. The computed $\Delta E_{BZ}{}^{\ddagger}{}_{d}$ (Table 5.1) are 20.1 kcal mol^{-1} for I^{t}Bu (**1a**), 20.6 kcal mol^{-1} for IPr (**1b**), 9.6 kcal mol^{-1} for IMes* (**1c**), and 9.0 kcal mol^{-1} for IMes (**1d**). Notably, the distortion energies involving **1c** and **1d** are ca. 10 kcal mol^{-1} lower than **1a** and **1b**. This outcome follows the trend observed for the energy barriers $\Delta E_{BZ}{}^{\ddagger}$(**TS1-4**) (Figure 5.3 and Table 5.1).

Table 5.1 $\%V_{bur}$ and selected energy terms (see text). All energies in kcal mol^{-1}.

	$\%V_{bur}$(in **1**)	$\Delta E_{BZ}{}^{\ddagger}{}_{d}$(**TS1-4'**)	$\Delta E_{BZ}{}^{\ddagger}$(**TS1-4**)	ΔE_{BZ}(**2**)
I^{t}Bu **a**	38.9	*20.1*	*40.4*	13.8
IPr **b**	40.1	*20.6*	*48.7*	11.8
IMes* **c**	35.1	*9.6*	*30.1*	–0.4
IMes **d**	34.9	*9.0*	*30.0*	2.2

The challenge of creating a pocket to accommodate an incoming benzene molecule is also reflected on the relative energies (Table 5.1) and the structures (Figure 5.2) of phenyl products **2**. A significant rearrangement of I^{t}Bu ligands is required, in which the dihedral angle between the two NHC ligands evolves from 85° in reactant **1a** to 57° in product **2a**. In the case of IPr ligands, although the change of the dihedral angle is less noticeable, the branched isopropyl groups in **2b** indeed collide with the phenyl ligand.

As concerns the relative stabilities of **2c** and **2d** species, the presence of methyl groups at the 4- and 5-positions of the imidazole ring as in IMes* (**c**) slightly favours the formation of the phenyl products. Since steric contributions from IMes* and IMes are essentially the same,[346] one turns to the more electron donating character of IMes* with respect to IMes.[347,354] To gain further insight on this point, thermodynamics of hypothetic IMes^{X} derivatives have been studied considering different electron-donating groups on the imidazole ring (Scheme 5.8). X stands for the SiH_3 (**e**) and NH_2 (**f**) groups which exhibit inductive and mesomeric characters, respectively. In line with **2c**, the phenyl products **2e,f** appears at –0.7 and –1.0 kcal mol^{-1}, i.e., more stable than the cyclometalated reactants **1e,f**. In these cases the electron-donating effect of X seems to follow a trend. The changes are however rather small, thus no definitive conclusions should be drawn.

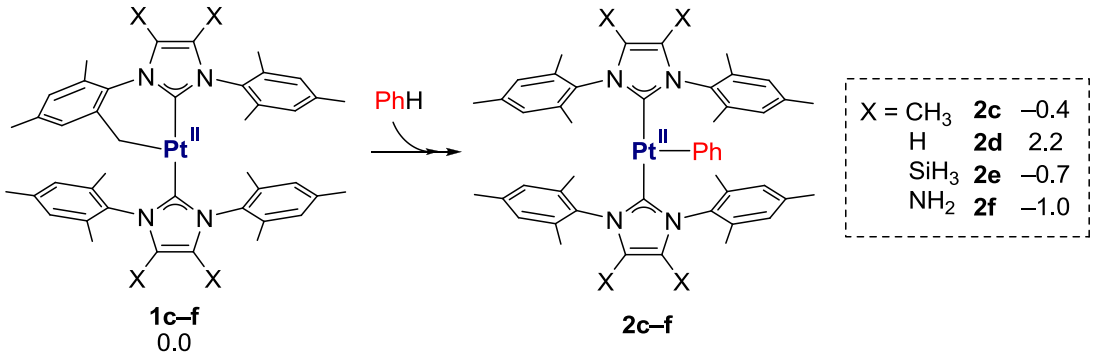

Scheme 5.8 Relative stabilities of **2c–f**. ΔE_{BZ} in kcal mol^{-1}.

5.5. Conclusions

Benzene and toluene C–H bond activations promoted by 14-electron Pt–NHC complexes have been theoretically addressed and the outcome fairly reproduces experimental evidence. Computational findings are collected as follows.

- For complexes bearing I^{t}Bu **1a** and IPr **1b**, kinetics and thermodynamics preclude the formation of the phenyl products.
- For complexes bearing IMes* **1c** and IMes **1d**, feasible energy barriers are obtained to yield the phenyl products. The preference of **2c** over **2d** arises from thermodynamics.
- The distribution of toluene activation products promoted by **1c** comes from a thermodynamic control. Only *m*-**3c** and *p*-**3c** species are likely to be detected.
- Fine-tuning of NHC properties allows the reaction to proceed. Steric contributions mainly govern kinetics and thermodynamics. Further subtle electronic modifications through the imidazole backbone also influence the stability of products.

6. Pd-Catalysed Suzuki–Miyaura Reaction

This investigation is devoted to analyse by computational means the transmetalation process of the Suzuki–Miyaura cross-coupling reaction. Each section is presented as follows. *Introduction* offers an overview of previous contributions supporting different transmetalation reaction pathways. *Computational Details* specifies the computational procedure that has been applied. As concerns the results, *Transmetalation of Vinyl Groups* and *Transmetalation of Phenyl Groups* analyse the role of the base as well as the Pd-C bond formation step for vinyl and phenyl organic groups, whereas *Merging Experiment with Computation* discusses the theoretical results according to the experimental evidence. *Conclusions* finally summarises the information that computation has provided.

This computational study has been published as shown in Annex A.[355]

6.1. Introduction

Pd-catalysed cross-coupling reactions have revolutionised organic synthesis. Several kinds of reactions are available as pointed out in Section 1.2.2. Particularly, in Suzuki–Miyaura conditions,[84,85] organohalides are coupled with organoboron reagents[356] in the presence of base (Scheme 6.1).

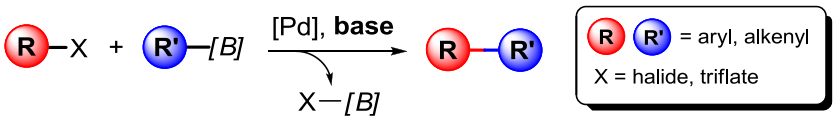

Scheme 6.1 Typical Suzuki–Miyaura cross-coupling reaction.

The general reaction mechanism consists of oxidative addition, transmetalation, and reductive elimination steps (Scheme 1.3). As concerns the transmetalation process, two different pathways have been proposed relying on the role of the base, i.e., hydroxide in this case (Scheme 6.2).[357] The so-called boronate mechanism, path A, entails prior formation of boronate species **A** via nucleophilic attack of hydroxide to boronic acid. The resulting boronate lately displaces the halide and undergoes transmetalation. In the Pd–hydroxo mechanism, path B, hydroxide initially substitutes halide and coordinates to Pd forming intermediate **B**. This Pd–hydroxo species eventually adds boronic acid in order to promote transmetalation. Interestingly, experimental and theoretical studies supporting both pathways have been reported, thus the transmetalation reaction mechanism is still under debate.[358] Relevant contributions are reviewed below.

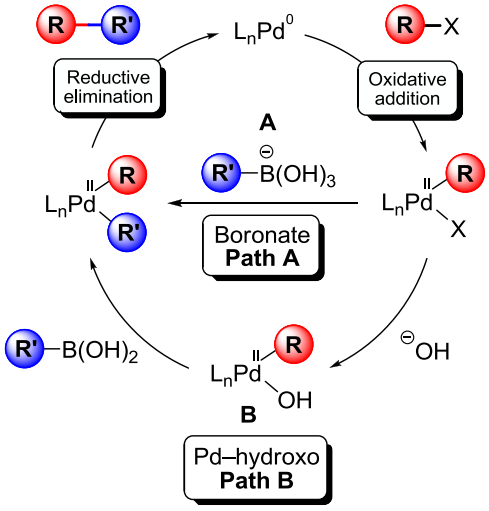

Scheme 6.2 Proposed mechanisms for Suzuki–Miyaura reaction (base = OH^-).

Matos and Soderquist reported a thorough study on the Suzuki–Miyaura reaction involving 9-borabicyclo(3.3.1)nonane derivatives in THF solution (Scheme 6.3).[359] They found a fast displacement of bromide by hydroxyborate via intermediate **D** (path A). On the contrary, the formation of the Pd–hydroxo **E** took place slowly (path B).

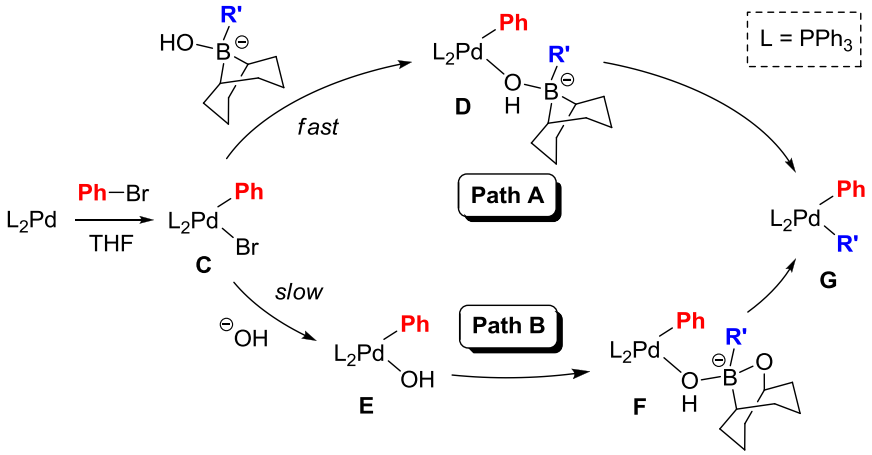

Scheme 6.3 Roles of the base proposed by Matos and Soderquist.[359]

Sakaki and co-workers firstly reported DFT calculations on the transmetalation of diboron reagents starting from both Pd–halide and Pd–hydroxo species.[360] Soon after Ujaque and co-workers addressed the role of the base in the transmetalation step by means of B3LYP calculations, modelling phosphines by PH_3 (Scheme 6.4).[361] They initially considered the displacement of bromide by vinylboronate via path A (**TS-HI**). However, the bromide-by-hydroxide substitution via path B (**TS-HJ**) could not be located for such a model system. Instead, the oxidation of a phosphine ligand to form **K** was characterised. The reaction can take place starting from the Pd–hydroxo **J** via **TS-JI**. Both transition states **TS-HI** and **TS-JI** were lower in energy than the one which describes the Pd–C bond formation step. The boronate mechanism (path A) was also computed for aryl derivatives.[362]

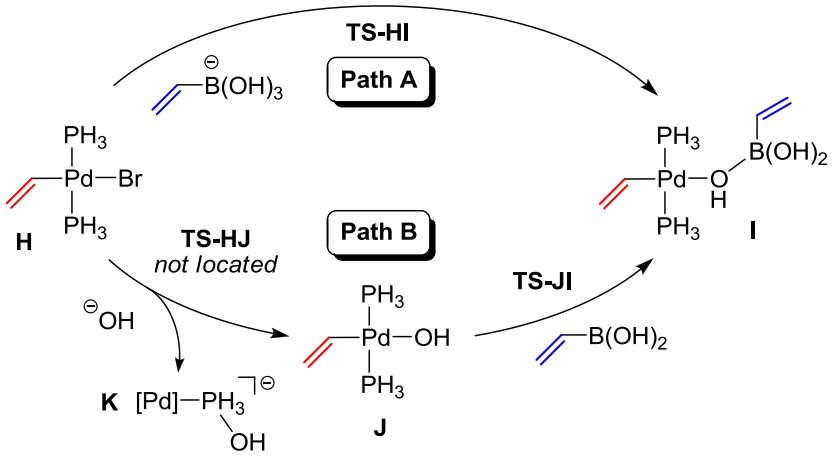

Scheme 6.4 Computed reaction mechanisms reported by Ujaque and co-workers.[361]

The influence of other bases different from hydroxide in the transmetalation step was computationally investigated for diimine chelated Pd complexes,[363] although the mechanism to form Pd–borate species (analogous of **I** in Scheme 6.4) was not discussed.

Nunes and Monteiro employed mass spectroscopy to detect borate species during Suzuki–Miyaura coupling reactions.[364] Their findings support an initial attack of the base OH^- to form the reactive borates intermediates. Indeed, arylboronate salts can be directly used as reagents in a base-free protocol.[365,366] However, caution is needed here because the release of hydroxide anions during the course of the reaction cannot be fully excluded.[356]

Recently, experimental studies claim for the participation of Pd–hydroxo intermediates (path B). Carrow and Hartwig showed that the populations of Pd–hydroxo and Pd–halide complexes in THF/H_2O mixtures are comparable.[367] Kinetic studies were then performed in order to discern between paths A and B (Scheme 6.5). The reaction between Pd–bromide **L** and *p*-tolylboronate was very slow, less than 10% conversion after 11 h. In contrast, Pd–hydroxo **M** was able to react with *p*-tolylboronic acid in the same conditions. Therefore, the reaction rate involving the Pd–bromide **L** and the boronate resulted to be quite smaller than the one starting from the Pd–hydroxo **M**, thus favouring path B.[367] Schmidt et al. also made use of reaction rates to rule out the participation of boronate intermediates for a related system catalysed by phosphine-free Pd species in DMF/H_2O.[368]

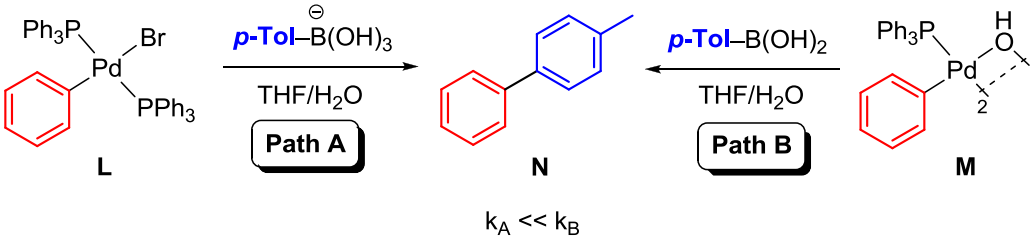

Scheme 6.5 Kinetics studies on paths A and B reported by Carrow and Hartwig.[367]

Amatore et al. also studied the role of the base.[369] The reliability of boronate species to promote transmetalation was tested towards the Pd–bromide **O** in DMF solution (Scheme 6.6). In order to hamper the formation of Pd–hydroxo complexes, the reaction was performed in the presence of a large excess of halide. In such conditions, phenylboronate did not react with Pd–bromide **O** after 3 h. Consequently, the participation of boronate species via path A was precluded.

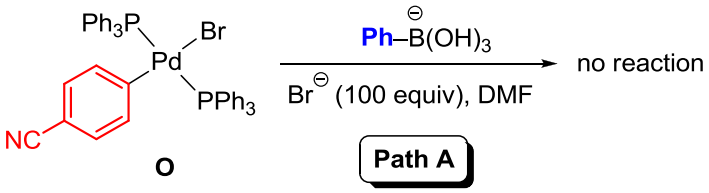

Scheme 6.6 Lack of reactivity of boronate species reported by Amatore et al.[369]

On the contrary, Lima et al. recently suggested that, in DMF/H_2O mixtures, the main role of the base is to activate the boronic acid forming the boronate intermediate via path A, albeit Pd–OH species were not excluded.[370]

In this scenario where different studies seem to disagree, the role of the base should be computationally revisited. Therefore, DFT calculations have been carried out using the real catalyst [$Pd(PPh_3)_2$] and an improved description of the hydroxide base. The Suzuki–Miyaura cross-coupling reaction takes place via oxidative addition[371–378], transmetalation, and reductive elimination[379–383] processes. The present study is focused on the transmetalation event where the base plays its main role. Both vinyl and phenyl groups are considered in the calculations (Scheme 6.7).

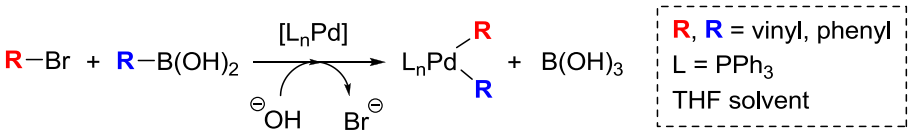

Scheme 6.7 Suzuki–Miyaura transmetalation reactions under study.

This investigation has the clear purpose of unravelling the dilemma between boronate (path A) and Pd–hydroxo (path B) reaction mechanisms in Suzuki–Miyaura transmetalation processes.

6.2. Computational Details

Forthcoming calculations were performed at the DFT level by means of the M06 functional[168] with an ultrafine grid[384] as implemented in Gaussian 09.[265] This functional correctly accounts for dispersion interactions and is recommended for transition metal chemistry.[180,181,189] The Br and Pd heavy atoms were described using scalar-relativistic

Stuttgart-Dresden SDD effective core potentials and their associated double-ζ basis sets,[266] complemented with a set of f-polarisation functions.[267,268] The 6-31G** basis set was used for the H,[269] B, C, O, and P atoms.[270] Diffuse functions were added to O atoms.[271] Tetrahydrofuran (THF, ε = 7.426) solvent effects were included through SMD[215] single-point calculations on gas-phase optimised geometries. The structures of reactants, intermediates, transition states, and products were fully optimised without any symmetry restriction. Transition states were identified by having one imaginary frequency in the Hessian matrix. It was confirmed that transition states connect with the corresponding intermediates by means of application of an eigenvector corresponding to the imaginary frequency and subsequent optimisation of the resulting structures. Gibbs energies in THF (ΔG_{THF}) are computed according to the following formula,

$$\Delta G_{THF} = \Delta E_{THF} + \Delta G_{gp} - \Delta E_{gp} \qquad [6.1]$$

where suffix gp means gas-phase.

6.3. Transmetalation of Vinyl Groups

The boronate $[R–B(OH)_3]^-$ plus the complex *trans*-$[(PPh_3)_2Pd(R)(Br)]$ **1**, coming from the oxidative addition of R–Br, have been taken as zero of energies (R = vinyl). Firstly, the specific role of the base is analysed; secondly, the steps involved in the transmetalation process are computed.

6.3.1. Role of the base

The displacement of bromide by hydroxide to form the Pd–hydroxo intermediate **2** (path B in Scheme 6.2) is first analysed. Starting from **1**, the substitution transition state **TS1-2⁰** is located at 32.5 kcal mol^{-1} above reactants (Figure 6.1). Such a high barrier could be related to the crude description of the base as a bare hydroxide anion. Since the presence of water is likely in the experiments, coming from either hydration of base or solvent mixtures, the inclusion of explicit water molecules[216] surrounding the anions is therefore considered. Figure 6.1 collects the Gibbs energy profiles obtained after the inclusion of n water molecules, ranging from 1 to 4. Overall, the coordination of water molecules to the negatively charged boronate and hydroxide species has a gradual stabilising role. **1** plus solvated boronate reactants lay 7.3 and 7.4 kcal mol^{-1} below **1** plus non-solvated boronate species in presence of 3 and 4 water molecules, respectively. The same trend is observed for the substitution transition states denoted as **TS1-2ⁿ**, being n the number of water molecules involved. The transition state Gibbs energies decrease producing similar barriers for 3 and 4 water molecules, i.e., 24.2 kcal mol^{-1} via **TS1-2³** and 22.9 kcal mol^{-1} via **TS1-2⁴** (Figure 6.1).

After the substitution process the water molecules are located solvating the bromide anion. Since these results differ in ca. 1 kcal mol^{-1}, the series is assumed to be converged for n= 3.

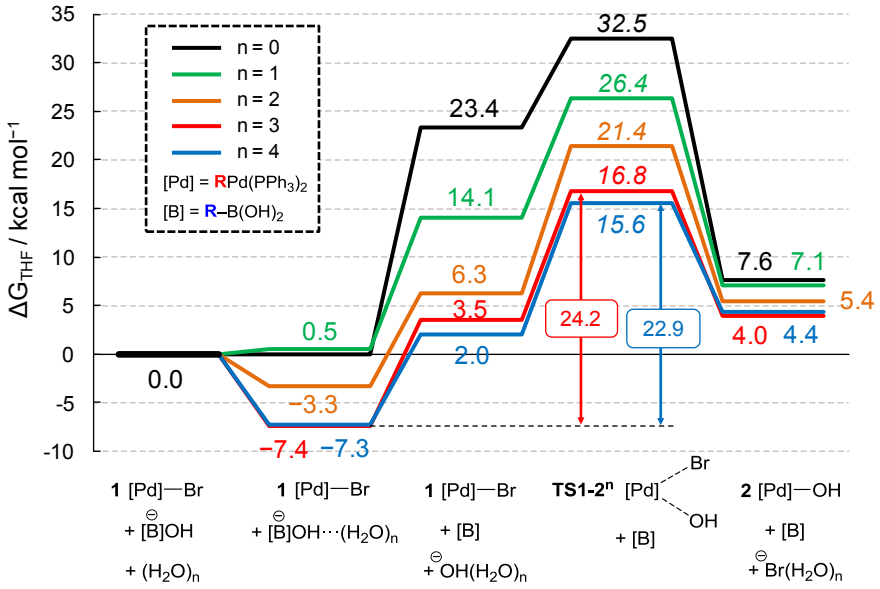

Figure 6.1 Gibbs energy profiles for path B including 0–4 water molecules (R = vinyl).

As shown in Figure 6.1, transition states **TS1-2^n** have been computed ignoring the boronic acid, i.e., the Gibbs energy of the boronic acid is added separately. In order to consider all species within the same calculation, the transition state **TS1-2^3** is revaluated by including the boronic acid in the model explicitly. The new transition state **TS1-2^{3}B** is placed at 15.3 kcal mol^{-1} and involves a Gibbs energy barrier of 22.7 kcal mol^{-1}. Similar values were found for the transition states **TS1-2^3** and **TS1-2^4** (24.2 and 22.9 kcal mol^{-1}, respectively), thus only **TS1-2^{3}B** will be discussed. The optimised transition state structures including no water (**TS1-2^0**), 3 water molecules (**TS1-2^3**), and 3 water molecules plus boronic acid (**TS1-2^{3}B**) can be consulted in Figure 6.2.

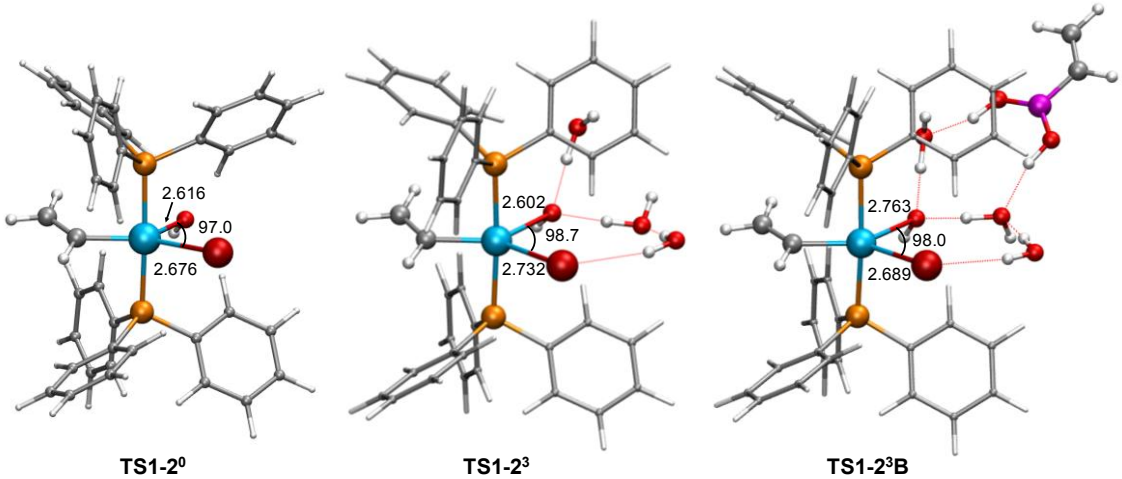

Figure 6.2 Optimised geometries of **TS1-2^0**, **TS1-2^3**, and **TS1-2^{3}B**. Distances in Å, angles in degrees.

Alternatively, the removal of bromide by boronate to produce the Pd–boronate intermediate **3** (Path A in Scheme 6.2) is next considered. Starting from **1**, the substitution transition state **TS1-3⁰** is placed at 14.6 kcal mol^{-1} above reactants (Figure 6.3). In line with path B, the effect of the presence of water molecules is also evaluated. Figure 6.3 shows the computed Gibbs energy profiles when up to 4 water molecules are included in the calculations. The Gibbs energies of the transitions states **TS1-3ⁿ** diminish in the same extent as the ones for the reactants and therefore, regardless of n, the overall barriers remain almost constant in the range of 14–16 kcal mol^{-1} (Figure 6.3). Similar Gibbs energies are obtained for 3 and 4 water molecules and the series is assumed to be converged for n = 3 as in path B. The optimised transition state structures including no water (**TS1-3⁰**) and 3 water molecules (**TS1-3³**) are displayed in Figure 6.4.

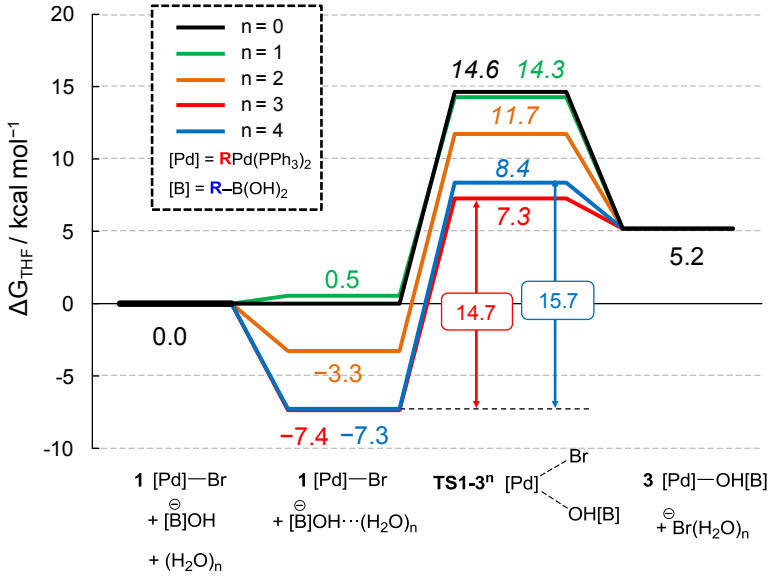

Figure 6.3 Gibbs energy profiles for path A including 0–4 water molecules (R = vinyl).

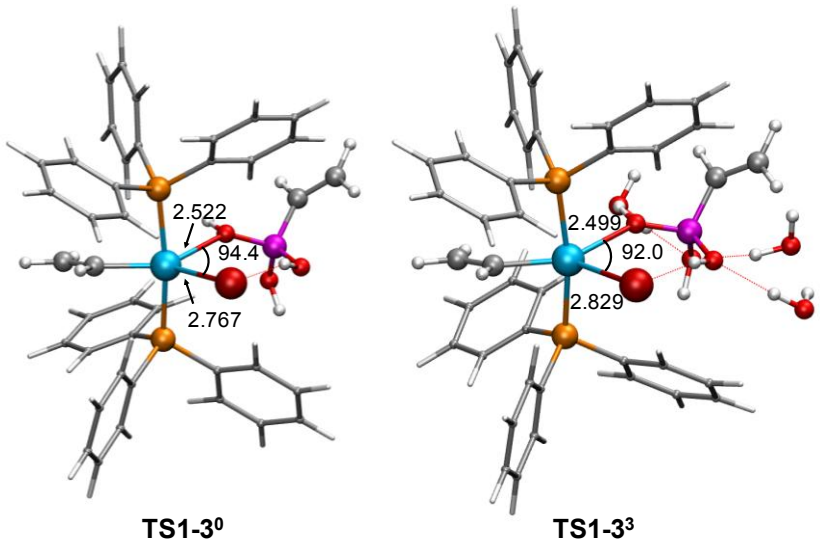

Figure 6.4 Optimised geometries of **TS1-3⁰** and **TS1-3³**. Distances in Å, angles in degrees.

According to the aforementioned calculations, the transition states **TS1-2^{3}B** and **TS1-3^3** contain the same number of atoms and share the origin of energies; hence, they can be compared right away. The computed Gibbs energy barrier for path B via **TS1-2^{3}B** is 22.7 kcal mol^{-1}, whereas the one for path A via **TS1-3^3** is 14.7 kcal mol^{-1}. It means that the boronate mechanism is clearly endorsed since it demands 8.0 kcal mol^{-1} less than the Pd–hydroxo route.

6.3.2. Transmetalation process

The entire transmetalation process considering three water molecules is computed. Relative Gibbs energies are shown in Scheme 6.8 and Gibbs energy barriers with respect to the most stable reactants (**1** plus solvated boronate species at –7.4 kcalmol^{-1}) are discussed as follows. As stated before, **1** evolves towards the Pd–boronate intermediate **3** via **TS1-3^3** (path A) involving 14.7 kcal mol^{-1}. Alternatively, **1** can produce the Pd–hydroxo intermediate **2** via **TS1-2^{3}B** (path B) demanding 22.7 kcal mol^{-1}. Subsequent attack of boronic acid to hydroxo ligand in **2** generates **3** via **TS2-3**, placed at 18.6 kcal mol^{-1} above **1**. Once bromide is released and **3** is formed, the boronate ligand should change its coordination mode from η^1-O in **3** to η^2-vinyl in **4** via **TS3-4** which requires 20.4 kcal mol^{-1}. Then, the Pd–C bond formation takes place via **TS4-5** involving 25.4 kcal mol^{-1}. *Trans–cis* isomerisation and reductive elimination processes are assumed to occur yielding the final product and regenerating the Pd catalyst.

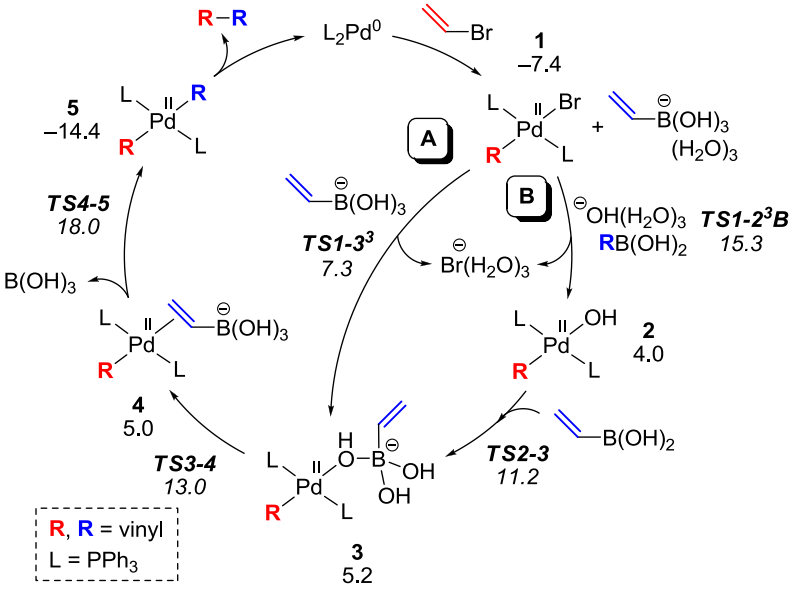

Scheme 6.8 Transmetalation reaction mechanisms (R = vinyl). ΔG_{THF} in kcal mol^{-1}.

The relative Gibbs energies of Scheme 6.8 are plotted as reaction profiles in Figure 6.5. Path A via boronate-by-bromide substitution (blue line in Figure 6.5) demands 14.7 kcal mol^{-1} whereas path B via hydroxide-by-bromide substitution (red line in Figure 6.5) requires 22.7 kcal mol^{-1}. Moreover, both pathways are lower in energy than the Pd–C bond

formation step which consumes 25.4 kcal mol^{-1} via **TS4-5**. These results suggest that path A is preferred over path B, although this decision hardly influences the transmetalation reaction rate governed by the transition state **TS4-5**.

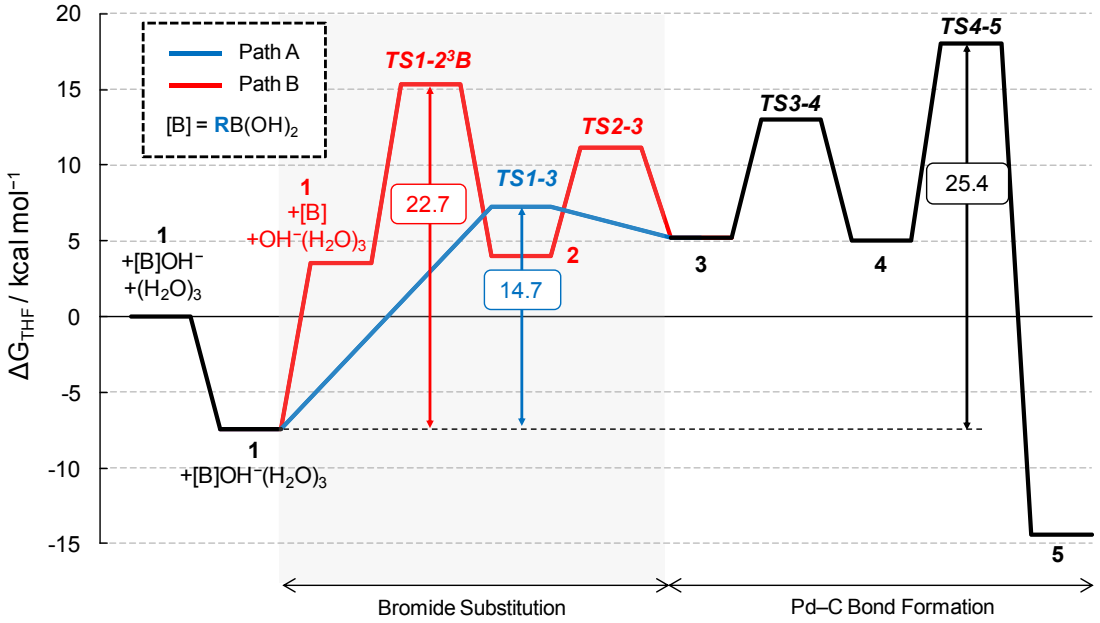

Figure 6.5 Gibbs energy profiles for transmetalation reaction mechanisms (R = vinyl).

6.4. Transmetalation of Phenyl Groups

The same procedure applied to vinyl species (Section 6.3) is performed for phenyl derivatives. The boronate [R–B(OH)$_3$]$^-$ plus the complex *trans*-[(PPh$_3$)$_2$Pd(R)(Br)] **Ph-1** have been taken as zero of energies (R = phenyl). Both the role of the base and the entire transmetalation process are calculated.

6.4.1. Role of the base

The substitution of bromide by hydroxide to form the Pd–hydroxo intermediate **Ph-2** (path B in Scheme 6.2) via **Ph-TS1-2^0** is located at 32.8 kcal mol^{-1} above reactants (Figure 6.6). As for vinyl species, the inclusion of water molecules is also considered. According to previous results, Figure 6.6 only shows the Gibbs energy profiles including 3 and 4 water molecules. **Ph-1** plus solvated boronate reactants are stabilised to ca. 6–7 kcal mol^{-1}. The energies of the transition states **Ph-TS1-2^3** and **Ph-TS1-2^4** also decrease until ca. 21 kcal mol^{-1}. The final Gibbs energy barriers become 27.9 and 27.2 kcal mol^{-1} for 3 and 4 water molecules, respectively (Figure 6.6). The small difference in Gibbs energies allows to assume convergence for n = 3.

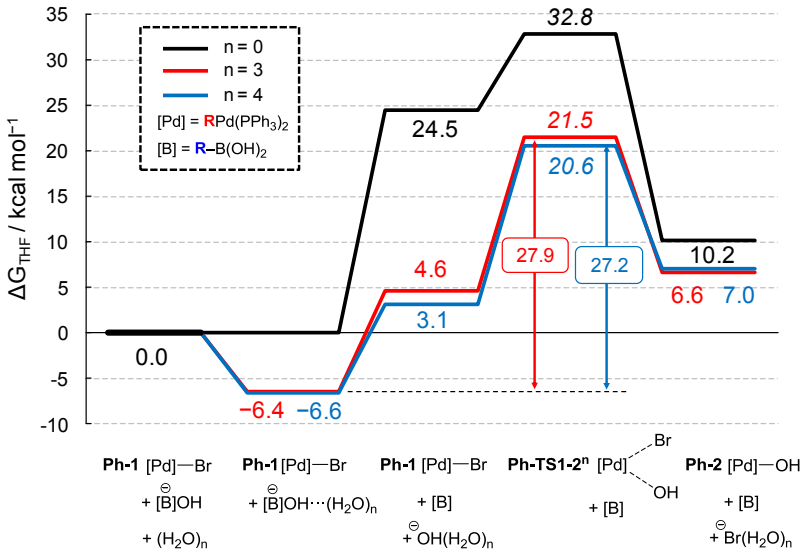

Figure 6.6 Gibbs energy profiles for path B including 0, 3, and 4 water molecules (R = phenyl).

As for vinyl species, the boronic acid is explicitly included in the model in order to consider all species within the same calculation. Recomputation of **Ph-TS1-2³** gives **Ph-TS1-2³B** which is located at 18.6 kcal mol^{-1} and requires a Gibbs energy barrier of 25.0 kcal mol^{-1}. Slightly larger barriers were found for the transition states **Ph-TS1-2³** and **Ph-TS1-2⁴** (27.9 and 27.2 kcal mol^{-1}, respectively), thus only **Ph-TS1-2³B** will be considered.

The displacement of bromide by boronate to produce the Pd–boronate **Ph-3** (Path A in Scheme 6.2) is described by **Ph-TS1-3⁰**, which is placed at 19.4 kcal mol^{-1} above reactants (Figure 6.7). Following the systematic solvation procedure, Figure 6.7 displays the Gibbs energy profiles after the inclusion of 3 and 4 water molecules. In line with vinyl species, the Gibbs energies of both reactants and transition states decrease almost equally and the Gibbs energy barriers remain at ca. 19 kcal mol^{-1}. The series is assumed to be converged for n = 3.

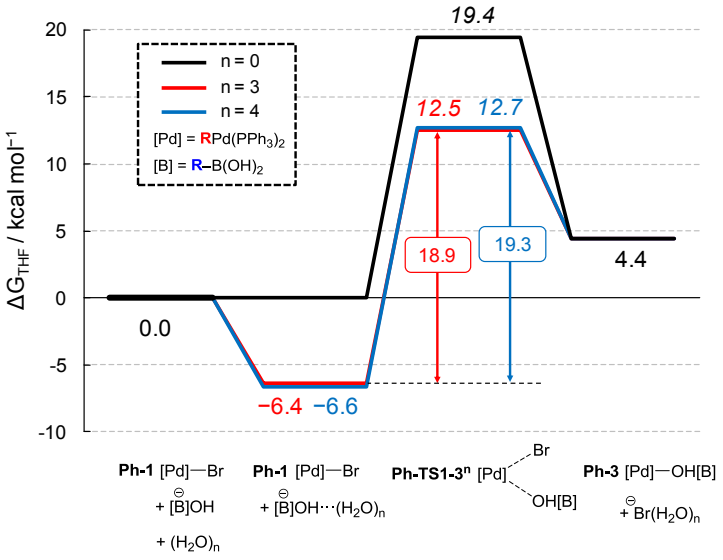

Figure 6.7 Gibbs energy profiles for path A including 0, 3, and 4 water molecules (R = phenyl).

Previous calculations indicated that the comparison between reaction mechanisms for the bromide substitution should be made in the basis of transition states **Ph-TS1-2³B** for path B and **Ph-TS1-3³** for path A. The corresponding Gibbs energy barriers are 25.0 and 18.9 kcal mol^{-1} for paths B and A, respectively. In the same manner as for vinyl counterparts, one achieves the same outcome, i.e., the boronate mechanism is preferred by 6.1 kcal mol^{-1}.

6.4.2. Transmetalation process

After the detailed study of the role of the base, the global transmetalation process is then analysed. Relative Gibbs energies are shown in Scheme 6.9 and Gibbs energy barriers with respect to the most stable reactants (**Ph-1** plus solvated boronate species at –6.4 kcal mol^{-1}) are discussed as follows. The bromide substitution from **Ph-1** is produced by either the boronate species via **Ph-TS1-3³** involving 18.9 kcal mol^{-1} (path A) or the hydroxide anion via **Ph-TS1-2³B** demanding 25.0 kcal mol^{-1} (path B). In the latter case, an additional step is required in which boronic acid attacks hydroxide ligand via **Ph-TS2-3**. Once the Pd–boronate intermediate **Ph-3** is formed, the Pd–C bond formation can take place via **Ph-TS3-5** involving 39.0 kcal mol^{-1} since no prior coordination change is needed for phenyl substrates.[362] Such a high barrier certainly blocks this reaction pathway. It has been shown that conformational diversity may be an error source to take into account.[385] In this regard, another conformational structure for the phosphine ligands in **Ph-TS3-5** (extracted from ref. 385) has been considered. The transition state **Ph-TS3-5-con** involves a barrier of 40.4 kcal mol^{-1}, thus no energy drop is obtained using such a conformation. Additionally, a *cis* configuration of the phosphine ligands in **Ph-TS3-5** has also been evaluated. The corresponding transition state **Ph-TS3-5-cis** still entails a barrier of 40.3 kcal mol^{-1}.

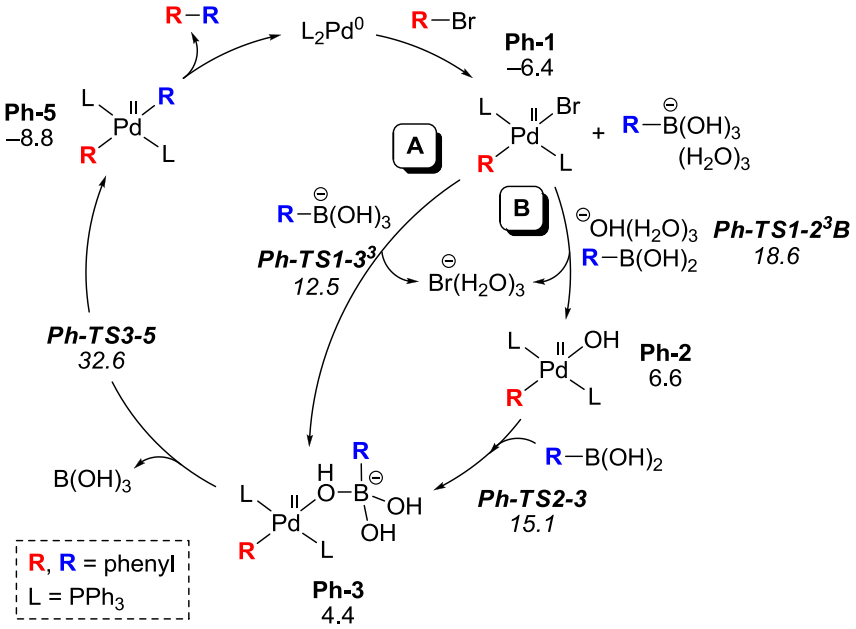

Scheme 6.9 Bisphosphine transmetalation reaction mechanisms (R = phenyl). ΔG_{THF} in kcal mol^{-1}.

As alternative route, the release of one phosphine ligand is proposed in Scheme 6.10. Indeed, monophosphine reaction mechanisms have been previously reported by others.[360,386–389] In the current study the displacement of the phosphine is promoted by the boronate ligand itself via **Ph-TS3-6**. The associative substitution requires 24.3 kcal mol^{-1} producing a κ^2-boronate intermediate **Ph-6**. Then, the phenyl group should coordinate to Pd by displacing one OH group from the boronate ligand (Scheme 6.10). At this state the entering η^2-phenyl group (in blue) can be placed in *trans* or *cis* position with respect to the η^1-phenyl ligand (in red).[388] For the *cis* mechanism (**c** suffix), the transition states of both the phenyl coordination **Ph-TS6-7c** and the Pd–C bond formation **Ph-TS7c-8c** are located at 19.3 and 18.4 kcal mol^{-1}, respectively, thus involving Gibbs energy barriers of ca. 25–26 kcal mol^{-1}. For the *trans* mechanism (**t** suffix), the phenyl coordination via **Ph-TS6-7t** is placed at 18.8 kcal mol^{-1}, whereas the Pd–C bond formation via **Ph-TS7t-8t** is placed at 24.8 kcal mol^{-1} and entails a Gibbs energy barrier of 31.2 kcal mol^{-1}. Reductive elimination and phosphine coordination processes are assumed to occur yielding the final product and regenerating the Pd catalyst.

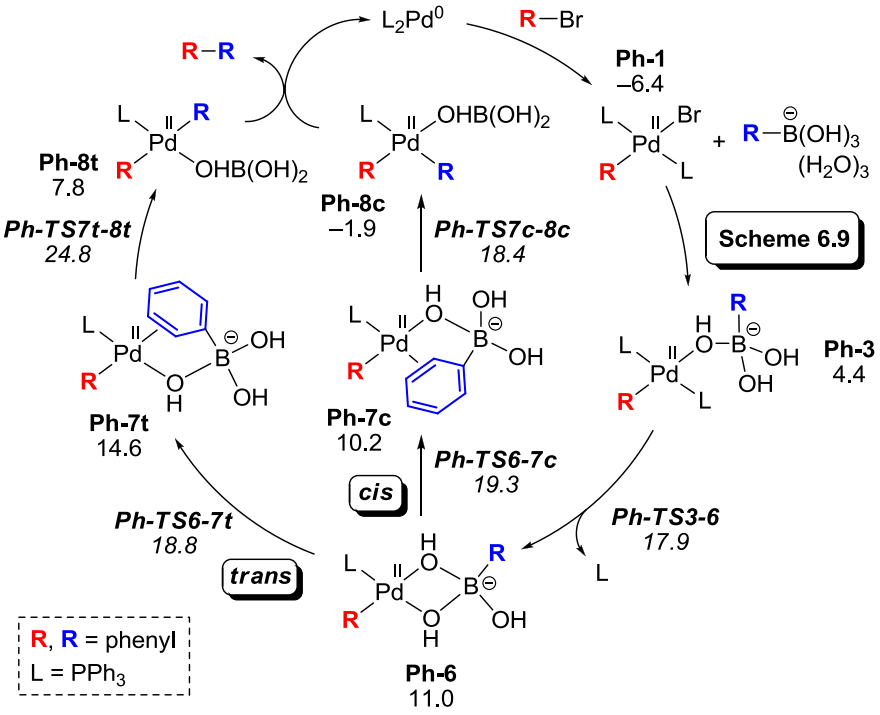

Scheme 6.10 Monophosphine transmetalation reaction mechanisms (R = phenyl). ΔG_{THF} in kcal mol^{-1}.

The relative Gibbs energies of Scheme 6.10 are plotted as reaction profiles in Figure 6.8. As concerns the bromide substitution, path A via **Ph-TS1-3^3** (blue line in Figure 6.8) demands 18.9 kcal mol^{-1} and path B via **Ph-TS1-2^{3}B** (red line in Figure 6.8) requires 25.0 kcal mol^{-1}. According to these barriers, the boronate substitution is also favoured for phenyl species by 6.1 kcal mol^{-1}. After the phosphine release via **Ph-TS3-6**, the Pd–C bond

formation bifurcates in two routes, *cis* (dashed blue line in Figure 6.8) and *trans* (dashed red line in Figure 6.8). The first step involving the phenyl coordination is quite similar in both routes. For the Pd–C bond formation the *cis* route takes 24.8 kcal mol^{-1} via **Ph-TS7c-8c** whereas the *trans* route involves a higher value of 31.2 kcal mol^{-1} via **Ph-TS7t-8t**. Overall, path A and *cis* route (solid and dashed blue lines in Figure 6.8) are the preferred reaction mechanisms. Gibbs energy barriers of ca. 25–26 kcal mol^{-1} are found for the Pd–C bond formation steps.

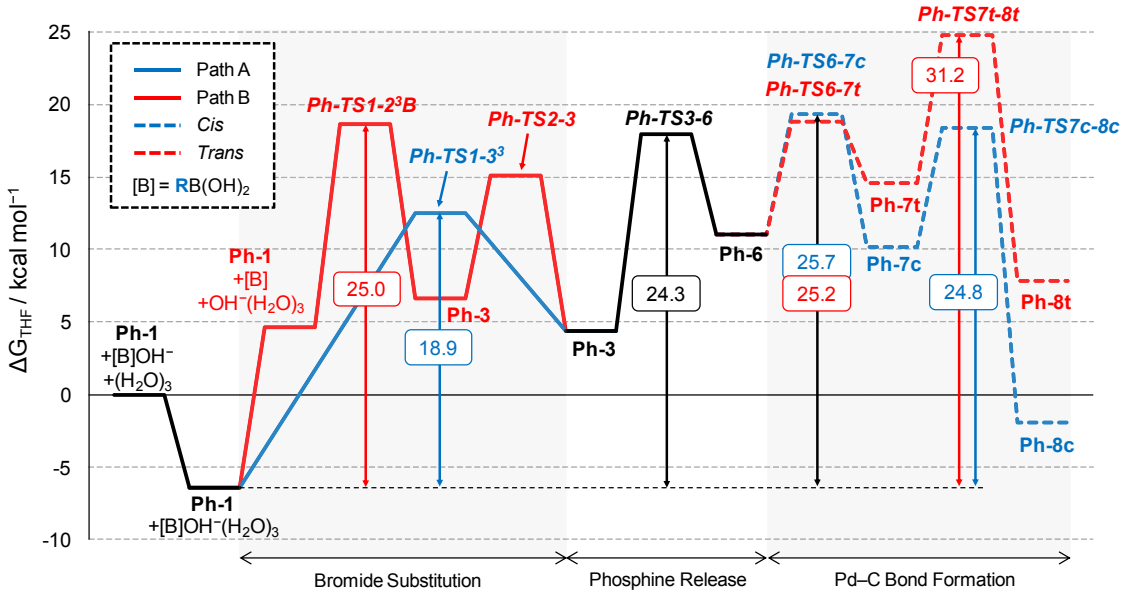

Figure 6.8 Gibbs energy profiles for monophosphine transmetalation reaction mechanisms (R = phenyl).

6.5. Merging Experiment with Computation

The above-discussed calculations support the involvement of boronate as active species at the first stage of the Suzuki–Miyaura transmetalation, namely path A. However, as pointed out in the introduction, recent experimental evidence claims for the participation of Pd–hydroxo intermediates, namely path B.[367–369] This section is therefore devoted to compare both computational and experimental results. One point of caution is worth here, since calculations assume a standard state of 1M for all species. Although the energies may differ in catalytic conditions —ca. 1.4 kcal mol^{-1} for each order of magnitude of concentration difference[22]—, the computational study still provide reliable mechanistic insight to take into consideration.

Firstly, Carrow and Hartwig demonstrated that, in absence of boronic acid, the populations of [L$_2$Pd(Ph)(Br)] and [L$_2$Pd(Ph)(OH)] are similar in THF/H$_2$O mixtures.[367] To address this issue, one must draw attention to species **Ph-1** and **Ph-2** in Figure 6.6 where the boronic acid appears in both sites and its energy contribution cancels. **Ph-1** (4.6 kcal mol^{-1})

is only 2.0 kcal mol^{-1} more stable than **Ph-2** (6.6 kcal mol^{-1}). Hence, a priori, both species could be formed in solution. They also showed that the reaction between Pd–OH and boronic acid is faster than the one between Pd–Br and boronate (Scheme 6.5).[367] The same trend has been reported by Schmidt et al. in other related system.[368] Calculations actually reproduce these facts due to a *ground state effect* as shown in Figure 6.8. **Ph-1** plus boronate species are more stable than **Ph-2** plus boronic acid. Since both of them have to reach the same Pd–C bond formation transition states, the barrier from **Ph-2** is necessarily lower since it lies above **Ph-1**. Overall, the Pd–OH intermediate **Ph-2** is accessible but not mandatory.

Besides, Amatore et al. set up an experiment to test the reaction between Pd–Br and boronate.[369] To preclude the putative formation of Pd–OH species, a large excess of bromide was introduced (100 equivalents). In such conditions, neither Pd–OH species nor reaction products were detected. They suggested that, since the path involving the Pd-hydroxo intermediate is putatively blocked, no reaction takes place. According to calculations, the rate-limiting transition state is shared for paths A and B and involves the Pd–C bond formation via **Ph-TS6-7c** and **Ph-TS7c-8c**. Therefore, all species prior to this point can be assumed to be in equilibrium. Since the bromide is eventually released, an excess of this species should displace all equilibria towards reactants. In other words, not only path B but also path A should be hampered. Additionally, other uncharacterised compounds such as $[Pd_2Br_6]^{2-}$ or $[Pd_2R_2Br_4]^{2-}$ may be formed.[390,391] Finally, they also found that the ratio base/boronic acid plays an important role.[369] At low hydroxide concentrations, either $[Ph–B(OH)_3]^-$ or Pd–OH species are hardly present, hence the reaction rate is slow for paths A and B. At high hydroxide concentrations, the formation of both $[Ph–B(OH)_3]^-$ and Pd–OH species is favoured. The reaction between them is however not productive and the reaction rate is again slow for paths A and B. None of these findings contradict calculations.

6.6. Conclusions

Boronate (path A) and Pd–hydroxo (path B) reaction mechanisms for the Suzuki–Miyaura cross-coupling of vinyl and phenyl reactants have been computed and their reliability has been compared to experimental evidence. Computational results are summarised as follows.

- Explicit solvation of the base (hydroxide anion) is necessary to obtain a better representation of the system.

- For vinyl and phenyl species, path A (via boronate intermediate) is preferred over path B (via Pd–hydroxo intermediate) by 6–8 kcal mol^{-1}.

- For vinyl species, the rate-limiting transition state corresponds with the Pd–C bond formation. The bromide displacement via path A or B hardly influences the overall reaction rate.

- For phenyl species, the bisphosphine transmetalation seems to be inoperative; instead, a monophosphine reaction mechanism is proposed. The rate-limiting transition states also involve Pd–C bond formation steps.

- After re-examination of recent experimental reports, computational results fit the available data. We conclude that palladium hydroxo intermediates are feasible but not mandatory for the transmetalation to occur.

7. Pd-Catalysed Si-based Vinylation in Water

This computational study attempts to provide a reliable mechanistic landscape on Pd-catalysed Si-based vinylation reactions in water. Several reaction mechanisms are proposed to account for the different reaction products experimentally observed. Each section is presented as follows. *Introduction* reviews some mechanistic considerations of organosilicon compounds and presents the experimental system under investigation. *Computational Details* gathers the specifications of the theoretical method. As concerns the results, *Initial Steps* describes the common processes that all forthcoming pathways share. *Hiyama vs. Heck* and *Transmetalation vs. Reinsertion* are devoted to illustrate and evaluate the proposed reaction mechanisms. *General Scenario* puts all pathways together revealing the overall mechanistic picture. Lastly, *Conclusions* compiles the main findings that computation has provided.

These computational results have been published as shown in Annex A.[392]

7.1. Introduction

The efficient synthesis of styrene derivatives —a terminal alkene with an aryl substituent— is crucial because they are important building blocks in fine and polymer chemistry.[393] Scheme 7.1 shows several synthetic strategies to form a terminal alkene, so-called vinyl: (i) elimination, (ii) olefination, (iii) partial reduction of alkynes, and (iv) cross-coupling reactions.[394] The latter procedure can involve different kinds of organometallic partners as discussed in Section 1.2.2. In this regard, organosilicon compounds appear as interesting reagents due to their low cost, low toxicity, and high chemical stability.[87,395] Their value in synthesis has been demonstrated.[396]

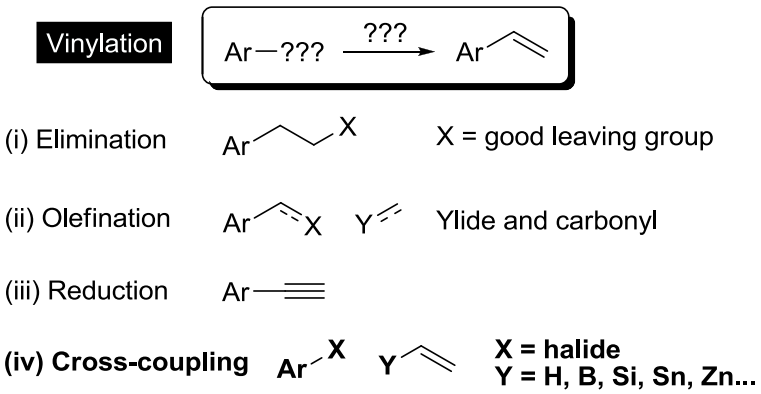

Scheme 7.1 Synthetic strategies to approach vinylation.

Hallberg and Westerlund firstly reported a Pd-catalysed Si-based procedure to couple vinyl and aryl moieties.[397] However, the organosilicon compounds actually underwent Heck

coupling followed by desilylation (Scheme 7.2).[398–399] Later, the addition of fluoride anions in the presence of alkylsilane[400] and alkoxysilane[401] species promoted the C–Si bond breaking process with concomitant transmetalation to Pd, also known as Hiyama coupling. The facile Si–F bond formation yielding five-coordinate silicon intermediates is assumed to activate the low-polar C–Si bond (Scheme 7.2),[88] although recent experiments claim otherwise.[a] The presence of NaOH[402] or Ag_2O[403,404] —fluoride-free conditions— also prompted the Hiyama coupling. Supporting these findings, Sakaki and co-workers theoretically modelled the activating role of both fluoride and hydroxide anions during the C–Si bond breaking process.[405] Denmark and Sweis later discovered that this promoting effect can be played by silanolate species formed by deprotonation of silanols with Brønsted bases.[406,407] The presence of Pd–O–Si linkages was found to be a key feature.[408] The transmetalation of silanolate reactants can proceed via four-coordinate (thermal pathway) and five-coordinate (activated pathway) silicon intermediates.[409]

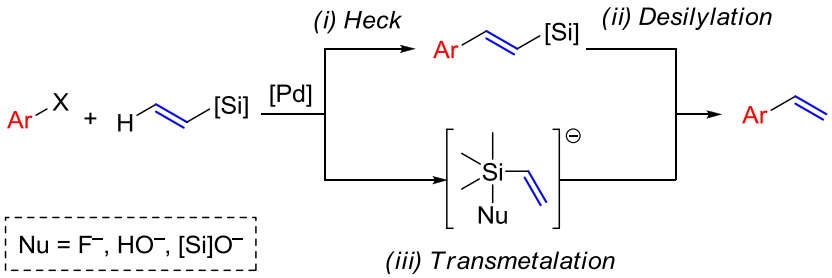

Scheme 7.2 Heck-desilylation vs. transmetalation mechanisms.

Usually, the computation of Heck and Hiyama pathways is considered separately. Several reaction mechanisms for the Pd-catalysed Heck coupling have been calculated,[94] see for instance some representative systems based on phosphine,[109,410–412] carbene,[413] and several bidentate ligands.[414] Likewise, theoretical studies in *ligand-free* conditions have also been performed.[415] Scarce literature is however available for the Hiyama transmetalation process.[405] Recently, a computational study on an oxidative Heck/Suzuki reaction compared β-hydride elimination and transmetalation. The latter was found to be favoured in the presence of 1,4-benzoquinone.[416]

In line with the aforementioned *green* features of organosilicon compounds,[87] water is the preferred solvent from both economics and environmental standpoints, though additional aspects should be taken into account.[417] Common organic synthesis used to avoid water but the picture has changed nowadays.[418–420] Water is a reactive media indeed, thus the comprehension of the reaction mechanisms at work is needed for a rational design of

[a] Some authors suggest the participation of [Pd–F] intermediates when arylsilane reactants are involved, see C. Amatore, L. Grimaud, G. Le Duc, A. Jutand, *Angew. Chem. Int. Ed.* **2014**, *53*, 6982–6985.

processes. Focusing on vinylation, the Pd-catalysed Si-based cross-coupling reaction in aqueous media has already been reported.[421,422] Particularly, de Jesús and co-workers efficiently performed the coupling between triethoxyvinylsilanes and aryl bromides in basic aqueous media with [Pd(OAc)$_2$] as precursor (Scheme 7.3).[423] To further unveil the operating mechanism, the reactions were carried out using deuterated vinylsilanes. The deuterium distribution of the products indicated that the Heck mechanism via putative Pd–hydride intermediates is at work.[424] A more thorough and comprehensive study was lately reported in which the scope was extended to other substrates and Pd precursors.[392] The addition of different aryl reactants in a two-step one-pot proceeding also allowed the synthesis of asymmetric *E*-1,2-diarylethene derivatives (Scheme 7.3).[392]

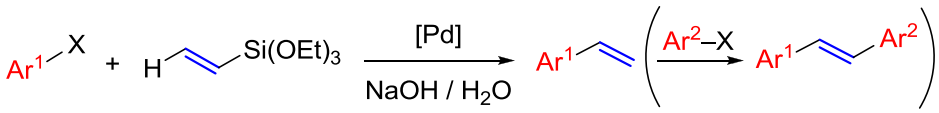

Scheme 7.3 General synthesis of vinylarene (and *E*-1,2-diarylethene) derivatives.

Prior to address mechanistic investigations, some aspects should be considered.[392] Firstly, aryl iodide reagents are preferred because their coupling reaction can be performed at room temperature. The actual speciation of vinylsilanes in solution is also an issue to deal with. According to ESI-TOF and NMR spectroscopy, ethoxyvinylsilanes vinyl–Si(OEt)$_3$ undergo hydrolysis in basic media producing vinylsilanolates [vinyl–Si(OH)$_2$O]$^-$. Regarding the catalyst, transmission electronic microscopy images indicated the presence of Pd nanoparticles for all precursors but [PdCl$_2$(en)] (en = ethylenediamine) which seems to work in a homogeneous regimen. Putting all together, both experimental and computational studies here discussed will concern the coupling of iodobenzene with vinylsilanolate in presence of [PdCl$_2$(en)] as depicted in Scheme 7.4. In such conditions, the reaction yields styrene as major product, although β-silylated styrene is obtained in less extent.

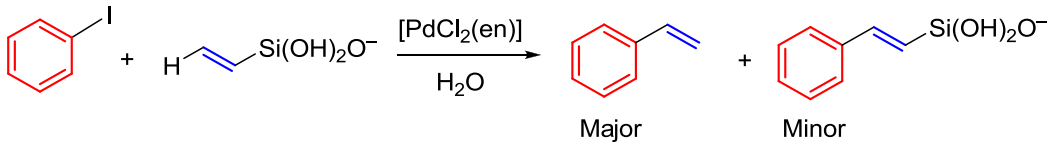

Scheme 7.4 Coupling reaction under study.

From the experimental side, exhaustive labelling studies were carried out using different deuterated vinylsilanes in order to distinguish between reaction mechanisms.[392] The final outcome deduced from these experiments is summarised in Scheme 7.5 by labelling the participant hydrogen atoms with the tags a, b, and c (abc pattern). Three competing pathways are proposed to account for the observed products: (i) Hiyama, (ii) Heck, and (iii) desilylation.[425] Firstly, the Hiyama coupling entails the transmetalation of the vinyl group

from Si to Pd and subsequent reductive elimination. Since no hydrogen atoms are involved in the process, the hydrogen distribution pattern of the styrene product **A** remains unchanged. **A** only accounts for 1% of the reaction yield, thus this pathway is unlikely operative. On the other hand, the Heck coupling involves a C–H bond activation producing the β-silylated styrene **B**. In this step the hydrogen atom H_c goes to the palladium centre forming the Pd–hydride **C**. The reaction does continue and H_c from **C** can be reincorporated to **B** with concomitant silicon removal. The entering H_c can be located in *trans* or *cis* positions with respect to the phenyl group, giving rise to the styrene species **D** and **E**, respectively. The latter **E** appears as the major product (75%). Overall, consecutive Heck and desilylation processes should prevail.

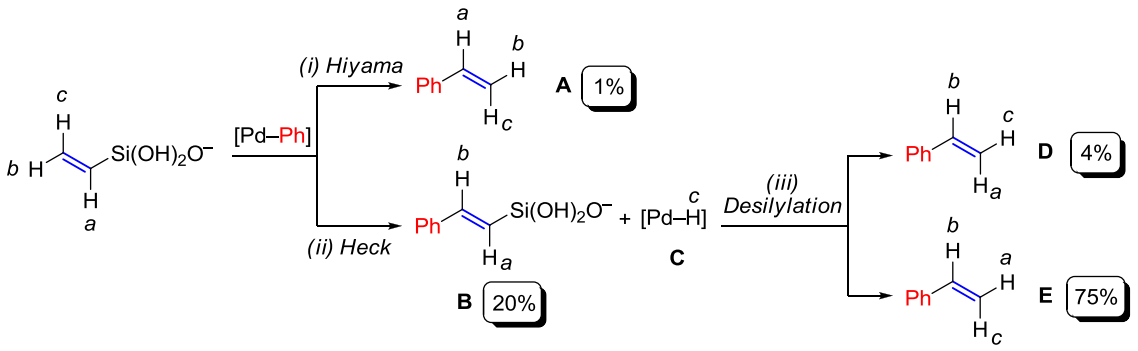

Scheme 7.5 Results from labelling studies. Yields determined by ^{1}H NMR analysis of crude reaction mixtures.

With all this information at hand, a computational study is performed to reveal the mechanistic details at microscopic level. The main purpose is to evaluate the operating reaction mechanisms that account for the formation of the major product **E** as well as the detection of the minor products **A**, **B**, and **D**. The Hiyama/Heck competition is first analysed and two desilylation mechanisms are then proposed.

7.2. Computational Details

Forthcoming calculations were performed at the DFT level by means of the M06 functional[168] with an ultrafine grid[384] as implemented in Gaussian 09.[265] This functional have been tested against dispersion interactions and transition metal chemistry providing satisfactory results.[180,181,189] The Pd and I heavy atoms were described using scalar-relativistic Stuttgart-Dresden SDD effective core potentials and their associated double-ζ basis sets,[266] complemented with a set of f-polarisation functions.[267,268] The 6-31G** basis set (DZ) was used for the H,[269] C, N, O, and Si atoms.[270]. Diffuse functions were added to O atoms.[271] Water (ε = 78.4) solvent effects were included through SMD[215] single-point calculations on gas-phase optimised geometries using the 6-311++G** basis set (TZ) for the H, C, N, O, and Si atoms.[271,426] The structures of reactants, intermediates, transition states, and products were

fully optimised without any symmetry restriction. Transition states were identified by having one imaginary frequency in the Hessian matrix. It was confirmed that transition states connect with the corresponding intermediates by means of application of an eigenvector corresponding to the imaginary frequency and subsequent optimisation of the resulting structures. Gibbs energies in water (ΔG_w) are computed according to the following formula,

$$\Delta G_w = \Delta E_w(TZ) + \Delta G_{gp}(DZ) - \Delta E_{gp}(DZ) \qquad [7.1]$$

where suffixes w and gp stand for water and gas phase, respectively.

7.3. Initial Steps

Both Heck and Hiyama couplings share the first steps of the reaction, i.e., (i) oxidative addition and (ii) coordination of [vinyl–$Si(OH)_2O]^-$ via iodide removal. First, the unsaturated Pd(0) complex [Pd(en)] is assumed as initial catalyst.[102] After the coordination of one molecule of iodobenzene forming the adduct **1**, the oxidative addition takes place via the three-centred transition state **TS1-2** (Scheme 7.6). The relative Gibbs energy barrier with respect to **1** is only 4.4 kcal mol^{-1}. The resulting product **2** is taken as zero of energies. Since the vinylsilanolate is negatively charged, one water molecule is coordinated to the negative oxygen in order to better describe its solvation sphere.

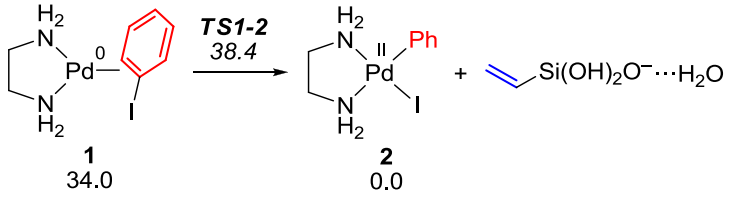

Scheme 7.6 Oxidative addition. ΔG_w in kcal mol^{-1}.

The reactant [vinyl–$Si(OH)_2O]^-$ should now coordinate to Pd in the oxidative addition product **2**. This process entails the release of iodide and is found to be stepwise (Scheme 7.7). The negatively charged oxygen atom of [vinyl–$Si(OH)_2O]^-$ first displaces one amine of the bidentate ligand in **2** via **TS2-3**, particularly the one which is located *trans* to the iodide ligand. Such iodide is then substituted by the non-coordinated amine in **3** via **TS3-4** in order to recover the chelating situation. Both transition states **TS2-3** and **TS3-4** involve similar barriers of ca. 17 kcal mol^{-1}. Interestingly, no direct O-by-I substitution connecting **2** and **4** could be located. A subsequent reorganization of the ligand [vinyl–$Si(OH)_2O]^-$ is needed to change its coordination mode from η^1-O in **4** to η^2-CC in **5**. The corresponding transition state **TS4-5** demands 19.0 kcal mol^{-1} from **2**. The water molecule in **5** coordinates to the negative oxygen of the vinylsilanolate ligand.

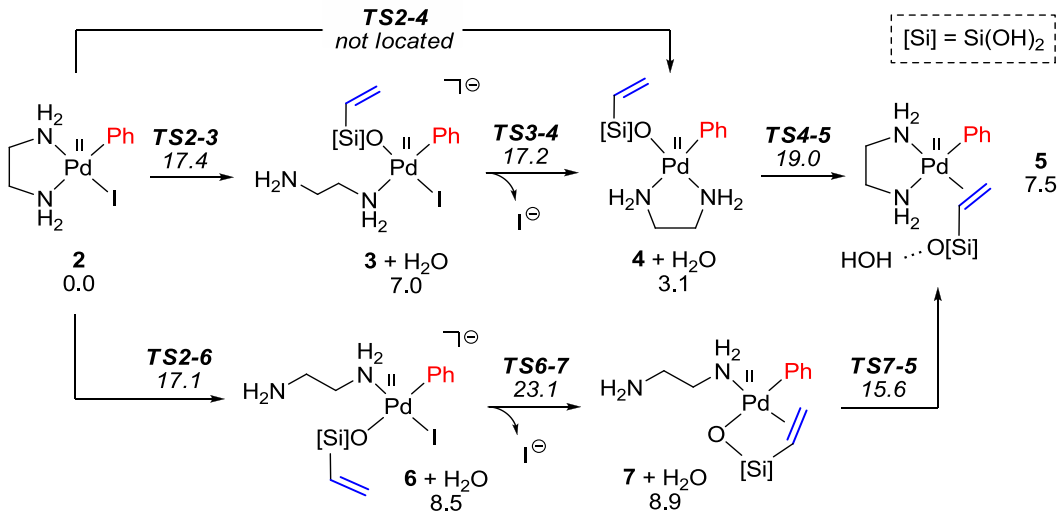

Scheme 7.7 Vinylsilanolate coordination. ΔG_w in kcal mol^{-1}.

An alternative substitution pathway to skip **TS4-5** can be envisaged (Scheme 7.7). In this case, the entering [vinyl–Si(OH)$_2$O]$^-$ displaces the nitrogen atom located *cis* to iodide via **TS2-6**. The vinyl group then displaces the iodide ligand (**TS6-7**) and the free amine again coordinates to Pd (**TS7-5**) forming **5**. Since the highest transition state **TS6-7** is placed at 23.1 kcal mol^{-1}, i.e., 4.1 kcal mol^{-1} above **TS4-5**, this pathway is less favoured and not considered in further discussions.

7.4. Hiyama vs. Heck

Starting from intermediate **5**, the course of the reaction diverges towards Hiyama and Heck reaction mechanisms giving rise to the products **A** and **B**, respectively (Scheme 7.5). Hydrogen atoms are labelled according to the abc pattern shown in Scheme 7.5 in order to facilitate the tracking procedure.

The Hiyama mechanism (HI) is shown in Scheme 7.8a. All intermediates of this pathway are labelled with the prefix **hi**. It starts with the activation of the C–Si bond. Due to the presence of a negative charge in the vinylsilanolate ligand, the addition of a hydroxide anion[405] is quite unlikely. Instead, one water molecule is added to Si in **5** to produce the five-coordinate silicon intermediate **hi1**. The corresponding transition state **TS5-hi1** describes how the negative oxygen atom deprotonates the entering water molecule and the resulting hydroxide binds Si. The formation of **hi1** weakens the C–Si bond and promotes the transmetalation of the vinyl group from Si (**hi1**) to Pd (**hi2**) via **TShi1-h2**. The C–Si bond activation and transmetalation transition states are placed at 23.0 and 24.7 kcal mol^{-1}, respectively. Then, the reductive elimination takes place via **TShi2-hi3** at 13.4 kcal mol^{-1} above **hi2**. No hydrogen atoms are actively involved in the reaction mechanism, thus the

abc pattern remains unaltered. The last step regenerates the catalyst [Pd(en)] and yields the styrene product **A**.

As a competitive route, the Heck mechanism (HE) is illustrated in Scheme 7.8b. All intermediates of this pathway are labelled with the prefix **he**. Firstly, the [vinyl–Si(OH)$_2$O]$^-$ ligand inserts into the Pd–Ph bond via **TS5-he1**, placed at 16.0 kcal mol^{-1}. The intermediate **he1** resulting from the C–C bond formation lays 4.7 kcal mol^{-1} below **2**. Then, the agostic intermediate **he2** is formed via the C–C bond rotation process **TShe1-he2** (4.4 kcal mol^{-1}) at 9.1 kcal mol^{-1} above **he1**. Subsequent β-hydride elimination proceeds via **TShe2-he3** (2.1 kcal mol^{-1}) at 6.8 kcal mol^{-1} above **he1** and gives the hydride species **he3**. The hydride ligand in **he3** corresponds to H$_c$ whereas H$_a$ is now settled in *trans* position to H$_b$ due to the C–C bond rotation. The reaction of **he3** with base eventually delivers the β-silylated product **B** and regenerates the catalyst.

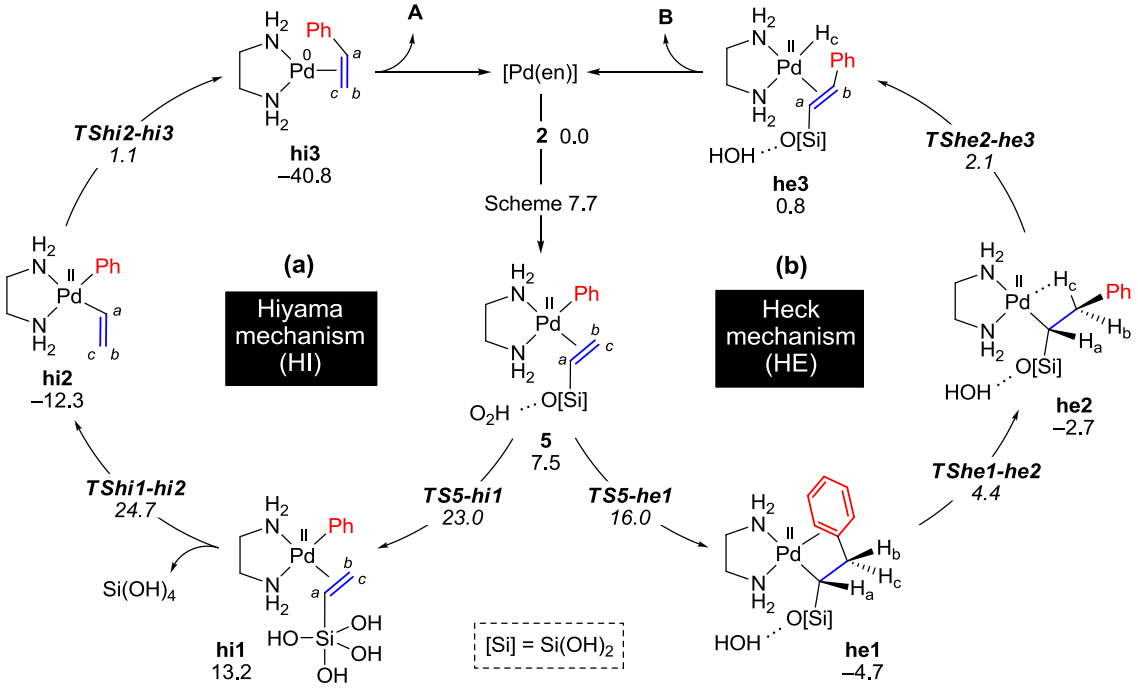

Scheme 7.8 (a) Hiyama and (b) Heck mechanisms. ΔG$_w$ in kcal mol^{-1}.

Figure 7.1 depicts the optimised structures of the intermediate **5** together with the rate-determining transition states **TShi1-hi2** and **TS5-he1** in HI and HE, respectively. Intermediate **5** represents a η^2-CC coordination of the reactant [vinyl–Si(OH)$_2$O]$^-$. The explicit water molecule forms a hydrogen bond with the negative oxygen atom. The transmetalation process in **TShi1-hi2** features a five-coordinate silicon atom and an elongated C–Si bond. The insertion step in **TS5-he1** brings closer the carbons atoms preserving a tetrahedral moiety for the vinylsilanolate.

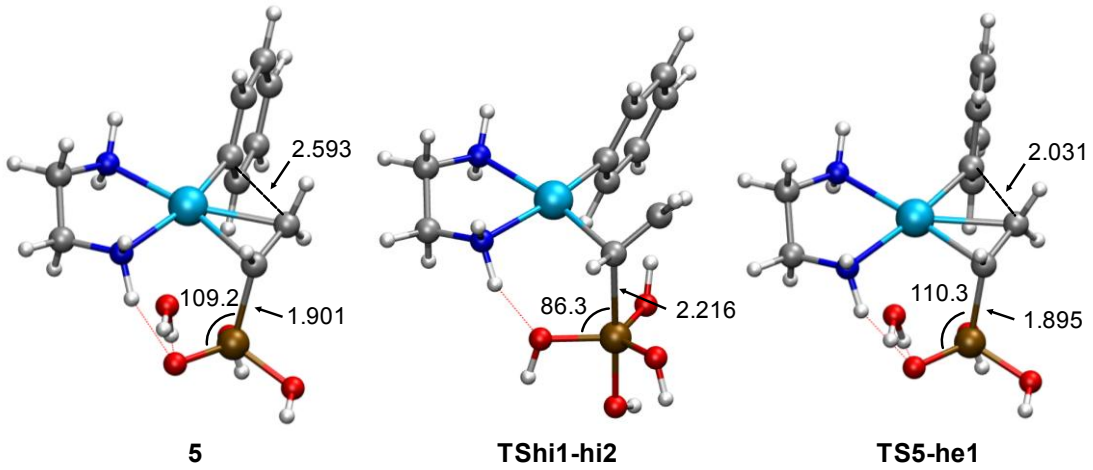

Figure 7.1 Optimised geometries of **5**, **TShi1-hi2**, and **TS5-he1**. Distances in Å, angles in degrees.

For comparative purposes, vinylsilanolate coordination (Scheme 7.7) together with HI and HE (Scheme 7.8) are plotted as Gibbs energy profiles in Figure 7.2. As concerns the initial steps of the reaction (black line in Figure 7.2), the highest transition state describes the η^2-CC coordination of [vinyl–Si(OH)$_2$O]$^-$ and involves a barrier of 19.0 kcal mol^{-1} (**TS4-5**). Once **5** is formed, the reaction pathway splits into two different routes. On one hand, HI (red line in Figure 7.2) requires 23.0 (**TS5-hi1**) and 24.7 kcal mol^{-1} (**TShi1-hi2**) to overcome the water-promoted C–Si bond activation and transmetalation, respectively. On the other hand, HE (blue line in Figure 7.2) takes 16.0 kcal mol^{-1} (**TS5-he1**) to proceed with the insertion step. The energy difference between the transmetalation in HI (24.7 kcal mol^{-1} via **TShi1-hi2**) and the insertion in HE (16.0 kcal mol^{-1} via **TS5-he1**) is 8.7 kcal mol^{-1}, hence the latter evolves faster. As a result, the formation of **B** may be preferred over **A** in agreement with the yields shown in Scheme 7.5. It is worth noting that the overall barrier for HE actually involves the vinylsilanolate coordination via **TS4-5** taking 19.0 kcal mol^{-1}.

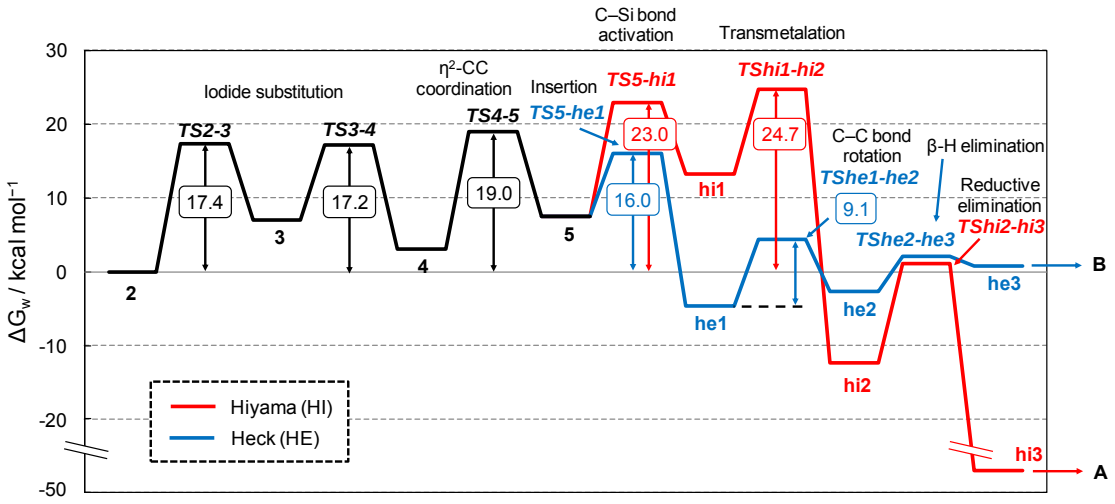

Figure 7.2 Gibbs energy profiles for Hiyama (red line) and Heck (blue line) mechanisms.

7.5. Transmetalation vs. Reinsertion

Previous calculations indicated the dominant role of the Heck mechanism to yield the β-silylated styrene **B** (Scheme 7.8b). However, according to experimental evidence, the reaction continues to yield styrenes **D** and **E** (Scheme 7.5). These products lack the silicon moiety, thus a kind of desilylation process must occur. Two pathways are then proposed, namely Heck-transmetalation and Heck-reinsertion. Both reaction mechanisms share the stable intermediate **he1** but bifurcate from **he3**. Again, hydrogen atoms are labelled according to the abc pattern shown in Scheme 7.5 to make easier the tracking procedure.

The Heck-transmetalation mechanism (HT) is shown in Scheme 7.9a. All intermediates of this pathway are labelled with the prefix **t**. This proposal suggests a transmetalation process in order to remove the silicon moiety. In line with the Hiyama mechanism (Scheme 7.8a), the initial step entails a water-promoted C–Si bond activation via **TShe3-t1**. Once the five-coordinate silicon intermediate **t1** is formed, the C–Si bond cleaves and the styryl moiety is transferred from Si to Pd via **TSt1-t2**. The C–Si bond activation and transmetalation transition states are placed at 15.9 and 14.9 kcal mol^{-1}, respectively (20.6 and 19.6 kcal mol^{-1} above **he1**, respectively). Then, the reductive elimination between the hydride and styryl ligands occurs via **TSt2-t3** at 5.1 kcal mol^{-1} above **t2**. In this mechanism, H_a remains *trans* to H_b and H_c occupies the position of the former silicon group. The product **D** is eventually released from **t3** regenerating the catalyst.

As an alternative route, the Heck-reinsertion mechanism (HR) is considered in Scheme 7.9b. All intermediates of this pathway are labelled with the prefix **r**. This mechanism is based on the readdition of the hydride ligand to the β-silylated styryl moiety. Initially, the rotation of the alkene ligand in **he3** takes place via **TShe3'** (5.1 kcal mol^{-1}) at 9.8 kcal mol^{-1} above **he1**.[a] The alkene ligand in **he3'** can now insert into the Pd–H bond via **TShe3'-r1** (5.7 kcal mol^{-1}) at 10.4 kcal mol^{-1} above **he1**. The agostic intermediate **r1** undergoes a rapid C–C bond rotation process via **TSr1-r2** producing a stable Pd–O–Si linkage in **r2** at 14.5 kcal mol^{-1} below **2**. The formation of the Pd–O bond defines a *syn* stereochemistry between the Pd and Si atoms and also imposes a *syn* configuration for the atoms H_a and H_b. The C–Si bond activation is again mediated by one water molecule via **TSr2-r3**. From the five-coordinate silicon species **r3**, the C–Si bond splits by means of a *syn* Pd–Si elimination process via **TSr3-r4**. The C–Si bond activation and elimination transition states display energies of 6.4 and 5.4 kcal mol^{-1} and are located at 20.9 and 19.9 kcal mol^{-1} above **r2**, respectively. Intermediate **r4** finally delivers the styrene **E** regenerating the catalyst.

[a] The olefin rotation process actually involves an additional transition state but it lies below **TShe3'**.

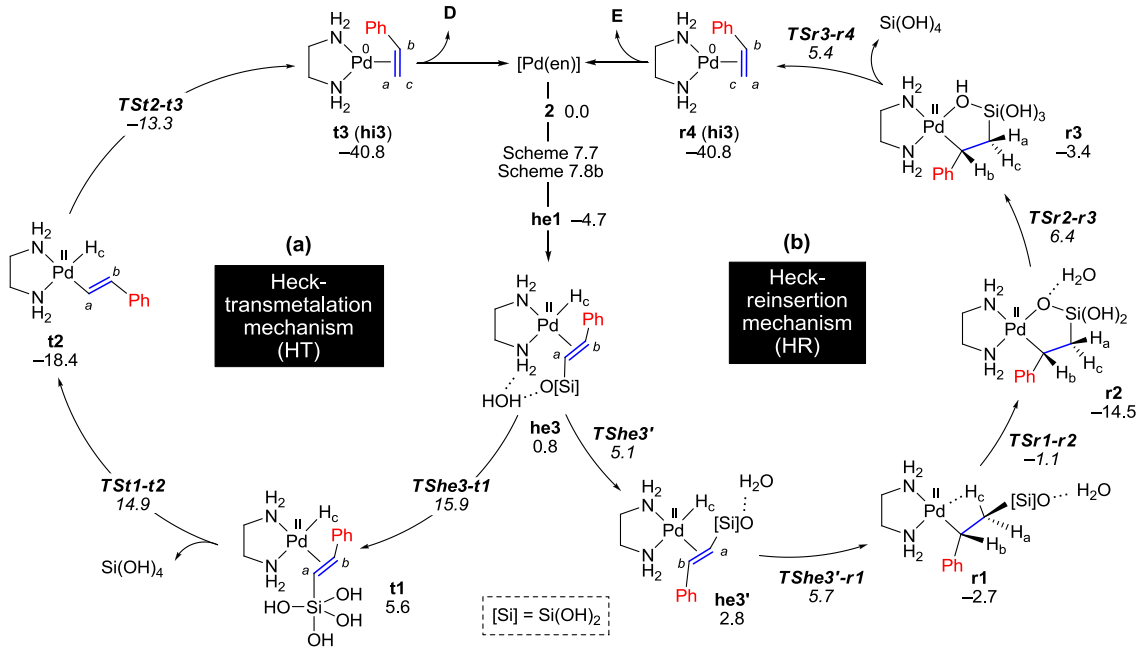

Scheme 7.9 (a) Heck-transmetalation and (b) Heck-reinsertion mechanisms. ΔG_w in kcal mol^{-1}.

Figure 7.3 represents the optimised structures of the intermediate **he3** and transition states **TShe3-t1** and **TSt1-t2** in HT. Intermediate **he3** coming from HE contains the hydride and η²-CC vinylsilanolate ligands. The C–Si bond activation in **TShe3-t1** occurs via deprotonation of the entering water molecule whilst the concomitant hydroxide anion coordinates to Si. Similarly to **TShi1-hi2** (Figure 7.1), the transmetalation step in **TSt1-t2** exhibits a five-coordinate Si atom and an elongated C–Si bond.

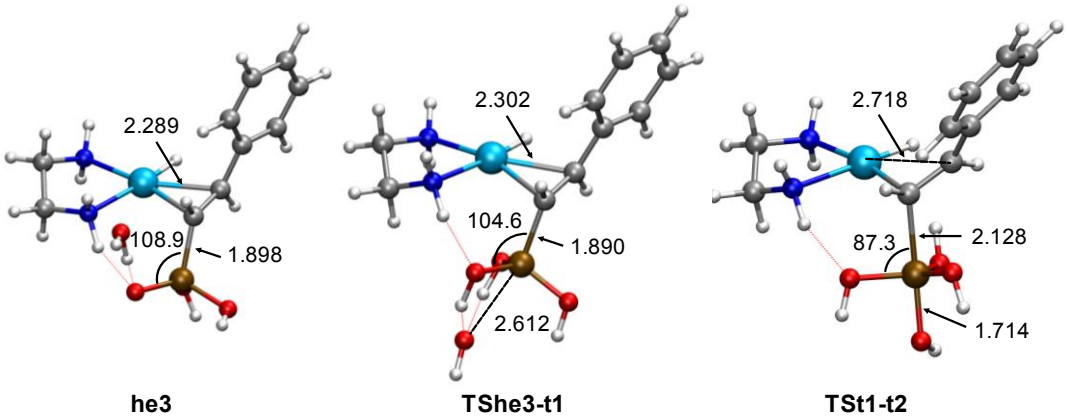

Figure 7.3 Optimised geometries of **he3**, **TShe3-t1**, and **TSt1-t2**. Distances in Å, angles in degrees.

Figure 7.4 displays the optimised structures of the intermediate **r2** and transition states **TSr2-r3** and **TSr3-r4** in HR. Intermediate **r2** contains a Pd–O–Si linkage as part of a five-membered metalocycle. The C–Si bond activation in **TSr2-r3** begins with the deprotonation of water by the oxygen atom coordinated to Pd and the freshly-formed hydroxide anion approaches to Si. The *syn*-elimination in **TSr3-r4** entails the lengthening of the C–Si bond as long as the $Si(OH)_4$ moiety leaves the coordination sphere of the metal.

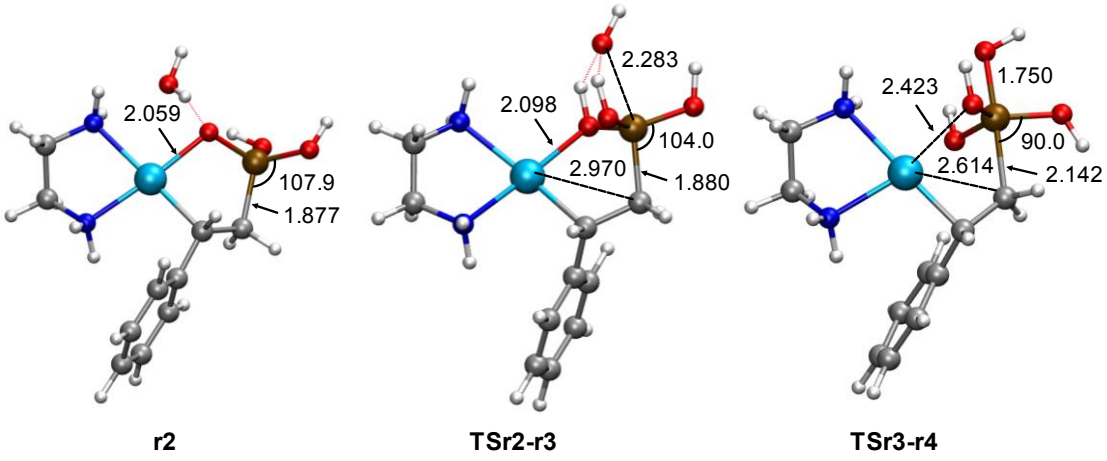

Figure 7.4 Optimised geometries of **r2**, **TSr2-r3**, and **TSr3-r4**. Distances in Å, angles in degrees.

The above-mentioned calculations are gathered as Gibbs energy profiles in Figure 7.5. After the formation of **he1** via 19.0 kcal mol^{-1} and **he3** via 9.1 kcal mol^{-1} (Figure 7.2), the reaction mechanism diverges. HT (red line in Figure 7.5) involves barriers of 20.6 and 19.6 kcal mol^{-1} for the C–Si bond activation (**TShe3-t1**) and transmetalation (**TSt1-t2**) steps, whereas HR (blue line in Figure 7.5) takes lower barriers of 9.8 and 10.4 kcal mol^{-1} for the alkene rotation (**TShe3'**) and reinsertion (**TShe3'-r1**) processes. The energy difference between **TShe3-t1** in HT and **TShe3'-r1** in HR is 10.2 kcal mol^{-1} favouring the latter. As a result, once **he3** is formed, the reaction mainly evolves via HR generating the stable intermediate **r2**. At this point there is no turning back in the process. The new barrier required to return and reach **TShe3-t1** in HT is 30.4 kcal mol^{-1} and, therefore, quite unlikely to overcome. Alternatively, **r2** can undergo C–Si bond activation and elimination processes consuming 20.9 and 19.9 kcal mol^{-1}. Although the overall barriers for HT and HR are similar, the latter pathway should proceed faster. This scenario suggests that **D** may be detected but **E** should be the major product, in agreement with experiments (Scheme 7.5).

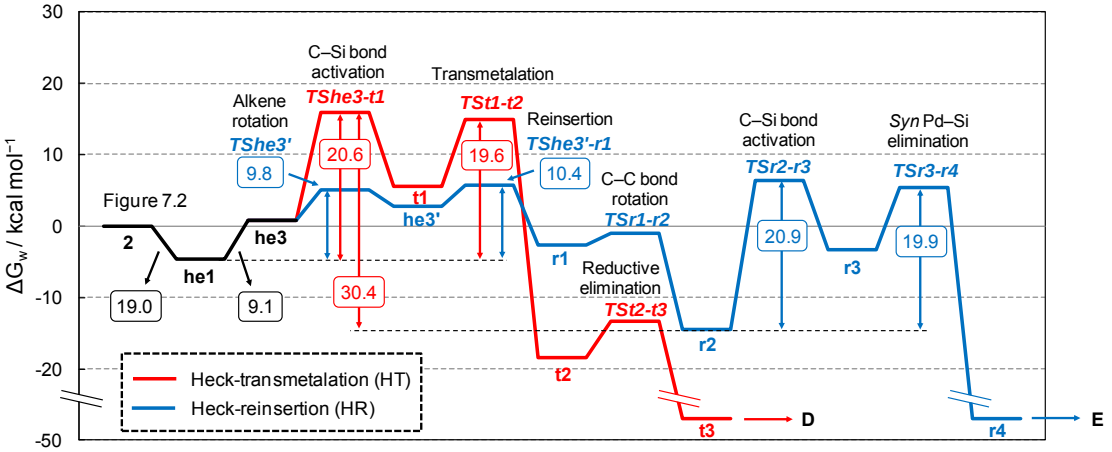

Figure 7.5 Gibbs energy profiles for Heck-transmetalation (red line) and Heck-reinsertion (blue line) mechanisms.

7.6. General Scenario

All computational results are summarised in Scheme 7.10. After the fast oxidative addition of iodobenzene, the coordination of [vinyl–Si(OH)$_2$O]$^-$ demands 19.0 kcal mol^{-1}. From **5**, the reaction pathway diverges. Transmetalation in HI entails 24.7 kcal mol^{-1} forming **A**, whereas insertion in HE consumes 16.0 kcal mol^{-1} producing **he3** and, eventually, **B**. HI takes 8.7 kcal mol^{-1} more than HE thus the latter prevails. From **he3**, the reaction pathway splits again. C–Si bond activation in HT requires 20.6 kcal mol^{-1} generating **D** whereas reinsertion in HR takes 10.4 kcal mol^{-1} giving rise to **r2**, which finally evolves to yield **E**. HT involves 10.2 kcal mol^{-1} more than HR and, as a result, the latter becomes faster. Subsequent C–Si bond activation in HR requires 20.9 kcal mol^{-1} producing **E** as major product.

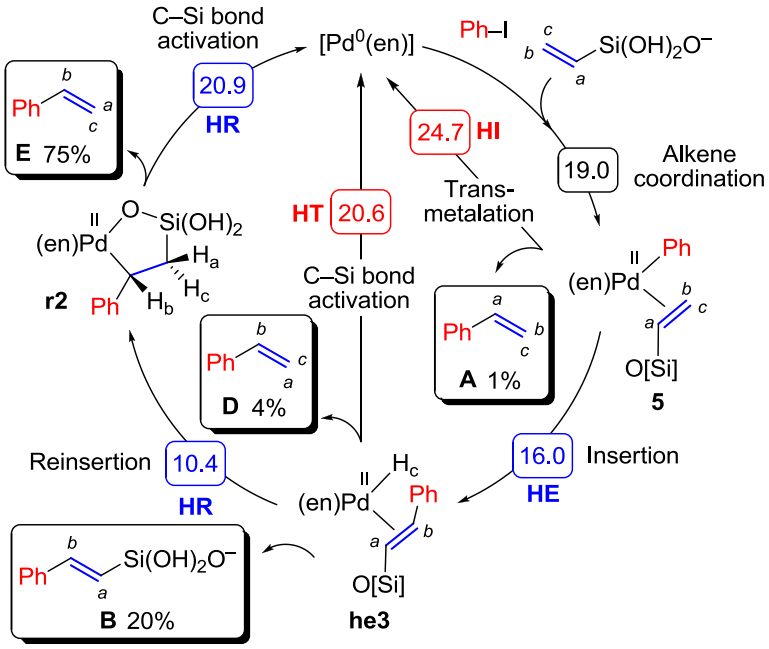

Scheme 7.10 All proposed reaction mechanisms. Gibbs energy barriers in kcal mol^{-1}.

7.7. Conclusions

The Pd-catalysed coupling between PhI and [vinyl–Si(OH)$_2$O]$^-$ in water has been analysed by computational means. Several reaction mechanisms have been considered to account for the products experimentally observed. Hiyama (HI), Heck (HE), Heck-transmetalation (HT), and Heck-reinsertion (HR) pathways lead to the products **A**, **B**, **D**, and **E**, respectively. Computational highlights are summarised as follows.

- The coordination of the vinylsilanolate compound to form **5** involves a transient decoordination of the bidentate ligand of the catalyst and overall takes 19.0 kcal mol^{-1}.

- From **5**, the insertion in HE is faster than the water-promoted transmetalation in HI ($\Delta\Delta G^{\ddagger}$ = 8.7 kcal mol^{-1}), hence favouring the formation of **B** over **A**.

- Once the hydride species **he3** is formed from HE, the reaction continues via desilylation. The reinsertion in HR is faster than the water-promoted transmetalation in HT ($\Delta\Delta G^{\ddagger}$ = 10.2 kcal mol^{-1}), hence favouring the formation of **E** over **D**.

- For HR, the presence of a Pd–O–Si linkage in **r2** imposes a *syn* configuration of Pd and Si moieties prior to elimination which exclusively yields **E**.

- The proposed reaction mechanisms explain at microscopic level the experimentally observed products.

V

Properties

An animal doesn't need to develop curiosity and intelligence
if it has no problems that need solving.

"Dragon's Egg" by Robert L. Forward

8. Acidity of Dihydrogen Complexes in Water

This investigation is focused on the computation of the pK_a in water (pK_a^{water}) in a series of transition metal dihydrogen complexes. Each section is presented as follows. *Introduction* presents the motivation of the study as well as previous contributions in the field. *Computational Details* indicates the theoretical methods and *Size of Solvent Clusters* accounts for the procedure to optimise the number of solvent molecules considered in further calculations. *Dihydrogen and Hydride Complexes* introduces the set of water-soluble dihydrogen complexes under study and their corresponding hydride counterparts. *Validating the Protocol in THF* initially tests the computational approach against the pK_a values in tetrahydrofuran of some dihydrogen complexes, and subsequent *Estimation of pK_a Values in Water* presents the predicted pK_a^{water} for the given set of complexes. Later on, *Discussion of pK_a Values in Water* analyses and rationalises the results. Finally, *Conclusions* collects the main outcomes.

8.1. Introduction

Since the characterisation of the first η^2-H_2 complex by Kubas and co-workers,[12] a lot of efforts has been made in this field proving that transition metal complexes can successfully coordinate molecular H_2.[115] This binding situation may entail the activation of the H–H bond, which splitting process can proceed via homolytic or heterolytic pathways as discussed in Section 1.3. The latter is involved in relevant *bio-inspired* processes such as those concerning hydrogenases.[427,428] As concerns the solvent, water is a desirable election due to its economics and environmental advantages. In this scenario, the understanding of the behaviour of dihydrogen species in water becomes mandatory.[429] A number of studies have been devoted to survey dihydrogen species in organic solvents,[117] but less is known in aqueous media.

An important issue regarding the behaviour of dihydrogen in water is its acidity. As mentioned in Section 1.3, transition metal can significantly increase the acidity of H_2, thus determining pK_a^{water} becomes relevant for its reactivity. Nonetheless, pK_a measurements in aqueous media are neither easy nor straightforward because of the levelling effect of the solvent and the solubility of the species. In those cases in which experimental data are elusive, theoretical models come to aim. The proper calculation of solvation Gibbs energies by describing the solvent in both implicit and explicit ways allows a fair estimation of acid dissociation constants.[230–232] In transition metal chemistry, some examples of pK_a computation using such hybrid cluster–continuum models have been reported in both organic solvents[430,431] and water.[432,433] Water-soluble transition metal (Fe, Ru, Os)

dihydrogen complexes appear as quite interesting species to get insight into. Both synthesis and characterisation of these species in water are difficult tasks, hence literature is scarce.

Recently, Morris proposed an empirical equation to estimate pK_a values in THF based on a large database of diamagnetic transition metal hydride and dihydrogen complexes,[434]

$$pK_a^{THF} = \sum A_L + C_{charge} + C_{nd} + C_{d6} \quad [8.1]$$

where the acidity constants of each ligand A_L are added along with corrections for the charge, C_{charge}, the periodic row, C_{nd}, and d^6 octahedral acids, C_{d6}. The resulting pK_a^{THF} of cationic acids can be converted to pK_a^{water} by using the following correlation,[128,434]

$$pK_a^{water} = 1.0 \cdot pK_a^{THF} - 0.7 \quad [8.2]$$

The goal of the present study pursues (i) the initial refinement of the computational protocol, (ii) the pK_a estimation of η^2-H_2 transition metal species in aqueous solution, and (ii) the rationalisation of the observed trends.

8.2. Computational Details

Forthcoming calculations have been carried out at the DFT level using the M06 functional[168] with an ultrafine grid[384] as implemented in Gaussian 09.[265] This functional describes dispersion interactions and performs well in transition metal chemistry.[180,181,189] The Fe, Ru, and Os heavy atoms were described by means of scalar-relativistic Stuttgart-Dresden SDD effective core potentials for the inner electrons and their associated double-ζ basis set for the outer ones,[266] complemented with a set of f-polarisation functions.[267] The 6-31G** basis set (DZ) was used for the H,[269] C, N, O, F, P, and Cl atoms.[270] Diffuse functions were added to O, F, and Cl atoms.[271] This basis set is called I. Geometries were optimized in gas phase without any symmetry restrictions and the nature of the minima has been verified with analytical frequency calculations. Gibbs energy calculations have been performed at 298.15 K and 1 atmosphere.

Single point calculations were performed on previous gas-phase geometries using 6-311++G** on H, C, N, O, F, P, and Cl atoms,[271,426] namely basis set II. Then, $\Delta G_{gp}(II)$ was obtained by adding the gas-phase entropic contribution —computed with basis set I— to $\Delta E_{gp}(II)$,

$$\Delta G_{gp}(II) = \Delta E_{gp}(II) + [\Delta G_{gp}(I) - \Delta E_{gp}(I)] \quad [8.3]$$

where suffix gp stands for gas phase.

Tetrahydrofuran (THF, ε = 7.43) and water (ε = 78.36) solvents have been described as a continuum using the SMD method.[215] Single point calculations in solvent were carried out using the basis set II and $\Delta G_{sol}(II)$ values were deduced by adding the gas-phase entropic contribution —computed with basis set I— to $\Delta E_{sol}(II)$,

$$\Delta G_{sol}(II) = \Delta E_{sol}(II) + [\Delta G_{gp}(I) - \Delta E_{gp}(I)] \quad [8.4]$$

where suffix sol means solvent, either THF or water.

As concerns the calculation of pK_a, full details about the cluster–continuum thermodynamic cycle can be consulted in Section 2.5.3. All reported pK_a values were computed at 298.15 K. The proper number of solvent molecules —THF and water— required to form the clusters is discussed as follows.

8.3. Size of Solvent Clusters

According to a hybrid cluster–continuum thermodynamic cycle, the number of solvent molecules forming the cluster, n, is that which converges the value of the solvation Gibbs energy of the proton, $\Delta G^*_{sol}(H^+)$.[226] Following the procedure depicted in Scheme 2.3 (page 39), the size of the cluster is estimated for THF and water solvents. The structures of the clusters S_n and H^+S_n —where S means solvent molecule— are first optimised in gas phase. Continuum solvation effects are then considered via [8.4] affording $\Delta G^*_{sol}(S_n)$ and $\Delta G^*_{sol}(H^+S_n)$. Finally, these two terms are used to obtain $\Delta G^*_{sol}(H^+)$ as described in [2.22] (page 39). The number of solvent molecules n that best describes $\Delta G^*_{sol}(H^+)$ will be used for subsequent pK_a calculations.

Small THF clusters are considered using up to 3 molecules. Figure 8.1a displays the structures of $(THF)_n$. In the case of $(THF)_3$, two main subclasses of conformations are found when adding a third molecule to $(THF)_2$, namely stacked and non-stacked structures. Several configurations for both subclasses have been computed but only the most stable ones are shown. The non-stacked structure is finally selected for further calculations since it is 0.5 kcal mol^{-1} more stable than the stacked one. On the other hand, Figure 8.1b shows the explicit proton solvation as $H^+(THF)_n$ clusters. In these species the proton is strongly solvated by the oxygen atoms of two THF molecules, displaying O···H distances of ca. 1.19 Å. The third THF molecule interacts quite less with the proton, showing a O···H distance of 2.651 Å; hence, no additional molecules are further considered in order to simplify the conformational space.

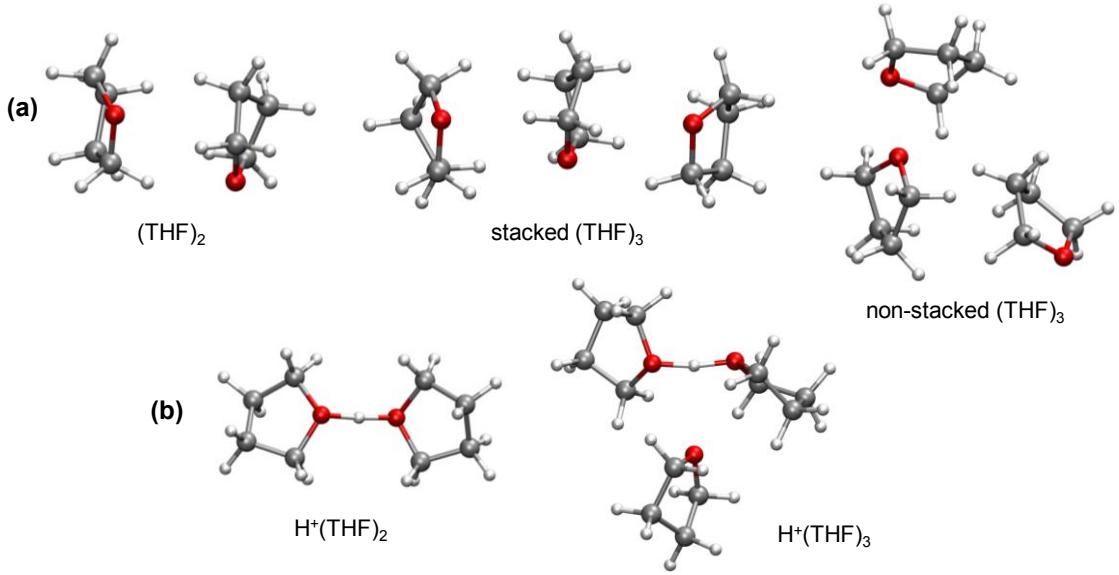

Figure 8.1 Optimised structures of (a) $(THF)_n$ and (b) $H^+(THF)_n$ clusters for n = 2, 3.

The calculated $\Delta G^*_{sol}(H^+)$ values for the clusters containing 1–3 THF molecules are collected in Table 8.1. Unfortunately, accurate data of $\Delta G^*_{sol}(H^+)$ in non-aqueous solvents are less available. An experimental value of –256.3 kcal mol^{-1} has been estimated by adding a correction term to $\Delta G^*_{sol}(H^+)$ in water.[430,435] Convergence is assumed for the system containing 3 molecules since the Gibbs energy difference with respect to that with 2 molecules is only 1.7 kcal mol^{-1}. Thus, clusters with n = 3 are used herein. The values of $\Delta G^*_{sol}(H^+(THF)_3)$ and $\Delta G^*_{sol}((THF)_3)$ are –43.9 and –9.4 kcal mol^{-1}, respectively.

Table 8.1 $\Delta G^*_{sol}(H^+)$ values in THF in kcal mol^{-1}.

$(THF)_n$	$\Delta G^*_{sol}(H^+)$
1	–242.8
2	–258.8
3	**–260.5**
Expt.[430,435]	–256.3

The same procedure as for THF is repeated for water in order to estimate the proper number of molecules. Previous work showed that, for even numbers of water molecules, the $(H_2O)_n$ clusters can be divided into two subclasses, $(H_2O)_{4m}$ and $(H_2O)_{2+4m}$ (m = 1, 2, ...), being the latter more stable.[226] For m values higher than 2, the clustering scenario becomes more difficult due to the intricate network of hydrogen bonds. Since the mapping of water cluster configurations is not the goal of this study, only model systems with 1–4 molecules and small clusters with 6 and 10 molecules are considered herein. Selected $(H_2O)_n$ clusters are illustrated in Figure 8.2a. Whereas $(H_2O)_4$ is expected to form a cyclic species, $(H_2O)_6$ generates more controversy. Previous calculations suggest that the prism and cage

conformations are preferred[436] but, according to the present level of theory, the cyclic form prevails[437] being ca. 3–5 kcal mol^{-1} more stable than the formers. The structure of $(H_2O)_{10}$ is computed as reported in literature.[437] As concerns the solvated proton structures in Figure 8.2b, $H^+(H_2O)_6$ is optimised from experimental evidence provided by IR spectroscopy,[438,439] whereas $H^+(H_2O)_{10}$ is taken from previous calculations.[226]

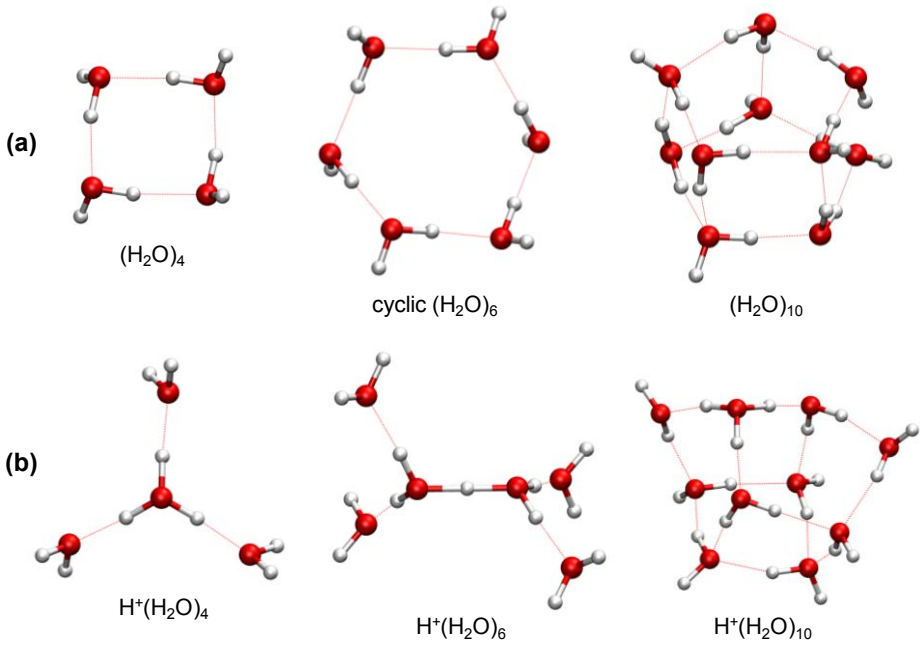

Figure 8.2 Optimised structures of (a) $(H_2O)_n$ and (b) $H^+(H_2O)_n$ clusters for n = 4, 6, 10.

The calculated $\Delta G^*_{sol}(H^+)$ values for the clusters containing 1–4, 6, and 10 water molecules are collected in Table 8.2. The solvation sphere of the proton is poorly described just considering 1 and 2 water molecules, but $\Delta G^*_{sol}(H^+)$ rapidly decreases when including up to 3 and 4 molecules. The inclusion of 6 and 10 water molecules further improves the result. The values of $\Delta G^*_{sol}(H^+)$ with 6 and 10 molecules are –264.5 and –265.7 kcal mol^{-1}, respectively. The difference results in 1.2 kcal mol^{-1}, thus convergence is assumed and the system with n = 10 is used.

Table 8.2 $\Delta G^*_{sol}(H^+)$ values in water in kcal mol^{-1}.

$(H_2O)_n$	$\Delta G^*_{sol}(H^+)$
1	–249.8
2	–255.4
3	–262.4
4	–263.5
6	–264.5
10	**–265.7**
Expt.[236,237]	–265.9

The present value of –265.7 kcal mol^{-1} agrees with that experimentally reported, –265.9 kcal mol^{-1},[236,237] and those deduced from computational studies, e.g., –266.7[226] and –266.1 kcal mol^{-1}.[229] The values of $\Delta G^*_{sol}(H^+(H_2O)_{10})$ and $\Delta G^*_{sol}((H_2O)_{10})$ are –64.3 and –23.4 kcal mol^{-1}, respectively.

8.4. Dihydrogen and Hydride Complexes

Experimentally reported water-soluble η^2-H_2 complexes under study are collected in Scheme 8.1; Fe(II)–phosphine **1**[440] and **2**,[441] Ru(II)–PTA **3** and **4**,[442,443] Ru(II)–phosphine **5**,[444] **6**, **7**,[445] and **8**,[446] Ru(II)–aquo **9**,[447] and Os(II)–amine **10**, **11**,[448,449] and **12**.[450] After optimisation in gas-phase conditions, the resulting H–H bond distances indicated in Scheme 8.1 resemble those reported in literature.[451] As reference value, the bond length of the free dihydrogen is 0.740 Å. In complexes **1**–**10**, the H–H bond distance ranges 0.83–0.90 Å which corresponds to a standard η^2-H_2 coordination mode.[118] This lengthening indicates back-donation from the metal to the anti-bonding orbital of the H_2 ligand. As expected from the stronger back-donation properties of Os, monocationic **11** and **12** behave as elongated H_2 complexes[119] with H–H bond distances of ca. 1.2–1.3 Å.

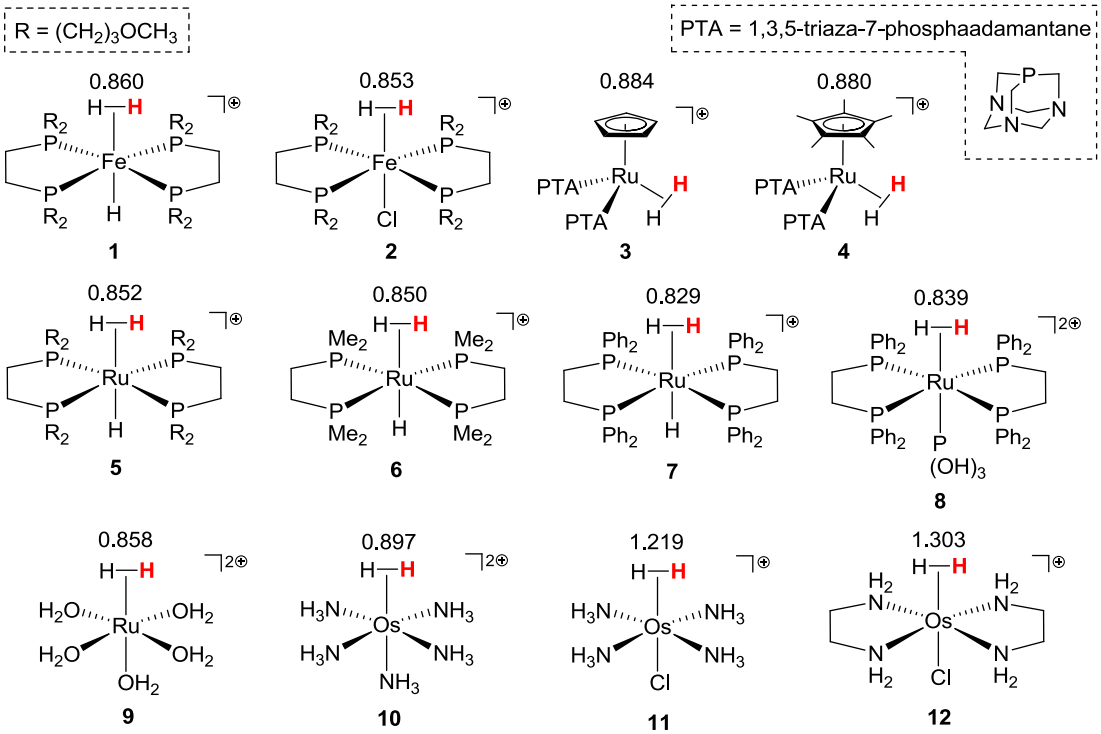

Scheme 8.1 Dihydrogen complexes **1**–**12**. Acidic hydrogens in bold red. H–H bond distances in Å.

The conjugated bases of the above-mentioned dihydrogen acids correspond to the hydrides **1'**–**12'** which are depicted in Scheme 8.2. The most important feature is that, after deprotonation of **1** and **5**–**7**, the *cis*-species **1'** and **5'**–**7'** are obtained instead of the *trans*-counterparts,[127,128] likely due to the strong *trans* influence mutually exerted by the hydrides.

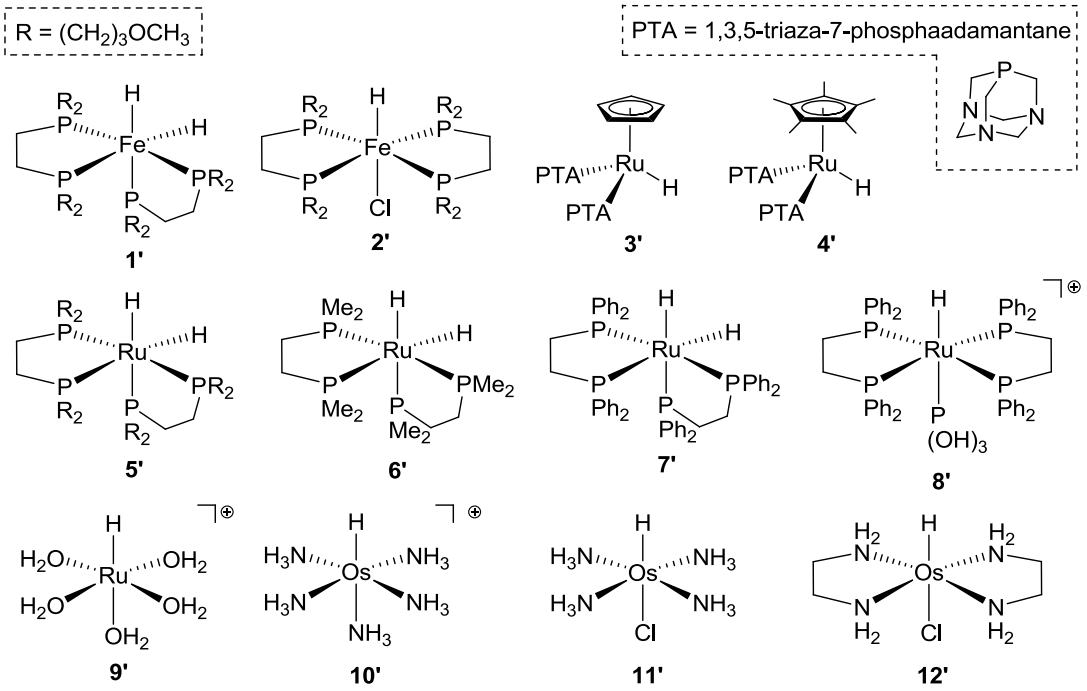

Scheme 8.2 Hydride complexes **1'**–**12'**.

8.5. Validating the Protocol in THF

The present research is actually focused on the calculation of pK_a values in water of several dihydrogen transition metal species. Although hybrid cluster–continuum approaches have been extensively and positively tested, no dihydrogen complexes have been evaluated so far. In order to check the reliability of the computational protocol, a direct comparison with experimental results is needed. In absence of data in aqueous solution, pK_a values in THF solvent are computed instead. Consulting the literature of **1**–**12**, only the pK_a^{THF} of **7** has been experimentally measured.[128] To extend the analysis, the species $[Ru(H_2)(H)(dape)_2]^+$ (Ar = *p*-methoxyphenyl) **13**, $[Fe(H_2)(H)(dppe)_2]^+$ **14**, $[Os(H_2)(H)(dppe)_2]^+$ **15**, $[CpRu(H_2)(dppm)]^+$ **16**, and $[Cp^*Ru(H_2)(dppm)]^+$ **17** are also considered (Scheme 8.3), for which the pK_a^{THF} values are experimentally reported.[128]

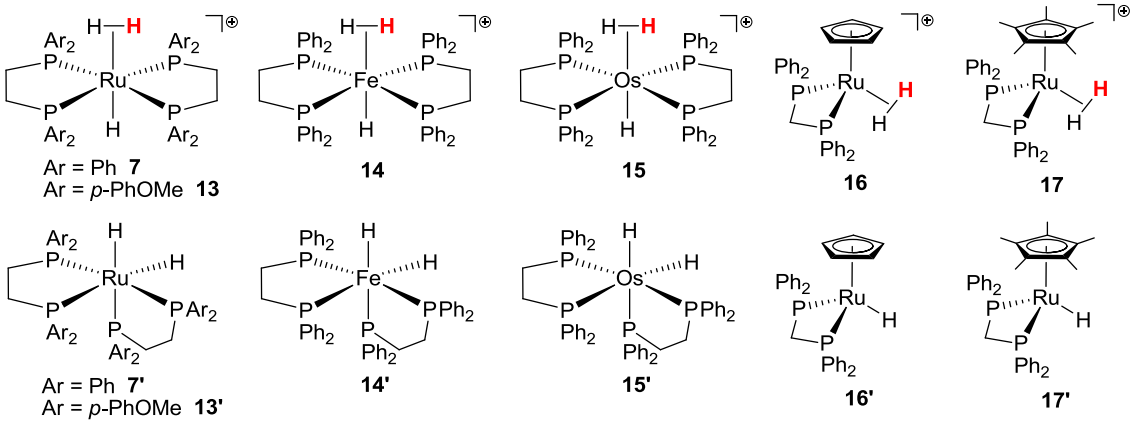

Scheme 8.3 Dihydrogen/hydride species studied in THF.

The pK_a^{THF} values of **7** and **13**–**17** are computed according to [2.20] and [2.21] and following the model reaction shown in Scheme 8.4. The results are collected in Table 8.3 where absolute differences range from 0.7 to 1.4 units. Taking 2 units as margin of error (i.e., 2.8 kcal mol^{-1} at 298 K),[230] one can conclude that the theoretical prediction is in agreement with respect to the estimated experimental values. Noteworthy, equation [8.1] predicts a pK_a^{THF} value of 12 for complex **13**, quite different from the experimental measure of 17.4.[434] Indeed, the present elaborate protocol based on DFT can captured the influence of the remote methoxy groups of the bis(phosphine) ligands providing a satisfactory value of 16.5. Although equation [8.1] is a very useful contribution that can be easily and widely employed, high level calculations must be invoked when dealing with subtle situations.

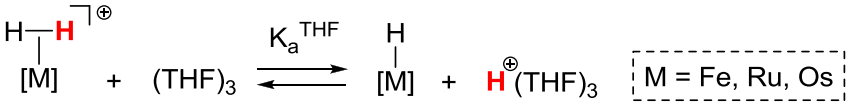

Scheme 8.4 Model deprotonation reaction of dihydrogen complexes in THF.

Table 8.3 Calculated and experimental[434] pK_a^{THF}.

Species	pK_a^{THF}(calc)	pK_a^{THF}(exp)	$\lvert\Delta pK_a^{THF}\rvert$
7	12.7	14.1	1.4
13	16.5	17.4	0.9
14	12.9	11.5	1.4
15	12.7	12.1	0.6
16	8.2	7.2	1.0
17	8.5	9.2	0.7
MAD[a]			1.0

[a] Mean absolute deviation from experiments.

8.6. Estimation of pK_a Values in Water

Once the protocol has been positively tested in THF solvent, the pK_a values of **1**–**12** are computed in aqueous medium according to [2.20] and [2.21] and following the model reaction shown in Scheme 8.5. The results are collected in Scheme 8.6 and range from 21.7 in **12** to –4.9 in **8**.

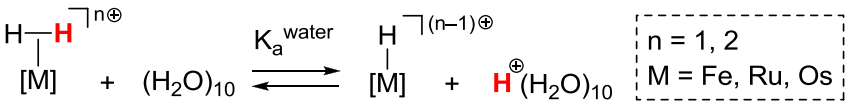

Scheme 8.5 Model deprotonation reaction of dihydrogen complexes in water.

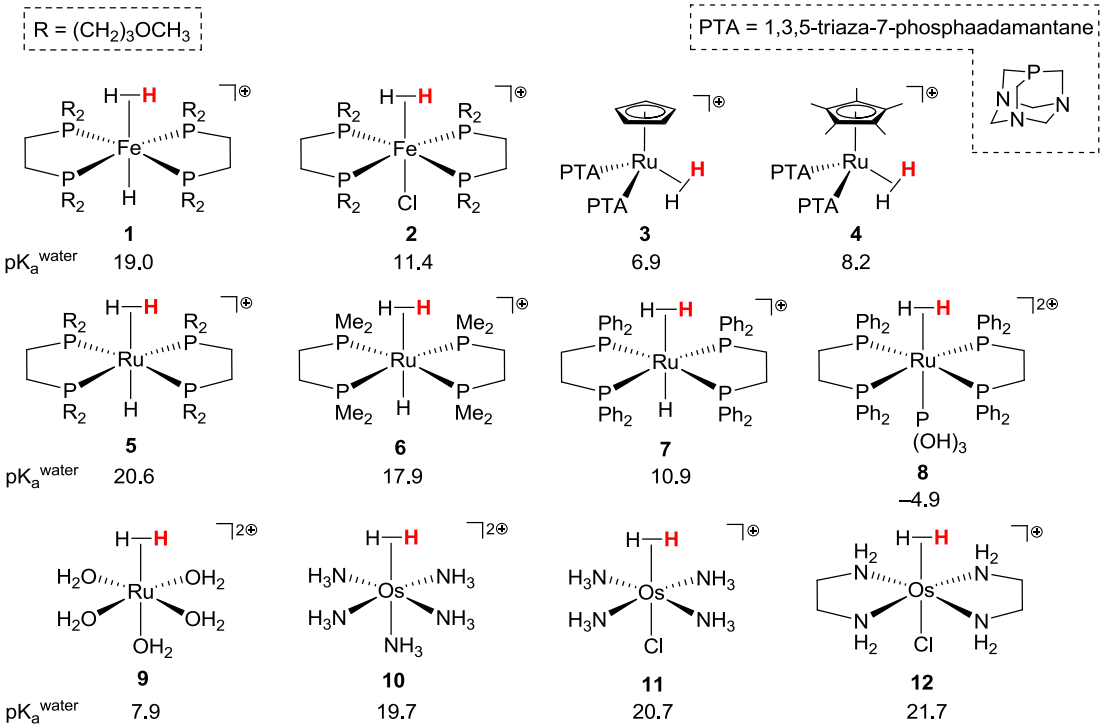

Scheme 8.6 Calculated pK_a^{water} of complexes **1**–**12**.

The expression of the pK_a [2.21] can be decomposed in two main contributions, namely $\Delta G^{o}_{g,deprot}$ and $\Delta\Delta G^{*}_{sol}$ as indicated in equation [8.5]. The term $\Delta G^{o}_{g,deprot}$ describes the thermodynamics of the deprotonation reaction in gas phase and represents the intrinsic acidity of the dihydrogen ligand in the transition metal complex. The other term $\Delta\Delta G^{*}_{sol}$ concerns the difference in ΔG^{*}_{sol} between products and reactants and accounts for the relative stability of these species due to solvation effects.

$$pK_a^{water} = \left(\Delta G^{o}_{g,deprot} + \Delta\Delta G^{*}_{sol} + constant\right)/2.303\ RT \qquad [8.5]$$

These two different contributions are shown in Figure 8.3 as blue bars for $\Delta G^{o}_{g,deprot}$ and red bars for $\Delta\Delta G^{*}_{sol}$. For monocationic **1**–**7**, **11**, and **12**, the positive values of $\Delta G^{o}_{g,deprot}$ indicate the difficulty to deprotonate the dihydrogen complexes to form the hydride counterparts. As concerns $\Delta\Delta G^{*}_{sol}$, all contributions are negative and relatively small, in the range of 2–14 kcal mol^{-1}. Due to the small effect of $\Delta\Delta G^{*}_{sol}$, one can conclude that the $\Delta G^{o}_{g,deprot}$ term mainly governs the acidity. Contrarily, dicationic species **8**–**10** behave the other way around, i.e., they present negative values of $\Delta G^{o}_{g,deprot}$ which means that the deprotonation of dicationic species is thermodynamically favoured. The solvation term $\Delta\Delta G^{*}_{sol}$ works in the opposite direction, where positive values indicate that the solvation of dicationic dihydrogen reactants becomes more relevant than that involving the monocationic hydride and $H^{+}(H_2O)_{10}$ products. However, both terms compensate and the resulting pK_a^{water} values of dicationic species are of the same order of magnitude than those of monocationic ones, apart from **8**.

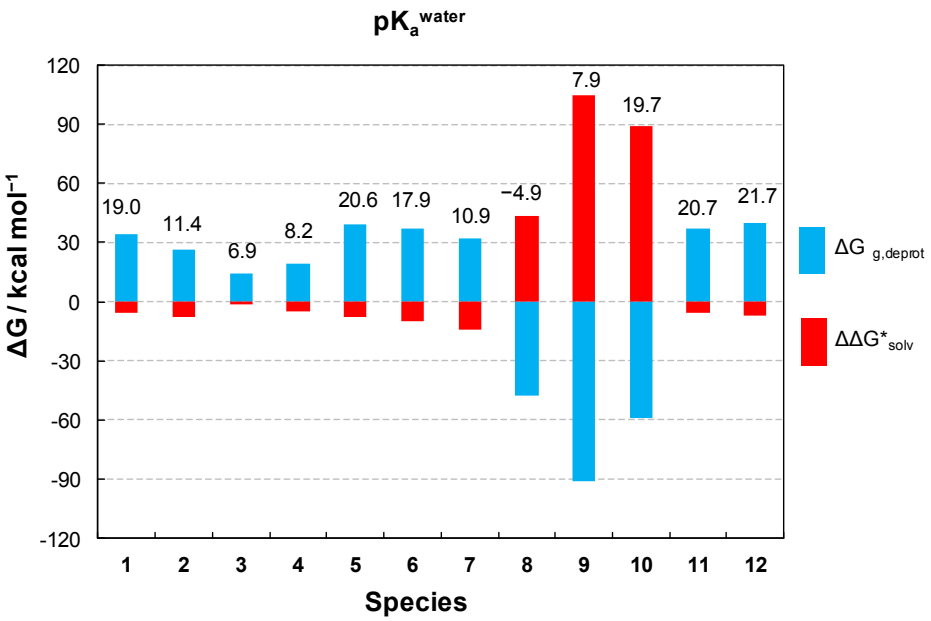

Figure 8.3 Bar chart containing pK_a^{water} values and related ΔG contributions for species **1**–**12**.

As previously mentioned, the $\Delta\Delta G^*_{sol}$ contribution is rather constant for monocationic species, thus a direct correlation can be found between pK_a^{water} and $\Delta G^o_{g,deprot}$. To stress this point, Figure 8.4 shows a plot of pK_a^{water} against $\Delta G^o_{g,deprot}$. Assuming the $\Delta\Delta G^*_{sol}$ term as a constant, the slope of the pK_a^{water} vs. $\Delta G^o_{g,deprot}$ representation should provide a slope of 0.73 (298 K) according to [8.5]. The calculated slope of the regression line in Figure 8.4 is indeed close, affording a value of 0.59. One can conclude that, for the monocationic dihydrogen species under inspection, the relative acidity can be roughly described using the gas-phase contribution $\Delta G^o_{g,deprot}$.

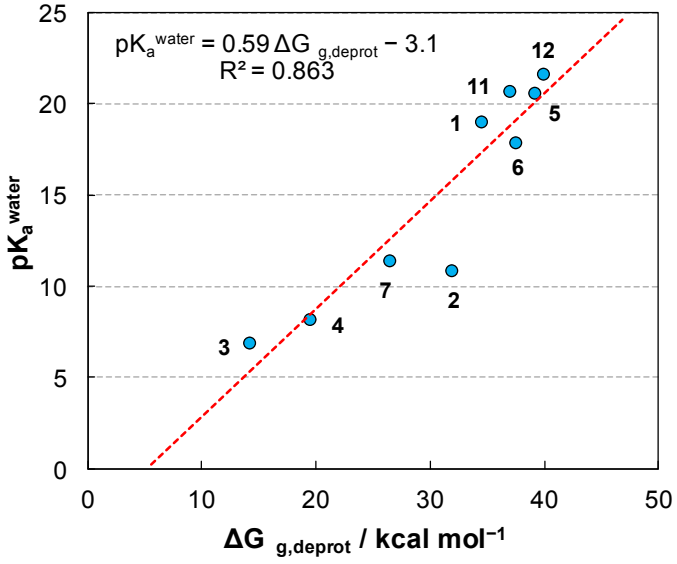

Figure 8.4. Plot of pK_a^{water} vs. $\Delta G^o_{g,deprot}$ involving monocationic species. Regression line in dashed red.

8.7. Discussion of pK_a Values in Water

This section will discuss the pK_a^{water} values reported in Scheme 8.6. As concerns the calculated structural parameters, no global correlation between pK_a^{water} and H–H bond distances in dihydrogen species **1**–**12** is found. That is, enlarged bond lengths do not systematically entail low pK_a^{water} values. Therefore, a detailed one-by-one inspection of dihydrogen complexes is carried out.

Starting with the Fe-based framework *trans*-$[Fe(H_2)(X)(P–P)_2]^+$, the pK_a^{water} of **1** (X = H) and **2** (X = Cl) are 19.0 and 11.4, respectively. The difference between **1** and **2** is 7.6 and mainly comes from the gas-phase deprotonation term ($\Delta\Delta G^o_{g,deprot}$ of 8.4 kcal mol^{-1}). Notably, **1'** adopts a *cis* rearrangement of phosphines whereas **2'** maintains the *trans* stereochemistry. Morris and co-workers reported similar results for a set of *trans*-$[Os(H_2)(X)(dppe)_2]^+$ species in dichloromethane solution. For X = H,[127] Cl, and Br ligands,[452] the corresponding pK_a values are 13.6, 7.4, and 5.4, respectively. The ΔpK_a between the Os-based complexes with H and Cl ligands is 6.2, in line with the 7.6 units previously mentioned for the Fe-derivatives **1** and **2**.

Gathering the monocationic Ru-based species **3**–**7** by ligands, some differences can be ascribed. Within the same family of ligands, more electron-donating ligands correlate to larger pK_a^{water}. For instance, the pK_a^{water} of Cp-derivative **3** is 1.3 units lower than that of Cp*-derivative **4**.[a] This trend shown by Cp and Cp* ligands has been experimentally detected for **16** and **17** (ΔpK_a^{THF} of 2.0 in Table 8.3)[434] and other related species.[453] A similar but more stressed trend is observed for the pK_a^{water} values of bis(phosphine) complexes *trans*-$[Ru(H_2)H(P–P)]^+$, being **7** (R = Ph, 10.9) quite more acidic than **6** (R = CH_3, 17.9), and **6** more acidic than **5** (R = $(CH_2)_3OCH_3$, 20.6). In these cases the steric and electronic properties are not fully separated. As computational exercise, Ru–bis(phosphine) complexes are calculated substituting methyl groups by H, CF_3, and F (Scheme 8.7), where steric contributions are rather similar among them but electronic effects are not. In this scenario, electron-withdrawing groups clearly enhance the acidity of dihydrogen complexes. In other words, the more electron-donating the ligands are, the less acidic the complex behave.[129] The chelating size of the bis(phosphine) ligands is not tackled herein, albeit it may also influence.[454,455]

[a] Calculations reported in literature[443] for species **3** and **4** —using B3LYP/PCM level of theory and a cluster of 4 water molecules— provided somehow lower pK_a^{water} values, but the difference of 1.6 units between Cp and Cp* derivatives agrees with the current result of 1.3.

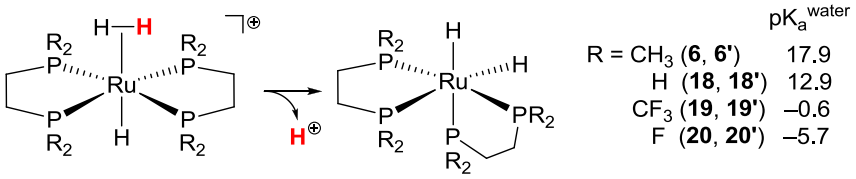

Scheme 8.7 Calculated pK_a^{water} of complexes **18**–**20** derived from **6**.

In the case of complex **7**, the pK_a has been computed in both THF and water solvents, resulting values of 12.7 and 10.9, respectively. According to [8.2], the pK_a difference between THF and water for cationic acids should be 0.7 units. The computed difference is 1.8, which stays in the range of error.

An interesting situation arises in complex **8**,[446] which exhibits superacidic properties according to the calculated pK_a^{water} of –4.9. The dicationic nature is indeed an important factor, but it is worth noting that dicationic species do not entail a strong acidic character systematically, see for instance **9** (7.9) and **10** (19.7). Others dihydrogen complexes acting as strong acids have been reported, e.g., monocationic $[Cp^*Re(H_2)(CO)(NO)]^+$ (pK_a ca. –2)[130] and dicationic $[Os(H_2)(CO)(dppp)_2]^{2+}$ (pK_a ca. –5.7)[131] and $[Os(H_2)(CH_3CN)(dppe)_2]^{2+}$ (pK_a ca. –2).[132] To further investigate this case, the pK_a^{water} values of additional species with other ligands L are calculated as shown in Scheme 8.8. Inspired by previous reports,[131,132] the $P(OH)_3$ ligand in **8** is substituted by CH_3CN **21** and CO **22**. In line with above-mentioned acids, the computed pK_a^{water} values of 1.1 for **21** and –1.6 for **22** clearly indicate superacidic behaviours. As a matter of fact, a solvent water molecule is also considered as ligand. The resulting complex **23** conserves the acidity, –1.9. One can suggest that the acidic behaviour of bis(phosphine) complexes mainly comes from their dicationic phosphine-based nature, although the kind of ligand L also influence but in less extent. Interestingly, the superacidic behaviour is absent in the dicationic complexes **9** and **10** containing O- and N-donor ligands, respectively.

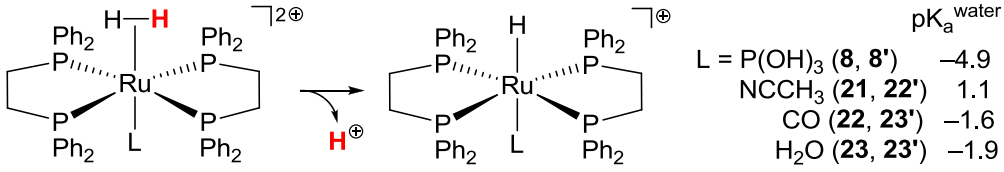

Scheme 8.8 Calculated pK_a^{water} of complexes **21**–**23** derived from **8**.

As concerns the osmium complexes **10**–**12**, the resulting pK_a^{water} values are rather similar and fewer conclusions can be made. Curiously, the dicationic species **10** exhibit a similar acidic behaviour than monocations **11** and **12**. However, **12** is slightly less acidic than **11** (1 unit) presumably due to the better electron-donor properties of primary amine ligands with respect to ammonia.

8.8. Conclusions

After optimisation and validation of the computational protocol, the pK_a^{water} values of a set of water-soluble dihydrogen transition metal —Fe, Ru, and Os— complexes have been calculated. Computational remarks are collected as follows.

- The cluster–continuum approach has been invoked to compute acid dissociation constants. Calibration calculations indicate that the inclusion of 3 and 10 solvent molecules is reliably appropriate to describe THF and water clusters, respectively.

- By direct comparison with experimental data, the protocol has provided trustworthy results in computing the pK_a^{THF} values of several dihydrogen complexes.

- Once the computational approach has been validated, it has been applied to predict the pK_a^{water} of a set of water-soluble dihydrogen complexes. No global correlation governing the pK_a^{water} has been detected. However, several trends have been found when analysing the species by series of ligands. As general rule, electron-donating ligands decrease the acidity.

9. ^{103}Rh Nuclear Magnetic Resonance Studies

This last section is dedicated to evaluate ^{103}Rh NMR chemical shifts in Rh–bis(phosphine) complexes as well as to inspect possible chemical shift correlations. Each section is presented as follows. *Introduction* collects previous theoretical studies and presents the experimental system under consideration. *Computational Details* indicates the procedure followed to calculate the geometries and chemical shifts. The results are divided into two main sections; *Geometries and ^{103}Rh Chemical Shifts* evaluates NMR parameters at different optimisation levels, and *^{103}Rh Chemical Shift–Structure Correlations* extends the study to investigate in detail the predicted chemical shift trends. Finally, *Conclusions* gathers the key findings that computation has provided.

These computational results have been published as shown in Annex A.[456]

9.1. Introduction

Rhodium plays an important role in a number of transition metal-catalysed processes. To further investigate its chemistry, ^{103}Rh NMR spectroscopy appears as a valuable tool.[142,143] Particularly, Rh–phosphine complexes are appropriate to be studied by this technique as found in literature.[142,143,457,458]

Generally speaking, chemical shifts are quite sensitive to the chemical environment, which can be easily tuned in coordination chemistry by varying the steric and electronic properties of the ligands. In this sense, computational approaches allow to thoroughly analyse the structure and properties of organometallic compounds in a systematic way. As concerns the computation of NMR chemical shifts,[136] early calculations dealt with a set of Rh compounds suitable to cover a chemical shift range of ca. 3600 ppm (Scheme 9.1).[245,459] The next step focused on complexes containing phosphine,[460,461] N-donor,[462] and alkene[463] ligands, including indacenyl[464] and porphyrin[465] derivatives.

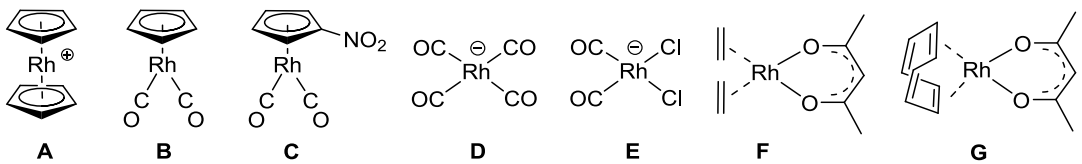

Scheme 9.1 Rh complexes **A**–**G** previously studied.

Within the fruitful rhodium chemistry, Rh–bis(phosphine) complexes performed excellent in several hydrogenation reactions;[466] for instance, cationic $[(COD)Rh(P–P)]^+$ complexes (COD = 1,5-cyclooctadiene, P–P = chelating bis(phosphine)) have provided good results in hydrogenation of enamines.[467] Fabrello et al. reported the ^{103}Rh NMR chemical

shifts of **1**–**7** (Scheme 9.2), and some of them were correlated to calculated relative stabilities[468] where stronger donor phosphine ligands entailed more shielded nuclei.

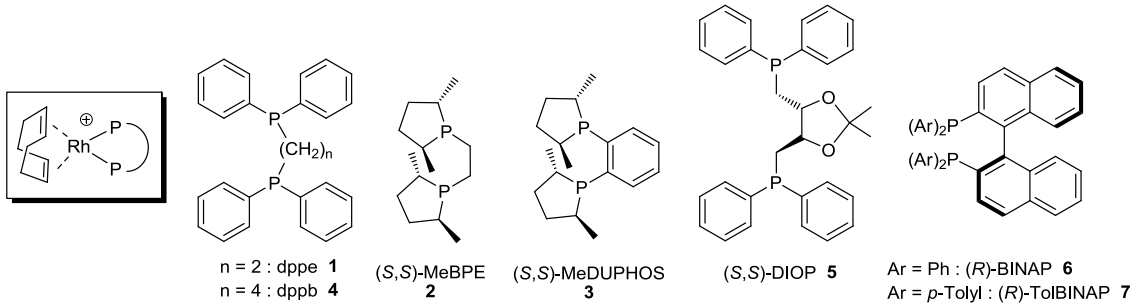

Scheme 9.2 Cationic Rh–bis(phosphine) species **1**–**7**.

This study initially focuses on species **1**–**7** to calculate ^{103}Rh chemical shifts in direct comparison with experimental data. Additional complexes are then considered (i) to systematically investigate the influence of steric and electronic properties of bis(phosphine) ligands and (ii) to unravel chemical shift correlations.

9.2. Computational Details

Forthcoming geometry optimisations have been performed at the DFT level using M06[168] —with an ultrafine grid[384]— and PBE0[162,170,171] functionals as implemented in Gaussian 09.[265] M06 accounts for dispersion interactions[180,181,189] and PBE0 properly describes the geometries of second-row transition metal complexes.[192] The Rh heavy atom was described using a scalar-relativistic Stuttgart-Dresden SDD effective core potential for the inner electrons and its associated double-ζ basis set for the outer ones,[266] complemented with a set of f-polarisation functions.[267] The 6-31G** basis set was used on H,[269] C, N, O, F, P, and Cl atoms.[270] Diffuse functions were added to O, F, and Cl atoms.[271] In selected cases, the chloroform solvent has been described as a continuum (ε = 4.71) using the SMD method.[215] Unless otherwise stated, the structures of complexes were fully optimised without any symmetry restrictions and the nature of the minima was verified with analytical frequency calculations. Enthalpies have been computed with the PBE0 functional at 298.15 K within the harmonic approximation.

Upon optimising at either M06 or PBE0 level, magnetic shielding tensors have been computed with the GIAO (gauge-including atomic orbitals) method[243] by means of the B3LYP functional[161,166,167] in gas phase as implemented in Gaussian 09.[265] The basis set consisted of a well-tempered [16s10p9d] all-electron basis on Rh,[469] IGLO-basis DZ on H, and IGLO-basis II on the rest of the atoms[246] —denoted basis II'. Because functional and basis set requirements are different for computing structural and spectroscopic parameters,

such a mixed single-point approach is common. This particular combination of levels has performed well in previous studies.[245,460–463]

To obtain the chemical shifts δ from the magnetic shieldings σ, a reference value is required. Due to the lack of a suitable compound for the ^{103}Rh nucleus, σ(standard) has been calculated as the intercepts at δ = 0 of the σ(calc) vs. δ(exp) linear regressions involving complexes **1**–**7** under study (Scheme 9.2) together with species **A**–**G** (Scheme 9.1) that cover a wide range of the ^{103}Rh chemical shift window.[245] The resulting σ(standard) values are –900 and –685 ppm for M06 and PBE0 geometries in the gas phase, respectively (Figure 9.1). These values have been used along the entire computational study. Finally, the theoretical chemical shifts have been computed according to [2.23] in Section 2.5.4.

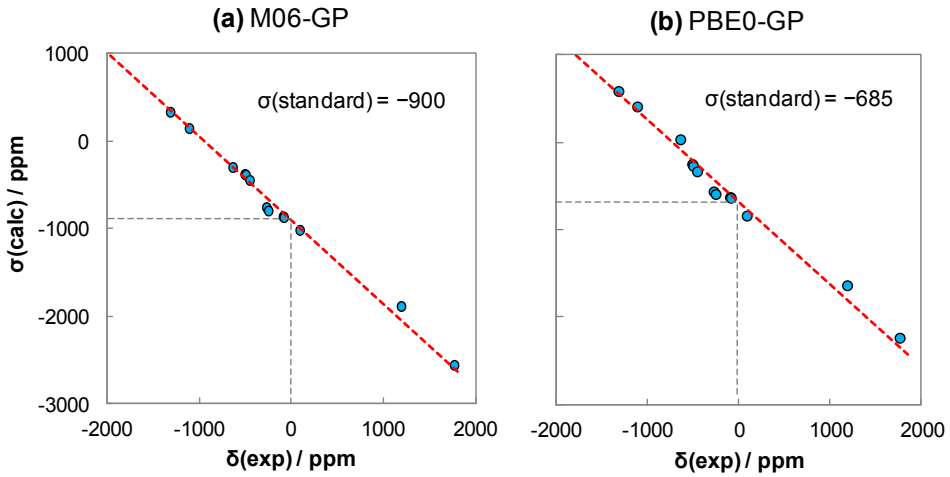

Figure 9.1 Plots of σ(^{103}Rh,calc) vs. δ(exp) according to (a) M06 and (b) PBE0 geometries of **A**–**G** and **1**–**7** in gas phase (GP). Regression lines in dashed red.

9.3. Geometries and ^{103}Rh Chemical Shifts

The cationic Rh–bis(phosphine) complexes **1**–**7** (Scheme 9.2)[468] were fully optimised in gas phase using the M06 and PBE0 functionals. The computed geometries fairly agree with the X-ray structures found for **1**,[470] **2**,[471] **3**,[470] **4**,[472] **5**,[468] and **6**.[473] These and related computational methods tend to overestimate the Rh–L (L = ligand) bond distances as previously found.[192] For instance, the Rh–P bond lengths are enlarged with respect to those in the solid-state structures by up to 0.080 and 0.065 Å for M06 and PBE0, respectively. Comparing methods, M06 distances are generally larger than PBE0 ones by up to 0.015 Å.

Magnetic shielding values are computed on the aforementioned structures of **1**–**7** (Scheme 9.2) and the resulting chemical shifts are shown in Table 9.1.

Table 9.1 Computed ^{103}Rh chemical shifts using M06 and PBE0 geometries of **1**–**7**.

Species	δ(calc)		δ(exp)
	M06	PBE0	
1	–526	–431	–513
2	–518	–410	–503
3	–458	–347	–460
4	–147	–117	–278
5	–108	–88	–257
6	–42	–53	–98
7	–33	–45	–90
Slope[a]	1.22	0.92	
MAD[b]	60	101	

[a] Slope of the δ(calc) vs. δ(exp) linear regression for species **1**–**7**.
[b] Mean absolute deviation from experiments.

To better appreciate the relationship between calculated and experimental data, plots of δ(calc) vs. δ(exp) are displayed in Figure 9.2. The slopes of the linear regressions indicate how well theory fits experiments, where unity means ideal correlation. M06 geometries give a slope of 1.22 which produces an overestimation of chemical shifts. On the other hand, PBE0 geometries afford a slope of 0.92 which is closer to the experimental trend. The mean absolute deviation (MAD) claims otherwise; the value for M06 geometries is lower than for PBE0 ones (Table 9.1). The lower MAD for M06 geometries comes from a good description of shielded species **1**–**3**, whereas the values for all PBE0 geometries are systematically biased. The MAD for the latter can be reduced (i) by using the shielding of one of the compounds **1**–**7** as σ(standard) —i.e., internal reference method— or (ii) by computing the σ(standard) from the σ(calc) vs. δ(exp) linear regression for species **1**–**7** only —i.e., excluding **A**–**G**. Neither procedure is however applied in order to preserve the general scope of the protocol.

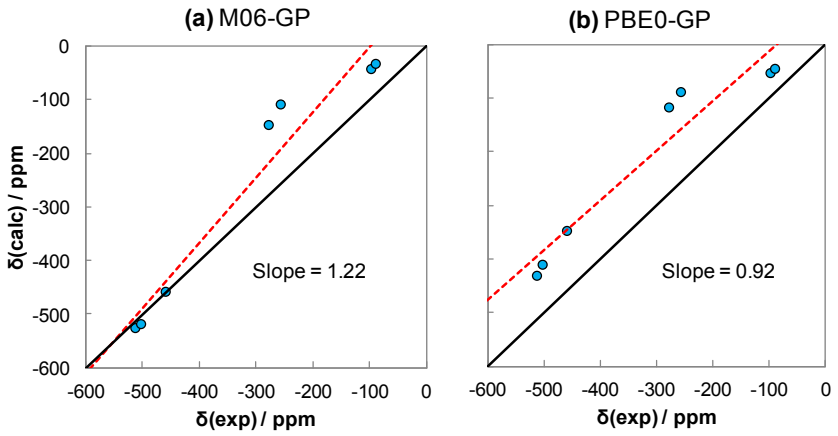

Figure 9.2 Plots of δ(^{103}Rh,calc) vs. δ(exp) according to (a) M06 and (b) PBE0 geometries of **1**–**7** in gas phase (GP). Regression lines in dashed red and ideal lines in solid black.

The different outcome between functionals may arise from the differences in Rh–ligand bond lengths, which importance has been already noted.[460,462] As computational exercise, **1**–**7** are optimised at M06 level but fixing all Rh–C and Rh–P bond distances to the PBE0 values. The energy differences between the fully optimised and distorted structures are lower than 0.5 kcal mol^{-1}. Figure 9.3 shows the magnetic shieldings computed on the constrained structures. The results for the new set of M06 geometries mostly resemble those for PBE0 ones. It can be deduced that the functional dependence of chemical shifts mainly arises from the proper optimisation of Rh–L bond distances.

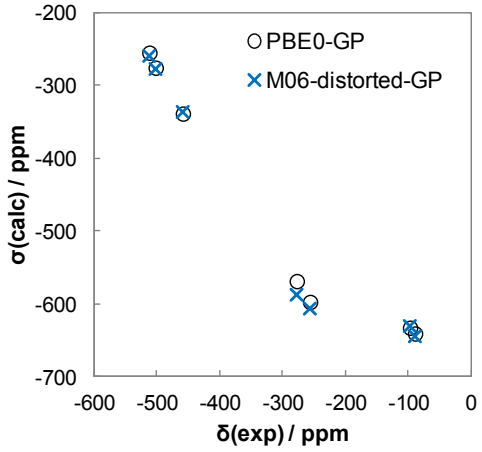

Figure 9.3 Plots of σ(^{103}Rh,calc) vs. δ(exp) according to PBE0 (open circles) and M06-distorted (blue crosses) geometries of **1**–**7** in gas phase (GP).

To underline and evaluate the influence of geometrical parameters, ^{103}Rh chemical shifts are computed on distorted structures of **1** at PBE0 level (Figure 9.4). From the fully optimised geometry, the Rh–P bond distances are settled at different values around the equilibrium distance (2.313 Å), keeping the P–Rh–P bite angle β fixed but optimising all other parameters. Likewise, the bite angle β is changed around the equilibrium value (83.3°), keeping the Rh–P bond distances fixed but optimising all other parameters. This procedure allows the distinction between geometrical contributions. As concerns the bond lengths, the plot of δ(calc) vs. d(Rh–P) fits a line with a slope of 3184 ppm Å^{-1} (Figure 9.4a). This result clearly indicates the dramatic influence of Rh–P bond distances on ^{103}Rh chemical shifts. The large value is in line with previous data reported on complexes involving rhodium[460,462] as well as other transition metals.[474] The effect of the bite angle is however less noticeable (Figure 9.4b). Although the plot of δ(calc) vs. β is polynomial rather than linear, the ratio Δδ/Δβ estimates a value of 12 ppm deg^{-1} —maximum of 20 ppm deg^{-1} at 89°.

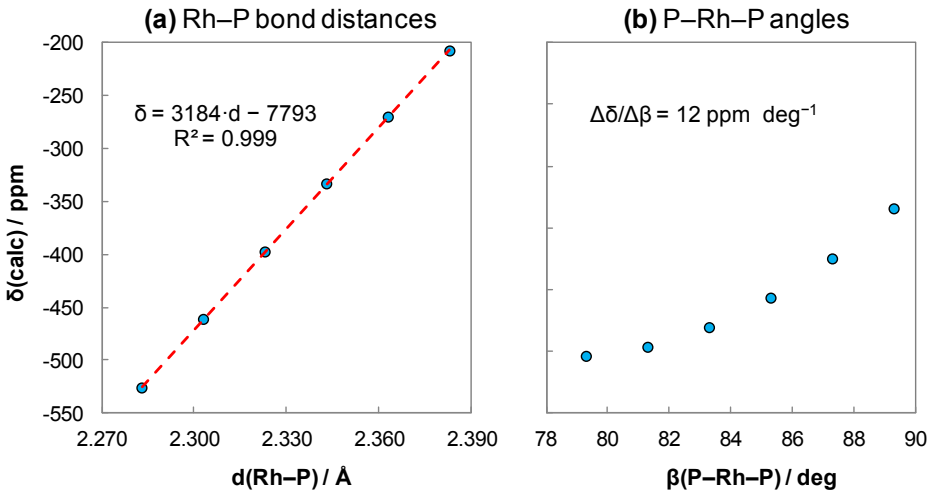

Figure 9.4 Variation of δ(¹⁰³Rh,calc) according to (a) Rh–P bond lengths and (b) P–Rh–P angle for PBE0-distorted geometries of **1** in gas phase (GP). Regression lines in dashed red.

So far all geometries have been computed in the gas phase. To explore the putative influence of the environment in solution, **1**–**7** are reoptimised using a continuum method to describe chloroform —the solvent used in the experiments.[468] The solvent-optimised species are denoted with the suffix **s**. The Rh–P bond distances of **1s**–**7s** hardly change, showing differences with respect to **1**–**7** of up to 0.007 Å. The chemical shifts are then computed in the gas phase as usual. The resulting slopes of the δ(calc) vs. δ(exp) linear regressions are 1.20 and 0.93 for M06 and PBE0 geometries, respectively. Since these values mimic the ones obtained for gas-phase geometries (1.22 and 0.92 in Table 9.1 and Figure 9.2), the influence of chloroform is not decisive in this situation.

One last point to consider concerns the impact of the counteranion. According to experiments, ¹⁰³Rh chemical shifts do not significantly change when either $[PF_6]^-$, $[BF_4]^-$, or tosylate is present.[468] However, pulsed gradient spin–echo (PGSE) diffusion studies[475] involving a cation similar to **6** suggest ion pairing in solution, despite the fact that chemical shifts are hardly altered.[476] Therefore, the mere presence of a counteranion should be evaluated. Accordingly, **1**–**7** are reoptimised in chloroform in presence of explicit $[PF_6]^-$ as counteranion. The solvent-optimised species including $[PF_6]^-$ are denoted with the suffixes **sc**. The counteranion is initially located at the apical position of the square-planar complex to favour putative interactions with the metal. PBE0 geometries of **1sc**–**7sc** exhibit large Rh···F distances, being the shortest value above 4 Å, thus no strong contacts are considered. Contrarily, M06 geometries of **1sc**–**7sc** set closer Rh···F distances of ca. 3.5 Å, hence the ion pairing seems to be driven by electrostatic as well as dispersion interactions. Figure 9.5 illustrates the position of $[PF_6]^-$ with respect to Rh for the PBE0 and M06 geometries of **5sc**.

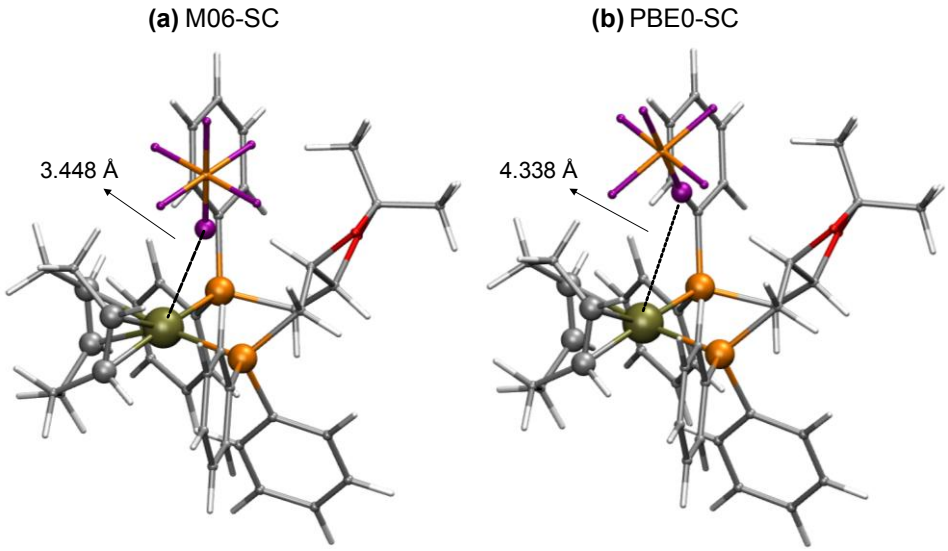

Figure 9.5 (a) M06 and (b) PBE0 geometries of **5sc** including solvent as a continuum and counteranion (SC).

Magnetic shielding values are computed on the structures of **1sc**–**7sc** and the resulting chemical shifts are shown in Table 9.2.

Table 9.2 Computed ^{103}Rh chemical shifts using M06 and PBE0 geometries of **1sc**–**7sc**.

Species	δ(calc)		δ(exp)
	M06	PBE0	
1sc	–399	–387	–513
2sc	–444	–389	–503
3sc	–399	–341	–460
4sc	–107	–94	–278
5sc	–85	–96	–257
6sc	–32	–51	–98
7sc	–36	–40	–90
Slope[a]	1.00	0.92	
MAD[b]	100	115	

[a] Slope of the δ(calc) vs. δ(exp) linear regression for species **1sc**–**7sc**.
[b] Mean absolute deviation from experiments.

In comparison with gas-phase geometries (Table 9.1), these results indicate that the values for the shielded species **1sc–3sc** are more affected than those for the deshielded ones. Consequently, the slopes of the δ(calc) vs. δ(exp) linear regressions decrease from 1.22 and 0.92 (dashed red lines in Figure 9.2) to 1.00 and 0.86 (dashed red lines in Figure 9.6) for M06 and PBE0 geometries, respectively. The corresponding MAD values are similar, 100 and 115 ppm. These new slopes can be due to (i) the explicit occurrence of the counteranion and (ii) the distortion of geometries after reoptimisation. To separate both contributions, the $[PF_6]^-$ counteranion is removed from calculations; subsequently, the chemical shifts are computed

for the resulting anion-free distorted structures —i.e., without further optimisation— denoted as **1s'**–**7s'**. The slopes of the δ(calc) vs. δ(exp) linear regressions are 1.08 and 0.89 for M06 and PBE0 geometries, respectively (dashed grey line in Figure 9.6). The slopes resulting from PBE0 geometries are rather similar (0.86 vs. 0.89), thus the distortion of the structure mainly governs the change. In the case of M06 geometries, the difference is more noticeable (1.00 vs. 1.08), hence the explicit presence of the counteranion also contributes.

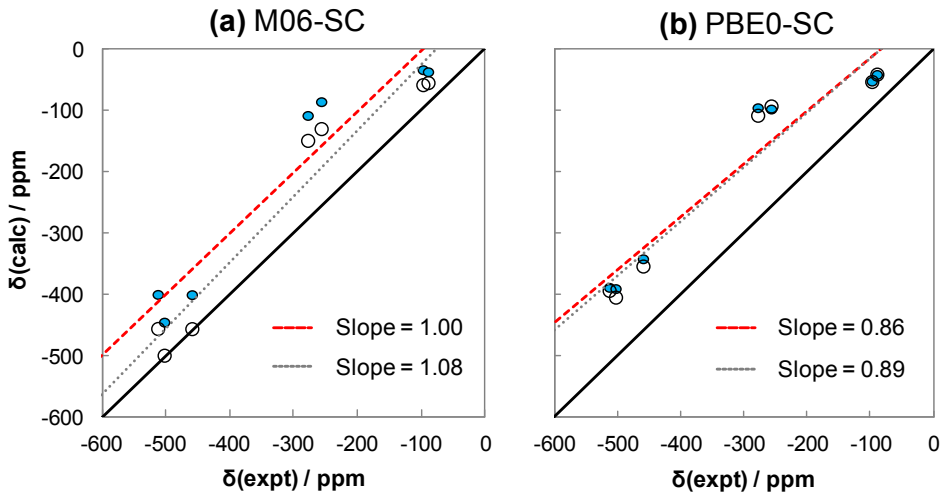

Figure 9.6 Plots of δ(^{103}Rh,calc) vs. δ(exp) according to distorted **1s'–7s'** (open circles) and fully-optimised **1sc–7sc** (blue circles) at (a) M06 and (b) PBE0 level including solvent and counteranion (SC). Regression lines in dashed grey and red and ideal lines in solid black.

Putting all together, gas-phase geometries at PBE0 level provide fairly accurate chemical shift trends (slope of 0.92 in Figure 9.2b). In this scenario, the Rh–P bond distances play an important role. The inclusion of the explicit counteranion improves the general trend but only when dispersion interactions are taken into account, e.g., using the M06 functional (slope of 1.00 in Figure 9.6a).

9.4. ^{103}Rh Chemical Shift–Structure Correlations

According to the previous section, the computation of B3LYP chemical shifts on PBE0 geometries in gas phase affords reliable results. This computational protocol is employed as follows to disclose the dependence of the chemical shift with respect to the chemical environment. To accomplish it, a new set of cationic complexes **8**–**20** is derived from **1** by systematically modifying the bis(phosphine) ligands through the chelating size, n, and the groups attached to the phosphorous atoms, R (Scheme 9.3). Conformations of five- (n = 2) and seven-membered (n = 4) rings are taken from the previous gas-phase structures of **1** and **4**, respectively. For the case of six-membered rings (n = 3), a chair-like conformation is used according to a reported solid-state structure of **17**.[477]

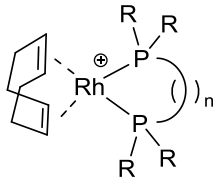

R = H n = 2 (**8**), 3 (**9**), 4 (**10**)
CH_3 n = 2 (**11**), 3 (**12**), 4 (**13**)
CF_3 n = 2 (**14**), 3 (**15**), 4 (**16**)
Ph n = 2 (**1**), 3 (**17**), 4 (**4**)
Cy n = 2 (**18**), 3 (**19**), 4 (**20**)

Scheme 9.3 Set of complexes **8**–**20** generated from **1**.

One interesting property that may correlate to ^{103}Rh chemical shifts is the relative thermodynamic stability of the complexes with regards to their binding energies. The donor properties of the bis(phosphine) ligands are evaluated through isodesmic[a] ligand exchange reactions[463,468] as shown in Scheme 9.4. The free ligands are optimised in conformations free of clashes between PR_2 groups. Magnetic shieldings are mainly affected by the atoms directly attached to the nucleus of interest. As a result, the shielding of the ^{103}Rh nucleus is unlikely influenced by entropy terms, and correlation between chemical shifts and Gibbs energies may be absent. Ligand exchange enthalpy values, ΔH_{LE}, are discussed instead since thermodynamic contributions regarding the Rh–P bond formation are inherently considered. All enthalpies are arbitrarily referred to **11**, in which more negative ΔH_{LE} values indicate higher affinity of the ligands towards the rhodium centre.

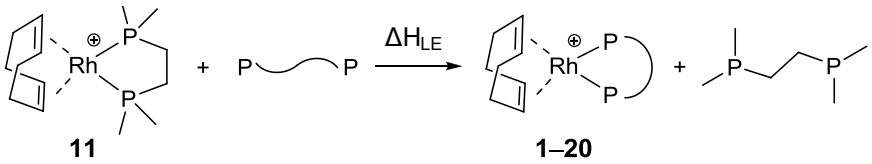

11 **1–20**

Scheme 9.4 Isodesmic ligand exchange reactions. **11** as reference compound.

Plots of δ(calc) vs. ΔH_{LE} are displayed in Figure 9.7. As concerns the initial set of complexes **1**–**7** in Figure 9.7a, more negative ΔH_{LE} values correlate with more deshielded species **1**–**3**, where higher ΔH_{LE} values correspond with more shielded species **4**–**7**. This trend is in line with the reported Gibbs energy correlation for some of these complexes.[468] However, according to the results obtained for the extended set of complexes **1**, **4**, and **8**–**20** in Figure 9.7b, a global trend cannot be settled to all kind of ligands. For complexes containing the same group R, the increment of the chelating size n entails an increment of both the chemical shift and ΔH_{LE}, excluding R = H for the latter. Regarding the electronic properties of the ligands, complexes with R = CF_3 (electron-poor ligands) show high positive ΔH_{LE} values, followed by those with R = H. Species with R = CH_3, Ph, and Cy (electron-rich ligands) produce similar ΔH_{LE} values within the same chelating size n. The trend in ΔH_{LE} as a function of the electronic properties of the ligands shows no clear dependence with ^{103}Rh

[a] In isodesmic reactions, the chemical bonds broken in reactants are of the same type as those formed in products, Rh–P bonds in this case.

chemical shifts. The lack of a global chemical shift–stability correlation was also found for Rh–bis(olefin) complexes.[463]

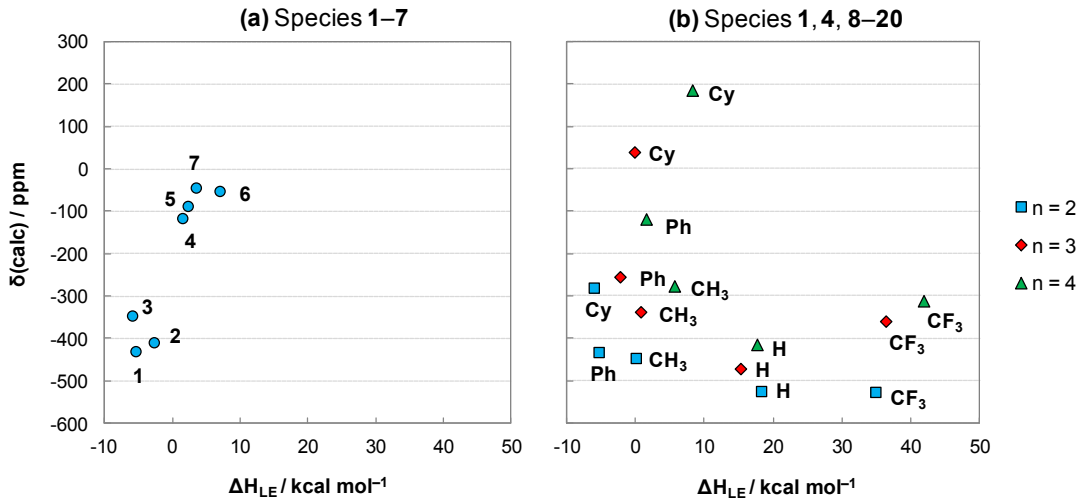

Figure 9.7 Plots of δ(¹⁰³Rh,calc) vs. ΔH_{LE} according to species (a) **1**–**7** and (b) **1**, **4**, **8**–**20**.

The previous section pointed out the Rh–P bond distance as a key parameter to investigate ¹⁰³Rh chemical shifts. In this spirit, δ(calc) is plotted against the average Rh–P bond distance in Figure 9.8. For the initial complexes **1**–**7** in Figure 9.8a, a linear regression is obtained with a slope of 5682 ppm Å^{-1} (R^2 = 0.952). More interestingly, for complexes **1**, **4**, and **8**–**20** in Figure 9.8b an analogous linear regression is found with a slope of 5285 ppm Å^{-1} (R^2 = 0.940). Analysing the chelating size separately, the slopes of complexes with n = 2, 3, and 4 are 3583 ppm Å^{-1} (R^2 = 0.867), 5862 ppm Å^{-1} (R^2 = 0.933), and 5513 ppm Å^{-1} (R^2 = 0.988), respectively. Putting all complexes together, i.e. **1**–**20**, the slope becomes 5338 ppm Å^{-1} (R^2 = 0.943). Although some deviations are detected for complexes with five-membered rings —which involve lower slopes, see also Figure 9.4—, the global trend is clear.

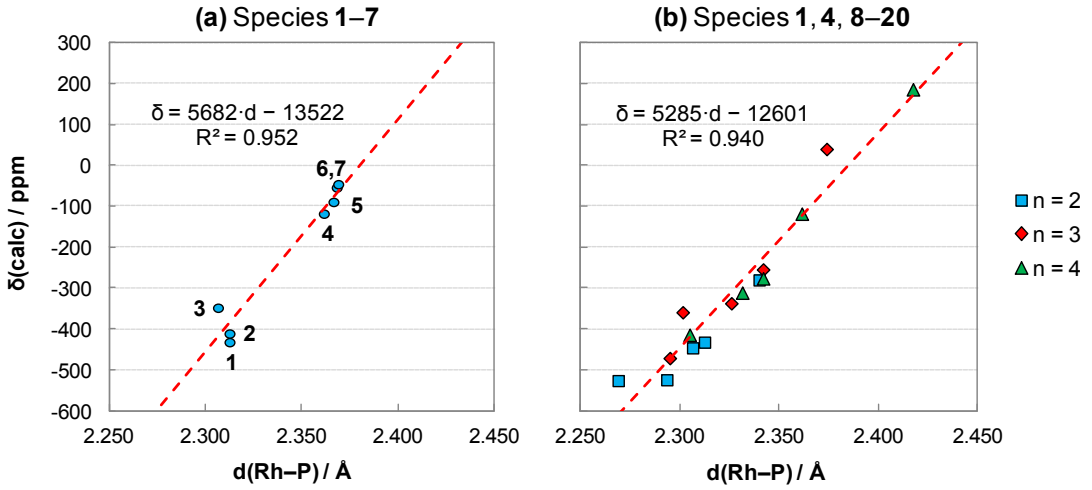

Figure 9.8 Plots of δ(¹⁰³Rh,calc) vs. d(Rh–P) according to species (a) **1**–**7** and (b) **1**, **4**, **8**–**20**.

As a conclusion, ^{103}Rh chemical shifts appear as sensitive probes to investigate Rh–P bond distances. They may be useful to describe chemical shift–structure correlations for bis(phosphine) ligands with different chelating sizes and electronic properties. Lastly, since shorter bond distances to transition metals do not always entails stronger bonding situations —*longer but stronger*[478,479]—, chemical shift–stability correlations may be missing as previously noticed.

To evaluate the sensitivity of this correlation, the study is extended to include more subtle modifications of the ligands. Following the substituting pattern of **6** and **7**, the substituents in *para* position of the aryl moieties are changed by different groups affording **21**–**24** (Scheme 9.5 left). Likewise, the application of this substituting pattern to **1**, **17**, and **4**, generates **25**–**29**, **30**–**34**, and **35**–**39** for n = 2, 3, and 4, respectively (Scheme 9.5 right). These groups can be described by Hammett σ_p constants, which usually refer to inductive effects. More positive (negative) values of σ_p indicate more electron-withdrawing (donating) character.[480,481]

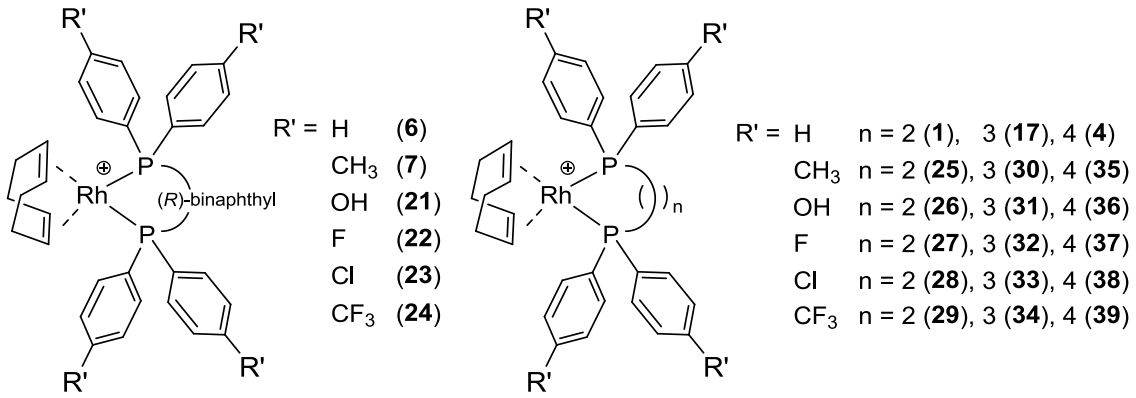

Scheme 9.5 Set of complexes **21**–**39** generated from **6**, **1**, **17**, and **4**.

Plot of δ(calc) vs. σ_p[482] involving species **6**, **7**, and **21**–**24** is shown in Figure 9.9a. A linear regression is indeed found (R^2 = 0.959) in agreement with literature.[457,460] As general trend, remote electron-withdrawing groups tend to shield nuclei. Then, δ(calc) is plotted against the average Rh–P bond distance in Figure 9.9b. Interestingly, the ^{103}Rh chemical shifts still correlate to Rh–P bond lengths at the picometer scale (R^2 = 0.941). Even more subtle structural variations between isotopomers can be disclosed using ^{103}Rh NMR, where Rh–L bond distances change within the femtometer scale.[483]

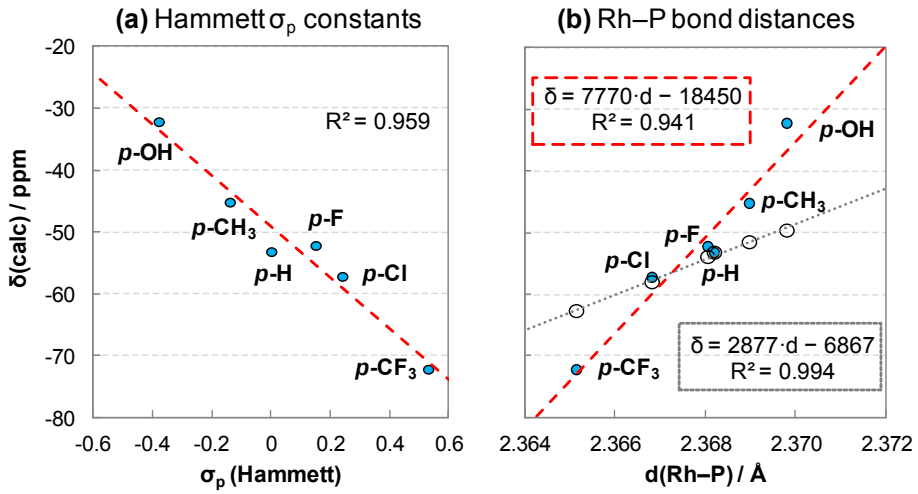

Figure 9.9 Plots of δ(¹⁰³Rh,calc) vs. (a) Hammett sp constants and (b) d(Rh–P) according to species **6**, **7**, **21**–**24** (blue circles) and distorted versions of **6** (open circles).

The slope of the δ(calc) vs. d(Rh–P) linear regression is 7770 ppm Å^{-1}, slightly larger than that of ca. 5300 ppm Å^{-1} obtained for species **1**–**20** (Figure 9.8). The influence of such remote substitutents can be due to (i) variation of Rh–P bond distances or (ii) direct electronic effects. The latter can be treated separately by changing the groups R' by H atoms. Subsequent reoptimisation keeping the Rh–P bond lengths fixed affords a set of distorted structures of **6** and the resulting chemical shifts are indicated as open circles in Figure 9.9b. The slope of the δ(calc) vs. d(Rh–P) linear regression is 2877 ppm Å^{-1} (R^2 = 0.994), in line with the value of ca. 3200 ppm Å^{-1} obtained for the distorted versions of **1** (Figure 9.4a). Despite steric and electronic effects are not fully isolated this way, the influence via bond distances is significant. This outcome indicates that ¹⁰³Rh chemical shifts correlate not only to direct electronic features of R', but also to indirect effects that remotely modify the Rh–P bond lengths.[a]

The same analyses are performed for **25**–**29**, **30**–**34**, and **31**–**35** derived from **1**, **17**, and **4**, respectively (Scheme 9.5). Plots of δ(calc) vs. σ_p produce excellent linear regressions (R^2 = 0.9 or superior).[456] As concerns the variation of δ(calc) with respect to Rh–P bond distances, the linear regressions range from moderate, R^2 = 0.780 for derivatives of **1**, to good, R^2 = 0.831 and 0.910 for derivatives of **17** and **4**, respectively. To achieve a fully global correlation, additional features such as the chelating size of the bis(phosphine) ligands should be taken into consideration somehow. Further studies may consider the role of spectator ligands, COD in this work.

[a] Although the correlations in Figure 9.8 may contain such direct electronic effect, a significant change of the slope is not expected among the substituents under consideration —excluding CF_3—; the Rh–P bond distance is indeed a decisive parameter.

9.5. Conclusions

^{103}Rh chemical shifts of several [(COD)Rh(P–P)]$^{+}$ species have been computed. The range of complexes under consideration has been systematically extended to explore potential chemical shift trends. Computational insight is commented as follows.

- Computation of δ(^{103}Rh) on gas-phase geometries at PBE0 level provide results in fairly agreement with experimental evidence, making the procedure suitable for routine calculations. When the counteranion is explicitly included, dispersion interactions should be taken into account during optimisation.

- According to ligand exchange enthalpies, ΔH_{LE}, δ(^{103}Rh) are not clearly related to complex stabilities for the set of complexes under consideration.

- δ(^{103}Rh) do correlate to Rh–P bond distances for a variety of bis(phosphine) ligands, where shorter bond lengths mean more shielding ^{103}Rh nuclei.

- This chemical shift–structure dependence is also found when more subtle modifications of the electronic properties of the ligands —characterised through Hammett σ_p constants— are brought into play.

VI

Conclusions

"Oh Deep Thought Computer", he said, *"the task we have designed you to perform is this. We want you to tell us... the Answer! The Answer to Life, the Universe, and Everything."*

[...]

"Forty-two", said Deep Thought, with infinite majesty and calm.
"Is that all you've got to show for seven and a half million years' work?"
"I checked it very thoroughly and that quite definitely is the answer. I think the problem, to be quite honest with you, is that you've never actually known what the question is."

"Hitchhiker's Guide to the Galaxy" by Douglas Adams

The current dissertation has demonstrated how computational chemistry can successfully be applied to a number of organometallic situations. Because of this, predictive features are becoming more important and reliable. The specific conclusions of each study have been recited in the corresponding section. Herein, a general overview of concluding remarks is presented.

Structure

Relevant information about the structure and bonding of transition metal complexes has been obtained by means of different computational techniques.

- The experimental structure of a paramagnetic Pt(III) complex has been computationally reproduced, exhibiting a metaloradical nature. Electronic —rather than steric— effects of strong σ-donating ligands distort the expected square-planar geometry, affording a see-saw disposition instead.

- The dynamic behaviour of agostic interactions of three representative T-shaped Pt(II) complexes have been analysed by considering explicit solvent molecules. Different kinds of agostic contacts have been found, ranging from strong to fluctuating ones. For these labile interactions, a realistic description of the solvent is recommended.

Reactivity

Calculations have provided feasible mechanistic pictures concerning topical organometallic transformations, leading to a better understanding of these processes.

- The impact of NHC ligands in a Pt-promoted C–H bond activation of arenes has been studied. I^{t}Bu and IPr are bulky enough to prevent the coordination of the substrate. Contrarily, steric and electronic features of IMes and IMes* favour both the thermodynamics and kinetics of the C–H bond activation reaction.

- The role of the base —hydroxide anion— in Pd-catalysed Suzuki–Miyaura cross-coupling reactions has been unravelled. Calculations strongly endorse the formation

of boronate species $[R–B(OH)_3]^-$ rather than Pd–hydroxo intermediates in the transmetalation step. These latter species are however accessible but not mandatory.

- Several reaction mechanisms of a Si-based Pd-catalyzed vinylation in water have been computed. The formation of the major products is explained on the basis of the faster insertion reactions with respect to the water-promoted Si-to-Pd transmetalation processes.

PROPERTIES

Computational protocols have proved their reliability in predicting chemical properties, as long as appropriate validating tests are performed.

- The pK_a^{water} values of a set of dihydrogen complexes have been estimated. Different contributions have been inspected in detail, revealing that the acidity of monocationic species mostly comes from the gas-phase deprotonation energy. The influence of ligands has also been evaluated for key species.

- ^{103}Rh NMR chemical shifts have been computed for a number of Rh–bis(phosphine) cationic complexes. According to calculations, ^{103}Rh chemical shifts do correlate with Rh–P bond distances intimately, even at the picometer scale.

VII

References

My brother has his sword, King Robert has his warhammer and I have my mind...
and a mind needs books as a sword needs a whetstone if it is to keep its edge.
That's why I read so much Jon Snow.

Tyrion Lannister in “Game of Thrones” by George R. R. Martin

1. D. Astruc, *Organometallic Chemistry and Catalysis*, Springer, Berlin, 2007.
2. C. Elschenbroich, A. Salzer, *Organometallics: A Concise Introduction*, Wiley-VCH, Weinheim, 2nd edn., 1992.
3. J. Hartwig, *Organotransition Metal Chemistry: From Bonding to Catalysis*, University Science Books, Sausalito, 2010.
4. R. H. Crabtree, *The Organometallic Chemistry of Transition Metals*, Jon Wiley & Sons, New York, 4th edn., 2001.
5. D. Seyferth, *Organometallics* **2001**, *20*, 1488–1498.
6. L. B. Hunt, *Platinum Metals Rev.* **1984**, *28*, 76–83.
7. T. J. Kealy, P. L. Pauson, *Nature* **1951**, *168*, 1039–1040.
8. S. A. Miller, J. A. Tebboth, J. F. Tremaine, *J. Chem. Soc.* **1952**, 632–635.
9. G. Wilkinson, M. Rosenblum, M. C. Withing, R. B. Woodward, *J. Am. Chem. Soc.* **1952**, *74*, 2125–2126.
10. M. Brookhart, M. L. H. Green, *J. Organomet. Chem.* **1983**, *250*, 395–408.
11. M. Brookhart, M. L. H. Green, L. L. Wong, *Prog. Inorg. Chem.* **1988**, *36*, 1–124.
12. G. J. Kubas, R. R. Ryan, B. I. Swanson, P. J. Vergamini, H. J. Wasserman, *J. Am. Chem. Soc.* **1984**, *106*, 451–452.
13. Nobel Prizes. Retrieved from www.nobelprize.org
14. *Organometallics as Catalysts in the Fine Chemical Industry*, Vol. 42 of *Topics in Organometallic Chemistry*, ed. M. Beller, H.-U. Blaser, Springer, Berlin, 2012.
15. *Molecular Organometallic Materials for Optics*, Vol. 28 of *Topics in Organometallic Chemistry*, ed. H. Bozec, V. Guerchais, Springer, Berlin, 2010.
16. *Conducting and Magnetic Organometallic Molecular Materials*, Vol. 27 of *Topics in Organometallic Chemistry*, ed. M. Fourmigué, L. Ouahab, Springer, Berlin, 2009.
17. *Bioorganometallic Chemistry*, Vol. 17 of *Topics in Organometallic Chemistry*, ed. G. Simonneaux, Springer, Berlin, 2006.
18. *Medicinal Organometallic Chemistry*, Vol. 32 of *Topics in Organometallic Chemistry*, ed. G. Jaouen, N. Metzler-Nolte, Springer, Berlin, 2010.

19. *Organometallics and Renewables*, Vol. 39 of *Topics in Organometallic Chemistry*, ed. M. A. R. Meier, B. M. Weckhuysen, P. C. A. Bruijnincx, Springer, Berlin, 2012.

20. R. H. Crabtree, *Organometallics* **2011**, *30*, 17–19.

21. N. S. Lewis, D. G. Nocera, *Proc. Natl. Acad. Sci. USA* **2006**, *103*, 15729–15735.

22. E. Clot, P.-O. Norrby, in *Innovate Catalysis in Organic Synthesis: Oxidation, Hydrogenation, and C–X Bond Forming Reactions*, ed. P. G. Andersson, Wiley-VCH, Weinheim, 2012, pp. 167–191.

23. *Computational Modeling for Homogeneous and Enzymatic Catalysis: A Knowledge-Base for Designing Efficient Catalysts*, ed. K. Morokuma, D. G. Musaev, Wiley-VCH, Weinheim, 2008.

24. T. Ziegler, J. Autschbach, *Chem. Rev.* **2005**, *105*, 2695–2722.

25. *Computational Modeling of Homogeneous Catalysis*, Vol. 25 of *Catalysis in Metal Complexes*, ed. F. Maseras, A. Lledós, Kluwer Academic Publishers, Dordrecht, 2002.

26. *Computational Organometallic Chemistry*, ed. T. R. Cundari, Marcel Dekker, New York, 2001.

27. E. R. Davidson, *Chem. Rev.* **2000**, *100*, special issue 2.

28. R. Hoffmann, *Angew. Chem. Int. Ed.* **1982**, *21*, 711–724.

29. C. Daniel, N. Koga, J. Han, X. Y. Fu, K. Morokuma, *J. Am. Chem. Soc.* **1988**, *110*, 3773–3781.

30. J. A. Gladysz, *Organometallics* **2011**, *30*, 1–4.

31. I. P. Beletskaya, V. P. Ananikov, *Organometallics* **2011**, *30*, 5–6.

32. S. J. Higgins, R. J. Nichols, S. Martin, P. Cea, H. S. J. van der Zant, M. M. Richter, P. J. Low, *Organometallics* **2011**, *30*, 7–12.

33. C. A. Tolman, *Chem. Soc. Rev.* **1972**, *1*, 337–353.

34. *Red Book: IUPAC Nomenclature of Inorganic Chemistry*, Blackwell Scientific Publications, Oxford, 3rd edn., 1990.

35. Y. Jean, *Molecular Orbitals of Transition Metal Complexes*, Oxford University Press, London, 2005.

36. T. Albright, J. K. Burdett, M. H. Whangbo, *Orbital Interactions in Chemistry*, John Wiley & Sons, New York, 1985.

37. J. Cirera, E. Ruiz, S. Alvarez, *Inorg. Chem.* **2008**, *47*, 2871–2889.

38. R. G. Pearson, *Proc. Nat. Acad. Sci. USA* **1975**, *72*, 2104–2106.

39. J. K. Burdett, *Molecular Shapes. Theoretical Models of Inorganic Stereochemistry*, John Wiley & Sons, New York, 1980.

40. J. Cirera, P. Alemany, S. Alvarez, *Chem. Eur. J.* **2004**, *10*, 190–207.

41. S. Alvarez, *Coord. Chem. Rev.* **1999**, *193–195*, 13–41.

42. S. Komiya, T. A. Albright, R. Hoffmann, J. K. Kochi, *J. Am. Chem. Soc.* **1976**, *98*, 7255–7265.

43. K. Tatsumi, R. Hoffmann, A. Yamamoto, J. K. Stille, *Bull. Chem. Soc. Jpn.* **1981**, *54*, 1857–1867.

44. S. Moncho, G. Ujaque, A. Lledós, P. Espinet, *Chem. Eur. J.* **2008**, *14*, 8986–8994.

45. M. A. Ortuño, S. Conejero, A. Lledós, *Beilstein J. Org. Chem.* **2013**, *9*, 1352–1382.

46. J. A. Casares, P. Espinet, G. Salas, *Chem. Eur. J.* **2002**, *8*, 4843–4853.

47. M. Brookhart, M. L. H. Green, G. Parkin, *Proc. Natl. Acad. Sci. USA* **2007**, *104*, 6908–6914.

48. L. Schwartsburd, E. Poverenov, L. J. W. Shimon, D. Milstein, *Organometallics* **2007**, *26*, 2931–2936.

49. O. V. Ozerov, L. A. Watson, M. Pink, K. G. Caulton, *J. Am. Chem. Soc.* **2007**, *129*, 6003–6016.

50. G. Berthon-Gelloz, B. de Bruin, B. Tinant, I. E. Markó, *Angew. Chem. Int. Ed.* **2009**, *48*, 3161–3164.

51. N. Takagi, S. Sakaki, *J. Am. Chem. Soc.* **2012**, *134*, 11749–11759.

52. P. Vidossich, A. Lledós, *Dalton Trans.* **2014**, 43, 11145–11151.

53. R. B. Jordan, *Reaction Mechanisms of Inorganic and Organometallic Systems*, Oxford University Press, New York, 3rd edn., 2007.

54. R. B. Grossman, *The Art of Writing Reasonable Organic Reaction Mechanisms*, Springer, New York, 1999.

55. S. Kozuch, J. M. L. Martin, *ChemPhysChem* **2011**, *12*, 1413–1418.

56. J. K. Nørskov, T. Bligaard, J. Kleis, *Science* **2009**, *324*, 1655–1656.

57. C. Stegelmann, A. Andreasen, C. T. Campbell, *J. Am. Chem. Soc.* **2009**, *131*, 8077–8082.

58. S. Kozuch, *WIREs Comput. Mol. Sci.* **2012**, *2*, 795–815.

59. S. Kozuch, S. Shaik, *Acc. Chem. Res.* **2011**, *44*, 101–110.

60. S. Kozuch, S. Shaik, *J. Am. Chem. Soc.* **2006**, *128*, 3355–3365.

61. S. Kozuch, J. M. L. Martin, *ACS Catal.* **2011**, *1*, 246–253.

62. D. Balcells, E. Clot, O. Eisenstein, *Chem. Rev.* **2010**, *110*, 749–823.

63. R. G. Bergman, *Nature* **2007**, *446*, 391–393.

64. R. H. Crabtree, *J. Organomet. Chem.* **2004**, *689*, 4083–4091.

65. J. A. Labinger, J. E. Bercaw, *Nature* **2002**, *417*, 507–514.

66. A. E. Shilov, G. B. Shul'pin, *Chem. Rev.* **1997**, *97*, 2879–2932.

67. I. Omae, *J. Organomet. Chem.* **2011**, *696*, 1128–1145.

68. M. Albrecht, *Chem. Rev.* **2010**, *110*, 576–623.

69. B. Butschke, H. Schwarz, *Chem. Sci.* **2012**, *3*, 308–326.

70. M. Lersch, M. Tilset, *Chem. Rev.* **2005**, *105*, 2471–2526.

71. U. Fekl, K. I. Goldberg, *Adv. Inorg. Chem.* **2003**, *54*, 259–320.

72. R. A. Periana, D. J. Taube, S. Gamble, H. Taube, T. Satoh, H. Fujii, *Science* **1998**, *280*, 560–564.

73. A. Caballero, E. Despagnet-Ayoub, M. M. Díaz-Requejo, A. Díaz-Rodríguez, M. E. González-Núñez, R. Mello, B. K. Muñoz, W.-S. Ojo, G. Asensio, M. Etienne, P. J. Pérez, *Science* **2011**, *332*, 835–838.

74. Y. Boutadla, D. L. Davies, S. A. Macgregor, A. I. Poblador-Bahamonde, *Dalton Trans.* **2009**, 5820–5831.

75. Z. Y. Lin, *Coord. Chem. Rev.* **2007**, *251*, 2280–2291.

76. B. A. Vastine, M. B. Hall, *Coord. Chem. Rev.* **2009**, *253*, 1202–1218.

77. R. Romeo, *Comments Inorg. Chem.* **1990**, *11*, 21–57.

78. J. Oxgaard, R. P. Muller, W. A. Goddard III, R. A. Periana, *J. Am. Chem. Soc.* **2004**, *126*, 352–363.

79. R. N. Perutz, S. Sabo-Etienne, *Angew. Chem. Int. Ed.* **2007**, *46*, 2578–2592.

80. B. A. Vastine, M. B. Hall, *J. Am. Chem. Soc.* **2007**, *129*, 12068–12069.

81. D. H. Ess, R. J. Nielsen, W. A. Goddard III, R. A. Periana, *J. Am. Chem. Soc.* **2009**, *131*, 11686–11688.

82. D. H. Ess, W. A. Goddard III, R. A. Periana, *Organometallics* **2010**, *29*, 6459–6472.

83. *Metal Catalyzed Cross-Coupling Reactions*, ed. F. Diederich, A. de Mejiere, John Wiley & Sons, New York, 2004.

84. A. Suzuki, *Angew. Chem. Int. Ed.* **2011**, *50*, 6723–6737.

85. A. Suzuki, N. Miyaura, *Chem. Rev.* **1995**, *95*, 2457–2483.

86. E. Negishi, *Bull. Chem. Soc. Jpn.* **2007**, *80*, 233–257.

87. Y. Nakao, T. Hiyama, *Chem. Soc. Rev.* **2011**, *40*, 4893–4901.

88. T. Hiyama, *J. Organomet. Chem.* **2002**, *653*, 58–61.

89. J.-P. Corbet, G. Mignani, *Chem. Rev.* **2006**, *106*, 2651–2710.

90. A. O. King, N. Yasuda, *Organometallics in Process Chemistry*, Vol. 6 of *Topics in Organometallic Chemistry*, ed. R. D. Larsen, Springer, Berlin, 2004, pp. 205–245.

91. A. Zapf, M. Beller, *Top. Catal.* **2002**, *19*, 101–109.

92. C. C. C. J. Seechurn, M. O. Kitching, T. J. Colacot, V. Snieckus, *Angew. Chem. Int. Ed.* **2012**, *51*, 5062–5085.

93. M. García-Melchor, A. A. C. Braga, A. Lledós, G. Ujaque, F. Maseras, *Acc. Chem. Res.* **2013**, *46*, 2626–2634.

94. L. Xue, Z. Lin, *Chem. Soc. Rev.* **2010**, *39*, 1692–1705.

95. A. A. C. Braga, G. Ujaque, F. Maseras, *Computational Modeling for Homogeneous and Enzymatic Catalysis: A Knowledge-Base for Designing Efficient Catalysts*, ed. K. Morokuma, D. G. Musaev, Wiley-VCH, Weinheim, 2008, pp. 109–130.

96. C. Amatore, A. Jutand, *Acc. Chem. Res.* **2000**, *33*, 314–321.

97. F. Proutiere, F. Schoenebeck, *Angew. Chem. Int. Ed.* **2011**, *50*, 8192–8195.

98. S. Kozuch, C. Amatore, A. Jutand, S. Shaik, *Organometallics* **2005**, *24*, 2319–2330.

99. L. J. Goossen, D. Koley, H. L. Hermann, W. Thiel, *J. Am. Chem. Soc.* **2005**, *127*, 11102–11114.

100. T. Mizoroki, K. Mori, A. Ozaki, *Bull. Chem. Soc. Jpn.* **1971**, *44*, 581.

101. R. F. Heck, J. P. Nolley, *J. Org. Chem.* **1972**, *37*, 2320–2322.

102. I. P. Beletskaya, A. V. Cheprakov, *Chem. Rev.* **2000**, *100*, 3009–3066.

103. J. P. Knowles, A. Whiting, *Org. Biomol. Chem.* **2007**, *5*, 31–44.

104. D. McCartney, P. J. Guiry, *Chem. Soc. Rev.* **2011**, *40*, 5122–5150.

105. M. Prashad, *Organometallics in Process Chemistry*, Vol. 6 of *Topics in Organometallic Chemistry*, ed. R. D. Larsen, Springer, Berlin, 2004, pp. 181–203.

106. F. Juliá-Hernández, A. Arcas, J. Vicente, *Chem. Eur. J.* **2012**, *18*, 7780–7786.

107. B. L. Shaw, S. D. Perera, E. A. Staley, *Chem. Commun.* **1998**, 1361–1362.

108. M. Ohff, A. Ohff, M. E. van der Boom, D. Milstein, *J. Am. Chem. Soc.* **1997**, *119*, 11687–11688.

109. A. Sundermann, O. Uzan, J. M. L. Martin, *Chem. Eur. J.* **2001**, *7*, 1703–1711.

110. O. Blacque, C. M. Frech, *Chem. Eur. J.* **2010**, *16*, 1521–1531.

111. R. Coontz, B. Hanson, *Science* **2004**, *305*, 957.

112. G. J. Kubas, *J. Organomet. Chem.* **2013**, *751*, 33–49.

113. G. J. Kubas, *Comm. Inorg. Chem.* **2012**, *33*, 102–121.

114. G. J. Kubas, *J. Organomet. Chem.* **2009**, *694*, 2648–2653.

115. G. J. Kubas, *Chem. Rev.* **2007**, *107*, 4152–4205.

116. G. J. Kubas, *P. Natl. Acad. Sci. USA* **2007**, *104*, 6901–6907.

117. G. J. Kubas, *Metal-Dihydrogen and σ-Bond Complexes: Structure, Bonding, and Reactivity*, Kluwer Academic/Plenum, New York, 2001.

118. G. J. Kubas, *J. Organomet. Chem.* **2001**, *635*, 37–68.

119. D. M. Heinekey, A. Lledós, J. M. Lluch, *Chem. Soc. Rev.* **2004**, *33*, 175–182.

120. D. Devarajan, D. H. Ess, *Inorg. Chem.* **2012**, *51*, 6367–6375.

121. M. Besora, A. Lledós, F. Maseras, *Chem. Soc. Rev.* **2009**, *38*, 957–966.

122. N. V. Belkova, E. S. Shubina, L. M. Epstein, *Acc. Chem. Res.* **2005**, *38*, 624–631.

123. G. C. Welch, R. R. S. Juan, J. D. Masuda, D. W. Stephan, *Science* **2006**, *314*, 1124–1126.

124. D. W. Stephan, G. Erker, *Angew. Chem. Int. Ed.* **2010**, *49*, 46–76.

125. E. Buncel, B. Menon, *J. Am. Chem. Soc.* **1977**, *99*, 4457–4461.

126. M. S. Chinn, D. M. Heinekey, *J. Am. Chem. Soc.* **1987**, *109*, 5865–5867.

127. E. P. Cappellani, S. D. Drouin, G. Jia, P. A. Maltby, R. H. Morris, C. T. Schweitzer, *J. Am. Chem. Soc.* **1994**, *116*, 3375–3388.

128. K. Abdur-Rashid, T. P. Fong, B. Greaves, D. G. Gusev, J. G. Hinman, S. E. Landau, A. J. Lough, R. H. Morris, *J. Am. Chem. Soc.* **2000**, *122*, 9155–9171.

129. G. Jia, C. P. Lau, *Coord. Chem. Rev.* **1999**, *190–192*, 83–118.

130. M. S. Chinn, D. M. Heinekey, N. G. Payne, C. D. Sofield, *Organometallics* **1989**, *8*, 1824–1826.

131. E. R. Rocchini, A. Mezzetti, H. Rüegger, U. Burckhardt, V. Gramlich, A. del Zotto, P. Martinuzzi, P. Rigo, *Inorg. Chem.* **1997**, *36*, 711–720

132. M. Schlaf, A. J. Lough, P. A. Maltby, R. H. Morris, *Organometallics* **1996**, *15*, 2270–2278.

133. L. Ronconi, P. J. Sadler, *Coord. Chem. Rev.* **2008**, *252*, 2239–2277.

134. W. von Philipsborn, *Chem. Soc. Rev.* **1999**, *28*, 95–105.

135. *Transition Metal Nuclear Magnetic Resonance*, ed. P. S. Pregosin, Elsevier, Amsterdam, 1991.

136. *Calculation of NMR and EPR Parameters. Theory and Applications*, ed. M. Kaupp, M. Bühl, V. G. Malkin, Wiley-VCH, Weinheim, 2004.

137. M. Bühl, T. Van Mourik, *WIREs Comput. Mol. Sci.* **2011**, *1*, 634–647.

138. M. Kaupp, M. Bühl, *Computational Inorganic and Bioinorganic Chemistry (Encyclopedia of Inorganic and Bioinorganic Chemistry)*, ed. R. B. King, Wiley, New York, 2009, pp. 91–108.

139. M. Bühl, *Annu. Rep. NMR Spectrosc.* **2008**, *64*, 77–126.

140. M. Bühl, M. Parrinello, *Chem. Eur. J.* **2001**, *7*, 4487–4494.

141. L. A. Truflandier, J. Autschbach, *J. Am. Chem. Soc.* **2010**, *132*, 3472–3483.

142. L. Carlton, *Annu. Rep. NMR Spectrosc.* **2008**, *63*, 49–178.

143. J. M. Ernsting, S. Gaemers, C. J. Elsevier, *Magn. Reson. Chem.* **2004**, *42*, 721–736.

144. M. Koller, W. von Philipsborn, *Organometallics* **1992**, *11*, 467–469.

145. V. Tedesco, W. von Philipsborn, *Organometallics* **1995**, *14*, 3600–3602.

146. B. R. Bender, M. Koller, D. Nanz, W. von Philipsborn, *J. Am. Chem. Soc.* **1993**, 115, 5889–5890.

147. B. Åkermark, M. R. A. Blomberg, J. Glaser, L. Öhrström, S. Wahlberg, K. Wärnmark, K. Zetterber, *J. Am. Chem. Soc.* **1994**, *116*, 3405–3413.

148. J. R. Houston, M. M. Olmstead, W. H. Casey, *Inorg. Chem.* **2006**, *45*, 7799–7805.

149. F. Jensen, *Introduction to Computational Chemistry*, John Wiley & Sons, Chichester, 2nd edn., 2007.

150. C. Cramer, *Essentials of Computational Chemistry*, John Wiley & Sons, Chichester, 2nd edn., 2004.

151. A. Szabo, N. S. Ostlund, *Modern Quantum Chemistry: Introduction to Advanced Electronic Structure Theory*, Dover Publications, New York, 1982.

152. W. Koch, M. C. Holthausen, *A Chemist's Guide to Density Functional Theory*, Wiley-VCH, Weinheim, 2nd edn., 2001.

153. K. Burke, *J. Chem. Phys.* **2012**, *136*, 150901.

154. A. D. Becke, *J. Chem. Phys.* **2014**, *140*, 18A301.

155. P. Hohenberg, W. Kohn, *Phys. Rev. B* **1964**, *136*, 864–871.

156. W. Kohn, L. J. Sham, *Phys. Rev. A* **1965**, *140*, 1133–1138.

157. A. J. Cohen, P. Mori-Sánchez, W. Yang, *Chem. Rev.* **2012**, *112*, 289–320.

158. J. C. Slater, *Phys. Rev.* **1951**, *81*, 385–390.

159. S. H. Vosko, L. Wilk, M. Nusair, *Can. J. Phys.* **1980**, *58*, 1200–1211.

160. A. D. Becke, *J. Chem. Phys.* **1986**, *84*, 4524–4529.

161. C. Lee, W. Yang, R. G. Parr, *Phys. Rev. B* **1988**, *37*, 785–789.

162. J. P. Perdew, K. Burke, M. Ernzerhof, *Phys. Rev. Lett.* **1996**, *77*, 3865–3868.

163. T. van Voorhis, G. E. Scuseria, *J. Chem. Phys.* **1998**, *109*, 400–410.

164. J. Tao, J. P. Perdew, V. N. Staroverov, G. E. Scuseria, *Phys. Rev. Lett.* **2003**, *91*, 146401.

165. A. D. Becke, *J. Chem. Phys.* **1993**, *98*, 1372–1377.

166. A. D. Becke, *J. Chem. Phys.* **1993**, *98*, 5648–5652.

167. P. J. Stephens, F. J. Devlin, C. F. Chabalowski, M. J. Frisch, *J. Phys. Chem.* **1994**, *98*, 11623–11627.

168. Y. Zhao, D. G. Truhlar, *Theor. Chem. Acc.* **2008**, *120*, 215–241.

169. K. Burke, M. Ernzerhof, J. P. Perdew, *Chem. Phys. Lett.* **1997**, *265*, 115–120.

170. J. P. Perdew, M. Ernzerhof, K. Burke, *J. Chem. Phys.* **1996**, *105*, 9982–9985.

171. C. Adamo, V. Barone, *J. Chem. Phys.* **1999**, *110*, 6158–6169.

172. H. Eshuis, J. E. Bates, F. Furche, *Theor. Chem. Acc.* **2012**, *131*, 1084.

173. H. Eshuis, F. Furche, *J. Phys. Chem. Lett.* **2011**, *2*, 983–989.

174. T. Schwabe, S. Grimme, *Acc. Chem. Res.* **2008**, *41*, 569–579.

175. J. P. Perdew, A. Ruzsinszky, L. A. Constantin, J. Sun, G. I. Csonka, *J. Chem. Theory Comput.* **2009**, *5*, 902–908.

176. J. P. Perdew, A. Ruzsinszky, J. Tao, V. N. Staroverov, G. E. Scuseria, G. I. Csonka, *J. Chem. Phys.* **2005**, *123*, 062201.

177. D. Rappoport, N. R. M. Crawford, F. Furche, K. Burke, *Computational Inorganic and Bioinorganic Chemistry (Encyclopedia of Inorganic and Bioinorganic Chemistry)*, ed. R. B. King, Wiley, New York, 2009, pp. 159–172.

178. L. Goerigk, S. Grimme, *Phys. Chem. Chem. Phys.* **2011**, *13*, 6670–6688.

179. S. F. Sousa, P. A. Fernandes, M. J. Ramos, *J. Phys. Chem. A* **2007**, *111*, 10439–10452.

180. Y. Zhao, D. G. Truhlar, *Acc. Chem. Res.* **2008**, 157–167.

181. Y. Zhao, D. G. Truhlar, *Chem. Phys. Lett.* **2011**, *502*, 1–13.

182. S. Grimme, J. Antony, S. Ehrlich, H. Krieg, *J. Chem. Phys.* **2010**, *132*, 154104.

183. S. Grimme, *WIREs Comput. Mol. Sci.* **2011**, *1*, 211–228.

184. C. J. Cramer, D. G. Truhlar, *Phys. Chem. Chem. Phys.* **2009**, *11*, 10757–10816.

185. M. M. Quintal, A. Karton, M. A. Iron, A. D. Boese, J. M. L. Martin, *J. Phys. Chem. A* **2006**, *110*, 709–716.

186. W. Lai, J. Yao, S. Shaik, H. Chen, *J. Chem. Theory Comput.* **2012**, *8*, 2991–2996.

187. M. Steinmetz, S. Grimme, *ChemistryOpen* **2013**, *2*, 115–124.

188. T. Weymuth, E. P. A. Couzijn, P. Chen, M. Reiher, *J. Chem. Theory Comput.* **2014**, 10, 3092–3103.

189. N. Sieffert, M. Bühl, *Inorg. Chem.* **2009**, *48*, 4622–4624.

190. D. A. Pantazis, J. E. McGrady, F. Maseras, M. Etienne, *J. Chem. Theory Comput.* **2007**, *3*, 1329–1336.

191. V. Tognetti, L. Joubert, P. Cortona, C. Adamo, *J. Phys. Chem. A* **2009**, *113*, 12322–12327.

192. M. P. Waller, H. Braun, N. Hojdis, M. Bühl, *J. Chem. Theory Comput.* **2007**, *3*, 2234–2242.

193. M. Bühl, C. Reimann, D. A. Pantazis, T. Bredow, F. Neese, *J. Chem. Theory Comput.* **2008**, *4*, 1449–1459.

194. C. A. Jiménez-Hoyos, B. G. Janesko, G. E. Scuseria, *J. Phys. Chem. A* **2009**, *113*, 11742–11749.

195. R. Rios-Font, M. Sodupe, L. Rodríguez-Santiago, P. R. Taylor, *J. Phys. Chem. A* **2010**, *114*, 10857–10863.

196. J. Poater, M. Solà, A. Rimola, L. Rodríguez-Santiago, M. Sodupe, *J. Phys. Chem. A* **2004**, *108*, 6072–6078.

197. P. Comba, T. W. Hambley, B. Martin, *Molecular Modeling of Inorganic Compounds*, Wiley-VCH, Weinheim, 3rd edn., 2009.

198. W. D. Cornell, P. Cieplak, C. I. Bayly, I. R. Gould, K. M. Merz, Jr., D. M. Ferguson, D. C. Spellmeyer, T. Fox, J. W. Caldwell, P. A. Kollman, *J. Am. Chem. Soc.* **1995**, *117*, 5179–5197.

199. B. L. Foley, M. B. Tessier, R. J. Woods, *WIREs Comput. Mol. Sci.* **2012**, *2*, 652–697.

200. G. Zhao, J. R. Perilla, E. L. Yufenyuy, X. Meng, B. Chen, J. Ning, J. Ahn, A. M. Gronenborn, K. Schulten, C. Aiken, P. Zhang, *Nature* **2013**, *497*, 643–646.

201. R. J. Deeth, A. Anastasi, C. Diedrich, K. Randell, *Coord. Chem. Rev.* **2009**, *253*, 795–816.

202. J. M. Haile, *Molecular Dynamics Simulation*, Jon Wiley & Sons, New York, 1997.

203. L. Verlet, *Phys. Rev.* **1967**, *159*, 98–103.

204. M. P. Allen, D. J. Tildesley, *Computer Simulation of Liquids*, Oxford University Press, New York, 1987.

205. P. Carloni, U. Rothlisberger, M. Parrinello, *Acc. Chem. Res.* **2002**, *35*, 455–464.

206. T. K. Woo, P. M. Margl, L. Deng, L. Cavallo, T. Ziegler, *Catal. Today* **1999**, *50*, 479–500.

207. D. Marx, J. Hutter, *Ab Initio Molecular Dynamics: Basic Theory and Advanced Methods*, Cambridge University Press, Cambridge, 2009.

208. K. Lindorff-Larsen, S. Piana, R. O. Dror, D. E. Shaw, *Science* **2011**, *334*, 517–520.

209. J. Kästner, *WIREs Comput. Mol. Sci.* **2011**, *1*, 932–942.

210. A. Barducci, M. Bonomi, M. Parrinello, *WIREs Comput. Mol. Sci.* **2011**, *1*, 826–843.

211. R. Car, M. Parrinello, *Phys. Rev. Lett.* **1985**, *55*, 2471–2474.

212. J. Hutter, *WIREs Comput. Mol. Sci.* **2012**, *2*, 604–612.

213. J. Tomasi, B. Mennucci, R. Cammi, *Chem. Rev.* **2005**, *105*, 2999–3093.

214. C. J. Cramer, D. G. Truhlar, *Chem. Rev.* **1999**, *99*, 2161–2200.

215. A. V. Marenich, C. J. Cramer, D. G. Truhlar, *J. Phys. Chem. B* **2009**, *113*, 6378–6396.

216. R. B. Sunoj, M. Anand, *Phys. Chem. Chem. Phys.* **2012**, *14*, 12715–12736.

217. A. Warshel, M. Levitt, *J. Mol. Biol.* **1976**, *103*, 227–249.

218. W. M. C. Sameera, F. Maseras, *WIREs Comput. Mol. Sci.* **2012**, *2*, 375–385.

219. C. Bo, F. Maseras, *Dalton Trans.* **2008**, 2911–2919.

220. H. M. Seen, W. Thiel, *Angew. Chem. Int. Ed.* **2009**, *48*, 1198–1229.

221. W. M. C. Sameera, F. Maseras, *Phys. Chem. Chem. Phys.* **2011**, *13*, 10520–10526.

222. F. Maseras, K. Morokuma, *J. Comput. Chem.* **1995**, *16*, 1170–1179.

223. M. Svensson, S. Humbel, R. D. J. Froese, T. Matsubara, S. Sieber, K. Morokuma, *J. Phys. Chem.* **1996**, *100*, 19357–19363.

224. H. B. Schlegel, *WIREs Comput. Mol. Sci.* **2011**, *1*, 790–809.

225. H. B. Schlegel, *J. Comput. Chem.* **2003**, *24*, 1514–1527.

226. V. S. Bryantsev, M. S. Diallo, W. A. Goddard III, *J. Phys. Chem. B* **2008**, *112*, 9709–9719.

227. C.-G. Zhan, D. A. Dixon, *J. Phys. Chem. A* **2001**, *105*, 11534–11540.

228. J. R. Pliego, Jr., J. M. Riveros, *J. Phys. Chem. A* **2001**, *105*, 7241–7247.

229. C. P. Kelly, C. J. Cramer, D. G. Truhlar, *J. Phys. Chem. B* **2006**, *110*, 16066–16081.

230. J. Ho, M. L. Coote, *Theor. Chem. Acc.* **2010**, *125*, 3–21.

231. J. Ho, M. L. Coote, *WIREs Comput. Mol. Sci.* **2011**, *1*, 649–660.

232. K. S. Alongi, G. C. Shields, *Ann. Rep. Comp. Chem.* **2010**, *6*, 113–138.

233. C. P. Kelly, C. J. Cramer, D. G. Truhlar, *J. Phys. Chem. A* **2006**, *110*, 2493–2499.

234. J. R. Pliego, Jr., J. M. Riveros, *J. Phys. Chem. A* **2002**, *106*, 7434–7439.

235. F. Ding, J. M. Smith, H. Wang, *J. Org. Chem.* **2009**, *74*, 2679–2691.

236. M. D. Tissandier, K. A. Cowen, W. Y. Feng, E. Gundlach, M. H. Cohen, A. D. Earhart, J. V. Coe, *J. Phys. Chem. A* **1998**, *102*, 7787–7794.

237. D. M. Camaioni, C. A. Schwerdtfeger, *J. Phys. Chem. A* **2005**, *109*, 10795–10797.

238. R. Bhattacharyya, S. C. Lahiri, *Z. Phys. Chem.* **2010**, *224*, 1389–1410.

239. L. B. Casabianca, A. C. de Dios, *J. Chem. Phys.* **2008**, *128*, 052201.

240. T. Helgaker, M. Jaszunski, K. Rudd, *Chem. Rev.* **1999**, *99*, 293–352.

241. M. Bühl, M. Kaupp, O. L. Malkina, V. G. Malkin, *J. Comput. Chem.* **1999**, *20*, 91–105.

242. G. Schreckenbach, T. Ziegler, *Theor. Chem. Acc.* **1998**, *99*, 71–82.

243. J. R. Cheeseman, G. W. Trucks, T. A. Keith, M. J. Frisch, *J. Chem. Phys.* **1996**, *104*, 5497–5509.

244. G. Schreckenbach, S. K. Wolff, T. Ziegler, *J. Phys. Chem. A* **2000**, *104*, 8244–8255.

245. M. Bühl, *Chem. Phys. Lett.* **1997**, *267*, 251–257.

246. W. Kutzelnigg, U. Fleischer, M. Schindler, *NMR Basic Principles and Progress* Vol. 23, Springer Verlag, Berlin, 1990, p. 165.

247. G. Schreckenbach, T. Ziegler, *Int. J. Quantum Chem.* **1996**, *60*, 753–766.

248. J. Autschbach, *J. Chem. Phys.* **2012**, *136*, 150902.

249. P. Pyykkö, *Annu. Rev. Phys. Chem.* **2012**, *63*, 45–64.

250. J. Autschbach, S. Zheng, *Annu. Rep. NMR Spectrosc.* **2009**, 67, 1–95.

251. J. Autschbach, *Calculation of NMR and EPR Parameters. Theory and Applications*, ed. M. Kaupp, M. Bühl, V. G. Malkin, Wiley-VCH, Weinheim, 2004, pp. 227–247.

252. O. Rivada-Wheelaghan, M. A. Ortuño, J. Díez, S. E. García-Garrido, C. Maya, A. Lledós, S. Conejero, *J. Am. Chem. Soc.* **2012**, *134*, 15261–15264.

253. J. A. Labinger, J. E. Bercaw, *Higher Oxidation State Organopalladium and Platinum Chemistry*, Vol. 35 of *Topics in Organometallic Chemistry*, ed. H. Bozec, V. Guerchais, Springer, Berlin, 2011, pp 29–60.

254. B. de Bruin, D. G. H. Hetterscheid, J. J. Koekkoek, H. Grützmacher, *Prog. Inorg. Chem.* **2007**, *55*, 247–354.

255. K. K. Pandey, *Coord. Chem. Rev.* **1992**, *121*, 1–42.

256. R. Usón, J. Forniés, M. Tomás, B. Menjón, K. Sünkel, R. Bau, *J. Chem. Soc., Chem. Commun.* **1984**, 751–752.

257. R. Usón, J. Forniés, M. Tomás, B. Menjón, R. Bau, K. Sünkel, E. Kuwabara, *Organometallics* **1986**, *5*, 1576–1581.

258. P. J. Alonso, R. Alcalá, R. Usón, J. Forniés, *J. Phys. Chem. Solids* **1991**, *52*, 975–978.

259. H. Bois, N. G. Connelly, J. G. Crossley, J.-C. Guillorit, G. R. Lewis, A. G. Orpen, P. Thornton, *J. Chem. Soc., Dalton Trans.* **1998**, 2833–2838.

260. H. Alves, D. Simão, I. C. Santos, V. Gama, R. T. Henriques, H. Novais, M. Almeida, *Eur. J. Inorg. Chem.* **2004**, 1318–1329.

261. E. Stephen, A. J. Blake, E. S. Davies, J. McMaster, M. Schröder, *Chem. Commun.* **2008**, 5707–5709.

262. O. Rivada-Wheelaghan, M. A. Ortuño, S. E. García-Garrido, J. Díez, P. J. Alonso, A. Lledós, S. Conejero, *Chem. Commun.* **2014**, *50*, 1299–1301.

263. B. Tumanskii, D. Sheberla, G. Molev, Y. Apeloig, *Angew. Chem. Int. Ed.* **2007**, *46*, 7408–7411.

264. J. A. S. Roberts, J. A. Franz, E. F. van der Eide, E. D. Walter, J. L. Petersen, D. L. DuBois, R. M. Bullock, *J. Am. Chem. Soc.* **2011**, *133*, 14593–14603.

265. M. J. Frisch et al., Gaussian 09; Gaussian, Inc.: Wallingford CT, 2009.

266. D. Andrae, U. Häeußermann, M. Dolg, H. Stoll, H. Preuß, *Theor. Chim. Acta* **1990**, *77*, 123–141.

267. A. W. Ehlers, M. Böhme, S. Dapprich, A. Gobbi, A. Hollwarth, V. Jonas, K. F. Köhler, R. Stegmann, A. Veldkamp, G. Frenking, *Chem. Phys. Lett.* **1993**, *208*, 111–114.

268. A. W. Ehlers, M. Böhme, S. Dapprich, A. Gobbi, A. Hollwarth, V. Jonas, K. F. Köhler, R. Stegmann, A. Veldkamp, G. Frenking, *Chem. Phys. Lett.* **1993**, *208*, 237–240.

269. W. J. Hehre, R. Ditchfield, J. A. Pople, *J. Chem. Phys.* **1972**, *56*, 2257–2261.

270. M. M. Francl, W. J. Pietro, W. J. Hehre, J. S. Binkley, M. S. Gordon, D. DeFrees, J. A. Pople, *J. Chem. Phys.* **1982**, *77*, 3654–3665.

271. T. Clark, J. Chandrasekhar, G. W. Spitznagel, P. V. R. Schleyer, *J. Comput. Chem.* **1983**, *4*, 294–301.

272. E. Ruiz, J. Cirera, S. Alvarez, *Coord. Chem. Rev.* **2005**, *249*, 2649–2660.

273. L. Yang, D. R. Powell, R. P. Houser, *Dalton Trans.* **2007**, 955–964.

274. M. A. Ortuño, P. Vidossich, G. Ujaque, S. Conejero, A. Lledós, *Dalton Trans.* **2013**, *42*, 12165–12172.

275. W. I. Sundquist, D. P. Bancroft, S. J. Lippard, *J. Am. Chem. Soc.* **1990**, *112*, 1590–1596.

276. W. Yao, O. Eisenstein, R. H. Crabtree, *Inorg. Chim. Acta* **1997**, *254*, 105–111.

277. L. Brammer, *Dalton Trans.* **2003**, 3145–3157.

278. N. Carr, B. J. Dunne, A. G. Orpen, J. L. Spencer, *J. Chem. Soc., Chem. Commun.* **1988**, 926–928.

279. N. Carr, B. J. Dunne, L. Mole, A. G. Orpen, J. L. Spencer, *J. Chem. Soc., Dalton Trans.* **1991**, 863–871.

280. L. Mole, J. L. Spencer, N. Carr, A. G. Orpen, *Organometallics* **1991**, *10*, 49–52.

281. N. Carr, L. Mole, A. G. Orpen, J. L. Spencer, *J. Chem. Soc., Dalton Trans.* **1992**, 2653–2662.

282. J. L. Spencer, G. S. Mhinzi, *J. Chem. Soc., Dalton Trans.* **1995**, 3819–3824.

283. W. Baratta, S. Stoccoro, A. Doppiu, E. Herdtweck, A. Zucca, P. Rigo, *Angew. Chem. Int. Ed.* **2003**, *42*, 105–108.

284. J. Campos, R. Peloso, E. Carmona, *Angew. Chem. Int. Ed.* **2012**, *51*, 8255–8258.

285. M. Ingleson, M. F. Mahon, A. S. Weller, *Chem. Commun.* **2004**, 2398–2399.

286. H. Braunschweig, K. Radacki, K. Uttinger, *Chem. Eur. J.* **2008**, *14*, 7858–7866.

287. S. H. Crosby, G. J. Clarkson, J. P. Rourke, *J. Am. Chem. Soc.* **2009**, *131*, 14142–14143.

288. O. Rivada-Wheelaghan, B. Donnadieu, C. Maya, S. Conejero, *Chem. Eur. J.* **2010**, *16*, 10323–10326.

289. E. Clot, O. Eisenstein, *Struct. Bonding* **2004**, *113*, 1–36.

290. M. Lein, *Coord. Chem. Rev.* **2009**, *253*, 625–634.

291. J. Saßmannshausen, *Dalton Trans.* **2012**, *41*, 1919–1923.

292. T. S. Thakur, G. R. Desiraju, *J. Mol. Struc. THEOCHEM* **2007**, *810*, 143–154.

293. X. Solans-Monfort, O. Eisenstein, *Polyhedron* **2006**, *25*, 339–348.

294. F. Blanc, J.-M. Basset, C. Copéret, A. Sinha, Z. J. Tonzetich, R. R. Schrock, X. Solans-Monfort, E. Clot, O. Eisenstein, A. Lesage, L. Emsley, *J. Am. Chem. Soc.* **2008**, *130*, 5886–5900.

295. W. Scherer, V. Herz, A. Brück, C. Hauf, F. Reiner, S. Altmannshofer, D. Leusser, D. Stalke, *Angew. Chem. Int. Ed.* **2011**, *50*, 2845–2849.

296. J. E. Barquera-Lozada, A. Obenhuber, C. Hauf, W. Scherer, *J. Phys. Chem. A* **2013**, *117*, 4304–4315.

297. R. J. Meier, G. H. J. van Doremaele, S. Iarlori, F. Buda, *J. Am. Chem. Soc.* **1994**, *116*, 7274–7281.

298. P. Margl, J. C. W. Lohrenz, T. Ziegler, P. E. Blöchl, *J. Am. Chem. Soc.* **1996**, *118*, 4434–4441.

299. T. K. Woo, P. M. Margl, J. C. W. Lohrenz, P. E. Blöchl, T. Ziegler, *J. Am. Chem. Soc.* **1996**, *118*, 13021–13030.

300. M. S. W. Chan, T. Ziegler, *Organometallics* **2000**, *19*, 5182–5189.

301. C. N. Rowley, T. K. Woo, *Organometallics* **2011**, *30*, 2071–2074.

302. The CP2K developers group, http://www.cp2k.org, 2014.

303. J. Hutter, M. Iannuzzi, F. Schiffmann, J. VandeVondele, *WIREs Comput. Mol. Sci.* **2014**, *4*, 15–25.

304. G. Bussi, D. Donadio, M. Parrinello, *J. Chem. Phys.* **2007**, *126*, 014101.

305. G. Lippert, J. Hutter, M. Parrinello, *Mol. Phys.* **1997**, *92*, 477–487.

306. J. VandeVondele, M. Krack, F. Mohamed, M. Parrinello, T. Chassaing, J. Hutter, *Comput. Phys. Commun.* **2005**, *167*, 103–128.

307. J. VandeVondele, J. Hutter, *J. Chem. Phys.* **2007**, *127*, 114105.

308. S. Goedecker, M. Teter, J. Hutter, *Phys. Rev. B* **1996**, *54*, 1703–1710.

309. M. Krack, *Theor. Chem. Acc.* **2005**, *114*, 145–152.

310. J. VandeVondele, J. Hutter, *J. Chem. Phys.* **2003**, *118*, 014515.

311. D. R. Lide, H. V. Kehiaian, *Handbook of Thermophysical and Thermochemical Data*, CRC Press, Boca Raton, 1994.

312. G. J. Martyna, M. E. Tuckerman, *J. Chem. Phys.* **1999**, *110*, 2810–2821.

313. T. Fox, P. Kollman, *J. Phys. Chem. B* **1998**, *102*, 8070–8079.

314. J. M. Seminario, *Int. J. Quantum Chem.* **1996**, *60*, 1271–1277.

315. T. Laino, F. Mohamed, A. Laio, M. Parrinello, *J. Chem. Theory Comput.* **2005**, *1*, 1176–1184.

316. S. F. Boys, F. Bernardi, *Mol. Phys.* **1970**, *19*, 553–566.

317. M. D. Butts, B. L. Scott, G. J. Kubas, *J. Am. Chem. Soc.* **1996**, *118*, 11831–11843.

318. S. S. Stahl, J. A. Labinger, J. E. Bercaw, *Inorg. Chem.* **1998**, *37*, 2422–2431.

319. B. F. M. Kimmich, R. M. Bullock, *Organometallics* **2002**, *21*, 1504–1507.

320. O. Rivada-Wheelaghan, M. Roselló-Merino, M. A. Ortuño, P. Vidossich, E. Gutiérrez-Puebla, A. Lledós, S. Conejero, *Inorg. Chem.* **2014**, *53*, 4257–4268.

321. L. A. Truflandier, K. Sutter, J. Autschbach, *Inorg. Chem.* **2011**, *50*, 1723–1732.

322. K. Sutter, L. A. Truflandier, J. Autschbach, *ChemPhysChem* **2011**, *12*, 1448–1455.

323. R. Romeo, G. D'Amico, E. Sicilia, N. Russo, S. Rizzato, *J. Am. Chem. Soc.* **2007**, *129*, 5744–5755.

324. N. Marzari, D. Vanderbilt, *Phys. Rev. B* **1997**, *56*, 12847–12865.

325. N. Marzari, A. A. Mostofi, J. R. Yates, I. Souza, D. Vanderbilt, *Rev. Mod. Phys.* **2012**, *84*, 1419–1475.

326. P. H.-L. Sit, F. Zipoli, J. Chen, R. Car, M. H. Cohen, A. Selloni, *Chem. Eur. J.* **2011**, *17*, 12136–12143.

327. M. Roselló-Merino, O. Rivada-Wheelaghan, M. A. Ortuño, P. Vidossich, J. Díez, A. Lledós, S. Conejero, *Organometallics* **2014**, *33*, 3746–3756.

328. L. J. L. Häller, M. J. Page, S. A. Macgregor, M. F. Mahon, M. K. Whittlesey, *J. Am. Chem. Soc.* **2009**, *131*, 4604–4605.

329. G. Ujaque, A. C. Cooper, F. Maseras, O. Eisenstein, K. G. Caulton, *J. Am. Chem. Soc.* **1998**, *120*, 361–365.

330. A. C. Cooper, E. Clot, J. C. Huffman, W. E. Streib, F. Maseras, O. Eisenstein, K. G. Caulton, *J. Am. Chem. Soc.* **1999**, *121*, 97–106.

331. J. Jaffart, M. Etienne, F. Maseras, J. E. McGrady, O. Eisenstein, *J. Am. Chem. Soc.* **2001**, *123*, 6000–6013.

332. A. Toner, J. Matthes, S. Gründemann, H.-H. Limbach, B. Chaudret, E. Clot, S. Sabo-Etienne, *Proc. Natl. Acad. Sci. USA* **2007**, *104*, 6945–6950.

333. F. Hasanayn, P. Achord, P. Braunstein, H. J. Magnier, K. Krogh-Jespersen, A. S. Goldman, *Organometallics* **2012**, *31*, 4680–4692.

334. B. Pudasaini, B. G. Janesko, *Organometallics* **2014**, *33*, 84–93.

335. H. Braunschweig, K. Radacki, D. Rais, D. Scheschkewitz, *Angew. Chem. Int. Ed.* **2005**, *44*, 5651–5654.

336. H. Braunschweig, P. Brenner, R. D. Dewhurst, J. O. C. Jimenez-Halla, T. Kupfer, D. Rais, K. Uttinger, *Angew. Chem. Int. Ed.* **2013**, *52*, 2981–2984.

337. E. F. van der Eide, P. Yang, R. M. Bullock, *Angew. Chem. Int. Ed.* **2013**, *52*, 10190–10194.

338. O. Rivada-Wheelaghan, M. A. Ortuño, J. Díez, A. Lledós, S. Conejero, *Angew. Chem. Int. Ed.* **2012**, *51*, 3936–3939.

339. D. D. Wick, K. I. Goldberg, *J. Am. Chem. Soc.* **1997**, *119*, 10235–10236.

340. M. P. Jensen, D. D. Wick, S. Reinartz, P. S. White, J. L. Templeton, K. I. Goldberg, *J. Am. Chem. Soc.* **2003**, *125*, 8614–8624.

341. B. Butschke, D. Schröder, H. Schwarz, *Organometallics* **2009**, *28*, 4340–43496.

342. B. Butschke, H. Schwarz, *Organometallics* **2011**, *30*, 1588–1598.

343. J. C. DeMott, N. Bhuvanesh, O. V. Ozerov, *Chem. Sci.* **2013**, *4*, 642–649.

344. W. A. Herrmann, *Angew. Chem. Int. Ed.* **2002**, *41*, 1290–1309.

345. T. Dröge, F. Glorius, *Angew. Chem. Int. Ed.* **2010**, *49*, 6940–6952.

346. H. Clavier, S. P. Nolan, *Chem. Commun.* **2010**, *46*, 841–861.

347. D. J. Nelson, S. P. Nolan, *Chem. Soc. Rev.* **2013**, *42*, 6723–6753.

348. A. C. Hillier, W. J. Sommer, B. S. Yong, J. L. Petersen, L. Cavallo, S. P. Nolan, *Organometallics* **2003**, *22*, 4322–4326.

349. A. Poater, B. Cosenza, A. Correa, S. Giudice, F. Ragone, V. Scaramo, L. Cavallo, *Eur. J. Inorg. Chem.* **2009**, 1759–1766.

350. C. A. Tolman, *Chem. Rev.* **1977**, *77*, 313–348.

351. R. S. Paton, K. Seonah, A. G. Ross, S. J. Danishefsky, K. N. Houk, *Angew. Chem. Int. Ed.* **2011**, *50*, 10366–10368.

352. W.-J. van Zeist, F. M. Bickelhaupt, *Org. Biomol. Chem.* **2010**, *8*, 3118–3127.

353. I. Fernández, F. M. Bickelhaupt, *Chem. Soc. Rev.* **2014**, *43*, 4953–4967.

354. S. Urban, M. Tursky, R. Frölich, F. Glorius, *Dalton Trans.* **2009**, 6934–6940.

355. M. A. Ortuño, A. Lledós, F. Maseras, G. Ujaque, *ChemCatChem* **2014**, DOI: 10.1002/cctc.201402326

356. A. J. J. Lennox, G. C. Lloyd-Jones, *Chem. Soc. Rev.* **2014**, *43*, 412–443.

357. N. Miyaura, *J. Organomet. Chem.* **2002**, *653*, 54–57.

358. A. J. J. Lennox, G. C. Llyod-Jones, *Angew. Chem. Int. Ed.* **2013**, *52*, 7362–7370.

359. K. Matos, J. A. Soderquist, *J. Org. Chem.* **1998**, *63*, 461–470.

360. M. Sumimoto, N. Iwane, T. Takahama, S. Sakaki, *J. Am. Chem. Soc.* **2004**, 126, 10457–10471.

361. A. A. C. Braga, N. H. Morgon, G. Ujaque, F. Maseras, *J. Am. Chem. Soc.* **2005**, *127*, 9298–9307.

362. A. A. C. Braga, N. H. Morgon, G. Ujaque, A. Lledós, F. Maseras, *J. Organomet. Chem.* **2006**, *691*, 4459–4466.

363. C.-M. Weng, F.-E. Hong, *Dalton Trans.* **2011**, *40*, 6458–6468.

364. C. M. Nunes, A. L. Monteiro, *J. Braz. Chem. Soc.* **2007**, *18*, 1443–1447.

365. A. N. Cammidge, V. H. M. Goddard, H. Gopee, N. L. Harrison, D. L. Hughes, C. J. Schubert, B. M. Sutton, G. L. Watts, A. J. Whitehead, *Org. Lett.* **2006**, *8*, 4071–4074.

366. B. Basu, K. Biswas, S. Kundu, S. Ghosh, *Green Chem.* **2010**, *12*, 1734–1738.

367. B. P. Carrow, J. F. Hartwig, *J. Am. Chem. Soc.* **2011**, *133*, 2116–2119.

368. A. F. Schmidt, A. A. Kurokhtina, E. V. Larina, *Russ. J. Gen. Chem.* **2011**, *81*, 1573–1574.

369. C. Amatore, A. Jutand, G. Le Duc, *Chem. Eur. J.* **2011**, *17*, 2492–2503.

370. C. F. R. A. C. Lima, A. S. M. C. Rodrigues, V. L. M. Silva, A. M. S. Silva, L. M. N. B. F. Santos, *ChemCatChem* **2014**, 6, 1291–1302.

371. H. M. Senn, T. Ziegler, *Organometallics* **2004**, *23*, 2980–2988.

372. L. J. Goossen, D. Koley, H. L. Hermann, W. Thiel, *Organometallics* **2005**, *24*, 2398–2410.

373. M. Ahlquist, P. Fristrup, D. Tanner, P.-O. Norrby, *Organometallics* **2006**, *25*, 2066–2073.

374. K. C. Lam, T. B. Marder, Z. Y. Lin, *Organometallics* **2007**, *26*, 758–760.

375. Z. Li, Y. Fu, Q.-X. Guo, L. Liu, *Organometallics* **2008**, *27*, 4043–4049.

376. C. L. McMullin, J. Jover, J. N. Harvey, N. Fey, *Dalton Trans.* **2010**, *39*, 10833–10836.

377. M. Besora, C. Gourlaouen, B. Yates, F. Maseras, *Dalton Trans.* **2011**, *40*, 11089–11094.

378. K. Vikse, T. Naka, J. S. McIndoe, M. Besora, F. Maseras, *ChemCatChem* **2013**, *5*, 3604–3609.

379. V. P. Ananikov, D. G. Musaev, K. Morokuma, *J. Am. Chem. Soc.* **2002**, *124*, 2839–2852.

380. V. P. Ananikov, D. G. Musaev, K. Morokuma, *Organometallics* **2005**, *24*, 715–723.

381. E. Zuidema, P. W. N. M. van Leeuwen, C. Bo, *Organometallics* **2005**, *24*, 3703–3710.

382. M. Pérez-Rodríguez, A. A. C. Braga, M. Garcia-Melchor, M. H. Pérez-Temprano, J. A. Casares, G. Ujaque, A. R. de Lera, R. Alvarez, F. Maseras, P. Espinet, *J. Am. Chem. Soc.* **2009**, *131*, 3650–3657.

383. P. K. Sajith, C. H. Suresh, *Inorg. Chem.* **2011**, *50*, 8085–8093.

384. S. E. Wheeler, K. N. Houk, *J. Chem. Theory Comput.* **2010**, *6*, 395–404.

385. M. Besora, A. A. C. Braga, G. Ujaque, F. Maseras, A. Lledós, *Theor. Chem. Acc.* **2011**, 128, 639–646.

386. L. J. Goossen, D. Koley, H. L. Hermann, W. Thiel, *J. Am. Chem. Soc.* **2005**, 127, 11102–11114.

387. L. J. Goossen, D. Koley, H. L. Hermann, W. Thiel, *Organometallics* **2006**, *25*, 54–67.

388. J. Jover, N. Fey, M. Purdie, G. C. Lloyd-Jones, J. N. Harvey, *J. Mol. Catal. A: Chem.* **2010**, *324*, 39–47.

389. S. Kozuch, J. M. L. Martin, *ACS Catal.* **2011**, *1*, 246–253.

390. P. F Kelly, A. M. Z. Slawin, A. Soriano-Rama, *J. Chem. Soc., Dalton Trans.* **1996**, 53–59.

391. B. P. Carrow, J. F. Hartwig, *J. Am. Chem. Soc.* **2010**, *132*, 79–81.

392. A. Gordillo, M. A. Ortuño, C. López-Mardomingo, A. Lledós, G. Ujaque, E. de Jesús, *J. Am. Chem. Soc.* **2013**, *135*, 13749–13763.

393. *Modern Styrenic Polymers: Polystyrenes and Styrenic Copolymers*, ed. J. Scheirs, D. B. Priddy, John Wiley & Sons, Chichester, 2003.

394. S. E. Denmark, C. R. Butler, *Chem. Commun.* **2009**, 20–33.

395. H. F. Sore, W. R. J. D. Galloway, D. R. Spring, *Chem. Soc. Rev.* **2012**, *41*, 1845–1866.

396. S. E. Denmark, J. H.-C. Liu, *Angew. Chem. Int. Ed.* **2010**, *49*, 2978–2986.

397. A. Hallberg, C. Westerlund, *Chem. Lett.* **1982**, 1993–1994.

398. K. Kikukawa, K. Ikenaga, K. Kono, K. Toritani, F. Wada, T. Matsuda, *J. Organomet. Chem.* **1984**, *270*, 277–282.

399. K. Karabelas, A. Hallberg, *J. Org. Chem.* **1986**, *51*, 5286–5290.

400. Y. Hatanaka, T. Hiyama, *J. Org. Chem.* **1988**, *53*, 918–920.

401. K. Tamao, K. Kobayashi, Y. Ito, *Tetrahedron Lett.* **1989**, *30*, 6051–6054.

402. E. Hagiwara, K. Gouda, Y. Hatanaka, T. Hiyama, *Tetrahedron Lett.* **1997**, *38*, 439–442.

403. K. Hirabayashi, J. Kawashima, Y. Nishihara, A. Mori, T. Hiyama, *Org. Lett.* **1999**, 1, 299–301.

404. K. Hirabayashi, A. Mori, J. Kawashima, M. Suguro, Y. Nishihara, T. Hiyama, *J. Org. Chem.* **2000**, *65*, 5342–5349.

405. A. Sugiyama, Y.-y. Ohnishi, M. Nakaoka, Y. Nakao, H. Sato, S. Sakaki, Y. Nakao, T. Hiyama, *J. Am. Chem. Soc.* **2008**, *130*, 12975–12985.

406. S. E: Denmark, R. F. Sweis, *J. Am. Chem. Soc.* **2001**, *123*, 6439–6440.

407. S. E: Denmark, R. F. Sweis, *Acc. Chem. Res.* **2002**, *35*, 835–846.

408. S. E. Denmark, C. S. Regens, *Acc. Chem. Res.* **2008**, *41*, 1486–1499.

409. S. E. Denmark, R. C. Smith, *J. Am. Chem. Soc.* **2010**, *132*, 1243–1245.

410. B.-L. Lin, L. Liu, Y. Fu, S.-W. Luo, Q. Chen, Q.-X. Guo, *Organometallics* **2004**, *23*, 2114–2123.

411. R. J. Deeth, A. Smith, J. M. Brown, *J. Am. Chem. Soc.* **2004**, *126*, 7144–7151.

412. C. Bäcktorp, P.-O. Norrby, *Dalton Trans.* **2011**, *40*, 11308–11314.

413. M.-T. Lee, H. M. Lee, C.-H. Hu, *Organometallics* **2007**, *26*, 1317–1324.

414. H. von Schenck, B. Åkermark, M. Svensson, *J. Am. Chem. Soc.* **2003**, *125*, 3503–3508.

415. P. Surawatanawong, M. B. Hall, *Organometallics*, **2008**, *27*, 6222–6232.

416. C. Sköld, J. Kleimark, A. Trejos, L. R. Odell, S. O. N. Lill, P.-O. Norrby, M. Larhed, *Chem. Eur. J.* **2012**, *18*, 4714–4722.

417. D. G. Blackmond, A. Armstrong, V. Coombe, A. Wells, *Angew. Chem. Int. Ed.* **2007**, *46*, 3798–3800.

418. C.-J. Li, *Chem. Rev.* **2005**, *105*, 3095–3165.

419. R. N. Butler, A. G. Coyne, *Chem. Rev.* **2010**, *110*, 6302–6337.

420. M.-O. Simon, C.-J. Li, *Chem. Soc. Rev.* **2012**, *41*, 1415–1427.

421. E. Alacid, C. Nájera, *Adv. Synth. Catal.* **2006**, *348*, 2085–2091.

422. E. Alacid, C. Nájera, *J. Org. Chem.* **2008**, *73*, 2315–2322.

423. A. Gordillo, E. de Jesús, C. López-Mardomingo, *Chem. Commun.* **2007**, 4056–4058.

424. A. Gordillo, E. de Jesús, C. López-Mardomingo, *J. Am. Chem. Soc.* **2009**, *131*, 4584–4585.

425. A. C. Albéniz, P. Espinet, R. López-Fernández, *Organometallics* **2006**, *25*, 5449–5455.

426. R. Krishnan, J. S. Binkley, R. Seeger, J. A. Pople, *J. Chem. Phys.* **1980**, *72*, 650–654.

427. P. E. M. Siegbahn, J. W. Tye, M. B. Hall, *Chem. Rev.* **2007**, *107*, 4414–4435.

428. J. C. Gordon, G. J. Kubas, *Organometallics* **2010**, *29*, 4682–4701.

429. N. K. Szymczak, D. R. Tyler, *Coord. Chem. Rev.* **2008**, *252*, 212–230.

430. F. Creati, C. Coletti, N. Re, *Organometallics* **2009**, *28*, 6603–6616.

431. M. Jiménez-Tenorio, M. C. Puerta, P. Valerga, M. A. Ortuño, G. Ujaque, A. Lledós, *Inorg. Chem.* **2013**, *52*, 8919–8932.

432. G. Kovács, A. Rossin, L. Gonsalvi, A. Lledós, M. Peruzzini, *Organometallics* **2010**, *29*, 5121–5131.

433. J. Díez, J. Gimeno, A. Lledós, F. J. Suárez, C. Vicent, *ACS Catal.* **2012**, *2*, 2087–2099.

434. R. H. Morris, *J. Am. Chem. Soc.* **2014**, *136*, 1948–1959.

435. Y. Markus, *Pure Appl. Chem.* **1983**, *55*, 977–1021.

436. B. Bandow, B. Hartke, *J. Phys. Chem. A* **2006**, *110*, 5809–5822.

437. J. T. Su, X. Xu, W. A. Goddard III, *J. Phys. Chem. A* **2004**, *108*, 10518–10526.

438. E. S. Stoyanov, I. V. Stoyanova, C. A. Reed, *J. Am. Chem. Soc.* **2010**, *132*, 1484–1485.

439. C. A. Reed, *Acc. Chem. Res.* **2013**, *46*, 2567–2575.

440. J. D. Gilbertson, N. K. Szymczak, D. R. Tyler, *Inorg. Chem.* **2004**, *43*, 3341–3343.

441. J. D. Gilbertson, N. K. Szymczak, J. L. Crossland, W. K. Miller, D. K. Lyon, B. M. Foxman, J. Davis, D. R. Tyler, *Inorg. Chem.* **2007**, *46*, 1205–1214.

442. D. N. Akbayeva, L. Gonsalvi, W. Oberhauser, M. Peruzzini, F. Vizza, P. Brüggeller, A. Romerosa, G. Sava, A. Bergamo, *Chem. Commun.* **2003**, 264–265.

443. A. Rossin, L. Gonsalvi, A. D. Phillips, O. Maresca, A. Lledós, M. Peruzzini, *Organometallics* **2007**, *26*, 3289–3296.

444. N. K. Szymczak, L. N. Zakharov, D. R. Tyler, *J. Am. Chem. Soc.* **2006**, *128*, 15830–15835.

445. N. K. Szymczak, D. A. Braden, J. L. Crossland, Y. Turov, L. N. Zakharov, D. R. Tyler, *Inorg. Chem.* **2009**, *48*, 2976–2984.

446. C. M. Nagaraja, M. Nethaji, B. R. Jagirdar, *Inorg. Chem.* **2005**, *44*, 4145–4147.

447. N. Aebischer, U. Frey, A. E. Merbach, *Chem. Commun.* **1998**, 2303–2304.

448. J. Malin, H. Taube, *Inorg. Chem.* **1971**, *10*, 2403–2406.

449. W. D. Harman, H. Taube, *J. Am. Chem. Soc.* **1990**, *112*, 2261–2263.

450. Z.-W. Li, H. Taube, *J. Am. Chem. Soc.* **1991**, *113*, 8946–8947.

451. R. H. Morris, *Coord. Chem. Rev.* **2008**, *252*, 2381–2394.

452. P. A. Maltby, M. Schlaf, M. Steinbeck, A. J. Lough, R. H. Morris, W. T. Klooster, T. F. Koetzle, R. C. Srivastava, *J. Am. Chem. Soc.* **1996**, *118*, 5396–5407.

453. G. Jia, R. H. Morris, *J. Am. Chem. Soc.* **1991**, *113*, 875–883.

454. J. R. Sowa, R. J. Angelici, *Inorg. Chem.* **1991**, *30*, 3534–3537.

455. J. R. Sowa, V. Zanotti, G. Facchin, R. J. Angelici, *J. Am. Chem. Soc.* **1992**, *114*, 160–165.

456. M. A. Ortuño, L. Castro, M. Bühl, *Organometallics* **2013**, *32*, 6437–6444.

457. F. R. Bregman, J. M. Ernsting, F. Müller, M. D. K. Boele, L. A. van der Veen, C. J. Elsevier, *J. Organomet. Chem.* **1999**, *592*, 306–311.

458. S. Filipuzzi, E. Männel, P. S. Pregosin, A. Albinati, S. Rizzato, L. F. Veiros, *Organometallics* **2008**, *27*, 4580–4588.

459. M. Bühl, *Organometallics* **1997**, *16*, 261–267.

460. W. Leitner, M. Bühl, R. Fornika, C. Six, W. Baumann, E. Dinjus, M. Kessler, C. Krüger, A. Rufińska, *Organometallics* **1999**, *18*, 1196–1206.

461. M. Bühl, W. Baumann, R. Kadyrov, A. Börner, *Helv. Chim. Acta* **1999**, *82*, 811–820.

462. J. G. Donkervoort, M. Bühl, J. M. Ernsting, C. J. Elsevier, *Eur. J. Inorg. Chem.* **1999**, 27–33.

463. M. Bühl, M. Hakånsson, A. H. Mahmoudkhani, L. Öhrström, *Organometallics* **2000**, *19*, 5589–5596.

464. L. Orian, A. Bisello, S. Santi, A. Ceccon, G. Saielli, *Chem. Eur. J.* **2004**, *10*, 4029–4040.

465. O. Q. Munro, G. L. Camp, L. Carlton, *Eur. J. Inorg. Chem.* **2009**, 2512–2523.

466. *The Handbook of Homogeneous Hydrogenation*, ed. J. G. de Vries, C. J. Elsevier, Wiley-VCH, Weinheim, 2007, Vols. 1–3.

467. A. Fabrello, A. Bachelier, M. Urrutigoïty, P. Kalck, *Coord. Chem. Rev.* **2010**, 254, 273–287.

468. A. Fabrello, C. Dioni, L. Perrin, P. Kalck, L. Maron, M. Urrutigoïty, O. Dechy-Cabaret, *Magn. Reson. Chem.* **2010**, *48*, 848–856.

469. S. Huzinaga, M. Klobukowski, *J. Mol. Struct.* **1988**, *167*, 1–209.

470. H.-J. Drexler, S. Zhang, A. Sun, A. Spannenberg, A. Arrieta, A. Preetz, D. Heller, *Tetrahedron: Asymmetry* **2004**, *15*, 2139–2150.

471. M. J. Burk, J. E. Feaster, R. L. Harlow, *Organometallics* **1990**, *9*, 2653–2655.

472. M. P. Anderson, L. H. Pignolet, *Inorg. Chem.* **1981**, *20*, 4101–4107.

473. A. Preetz, H.-J. Drexler, S. Schulz, D. Heller, *Tetrahedron: Asymmetry* **2010**, 21, 1226–1231.

474. S. Grigoleit, M. Bühl, *Chem. Eur. J.* **2004**, *10*, 5541–5552.

475. P. S. Pregosin, P. G. A. Kumar, I. Fernández, *Chem. Rev.* **2005**, *105*, 2977–2998.

476. P. G. A. Kumar, P. S. Pregosin, T. M. Schmid, G. Consiglio, *Magn. Reson. Chem.* **2004**, *42*, 795–800.

477. R. Kempe, A. Spannenberg, D. Z. Heller, *Kristallogr.-New Cryst. Struct.* **2001**, *216*, 153–156.

478. R. D. Ernst, J. W. Freeman, L. Stahl, D. R. Wilson, A. M. Arif, B. Nuber, M. L. Ziegler, *J. Am. Chem. Soc.* **1995**, *117*, 5075–5081.

479. G. Frenking, K. Wichmann, N. Fröhlich, J. Grobe, W. Golla, D. Le Van, B. Krebs, M. Läge, *Organometallics* **2002**, *21*, 2921–2930.

480. L. P. Hammett, *J. Am. Chem. Soc.* **1937**, *59*, 98–103.

481. C. Hansch, A. Leo, R. W. Taft, *Chem. Rev.* **1991**, *91*, 165–195.

482. J. March, *Advanced Organic Chemistry*, Wiley, New York, 3rd edn., 1985, p. 244.

483. J. C. Davis, M. Bühl, K. R. Koch, *J. Phys. Chem. A* **2013**, *117*, 8054–8064.

A

Annex

Published Papers
related to the PhD Thesis

The wizard who reads a thousand books is powerful.
The wizard who memorizes a thousand books is insane.

Battle of Wits in Magic the Gathering

Reference 252

JACS
JOURNAL OF THE AMERICAN CHEMICAL SOCIETY
Communication
pubs.acs.org/JACS

Characterization of a Paramagnetic, Mononuclear Pt(III)−Alkyl Complex Intermediate in Carbon−Halogen Bond Coupling Reactions

Orestes Rivada-Wheelaghan,[†] Manuel A. Ortuño,[‡] Josefina Díez,[§] Sergio E. García-Garrido,[§] Celia Maya,[†] Agustí Lledós,*[,‡] and Salvador Conejero*[,†]

[†]Instituto de Investigaciones Químicas (IIQ), Departamento de Química Inorgánica, CSIC and Universidad de Sevilla, Avda. Américo Vespucio 49, 41092, Sevilla, Spain

[‡]Departament de Química, Universitat Autònoma de Barcelona, Edifici Cn, 08193 Cerdanyola del Vallès, Spain

[§]Laboratorio de Compuestos Organometálicos y Catálisis (Unidad Asociada al CSIC), Departamento de Química Orgánica e Inorgánica, Universidad de Oviedo, C/Julián Clavería 8, 33006 Oviedo, Spain

Supporting Information

ABSTRACT: Addition of Br_2 or I_2 to 14-electron, cationic Pt(II)-alkyl complexes led to the formation of the corresponding carbon−halogen Pt(II) coupling products. Low temperature experiments with Br_2 allowed us to isolate and characterize crystallographically a very unusual mononuclear, paramagnetic Pt(III)-alkyl intermediate with a seesaw structure that can be further oxidized to a transient Pt(IV) species before reductive carbon−halogen coupling reaction takes place.

Oxidation of platinum(II) alkyl complexes is of central importance in the catalytic and/or stoichiometric functionalization of C−H bonds of hydrocarbons.[1] This is particularly true for the oxidation of methane to chloroform and methanol in the Shilov chemistry, for which several reports point to the participation of Pt(IV) complexes as key intermediates in the formation of the functionalized (oxidized) methane.[2] However, in a few occasions, it has been suggested that oxidation reactions (either chemical or electrochemical) of platinum(II) alkyls lead to the formation of transient paramagnetic Pt(III) species that with no exception are either very unstable toward disproportionation to Pt(II) and Pt(IV) or easily oxidized to Pt(IV), making it impossible to ascertain their nature.[3] For example, Labinger, Bercaw, and Goldberg reported that, during oxidation of dimethylplatinum(II) complexes $[Pt(CH_3)_2(L\text{-}L)]$ (L-L = bpy, phen, tmeda) by O_2, formation of blue solutions containing mixed-valence oligoplatinum paramagnetic species of similar nature than the so-called platinum blues[4] were detected before final oxidation to Pt(IV) compounds occurred.[3d] Similarly, Tilset found that electrochemical oxidation of bis(imine) dimethylplatinun(II) $[Pt(CH_3)_2(N\text{−}N)]$ complexes afford Pt(II) and Pt(IV) compounds formed through a formal disproportionation of short-lived Pt(III) species.[3c] Although dialkyl Pt(III) complexes appear to be very unstable,[5] Bercaw and Labinger have hinted that monomethyl-Pt(III) derivatives might have longer half-lives.[2a] Nevertheless, no reports on stable Pt(III)-monoalkyl complexes have been published. Herein, we describe the synthesis and X-ray characterization of the first mononuclear Pt(III)-alkyl complex that, in addition, is an intermediate in carbon−halogen coupling reactions during oxidation reactions of Pt(II)-alkyl compounds with bromine.[6]

We[7a,b] and others[8] have recently reported that N-heterocyclic carbene ligands (NHCs) promote rapid reductive elimination of ethane when reacted with the Pt(IV) tetramer $[PtMe_3I]_4$, leading to the formation of the thermodynamically favored Pt(II) complexes *trans*-$[PtMeI(NHC)_2]$. These latter complexes were used as precursors for the synthesis of coordinatively unsaturated, 14-electron Pt(II) species $[PtMe(NHC)_2]^+$ and $[Pt(NHC')(NHC)]^+$ (where NHC' stands for the cyclometalated NHC ligand).[7] Encouraged by the fact that the bulkiness of the NHC ligands destabilizes to some extent the formation of Pt(IV) complexes, we launched a research program aimed at investigating the reactivity of coordinatively unsaturated Pt(II) complexes toward halogens (Br_2 and I_2), having in mind that although a remarkable outburst of $C(sp^2)$−X (X = F, Cl, Br, I) bond forming reactions through C−H bond activation processes have appeared in recent years,[9] construction of $C(sp^3)$−X bonds is still rare.[10]

Addition of X_2 (X = Br, I) to dichloromethane solutions of the electron deficient cyclometalated complexes $[Pt(NHC')(NHC)][BAr^F]$ (NHC = IPr, **1a**; IMes*, **1b**; BAr^F = tetrakis[3,5-bis(trifluoromethyl)phenyl]borate), at rt, lead to the clean formation of complexes **2a**−**b** and **3a**−**b** (see Scheme 1) that have been identified as Pt(II) complexes on the basis of

Scheme 1

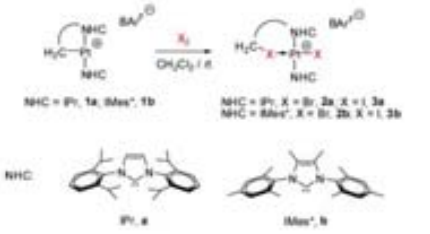

Received: July 20, 2012
Published: August 30, 2012

   dx.doi.org/10.1021/ja307139p | J. Am. Chem. Soc. 2012, 134, 15261−15264

Reference 274

Dalton Transactions

RSC Publishing

PAPER

View Article Online
View Journal | View Issue

Solution dynamics of agostic interactions in T-shaped Pt(II) complexes from *ab initio* molecular dynamics simulations†

Cite this: Dalton Trans., 2013, 42, 12165

Manuel A. Ortuño,[a] Pietro Vidossich,*[a] Gregori Ujaque,[a] Salvador Conejero[b] and Agustí Lledós*[a]

Received 21st March 2013,
Accepted 7th June 2013

DOI: 10.1039/c3dt50761k

www.rsc.org/dalton

Transition metal complexes forming agostic interactions have been extensively surveyed. However, the dynamic behaviour of these interactions is less documented though it could be crucial in chemical processes. For this purpose, *ab initio* molecular dynamics simulations (AIMD) of some representative T-shaped Pt(II) complexes (quantum mechanics) have been performed in an explicit dichloromethane solvent (molecular mechanics). The dynamics of the agostic interaction in solution strongly depends on the complex, going from stiff to flexible on–off agostic interactions at the time scale of the simulations (about 15 ps). Such behaviour can only be observed by using AIMD methods in solution.

Introduction

The concept of agostic interactions[1,2] has come a long way since Brookhart and Green coined this name to define the intramolecular interaction between a C–H bond and an electron deficient metal centre. Whilst they were initially considered to be rare, it is now accepted that they are rather common when describing coordinatively unsaturated transition metal complexes.[3] A lot of work has been devoted to assess the presence of agostic interactions. From the experimental side, the existence of a M···HC agostic interaction is mostly established by structural and spectroscopic techniques.[2] Calculations have also been used for this aim,[4–6] complementing geometry optimisations (usually in gas phase) to show the closeness of the C–H bond to the metal centre with analyses of the nature of the interaction using many theoretical tools (usually Bader's Atoms in Molecules Theory and Natural Bond Orbital Analysis).[7–16] Recently, these analyses have revealed significant differences in β-agostic interactions involving early and late transition metal complexes[17] and have allowed us to discriminate between agostic and non-agostic situations when a hydrogen atom is forced into close vicinity to the transition metal by steric factors.[18]

It is now apparent that the word "agostic" covers a wide variety of subtly different situations.[3,4] Even the role of the agostic interaction is ambivalent: in some cases it prompts a C–H bond activation process, whereas in other cases it only provides stabilisation of transition metal compounds featuring open coordination sites, protecting the metal from intruders. Three-coordinate T-shaped Pt(II) complexes sharply show the diversity of situations encompassing a common definition of agostic complexes. These unsaturated species have been proposed to participate as intermediates in several organometallic processes, including C–H bond activation reactions.[19,20] In these highly electrophilic, formally 14-electron species, the presence of an agostic interaction can relieve the unsaturation. Isolation of formally three-coordinate T-shaped Pt(II) species was achieved by means of bulky trialkyl phosphine ligands.[21–26] Recently, some of us have described the synthesis of this kind of species using *N*-heterocyclic carbene (NHC) ligands.[27,28] In almost all cases, agostic interactions are involved in the stabilisation of these unusual species.[29] The compounds structurally characterised by X-ray diffraction are collected in Scheme 1, together with the experimentally determined distances corresponding to the C–H bonds closest to the metal centre.

Although the solid state structures of complexes **1–6** already display notable differences regarding the agostic coordination, the largest disparity is found in their dynamic behaviour in solution. **1** and similar β-agostic complexes of the type [Pt(R)(P–P)]$^+$ (P–P = chelating diphosphine; R = alkyl) behave as arrested intermediates in intramolecular C–H bond activation

[a]Departament de Química, Universitat Autònoma de Barcelona, 08193 Cerdanyola del Vallès, Spain. E-mail: vido@klingon.uab.es, agusti@klingon.uab.es; Fax: +34-935812477
[b]Instituto de Investigaciones Químicas (IIQ), Departamento de Química Inorgánica, CSIC and Universidad de Sevilla, Avda. Américo Vespucio 49, 41092 Sevilla, Spain

†Electronic supplementary information (ESI) available: Computational details, Fig. S1–S5 and Cartesian coordinates of gas-phase geometries. See DOI: 10.1039/c3dt50761k

Reference 338

Angewandte Communications

Agostic Interactions

DOI: 10.1002/anie.201200070

Tuning N-Heterocyclic Carbenes in T-Shaped Pt^{II} Complexes for Intermolecular C–H Bond Activation of Arenes**

Orestes Rivada-Wheelaghan, Manuel A. Ortuño, Josefina Díez, Agustí Lledós, and Salvador Conejero**

Dedicated to Professor Guy Bertrand on the occasion of his 60th birthday

C–H bond activation of hydrocarbons promoted by Pt^{II} complexes have been intensively studied since Shilov's first report on the catalytic conversion of methane into methanol and methyl chloride by $PtCl_4^{2-}$ salts.[1] Mechanistically, the first step of this process, prior to C–H bond cleavage of methane, is coordination of the hydrocarbon to the platinum center, and this might occur either associatively or with prior dissociation of a coordinated ligand. Although in most cases the C–H bond activation at Pt^{II} centers seems to take place by an associative mechanism,[1b] there are theoretical and experimental evidences in good agreement with a dissociative pathway that involves the formation of transient T-shaped 14-electron Pt^{II} species.[2] Some of these coordinatively unsaturated highly electrophilic species have been isolated and crystallographically characterized,[3] and a few of them undergo intramolecular C–H bond activation (cyclometalation) reactions. Nevertheless, we are not aware of intermolecular C–H bond cleavage of hydrocarbons induced by stable T-shaped Pt^{II} complexes. Recently, we have described the synthesis of this kind of highly electrophilic species stabilized by agostic interactions with N-heterocyclic carbene (NHC) ligands.[4] Herein, we report that alteration of the environment of the NHC ligands allows fine tuning of the steric and electronic properties of their platinum complexes, thereby enabling intermolecular C–H bond activation of some arenes.[5]

Previously,[4] we prepared the unsaturated, cationic Pt^{II} compounds $[PtMe(IPr)_2][BAr^f_4]$ (**2b**) and $[Pt(NHC^*)(NHC)][BAr^f_4]$, where NHC* represents the cyclometalated ligands IrBu for compound **3a** and IPr for compound **3b** (Scheme 1a). The IrBu species **2a** converts rapidly into **3a** and

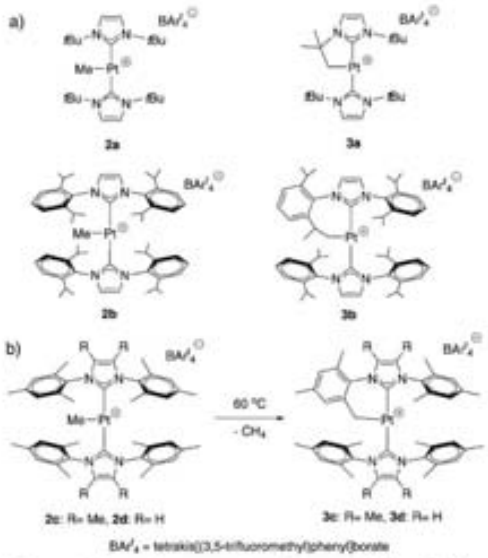

Scheme 1. a) Structural representations of compounds **2b** and **3a–b**, described in ref. [4], and of compound **2a**, which cannot be isolated but converts rapidly into **3a**. b) Synthesis of the cyclometalated complexes **3c–d**.

cannot be isolated. By following a similar synthetic method, namely reaction of $[PtMe_3I]_4$ with the corresponding NHC ligand and subsequent treatment with $NaBAr^f_4$, the analogous complexes **2c** and **3c** with the NHC ligand IMes* and complexes **2d** and **3d** with the NHC ligand IMes have been prepared and characterized (Scheme 1b).

The Lewis-acidic behavior of the cationic compounds **2b–c** and **3a–c** becomes evident in their reactions with aceto-

[*] O. Rivada-Wheelaghan, Dr. S. Conejero
Instituto de Investigaciones Químicas (IIQ)—Departamento de Química Inorgánica, CSIC/Universidad de Sevilla
Avda. Américo Vespucio 49, 41092 Sevilla (Spain)
E-mail: sconejero@iiq.csic.es
M. A. Ortuño, Prof. A. Lledós
Departament de Química
Universitat Autònoma de Barcelona (UAB)
Edifici Cn, 08193 Cerdanyola del Vallès (Spain)
E-mail: agusti@klingon.uab.es
Prof. J. Díez
Departamento de Química Orgánica e Inorgánica
Universidad de Oviedo
C/Julián Claveria 8, 33006 Oviedo (Spain)

[**] Financial support from the Junta de Andalucía (project No. FQM-3151) and the Spanish Ministerio de Ciencia e Innovación (projects CTQ2011-23336, CTQ2010-17476 and CONSOLIDER-INGENIO 2010 CSD2007-00006, FEDER support) is acknowledged. O.R.-W. and M.A.O. thank the Spanish Ministerio de Ciencia e Innovación for a research grant. The authors thank Prof. Ernesto Carmona for helpful discussions.

Supporting information for this article is available on the WWW under http://dx.doi.org/10.1002/anie.201200070.

Reference 355

M. A. Ortuño, A. Lledós, F. Maseras, G. Ujaque, *ChemCatChem* **2014**
DOI: 10.1002/cctc.201402326

Reference 392

JACS
JOURNAL OF THE AMERICAN CHEMICAL SOCIETY
Article
pubs.acs.org/JACS

Mechanistic Studies on the Pd-Catalyzed Vinylation of Aryl Halides with Vinylalkoxysilanes in Water: The Effect of the Solvent and NaOH Promoter

Alvaro Gordillo,[†] Manuel A. Ortuño,[‡] Carmen López-Mardomingo,[†] Agustí Lledós,[‡] Gregori Ujaque,*[,‡] and Ernesto de Jesús*[,†]

[†]Departamento de Química Orgánica y Química Inorgánica, Universidad de Alcalá, Edificio de Farmacia, Campus Universitario, E28871 Alcalá de Henares, Madrid, Spain

[‡]Departament de Química Física, Universitat Autònoma de Barcelona, Edifici C.n, 08193 Cerdanyola del Vallès, Catalonia, Spain

Supporting Information

ABSTRACT: The mechanism of the Pd-catalyzed vinylation of aryl halides with vinylalkoxysilanes in water has been studied using different catalytic precursors. The NaOH promoter converts the initial vinylalkoxysilane into a highly reactive water-soluble vinylsilanolate species. Similarly, deuterium-labeling experiments have shown that, irrespective of the catalytic precursor used, vinylation occurs exclusively at the CH vinylic functionality via a Heck reaction and not at the C–Si bond via a Hiyama cross-coupling. The involvement of a Heck mechanism is interpreted in terms of the reduced nucleophilicity of the base in water, which disfavors the transmetalation step. The Heck product (*β*-silylvinylarene) undergoes partial desilylation, with formation of a vinylarene, by three different routes: (a) hydrolytic desilylation by the aqueous solvent (only at high temperature); (b) transmetalation of the silyl olefin on the PdH Heck intermediate followed by reductive elimination of vinylarene; (c) reinsertion of the silyl olefin into the PdH bond of the Heck intermediate followed by *β*-Si *syn*-elimination. Both the Hiyama and Heck catalytic cycles and desilylation mechanisms b and c have been computationally evaluated for the $[Pd(en)Cl_2]$ precursor in water as solvent. The calculated Gibbs energy barriers support the reinsertion route proposed on the basis of the experimental results.

INTRODUCTION

Recent work in the field of Pd-catalyzed C–C coupling reactions between aryl or vinyl halides and organometallic species (organoboron, -tin, -silicon, -magnesium, etc.) has tended to concentrate on the search for processes that occur under mild conditions, employ readily available cost- and atom-efficient starting materials, and avoid the formation of byproducts or the use of toxic reagents.[1] In this context, organosilicon compounds are remarkable for their low toxicity, environmental friendliness, and high chemical stability.[2] The development of organosilanes as cross-coupling partners has lagged behind that of other organometallic compounds because of the lower reactivity of the low-polarized silicon–carbon bond. Although the first examples of the vinylation of aryl halides with vinyltrimethylsilanes were reported in the early 1980s,[3] these actually involved one of the C–H bonds of the vinyl group in a Mizoroki–Heck[4] process (Figure 1a).[5] As a result, the major product of the reaction was often a styrene due to loss of the silicon group via a hydrodesilylation process subsequent to the Heck coupling. The increasing synthetic interest in *β*-silylstyrene intermediates stimulated the search by groups such as those of Hallberg,[6] Kikukawa,[7] or Jeffery[8] for reaction conditions that could inhibit this desilylation step. A major breakthrough in this respect was reported in 1989, when Hiyama and Hatanaka published the fluoride-promoted cross-coupling of organosilanes and haloarenes (Figure 1b).[9] It was assumed that the formation of pentacoordinate silicates accelerated the rate-determining transmetalation step (Figure 1c). Accordingly, the alkenylsilanes became more reactive when their fluorophilicity was increased upon replacing methyl substituents with fluorides.[10] However, the preformation of a stable, pentacoordinate silicate intermediate prior to the transmetalation step may not be key to the cross-coupling reaction because theoretical calculations have suggested that formation of the Si–F bond may occur in a concerted manner with transfer of the vinyl group from Si to Pd, thus stabilizing the transition state of the transmetalation step.[11]

The subsequent introduction of silanols as coupling partners was aimed at improving the reactivity and selectivity of these reactions as a result of their ability to coordinate to palladium via the oxygen atom. In the course of these studies, Mori, Hiyama, and co-workers discovered that silver oxide promoted the cross-coupling of aryl- or alkenylsilanols under fluoride-free conditions.[12] A major breakthrough in this respect was the finding by Denmark and Sweis that the deprotonation of

Received: April 29, 2013
Published: August 22, 2013

dx.doi.org/10.1021/ja404255u | J. Am. Chem. Soc. 2013, 135, 13749–13763

Reference 456

ORGANOMETALLICS

Article

pubs.acs.org/Organometallics

Computational Insight into ^{103}Rh Chemical Shift−Structure Correlations in Rhodium Bis(phosphine) Complexes

Manuel A. Ortuño,[†] Ludovic Castro,[‡] and Michael Bühl*[,‡]

[†]Unitat de Química Física, Departament de Química, Universitat Autònoma de Barcelona, 08193 Cerdanyola del Vallès, Barcelona, Spain

[‡]School of Chemistry, University of St Andrews, North Haugh, St Andrews, Fife KY10 9ST, U.K.

Supporting Information

ABSTRACT: ^{103}Rh NMR chemical shifts have been computed at the GIAO-B3LYP level of density functional theory (DFT) for a number of [Rh(COD)(P∩P)]$^+$ complexes [COD = 1,5-cyclooctadiene, P∩P = chelating bis(phosphine) including bis(dimethylphosphino)ethane (dmpe), bis(diphenylphosphino)ethane (dmpe), MeDUPHOS, DIOP, BINAP, and others]. Structures have been optimized using PBE0 and M06 functionals in the gas phase, in a continuum modeling the solvent, and with $[PF_6]^-$ counteranion included explicitly. Observed trends in $\delta(^{103}Rh)$ are well reproduced for pristine PBE0-optimized cations in the gas phase or for ion pairs optimized in a continuum with M06. While there is no overall trend between computed $\delta(^{103}Rh)$ values and complex stabilities (evaluated through isodesmic ligand exchange reactions), there is a linear relationship between the ^{103}Rh chemical shifts and the mean Rh−P bond distances. This relationship appears to be remarkably general, encompassing various chelating ring sizes and substituents at P, including remote electron-donating and -withdrawing substituents that are characterized through their Hammett constants. The combination of ^{103}Rh NMR and DFT computations emerges as a useful tool for structure elucidation of Rh−phosphine complexes.

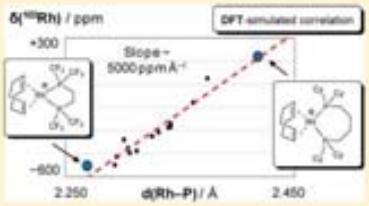

INTRODUCTION

Rhodium chemistry is a cornerstone in homogeneous catalysis since the corresponding complexes are key species in relevant processes such as hydrogenation reactions and hydroformylation of alkenes. The design of new and improved catalysts requires thorough analysis of such species. In order to obtain further insight, ^{103}Rh nuclear magnetic resonance (NMR) spectroscopy emerges as a captivating analytical tool to study the very center of these metal compounds,[1,2] including those of active catalysts.[3]

As rhodium complexes bearing phosphine ligands are particularly well suited to be studied with ^{103}Rh NMR spectroscopy, a wealth of experimental data are available.[2b,c,4−6]

A priori there is no straightforward general relationship between chemical shifts and reactivity. However, a number of such relationships have been established empirically within closely related families of compounds.[2a] For instance, ^{103}Rh chemical shifts have been correlated with rate constants of ligand exchange[7] and migration reactions,[8] enantioselectivities,[9] and stability constants.[10] More recently, rates of water substitution processes in rhodium clusters have been shown to correlate with chemical shifts.[11] Similar NMR−reactivity relations have also been observed or predicted in other organometallic systems, e.g., using ^{59}Co[12] or ^{51}V NMR.[13] As a whole, transition metal NMR is a useful tool to study structural features as well as reactivities.

The chemical environment about the metal can be adjusted by tuning and tailoring the ligands. Quantum-chemical computations can be a valuable complement because they can be used to study ligands or ligand configurations that are not accessible experimentally and to investigate properties of transition metal complexes in a systematic way. Theory can predict structures, energies, and NMR properties, and the resulting trends may be rationalized. In this regard, computational techniques based on density functional theory (DFT) have been successfully applied to reproduce ^{103}Rh chemical shifts, among other transition metals.[4,13] First computational studies on ^{103}Rh nuclei were devoted to organometallic compounds which span a sizable chemical shift range of ca. 3600 ppm.[16,17] The scope of this methodology has been extended to species containing phosphines,[18,19] N-donors,[20] and alkene ligands,[21] as well as imidazole-based radiosensitizers.[22] Other complexes including indacenyl[23] and porphyrin[24] derivatives have also been analyzed.

The Rh−bis(phosphine) fragment has provided excellent results in catalytic processes such as hydrogenation reactions.[25] In this context, a series of cationic [(COD)Rh(P∩P)]$^+$ complexes **1**−**7** (Figure 1, COD = 1,5-cyclooctadiene, P∩P = chelating bis(phosphine)), useful in hydrogenation of enamides,[26] has been studied recently, and their observed ^{103}Rh chemical shifts have been correlated with computed relative stabilities.[27] We now report geometries and ^{103}Rh chemical shifts of **1**−**7**, calculated with different and improved

Received: August 2, 2013
Published: October 4, 2013

dx.doi.org/10.1021/om400774y | Organometallics 2013, 32, 6437−6444

B

Annex

Published Papers

non-related to the PhD Thesis

Lisa, get in here!

In this house we obey the laws of thermodynamics!

Homer Simpson in The Simpsons

Reference 45

Beilstein Journal of Organic Chemistry

True and masked three-coordinate T-shaped platinum(II) intermediates

Manuel A. Ortuño[1], Salvador Conejero*[2] and Agustí Lledós*[1]

Review

Open Access

Address:
[1]Departament de Química, Universitat Autònoma de Barcelona, 08193 Cerdanyola del Vallès, Spain and [2]Instituto de Investigaciones Químicas (IIQ), Departamento de Química Inorgánica, CSIC and Universidad de Sevilla, Avda. Américo Vespucio 49, 41092 Sevilla, Spain

Email:
Salvador Conejero* - sconejero@iiq.csic.es; Agustí Lledós* - agusti@klingon.uab.es

* Corresponding author

Keywords:
C–H bond activation; intermediate; platinum(II); reactive intermediates; three-coordinate; T-shaped

Beilstein J. Org. Chem. **2013,** *9,* 1352–1382.
doi:10.3762/bjoc.9.153

Received: 05 April 2013
Accepted: 10 June 2013
Published: 09 July 2013

This article is part of the Thematic Series "New reactive intermediates in organic chemistry".

Guest Editor: G. Bucher

Abstract

Although four-coordinate square-planar geometries, with a formally 16-electron counting, are absolutely dominant in isolated Pt(II) complexes, three-coordinate, 14-electron Pt(II) complexes are believed to be key intermediates in a number of platinum-mediated organometallic transformations. Although very few authenticated three-coordinate Pt(II) complexes have been characterized, a much larger number of complexes can be described as operationally three-coordinate in a kinetic sense. In these compounds, which we have called masked T-shaped complexes, the fourth position is occupied by a very weak ligand (agostic bond, solvent molecule or counteranion), which can be easily displaced. This review summarizes the structural features of the true and masked T-shaped Pt(II) complexes reported so far and describes synthetic strategies employed for their formation. Moreover, recent experimental and theoretical reports are analyzed, which suggest the involvement of such intermediates in reaction mechanisms, particularly C–H bond-activation processes.

Review

Scope of this review

Reaction intermediates are transient species able to undergo transformations along chemical processes. Electron deficient transition-metal complexes with vacant coordination sites are well-suited to play such a role. Coordinatively and electronically unsaturated species have often been invoked as crucial intermediates in reactions involving late transition-metal complexes. Ligand dissociation, forming intermediates with open coordination sites, has been proposed as the initial step in many reactions involving square-planar d^8 organometallic complexes [1]. Four-coordinate square-planar structures, with a formally 16-electron counting, are absolutely dominant in isolated Pt(II) complexes. However, three-coordinate, 14-elec-

Reference 262

ChemComm

COMMUNICATION

View Article Online
View Journal | View Issue

A stable, mononuclear, cationic Pt(III) complex stabilised by bulky N-heterocyclic carbenes†

Cite this: Chem. Commun., 2014, 50, 1299

Received 8th November 2013,
Accepted 28th November 2013

DOI: 10.1039/c3cc48553f

www.rsc.org/chemcomm

Orestes Rivada-Wheelaghan,[a] Manuel A. Ortuño,[b] Sergio E. García-Garrido,[c] Josefina Díez,[c] Pablo J. Alonso,[d] Agustí Lledós*[b] and Salvador Conejero*[a]

The thermally stable, paramagnetic Pt(III) complex $[PtI_2(IPr)_2][BAr^F]$ has been prepared by oxidation of the Pt(II) complex $[PtI_2(IPr)_2]$ with iodine in the presence of $NaBAr^F$. X-ray crystallographic studies revealed the mononuclear nature of this species with a square-planar geometry. EPR and DFT studies pointed out to a metal-centred radical.

Platinum compounds in closed-shell oxidation states of (0), (II), and (IV) abound in the literature, but less is known about their (I) and (III) open-shell counterparts. Although dinuclear Pt(III) species are well known,[1] the scarcity of well characterised paramagnetic mononuclear Pt(III) species is noteworthy,[2] despite being postulated to be transient intermediates in several chemical transformations including oxidation of platinum alkyls and aryls,[3] and anticancer activity of *cis*-platin and carboplatin.[4] In 1984, Usón *et al.* reported the first crystallographically characterised anionic, mononuclear Pt(III) complex $[Pt(C_6Cl_5)_4]^-$.[2b] Since then only a few reports have appeared on the full characterisation of mononuclear Pt(III) complexes.[2] In most of the cases, the isolation was possible by using ligands that could easily delocalise the unpaired electron or preventing their dimerisation by blocking the axial coordination sites in their octahedral complexes. Bond and Colton reported that a bulky pincer phosphine ligand allowed for the spectroscopic (electron paramagnetic resonance, EPR) characterisation of a "*moderately stable Pt(III) cation*",[3] although the authors were not able to isolate it in the pure form as a consequence of its fast disproportionation into uncharacterised Pt(II) and Pt(IV) species. Some of us have very recently isolated a paramagnetic, mononuclear Pt(III) alkyl complex $[PtBr(IPr')(IPr)][BAr^F]$ stabilised by bulky N-heterocyclic carbene (NHC) ligands IPr (where IPr is 1,3-bis(2,6-diisopropylphenyl)imidazol-2-ylidene and IPr' indicates a cyclometallated ligand) that is an intermediate in the formation of a C–Br bond.[5] The X-ray structure of this complex exhibited an unprecedented see-saw geometry. According to computational studies, such structure was not due to steric constraints but to the effect of the alkyl group in *trans* to the bromine ligand.[5] In this report we have succeeded in the isolation and characterisation, including X-ray diffraction and EPR studies, of the first mononuclear, cationic, square-planar Pt(III) complex stabilised by NHCs, particularly IPr ligands. In fact the use of NHCs for the stabilisation of third-row radical complexes is limited to two other examples recently published, in one of which electron delocalisation on the imidazol ring has been proved.[7]

The complex *trans*-$[PtMeI(IPr)_2]$[6] **1** reacts with I_2 to yield, almost quantitatively, the pale-yellow bis-iodide derivative *trans*-$[PtI_2(IPr)_2]$ **2**, formed after rapid reductive elimination of methyl iodide without detecting any Pt(IV) intermediates (Scheme 1). Compound **2** has been spectroscopically and crystallographically characterised (see ESI†).

When complex **2** is reacted with half-equivalent of I_2 in the presence of $NaBAr^F$ ($NaBAr^F$ = sodium tetrakis[3,5-bis(trifluoromethyl)phenyl]borate) in dichloromethane an intense blue solution is formed almost immediately (Scheme 1). The ^{1}H NMR spectrum of the crude reaction mixture reveals the formation of a single product showing only broad signals in the range of −7.3 to 7.9 ppm for the carbene ligands that hints at the presence of a paramagnetic species in solution, from which it has been possible to isolate the Pt(III) complex **3**. It should be pointed out that addition of either I_2 or $NaBAr^F$ alone to **2** was not productive, recovering unaltered the reactants. Only when the three reagents are mixed together the formation of **3** is achieved. Therefore, variation of the concentration of iodide through precipitation as NaI is key for the reaction to proceed. Complex **3** is fairly air-stable

[a] Instituto de Investigaciones Químicas (IIQ), Departamento de Química Inorgánica, CSIC and Universidad de Sevilla, Avda. Américo Vespucio 49, 41092 Sevilla, Spain. E-mail: sconejero@iiq.csic.es; Tel: +34 954489563
[b] Departament de Química, Universitat Autònoma de Barcelona, 08193 Cerdanyola del Vallès, Spain. E-mail: agusti@klingon.uab.es; Fax: +34 935812477; Tel: +34 935811716
[c] Laboratorio de Compuestos Organometálicos y Catálisis (Unidad asociada al CSIC), Departamento de Química Orgánica e Inorgánica, Universidad de Oviedo, C/Julián Clavería 8, 33006, Oviedo, Spain
[d] Instituto de Ciencia de Materiales de Aragón (ICMA), Universidad de Zaragoza and CSIC, C/Pedro Cerbuna 12, 50009, Zaragoza, Spain

† Electronic supplementary information (ESI) available: Experimental section, details of density functional calculations, EPR and magnetic measurements, and X-ray crystallographic data. CCDC 969273 and 969274. For ESI and crystallographic data in CIF or other electronic format see DOI: 10.1039/c3cc48553f

Reference 320

Inorganic Chemistry

Article

pubs.acs.org/IC

Reactivity of Coordinatively Unsaturated Bis(N-heterocyclic carbene) Pt(II) Complexes toward H_2. Crystal Structure of a 14-Electron Pt(II) Hydride Complex

Orestes Rivada-Wheelaghan,[†] Marta Roselló-Merino,[†] Manuel A. Ortuño,[‡] Pietro Vidossich,[‡] Enrique Gutiérrez-Puebla,[§] Agustí Lledós,*[,‡] and Salvador Conejero*[,†]

[†]Departamento de Química Inorgánica, CSIC and Universidad de Sevilla, Instituto de Investigaciones Químicas (IIQ), Avda. Américo Vespucio 49, 41092, Sevilla, Spain

[‡]Departament de Química, Universitat Autònoma de Barcelona, 08193, Cerdanyola del Vallès, Spain

[§]Instituto de Ciencia de Materiales de Madrid, ICMM-CSIC, Cantoblanco, 28049, Madrid, Spain

Supporting Information

ABSTRACT: The reactivity toward H_2 of coordinatively unsaturated Pt(II) complexes, stabilized by N-heterocyclic carbene (NHC) ligands, is herein analyzed. The cationic platinum complexes $[Pt(NHC')(NHC)]^+$ (where NHC' stands for a cyclometalated NHC ligand) react very fast with H_2 at room temperature, leading to hydrogenolysis of the Pt−CH_2 bond and concomitant formation of hydride derivatives $[PtH(NHC)_2]^+$ or hydrido−dihydrogen complexes $[PtH(H_2)(NHC)_2]^+$. The latter species release H_2 when these compounds are subjected to vacuum. The X-ray structure of complex $[PtH(IPr)_2][SbF_6]$ revealed its unsaturated nature, exhibiting a true T-shaped structure without stabilization by agostic interactions. Density functional theory calculations indicate that the binding and reaction of H_2 in complexes $[PtH(H_2)(NHC)_2]^+$ is more favored for derivatives bearing aryl-substituted NHCs (IPr, 1,3-bis(2,6-diisopropylphenyl)-imidazol-2-ylidene and IMes = 1,3-dimesityl-1,3-dihydro-2H-imidazol-2-ylidene) than for those containing *tert*-butyl groups (I^{t}Bu). This outcome is related to the higher close-range steric effects of the I^{t}Bu ligands. Accordingly, H/D exchange reactions between hydrides $[PtH(NHC)_2]^+$ and D_2 take place considerably faster for IPr and IMes* derivatives than for I^{t}Bu ones. The reaction mechanisms for both H_2 addition and H/D exchange processes depend on the nature of the NHC ligand, operating through oxidative addition transition states in the case of IPr and IMes* or by a σ-complex assisted-metathesis mechanism in the case of I^{t}Bu.

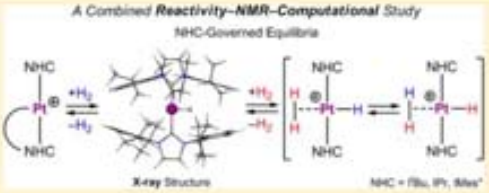

INTRODUCTION

The catalytic dehydrogenation of amine−boranes, and particularly ammonia−borane, has emerged as a powerful method for the generation of dihydrogen under mild conditions.[1] Several transition-metal complexes are known to be active in this process.[1d,2] Recently, we have reported that the low-electron count Pt(II) complex $[Pt(I^tBu')(I^tBu)][BAr^F]$ **1a** (where I^{t}Bu is 1,3-di-*tert*-butyl-imidazol-2-ylidene and I^{t}Bu' is the cyclometalated ligand) is able to dehydrogenate dimethylamine−borane (DMAB) very efficiently at room temperature.[3] We have seen that at the end of the reaction the released dihydrogen hydrogenates the Pt−CH_2 bond of the catalyst, leading to platinum hydride $[PtH(I^tBu)_2][BAr^F]$ as the sole platinum reaction product. This result contrasts with the partial hydrogenation of Pt−CH_2 bonds of electron-deficient cyclometalated Pt(II) species based on phosphine ligands.[4,5] Therefore, it is of paramount importance to analyze the reactivity of dihydrogen[6] toward coordinatively unsaturated Pt(II) complexes[7] and the affinity of H_2 to bind this metal center. In fact, in spite of the large number of dihydrogen complexes known at present,[8] very few are based on platinum, and in all cases phosphines have been used as ancillary ligands.[9] In this sense, although N-heterocyclic carbenes (NHCs) have been extensively used as an alternative to traditional phosphine ligands in transition-metal complexes, their ability to stabilize dihydrogen species has been scarcely explored.[10] The first organometallic compounds containing both dihydrogen and NHC ligands in the same coordination sphere, $(IMes)_xRu(H)_2(\eta^2\text{-}H_2)_2(PCy_3)_{2-x}$ (IMes = 1,3-dimesityl-1,3-dihydro-2*H*-imidazol-2-ylidene; x = 1, 2), were reported in 2003.[11] The influence of the size of the N substituent on the NHC ligand on the interaction with H_2 has been demonstrated by the study of the reactivity with H_2 of the three five-coordinate ruthenium NHC hydrido complexes $[Ru(I^iPr_2Me_2)_4H]^+$ ($I^iPr_2Me_2$ = 1,3-diisopropyl-4,5-dimethylimidazol-2-ylidene), $[Ru(IEt_2Me_2)_4H]^+$ (IEt_2Me_2 = 1,3-diethyl-4,5-dimethylimidazol-2-ylidene), and $[Ru(IMe_4)_4H]^+$ (IMe_4 = 1,3,4,5-tetramethylimi-

Received: March 26, 2014
Published: April 9, 2014

Reference 327

ORGANOMETALLICS

Article

pubs.acs.org/Organometallics

Coordinatively Unsaturated T-Shaped Platinum(II) Complexes Stabilized by Small N-Heterocyclic Carbene Ligands. Synthesis and Cyclometalation

Marta Roselló-Merino,[†] Orestes Rivada-Wheelaghan,[†] Manuel A. Ortuño,[‡] Pietro Vidossich,[‡] Josefina Díez,[§] Agustí Lledós,*[‡] and Salvador Conejero*[,†]

[†]Instituto de Investigaciones Químicas (IIQ), Departamento de Química Inorgánica, CSIC and Universidad de Sevilla, Avda. Américo Vespucio 49, 41092 Sevilla, Spain

[‡]Departament de Química, Universitat Autònoma de Barcelona, 08193 Cerdanyola del Vallès, Spain

[§]Departamento de Química Orgánica e Inorgánica, Universidad de Oviedo, C/Julián Clavería 8, 33006 Oviedo, Spain

Supporting Information

ABSTRACT: The reaction of the N-heterocyclic carbenes (NHCs) I^{t}Pr$_2$Me$_2$ and I^{t}Pr$_2$ with $[PtMe_3I]_4$ does not lead to the clean formation of complexes *trans*-$[PtMeI(NHC)_2]$, as previously found for bulkier NHCs. However, these species can be prepared in high yields by an alternative procedure using the dimethyl species $[PtMe_2(NHC)_2]$ and iodomethane. The halogenated complexes *trans*-$[PtMeI(NHC)_2]$ have been used as precursors for the formation of the coordinatively unsaturated Pt(II) derivatives $[PtMe(NHC)_2][SbF_6]$ using $AgSbF_6$ as a halogen abstractor, whereas $NaBAr^F$ is not reactive enough to completely remove the iodide ligand, leading instead to the dinuclear species $[Pt_2(\mu\text{-}I)(Me)_2(NHC)_4][BAr^F]$. Alternatively, low-coordinate T-shaped complexes $[PtMe(NHC)_2][BAr^F]$ can be prepared by protonation of the dimethyl species $[PtMe_2(NHC)_2]$ with $[H(OEt_2)_2][BAr^F]$. The complex $[PtMe(I^tPr_2Me_2)_2][BAr^F]$ undergoes a cyclometalation process under mild heating, leading to the derivative $[Pt(I^tPr_2Me_2')(I^tPr_2Me_2)][BAr^F]$ (where the prime denotes the cyclometalated ligand). This result is in contrast with the fast cyclometalation observed for the related Pt(II) complex bearing *tert*-butyl-substituted NHC (I^{t}Bu). Different cyclometalation reaction mechanisms have been computationally addressed. DFT calculations indicate that the cyclometalation involving complexes with not very bulky NHCs ligands occurs via *cis* intermediates. Cyclometalation products bearing *tert*-butyl-substituted NHCs are kinetically and thermodynamically favored over those involving isopropyl groups.

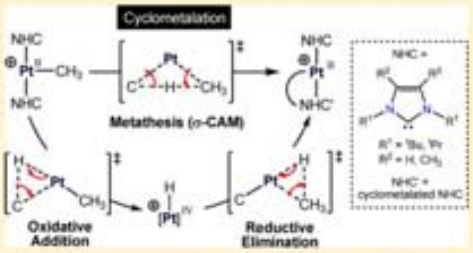

INTRODUCTION

Pt(II) complexes occupy a prominent place in the field of C−H bond activation reactions of both saturated and unsaturated hydrocarbons.[1] During the second half of the 20th century it was disclosed that some Pt(II) salts were able to exchange hydrogen atoms in C−H bonds of organic molecules by C−D bonds using D_2O as the deuterium source.[2] This impressive achievement triggered the search for new platinum-based systems for the catalytic conversion of hydrocarbons, including the very challenging methane, into more valuable chemicals.[1] Since then, a great deal of information has been obtained regarding the mechanism of C−H bond cleavage at Pt(II) centers, and some of these reports suggest the possibility of the participation of 3-coordinate, 14-electron Pt(II) species as key intermediates in these processes.[1c,d,3] Until fairly lately, very few of these unusual compounds have been isolated and crystallographically characterized, the coordinatively unsaturated Pt(II) center being stabilized by means of bulky phosphines or cyclometalated pyridine ligands.[4] Very recently, we have been involved in the isolation of these highly electrophilic species using bulky N-heterocyclic carbene (NHC) ligands.[5] According to DFT calculations, NMR spectroscopy, and X-ray diffraction studies, some of these compounds are stabilized by agostic interactions,[6] whereas others are not.[5a,c] We have also found that both the electronic and steric environments of the NHCs[7] are decisive to promote *intermolecular* C−H bond activation reactions of some aromatic compounds.[5c] Further use of these highly electrophilic species by our group includes the catalytic dehydrogenation of amine−boranes, for which a new mechanism has been found.[8]

We have previously reported that the Pt(IV) tetramer $[PtMe_3I]_4$ is an excellent precursor for the clean formation of *trans*-$[PtMeI(NHC)_2]$ species (NHC = 1,3-bis(2,6-diisopropylphenyl)imidazol-2-ylidene (IPr, **a**), 1,3-bis(2,4,6-trimethylphenyl)-4,5-dimethylimidazol-2-ylidene (IMes*, **b**),

Received: April 21, 2014
Published: July 16, 2014

Reference 431

Inorganic Chemistry

Article

pubs.acs.org/IC

Counteranion and Solvent Assistance in Ruthenium-Mediated Alkyne to Vinylidene Isomerizations

Manuel Jiménez-Tenorio,* M. Carmen Puerta,* and Pedro Valerga

Departamento de Ciencia de los Materiales e Ingeniería Metalúrgica y Química Inorgánica, Facultad de Ciencias, Universidad de Cádiz, 11510 Puerto Real, Cádiz, Spain

Manuel A. Ortuño, Gregori Ujaque, and Agustí Lledós*

Departament de Química, Universitat Autònoma de Barcelona, 08193 Cerdanyola del Vallès, Barcelona, Spain

Supporting Information

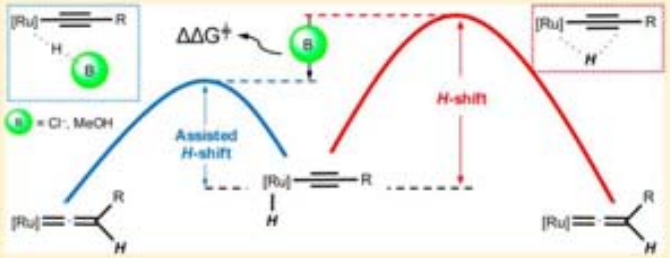

ABSTRACT: The complex [Cp*RuCl(^{i}Pr$_2$PNHPy)] (**1**) reacts with 1-alkynes HC≡CR (R = COOMe, $C_6H_4CF_3$) in dichloromethane furnishing the corresponding vinylidene complexes [Cp*Ru=C=CHR(^{i}Pr$_2$PNHPy)]Cl (R = COOMe (**2a-Cl**), $C_6H_4CF_3$ (**2b-Cl**)), whereas reaction of **1** with $NaBPh_4$ in MeOH followed by addition of HC≡CR (R = COOMe, $C_6H_4CF_3$) yields the metastable π-alkyne complexes [Cp*Ru(η^2-HC≡CR)(^{i}Pr$_2$PNHPy)][BPh_4] (R = COOMe (**3a-BPh$_4$**), $C_6H_4CF_3$ (**3b-BPh$_4$**)). The transformation of **3a-BPh$_4$**/**3b-BPh$_4$** into their respective vinylidene isomers in dichloromethane is very slow and requires hours to its completion. However, this process is accelerated by addition of LiCl in methanol solution. Reaction of **1** with HC≡CR (R = COOMe, $C_6H_4CF_3$) in MeOH goes through the intermediacy of the π-alkyne complexes [Cp*Ru(η^2-HC≡CR)(^{i}Pr$_2$PNHPy)]Cl (R = COOMe (**3a-Cl**), $C_6H_4CF_3$ (**3b-Cl**)), which rearrange to vinylidenes in minutes, i.e., much faster than their counterparts containing the [BPh_4]$^-$ anion. The kinetics of these isomerizations has been studied in solution by NMR. With the help of DFT studies, these observations have been interpreted in terms of chloride- and methanol-assisted hydrogen migrations. Calculations suggest participation of a hydrido−alkynyl intermediate in the process, in which the hydrogen atom can be transferred from the metal to the β-carbon by means of species with weak basic character acting as proton shuttles.

INTRODUCTION

Transition-metal-mediated alkyne to vinylidene isomerization is a well-known process which has attracted much attention from both experimental and theoretical points of view,[1−17] with particular emphasis on its relevance to the catalytic transformations of alkynes.[18−21] Detailed theoretical studies supported by experimental work have been performed on several systems.[5−11,13,15−17] Among those, systems containing ruthenium can be considered particularly remarkable.[2,3a,6,7c,9,10] Two mechanisms have been proposed to explain the alkyne to vinylidene isomerization process (Scheme 1): direct intramolecular 1,2-hydrogen shift in a π-alkyne complex (route **A**), or 1,3-hydrogen shift from a hydrido−alkynyl complex (route **B**), formed by oxidative addition of the 1-alkyne to the unsaturated metal center.

Variants of the two pathways shown before have been described in detail. The 1,2-H shift may occur through the intermediacy of a CH σ-bonded complex of the type [M(η^2-H−C≡CR)L_n][8−10,14] (route **AI**) or alternatively through formation of a η^2-vinylidene complex [M(η^2-C=CHR)L_n] (route **AII**). Theoretical studies suggest that the pathway involving the η^2-H−C≡CR complex is lower in energy (**AI**) and hence more feasible.[8−10,14] From the η^2-H−C≡CR intermediate, it is possible to access the hydrido−alkynyl complex [MH(C≡CR)L_n] in a straightforward manner. Ulterior 1,3-H shift leads to the final vinylidene product (route **B**).

Received: May 5, 2013
Published: July 8, 2013

dx.doi.org/10.1021/ic401117b | Inorg. Chem. 2013, 52, 8919−8932

ORGANOMETALLICS

Article

pubs.acs.org/Organometallics

Counteranion-Dependent Reaction Pathways in the Protonation of Cationic Ruthenium−Vinylidene Complexes

Manuel Jiménez-Tenorio,* M. Carmen Puerta,* and Pedro Valerga

Departamento de Ciencia de los Materiales e Ingeniería Metalúrgica y Química Inorgánica-INBIO, Facultad de Ciencias, Universidad de Cádiz, 11510 Puerto Real, Cádiz, Spain

Manuel A. Ortuño, Gregori Ujaque, and Agustí Lledós*

Departament de Química, Universitat Autònoma de Barcelona, 08193 Cerdanyola del Vallès, Barcelona, Spain

Supporting Information

ABSTRACT: The tetraphenylborate salts of the cationic vinylidene complexes $[Cp^*Ru{=}C{=}CHR(^tPr_2PNHPy)]^+$ (R = *p*-$C_6H_4CF_3$ (**1a-BPh$_4$**), Ph (**1b-BPh$_4$**), *p*-$C_6H_4CH_3$ (**1c-BPh$_4$**), *p*-C_6H_4Br (**1d-BPh$_4$**), ^{t}Bu (**1e-BPh$_4$**), H (**1f-BPh$_4$**)) have been protonated using an excess of HBF_4·OEt_2 in CD_2Cl_2, furnishing the dicationic carbyne complexes $[Cp^*Ru{\equiv}CCH_2R(^tPr_2PNHPy)]^{2+}$ (R = *p*-$C_6H_4CF_3$ (**2a**), Ph (**2b**), *p*-$C_6H_4CH_3$ (**2c**), *p*-C_6H_4Br (**2d**), ^{t}Bu (**2e**), H (**2f**)), which were characterized in solution at low temperature by NMR spectroscopy. The corresponding reaction of the chloride salts **1a-Cl**, **1b-Cl**, **1c-Cl**, and **1d-Cl** followed a different pathway, instead affording the novel alkene complexes $[Cp^*RuCl(\kappa^1(N),\eta^2(C,C)\text{-}C_5H_4N\text{-}NHP^tPr_2CH{=}CHR)][BF_4]$ (**3a−d**). In these species, the entering proton is located at the α-carbon atom of the former vinylidene ligand, which also forms a P−C bond with the phosphorus atom of the $^tPr_2PNHPy$ ligand. To shed light on the reaction mechanism, DFT calculations have been performed by considering several protonation sites. The computational results suggest metal protonation followed by insertion. The coordination of chloride to ruthenium leads to alkenyl species which can undergo a P−C coupling to yield the corresponding alkene complexes. The noncoordinating nature of $[BPh_4]^-$ does not allow the stabilization of the unsaturated species coming from the insertion step, thus preventing this alternative pathway.

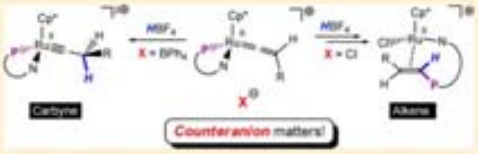

INTRODUCTION

Protonation of transition-metal vinylidene complexes is an established synthetic route for the preparation of cationic carbyne species.[1] In most cases, the β-carbon atom of the vinylidene ligand is selectively protonated, furnishing carbyne complexes (Scheme 1), although there might be alternative protonation sites in the complex leading to other feasible reaction products.[2]

Scheme 1. Protonation of Transition-Metal Vinylidene Species at the β-Carbon

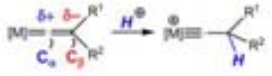

Ru−carbyne complexes are scarce.[3] At variance with this, Os−carbynes are well-known species[1b,4] due to the remarkable preference of osmium (versus ruthenium) for higher oxidation states and formation of new metal−ligand bonds.[5] Werner and co-workers reported the protonation of $[Ru{=}C{=}CHPh(H)(Cl)(PCy_3)_2]$ with acids HX having a noncoordinating anion X^- in coordinating solvents S to yield the six-coordinate Ru−carbynes $[Ru{\equiv}CCH_3(H)(Cl)(PCy_3)_2(S)]^+$ (S = Et_2O, H_2O, $PhNMe_2$).[6] In an analogous fashion, $[Ru{=}C{=}CHPh(Cl)_2(P^iPr_3)_2]$ and $[Ru{=}C{=}CHPh(CF_3COO)(Cl)(P^iPr_3)_2]$ react with $[H(OEt_2)_2][BAr'_4]$ (Ar′ = 3,5-bis(trifluoromethyl)-phenyl, $C_6H_4(CF_3)_2$) acids, yielding the carbyne complexes $[Ru{\equiv}CCH_2Ph(Cl)_2(PR_3)_2]^+$ and $[Ru{\equiv}CCH_2Ph(\kappa^2(O,O)\text{-}CF_3COO)(Cl)(PR_3)_2]^+$, respectively.[7] The neutral vinylidene complexes $[Cp^*Ru{=}C{=}CHR(Cl)(PPh_3)]$ (R = ^{t}Bu, ^{n}Bu, Ph) react with HBF_4·OEt_2 and $NaBAr'_4$, furnishing cationic carbyne derivatives of the type $[Cp^*Ru{\equiv}CCH_2R(Cl)(PPh_3)]^+$.[8] The addition of electrophiles to the β-carbon of a Ru−allenylidene complex has also been observed, leading to dicationic vinylcarbyne derivatives such as $[Cp^*Ru{\equiv}CCH{=}CRR'(dippe)]^{2+}$ (R = H, Ph; R′ = Ph; dippe = 1,2-bis(diisopropylphosphino)ethane)[9] and $[Cp^*Ru{\equiv}CCH{=}CRR'(PEt_3)_2]^{2+}$ (R = H, Ph; R′ = Ph).[10] Despite the fact that protonation usually takes place at the β-carbon of the vinylidene or allenylidene ligand, there are reports of apparent protonation at the α-carbon. This is the case for the reaction of the nitrosyl vinylidene complex $[Ru{=}C{=}CHC_6H_4Me(Cl)$-

Received: February 19, 2014
Published: May 5, 2014

dx.doi.org/10.1021/om500175x | Organometallics 2014, 33, 2549−2560

ORGANOMETALLICS

ARTICLE

pubs.acs.org/Organometallics

Internal Alkyne Isomerization to Vinylidene versus Stable π-Alkyne: Theoretical and Experimental Study on the Divergence of Analogous Cp*Ru and TpRu Systems

Vinay K. Singh,[†] Emilio Bustelo,[†] Isaac de los Ríos,[†] Ignacio Macías-Arce,[†] M. Carmen Puerta,*[,†] Pedro Valerga,*[,†] Manuel Ángel Ortuño,[‡] Gregori Ujaque,[‡] and Agustí Lledós*[,‡]

[†]Departamento de Ciencia de los Materiales e Ingeniería Metalúrgica y Química Inorgánica, Facultad de Ciencias, Universidad de Cádiz, 11510 Puerto Real (Cádiz), Spain

[‡]Departament de Química, Universitat Autònoma de Barcelona, 08193 Bellaterra, Barcelona, Spain

Supporting Information

ABSTRACT: The activation of internal alkynes by Cp*Ru and TpRu complexes gives respectively π-alkyne and disubstituted vinylidene as stable species, even though both systems bear identical pyridylphosphine ligands (κ^2-P,N-^{i}Pr$_2$PXPy, X = NH, CH$_2$, S). The activation of the alkynones PhC≡CCOR (R = Me, Ph) by [TpRuCl(^{i}Pr$_2$PXPy)] complexes allowed us to isolate and characterize metastable η^1-O═C(R)C≡CPh adducts. These complexes isomerize spontaneously to vinylidene both in solution and in the solid state. Kinetic studies have been carried out in solution by ^{31}P{^{1}H} NMR and in the solid state by IR spectroscopy, providing the Eyring and Avrami−Erofeev parameters, respectively. The activation of internal alkynes without ketone groups provided vinylidene species as well, but without isolable intermediates. In contrast with the TpRu system, the activation of alkynones by [Cp*RuCl(^{i}Pr$_2$PXPy)] always results in stable π-alkyne species. Representatives of both Cp*Ru−π-alkyne and TpRu−vinylidene compounds have been characterized by X-ray diffraction. DFT calculations have been carried out with the actual experimental complexes, including solvent effects, in order to analyze the mechanism of the π-alkyne to vinylidene isomerization of internal alkynes and to explain the divergent results obtained for Tp and Cp*.

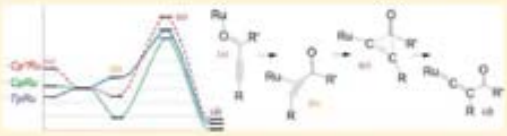

INTRODUCTION

It is well-known that the relative stability of alkyne and vinylidene isomers is reversed upon coordination to a variety of transition metals. This process (HC≡CR → :C═CHR) is the main synthetic route to vinylidene species[1,2] and is a key step for several catalytic alkyne transformations.[3] The simplest role of the metal is to stabilize the vinylidene lone pair of electrons by means of a dative carbon→metal bond, throughout a concerted 1,2-H rearrangement. A stronger participation of the metal involves the oxidative addition of the alkyne to yield alkynyl−hydride intermediates, followed by a formal 1,3-H migration. The nature and pathway of the migrating hydrogen have been the objects of numerous theoretical studies.[4] The concerted 1,2-H shift is predominant in ruthenium chemistry, with the remarkable exception of some electron-rich complexes such as [Cp*Ru(L)(PEt$_3$)$_2$][BAr$^F_4$], for which the full sequence of intermediates was isolated and characterized by X-ray diffraction (π-alkyne/alkynyl−hydride/vinylidene).[5]

The π-coordination of the alkyne to the metal is generally accepted as the first mechanistic step, but both electronic and steric factors contribute to favor the spontaneous rearrangement to the linear vinylidene chain. The higher thermodynamic stability of the vinylidene ligand is mainly explained by its better π-acceptor capability with respect to the π-alkyne isomer. As a general rule, the relative vinylidene stability will increase with the electron density on the metal center, particularly with the presence of stronger (and bulkier) donor ligands in the metal coordination sphere. This is the case of the numerous examples of stable vinylidene complexes of the type [Cp*Ru(═C═CHR)(PR$_3$)$_2$]$^+$.[6] In contrast, electron-poor dicarbonyl systems such as [CpFe(CO)$_2$(═C═CRR′)]$^+$ (R, R′ = Me, Ph) spontaneously undergo isomerization to π-alkyne complexes.[7] Intermediate situations have led to the observation of vinylidene/π-alkyne equilibria[4e] and to reversible alkyne/vinylidene isomerization, which is essential for several catalytic reactions via vinylidene intermediates.[8]

The conversion of internal alkynes to vinylidenes (RC≡CR′ → :C═CRR′) is a quite uncommon process that has just emerged during the last few years as a new promising route for the transformation of internal alkynes via vinylidene intermediates.[2] Earlier, this process had only been reported for a series of heteroatom-substituted alkynes, namely alkynylsilanes,[9] tin acetylides,[9] 1-iodo-1-alkynes,[10] and mercaptoacetylene.[11] In

Received: March 28, 2011
Published: July 05, 2011

CHEMPHYSCHEM

DOI: 10.1002/cphc.201100234

Do Metal···Water Hydrogen Bonds Hold in Solution? Insight from Ab Initio Molecular Dynamics Simulations

Pietro Vidossich,* Manuel Á. Ortuño, Gregori Ujaque, and Agustí Lledós*[a]

In recent years the scope of hydrogen bonds[1] has considerably expanded,[2] and the involvement of metal centers is one of these new fields.[3] Very recently, the neutron diffraction structure of *trans*-[$PtCl_2(NH_3)$(N-glycine)]·H_2O revealed two nonclassical intermolecular hydrogen bonds involving Pt, one with the NH_3 ligand of a neighboring complex and one with a water molecule.[4] This structure constituted the first experimental evidence for a hydrogen-bonding-like interaction between a water molecule and a d^8 metal ion and prompted the authors to propose that similar interactions should exist in solution too.[4] However, as pointed out by Falvello in his related commentary,[5] the water molecule is held fixed on top of Pt by two further H-bonds to and from the glycine carboxylic groups of adjacent complexes. Thus, the question arises to which extent the result provides indications of the hydration of Pt^{II} complexes in aqueous solution, an information which so far turned to be controversial by experimental techniques.[6] To support the conclusion that the extrapolation is appropriate, the authors supplemented the experimental finding with theoretical calculations showing that the H-bond interaction between Pt and a water molecule is indeed favorable by -4 kcal mol^{-1}.[4,7] Interestingly, we note that the Pt···HOH interaction is of similar strength as the H-bonding between water molecules and we wonder how the Pt solvation shell would adapt to account for it. Simulations in explicit solvent may provide valuable insight in this respect as they are capable of providing a detailed atomistic description of solute–solvent interactions.[8] Previous ab initio molecular dynamics (AIMD) simulations on Pt^{II} compounds showed a clear pattern of hydration in the axial region of the complex. Interestingly, both *anionic* (Pt···HOH) and *cationic* configurations (Pt···OH_2, see Scheme 1) were observed.[9–11] Furthermore, it turned out that the nature of the ligands strongly influences the hydration shell structure and the number of water molecules in the axial region.[11] It thus appears that the axial hydration pattern cannot be generalized and should be investigated for each complex of interest.

Herein, we present results from AIMD simulations of *trans*-[$PtCl_2(NH_3)$(N-glycine)] in order to provide a picture of the complex in solution and thus allow for the comparison with the interactions observed in the neutron diffraction determination. Simulations included ~100 explicit water molecules and were performed within periodic boundary conditions according to the Born–Oppenheimer approach using the CP2K program package[12] (see the Supporting Information for computational details). We based the simulations on two interaction potentials, the BLYP[13] exchange–correlation functional and the same functional supplemented by an empirical dispersion correction (BLYP-D3).[14] In fact, according to previous calculations, the anionic arrangement is favored by dispersion interactions.[4,7] Test calculations indicated that the BLYP functional provides a fair description of the energetics of the anionic arrangement compared to MP2 calculations, whereas for the cationic conformation BLYP-D3 provides a better agreement with MP2 results (see Figure S1 in the Supporting Information). We thus decided to explore how the explicit inclusion of dispersion forces would impact the outcome of the simulation.

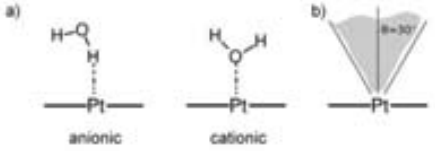

Scheme 1. a) Anionic and cationic modes of interaction of a water molecule with the Pt^{II} center of a square planar complex. b) Definition of the axial region used in the analysis. For each frame along the AIMD trajectory, the mean plane of the complex was computed. All atoms for which the angle between the vector distance from Pt and the normal vector of the plane was $< 30°$ were included in the analysis. The angle was chosen in order to avoid counting water molecules interacting with the ligands.

Following the analysis proposed by Beret et al.,[9] we restricted our attention to the axial region (see Scheme 1 for its definition) and computed the radial distribution function (rdf) taking into account only the water molecules entering this region. For the BLYP functional, the Pt···O rdf shows two peaks separated by ~1 Å (Figure 1 and Table 1). Each peak accounts for the presence of ~1 oxygen atom. On the contrary, in the Pt···O rdf from the BLYP-D3 simulation only one peak is present. Its position nearly coincides with the first peak of the BLYP Pt···O rdf although it is higher. The peak accounts for two oxygens atoms. The data indicate that for both simulations two water molecules are in the axial region within 5 Å from the metal center, one on each side of the plane of the complex. For comparison, in Section I of the Supporting Information we report the statistics of the Pt···O distances from a survey of experimentally determined crystal structures of square planar Pt^{II} complexes featuring water molecules in the axial region. As for the Pt···H rdf, both functionals give rise to two peaks, although

[a] Dr. P. Vidossich, M. Á. Ortuño, Dr. G. Ujaque, Prof. A. Lledós
Departament de Química
Universitat Autònoma de Barcelona
08193 Cerdanyola del Vallès (Spain)
Fax: (+34) 93-581 2920
E-mail: agusti@klingon.uab.es
vido@klingon.uab.es
Homepage: http://klingon.uab.cat/transmet

Supporting information for this article is available on the WWW under http://dx.doi.org/10.1002/cphc.201100234.